Controlling the Redox Properties of Organic Catalysts and Organic Photocatalysts – CO_2 Reduction by Renewable Organo-Hydrides and Photocatalyzed Polymerization using Visible Light

by

Chern-Hooi Lim

B.S., Chemical and Biological Engineering, Drexel University, 2010

A thesis submitted to the

Faculty of the Graduate School of the

University of Colorado in partial fulfillment

of the requirements for the degree of

Doctor of Philosophy

Department of Chemical and Biological Engineering

2015

This thesis entitled:

Controlling the Redox Properties of Organic Catalysts and Organic Photocatalysts – CO_2 Reduction by Renewable Organo-Hydrides and Photocatalyzed Polymerization using Visible Light

written by Chern-Hooi Lim

has been approved for the Department of Chemical and Biological Engineering,

University of Colorado Boulder

____

Charles B. Musgrave

____

Christopher N. Bowman

Date: ___________________

The final copy of this thesis has been examined by the signatories, and we find that both the content and the form meet acceptable presentation standards of scholarly work in the above mentioned discipline.

Abstract

Lim, Chern-Hooi (Ph.D., Chemical and Biological Engineering)

Controlling the Redox Properties of Organic Catalysts and Organic Photocatalysts – CO_2 Reduction by Renewable Organo-Hydrides and Photocatalyzed Polymerization using Visible Light

Thesis directed by Professor Charles B. Musgrave

The efficient chemical reduction of CO_2 to fuels has been of interest to scientists for decades with growing concerns about the impact of CO_2 on climate and future global energy demands motivating increasing efforts to meet this challenge. One conversion of specific interest — the reduction of CO_2 to methanol (CH_3OH) — is the focus of my thesis. Arguments here involve CH_3OH's utility as a practical C1 source for chemical synthesis and its attractive properties as a fuel not demanding the massive changes to the transportation fuels infrastructure required for a hydrogen economy.

My thesis focuses on understanding the role of pyridine in catalyzing the conversion of CO_2 to CH_3OH. In particular, I employed quantum chemical simulations as an invaluable tool to probe the redox properties of a number of pyridine-derived intermediates involved in the catalytic cycle of CO_2 reduction. Accurate determination of redox properties e.g. reduction potentials and hydricity is important to paint a detailed picture of energetics involved in the transformation of transient species during the course of CO_2 reduction, and thus the role of the catalytic species is revealed. One central aspect is the determination of the driving force to effect hydride transfer. 1,2-dihydropyridine (PyH_2) is a potent recyclable organo-hydride donor because it is driven by its proclivity to regain aromaticity; this mimics important aspects of the role of NADPH in the formation of C-H bonds in the photosynthetic CO_2 reduction process.

The aspect of controlling redox properties of molecules was applied to organic photocatalyst that affects photo-polymerization. In collaboration with the Stansbury's group, we elucidated the mechanism of polymer synthesis involving methylene blue chromophore with a sacrificial sterically-hindered amine reductant and an onium salt oxidant. The combination of these components yield interesting results: light-initiated free-radical polymerization continues over extended time intervals (hours) in the dark after brief (seconds) low-intensity illumination. We proposed that these observations are due to the latent production of free radicals from energy stored in a redox potential through a $2e^-/1H^+$ transfer process, which transforms the methylene blue chromophore to its high energy closed-shell intermediate of leuco methylene.

Dedication

To my mother, Lim Kee Moi, for her selfless sacrifices to put me through higher education.

To my late father, Lim Soon Seng, for instilling discipline and courage to help me face challenges.

To my sisters, Lim Lynn Hwee and Lim Tien Hwee, for encouragement you show me.

To my wife, Foo Mei Khoon, for being there for me during the highs and lows of my life.

To my host parents, Johnny and Debbie Abel, for helping me every step of the way through college and adapting a new life in the states.

To my badminton friends, for the joys and tears on the court.

Acknowledgements

Thanks to my advisor Prof. Charles Musgrave for cultivating my Ph.D. career for the last 5 ½ years; thanks to his openness and willingness to let me explore a wide-ranging of research topics that led to my successful Ph.D. experience. Thanks to my fellow thesis committee members, Prof. Will Medlin, Prof. Chris Bowman, Prof. James Hynes, and Prof. Andrew Bocarsly, for providing mentorship throughout my Ph.D. Thanks to Prof. Chris Bowman for generously allowing me to perform experimental work in his limited lab spaces. Thanks to Prof. James Hynes for spending countless hours with me to improve the manuscripts. Thanks to Prof. Garret Miyake for intellectual and stimulating discussions on Organo-catalyzed ATRP systems. Thanks to Dr. Aaron Holder for fruitful discussions on many research topics. Thanks to Dr. Brady Worrell for mentorship in organic synthesis. Thanks to Dr. Alan Aguirre for many long discussions on the methylene blue system. Thanks to Dr. Richard Shoemaker for helping me interpreting NMR results. Thanks to Dr. Jeremy Balsbaugh for patiently obtaining many ESI-MS spectra. Thanks to the donors of CU Crowdfunding for financial support of experimental work performed in Chapter 4. Chern-Hooi Lim was partially supported by Phillips 66 Fellowship.

Table of Contents

Chapter

Tables

Figures

Schemes

Introduction

The efficient chemical reduction of CO_2 to fuels has been of interest to scientists for decades with growing concerns about the impact of CO_2 on climate and future global energy demands motivating increasing efforts to meet this challenge. One conversion of specific interest — the reduction of CO_2 to methanol (CH_3OH) — is the focus of my thesis. Arguments here involve CH_3OH's utility as a practical C1 source for chemical synthesis and its attractive properties as a fuel not demanding the massive changes to the transportation fuels infrastructure required for a hydrogen economy. The partial reduction of CO_2 to CH_3OH is generally preferred over its complete reduction to methane; the former is a more valuable product, and is easier to handle and transport as a liquid fuel more compatible with existing transportation fuel technology.

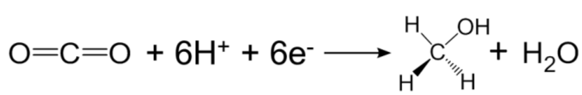

(1)

The conversion of CO_2 to CH_3OH is a six electron reduction described by the overall reaction eq. 1. When this reduction is carried out as a series of six one-electron transfers (ETs) and six proton transfers (PTs), every odd reduction necessarily produces a high-energy radical (open-shell) intermediate. Consequently, the three odd ETs generally result in slow kinetics and low selectivities unless these radicals are stabilized, for example by conjugation to an aromatic π-system or by orbital mixing with delocalized states of a metal surface. The issue of the difficulty of creating high-energy intermediates by the odd electron reductions is exemplified by the one-electron reduction of CO_2 to $CO_2^{-\bullet}$, which involves a very unfavorable reduction potential E^0 of -2.14 V vs. SCE.

The field of CO_2 reduction research has been largely dominated by the uses and studies of transition-metal catalysts. Despite many advances, many challenges remain: for example, CO_2 reduction has largely been confined to $2e^-$ products such as CO and formate, and in many cases large overpotentials are required to drive these reactions. In recent years, Bocarsly and coworkers employed pyridine in a photo-electrochemical system using a p-type GaP cathode to efficiently convert CO_2 to CH_3OH at 96% Faradaic efficiency and 300 mV of underpotential. Pyridine is a simple organic aromatic amine, in opposed to multifaceted transition metal complexes. The fact that it catalyzes the $6H^+$ and $6e^-$ reduction of CO_2 to CH_3OH is rather surprising. To date, pyridine is one of the most efficient and promising catalysts in converting CO_2 to CH_3OH; thus elucidation of pyridine's catalytic role will be of crucial importance in advancing the field of CO_2 reduction research.

My thesis focuses on understanding the role of pyridine in catalyzing the conversion of CO_2 to CH_3OH. In particular, I employed quantum chemical simulations as an invaluable tool to probe the redox properties of a number of pyridine-derived intermediates involved in the catalytic cycle of CO_2 reduction. Accurate determination of redox properties e.g. reduction potentials (E^0) is important to paint a detailed picture of energetics involved in the transformation of transient species during the course of CO_2 reduction, and thus the role of the catalytic species is revealed.

In Chapter 1 of my thesis, we examined in detail the nucleophilic attack of pyridinium radical (PyH^0) on CO_2 to form the transient pyridine carbamate ($PyCOOH^0$) species, which was proposed to be the key intermediate in the transformation of CO_2 to CH_3OH. PyH^0 can be formed by $1H^+$ and $1e^-$ transfers to pyridine (Py), where pK_a and E^0 are two thermodynamic parameters quantifying the likelihood of the PT and ET. Our work showed that the sequence of the PT and ET during the nucleophilic attack of PyH^0 on CO_2 is important. In particular, we showed that the N of PyH^0 first executes nucleophilic attack on the C of CO_2; this initiates an inner sphere ET process that forms a transient $PyH^+\bullet CO_2^{-\bullet}$ complex at the TS. This complex is stabilized by delocalization of the radical electron over PyH^+ and CO_2's conjugated π-system, thus avoiding the high energetic cost of forming the $CO_2^{-\bullet}$ anion radical. PT from $PyH^+\bullet CO_2^{-\bullet}$, to first form $Py\bullet CO_2^{-\bullet}$ and a transitory H_3O^+ and then $PyCOOH^0$ occurs along the exit channel. The PT producing the latter is mediated by a proton relay, an aspect detailed and discussed extensively in the chapter.

In Chapter 2 of my thesis, we studied the transformation of pyridine into a closed-shell hydride donor of 1,2-dihydropyridine (PyH_2). Hydride transfer reactions avoid the creation of open-shell radicals involving CO_2, thus creating low energy pathways for CO_2 reduction. First, Py undergoes a PT to form pyridinium (PyH^+), followed by an ET to produce PyH^0; this step is similar to the one examined in Chapter 1. We predicted that PyH^0 undergoes further PT-ET steps to form the key closed-shell, dearomatized (PyH_2) species. We then showed that the PyH_2/Py redox couple is kinetically and thermodynamically competent in catalytically effecting hydride and proton transfers (the latter often mediated by a proton relay chain) to CO_2 and its two succeeding intermediates, namely formic acid and formaldehyde, to ultimately form CH_3OH. One central aspect of Chapter 2 is the determination of PyH_2's driving force to effect hydride transfer. PyH_2 is a potent recyclable organo-hydride donor because it is driven by its proclivity to regain aromaticity; this mimics important aspects of the role of NADPH in the formation of C-H bonds in the photosynthetic CO_2 reduction process.

In Chapter 3, we moved on from the pyridine system to discover how frustrated Lewis pairs (FLP) catalyze the reduction of CO_2 by ammonia borane (AB). Stephan and coworkers employed FLP to activate CO_2 by irreversibly complexing with it to catalyze CO_2 reduction via hydride transfer (HT) from AB, where they observed 37-51% yield of CH_3OH was observed after 15 min. at ambient conditions. Our studies revealed that the LA (trichloroaluminum, $AlCl_3$) alone catalyzes hydride transfer (HT) to CO_2 while the LB (trimesitylenephosphine, $PMes_3$) actually hinders HT. The LB hinders HT by donating its lone pair to the LUMO of CO_2, increasing the electron density on the C atom and thus lowering its hydride affinity. Although the LB hinders HT, it nonetheless plays a crucial role by stabilizing the active FLP•CO_2 complex relative to the LA dimer, free CO_2 and free LB. This greatly increases the concentration of the reactive complex in the form FLP•CO_2 and thus increases the rate of reaction.

Chapter 4 highlighted my experimental efforts to synthesize organo-hydrides capable of reducing CO_2, in support of hydride transfer mechanism outlined in Chapter 2. Directed by computational designs we report the metal-free reduction of CO_2 to the formate anion, characterized and confirmed by ^{1}H-NMR, ^{13}C-NMR and ESI-MS, by use of a benzimidazole-based organo-hydride. We obtained the highest formate yield in the presence of potassium bromide under exceedingly mild conditions; the salt was proposed to stabilize the ionic products. Such benzimidazole-based organo-hydrides rival the hydride donating ability of noble metal-based hydrides, such as $[Ru(tpy)(bpy)H]^+$ and $[Pt(depe)_2H]^+$, thus demonstrating that these organo-hydrides stand as low-cost hydride transfer catalyst alternatives. Both benzimidazole and pyridine are aromatic amines that we suggest that the organo-hydrides derived from these two species harness the same dearomatization-aromatization driving force to effect hydride transfer reaction.

In Chapter 5, the aspect of controlling redox properties of molecules was applied to organic photocatalyst that affects photo-polymerization. In collaboration with the Stansbury's group, we set out to elucidate the mechanism of polymer synthesis involving visible-light organic photocatalysis of methylene blue chromophore with a sacrificial sterically-hindered amine reductant and an onium salt oxidant. The combination of these components yield interesting results: light-initiated free-radical polymerization continues over extended time intervals (hours) in the dark after brief (seconds) low-intensity illumination. We proposed that these observations are due to the latent production of free radicals from energy stored in a redox potential through a $2e^-/1H^+$ transfer process, which transforms the methylene blue chromophore to its high energy closed-shell intermediate of leuco methylene. This prevents immediate formation of open-shell (radical) intermediates from the amine upon light-absorption, and enables the 'storage' of light-energy without spontaneous initiation of the polymerization. Latent energy-release and radical production are then controlled by the subsequent light-independent reaction (analogous to the Calvin cycle) between leuco-methylene blue and the onium salt oxidant that is responsible for regeneration of the organic methylene blue photocatalyst.

1 Mechanism of Homogeneous Reduction of CO_2 by Pyridine: Proton Relay in Aqueous Solvent and Aromatic Stabilization

Chern-Hooi Lim,[†] Aaron M. Holder,[†,‡] and Charles B. Musgrave*[,†,‡]

[†]Department of Chemical and Biological Engineering, University of Colorado at Boulder, Boulder, Colorado 80309

[‡]Department of Chemistry and Biochemistry, University of Colorado at Boulder, Boulder, Colorado 80309

Journal of American Chemistry Society: dx.doi.org/10.1021/ja3064809

Abstract:

We employ quantum chemical calculations to investigate the mechanism of homogeneous CO_2 reduction by pyridine (Py) in the Py/p-GaP system. We find that CO_2 reduction by Py commences with $PyCOOH^0$ formation where: a) protonated Py (PyH^+) is reduced to PyH^0, b) PyH^0 then reduces CO_2 by one electron transfer (ET) via nucleophilic attack by its N lone pair on the C of CO_2 and finally c) proton transfer (PT) from PyH^0 to CO_2 produces $PyCOOH^0$. The predicted enthalpic barrier for this proton coupled ET (PCET) reaction is 45.7 kcal/mol for direct PT from PyH^0 to CO_2. However, when PT is mediated by one to three water molecules acting as a proton relay the barrier decreases to 29.5, 20.4 and 18.5 kcal/mol, respectively. The water proton relay reduces strain in the transition state (TS) and facilitates more complete ET. For PT mediated by a three water molecule proton relay, adding water molecules to explicitly solvate the core reaction system reduces the barrier to 13.6 - 16.5 kcal/mol, depending on the number and configuration of the solvating waters. This agrees with the experimentally determined barrier of 16.5 $\pm$ 2.4 kcal/mol. We calculate a pKa for PyH^0 of 31 indicating that PT preceding

ET is highly unfavorable. Moreover, we demonstrate that ET precedes PT in $PyCOOH^0$ formation, confirming PyH^0's pKa as irrelevant for predicting PT from PyH^0 to CO_2. Furthermore, we calculate adiabatic electron affinities in aqueous solvent for CO_2, Py and $Py{\bullet}CO_2$ of 47.4, 37.9, 66.3 kcal/mol respectively, indicating that the anionic complex $PyCOO^-$ stabilizes the anionic radicals CO_2^- and Py^- to facilitate low barrier ET. As the reduction of CO_2 proceeds through ET and then PT, the pyridine ring becomes aromatic and thus Py catalyzes CO_2 reduction by stabilizing the PCET TS and the $PyCOOH^0$ product through aromatic resonance stabilization. Our results suggest that Py catalyzes the homogeneous reductions of formic acid, and formaldehyde en route to formation of CH_3OH through a series of one-electron reductions analogous to the PCET reduction of CO_2 examined here, where the electrode only acts to reduce PyH^+ to PyH^0.

1.1 Introduction

Growing concern over the concentration of CO_2 in the atmosphere has motivated efforts to explore approaches to reduce the level of atmospheric CO_2.[1-3] One well-known proposal involves CO_2 sequestration and storage, which faces a number of difficult practical challenges including cost, efficiency, sustainability and safety.[4-8] Another possible approach involves chemical reduction of CO_2 into fuels, such as methanol (CH_3OH),[9-13] or C_n ($n \geq 2$) products, such as polyethylene.[3, 14] Despite its enormous potential benefits, efficient chemical conversion of CO_2 into useful reduced species remains a formidable challenge due to the thermodynamic and kinetic stability of CO_2 in its highly oxidized form.

Several chemical approaches have been explored in attempts to reduce CO_2 to CH_3OH, including homogeneous,[15-21] heterogeneous,[22-24] electrochemical[25-27], photochemical[28-31] and photoelectrochemical (PEC) reactions.[14, 32-38] PEC approaches show particularly significant promise because they can directly use sunlight as the renewable energy source to reduce CO_2. One especially intriguing PEC approach was discovered by Bocarsly *et al.* in 2008.[39] This system involves the use of pyridine (Py), which is suggested to undergo protonation to pyridinium (PyH^+) in acidic aqueous solutions and act as an electron transfer (ET) mediator that is electrochemically reduced to pyridinium radical (PyH^0) at a photoexcited p-type GaP electrode surface with an indirect bandgap of 2.24 eV.[39] PyH^0 has been proposed to act as the active catalyst that chemically reduces CO_2 to CH_3OH.[39-41] Although many details of the mechanism of CO_2 reduction by this system remain unknown, it is one of the most efficient PEC systems in reducing CO_2, converting CO_2 to CH_3OH at near 100% Faradaic efficiency at underpotentials ~300 mV below the standard potential of −0.52 V vs. SCE at a pH of 5.2.[39] PyH^+ was also observed to be electrochemically reduced by a Pd cathode, and to subsequently reduce CO_2 to CH_3OH at an overpotential of ~200mV.[42]

In 2010 Bocarsly *et al.* reported experimentally derived mechanistic steps for the reduction of CO_2 to CH_3OH by PyH^0, which they proposed occurs in the homogeneous phase.[40] However, Keith *et al*. argue that PyH^0 cannot be the active species that chemically reduces CO_2 in the homogeneous phase[43] based on their calculated homogeneous standard reduction potential (E^0) for PyH^+ of −1.47 V vs. SCE, which is −0.9 V more negative than the −0.58 V experimental value measured on a Pt electrode.[40] Thus, they conclude that PyH^0 should not be formed at E^0=−0.58 V and proceed to chemically reduce CO_2.[43] Their calculated E^0 agrees with the homogeneous PyH^+ reduction potentials calculated by ourselves (−1.31 V) and Tossell (−1.44 V).[44]

Because electrochemical reduction of PyH^+ is a highly surface dependent process[40, 45] experimentally measured reduction potentials on various electrode surfaces may deviate from calculated E^0s that assume a homogeneous process absent of surface effects. For example, in 1979 Yasukouchi *et al.* concluded that the PyH^+/PyH^0 reduction potential "at various metals (Pt, Pd, Au, Ti, Fe, Ni, Cd, Pb, Hg, etc.), on the whole, shifted to more negative potentials from platinum to mercury in the order similar to that of the well-known hydrogen overvoltage".[45] For instance, on Pt the peak potential, $E_p(PyH^+/PyH^0)$ is −0.41 V vs. SCE (−0.75 V vs. Ag/$AgClO_4$), which is consistent with E^0=−0.58 V vs. SCE measured by Bocarsly *et al.*[40] In contrast, on a dropping mercury electrode the measured −1.19 V vs. SCE (−1.53 V vs. Ag/$AgClO_4$) reduction half-wave potential approaches the calculated homogeneous E^0, which we propose results from diminishing surface effects of the Hg electrode on PyH^+ reduction. Conservation of energy dictates that the decreased reduction potential of PyH^+ exhibited on several surfaces, including Pt[40] and Pd,[42] must be accounted for by endothermic PyH^0 desorption, which may be overcome thermally or by applied overpotentials. Specifically, at least 16.8 kcal/mol or –0.73 V (the difference between the calculated homogeneous E^0 of –1.31 V and the experimentally measured –0.58 V) is required to produce PyH^0 in the homogeneous phase.

A number of experiments have demonstrated the surface-mediated reduction of PyH^+ to PyH^0, which then desorbs from the electrode and diffuses into the homogeneous phase.[39-42, 45-48] Yasukouchi *et al.* showed that peak currents in cyclic voltammograms (CV) a) varied linearly with acid concentration at constant Py concentration, and b) varied linearly with Py concentration at constant acid concentration, confirming that the protonated species PyH^+ is reduced to PyH^0.[45] These results are consistent with measurements performed independently by Bocarsly *et al.* in 1994 where at an electrolyte pH > 7 "no cyclic voltammetric features associated with pyridine are observed, indicating that the electroactive species is the protonated pyridinium cation".[42] The linear dependence of peak current on PyH^+ concentration shown by Yasukouchi *et al.* rules out the reduction of dimeric derivatives of PyH^+, such as the 4,4'–bipyridine dimer suggested by Keith *et al.*;[43] in agreement with Bocarsly *et al.*'s experimental observation that no Py is consumed to form dimers.[42] Furthermore, the oxidation current in CV observed when the potential scan was reversed indicates PyH^0 in the homogeneous phase.[40, 42, 45] Finally, in the PEC experiment performed by Bocarsly *et al.*, in addition to illumination of the p-GaP electrode, a negative electrical bias was applied.[39] Under these conditions the p-GaP electrode should possess a reduction potential significantly above the homogeneous E^0 of PyH^+ (−1.31 V), assuming that the conduction band edge of p-GaP is above the LUMO of PyH^+. Thus, PyH^0 should exist in the aqueous phase to homogeneously catalyze CO_2 reduction.

To further elucidate the surface dependence of PyH^+ electrochemical reduction we have performed calculations of PyH^+ adsorption on a water solvated unbiased Pt (111) surface (see Supporting Information (SI), section 1). Our calculations predict a strong binding interaction of PyH^+ with the electrode surface resulting in an adsorption energy of 1.0 eV/molecule on Pt (111). The strong binding energy of PyH^+ to the electrode surface is evident by the significant mixing of the adsorbate and surface states. This leads to broadening of the PyH^+ LUMO upon adsorption, resulting in transfer of $0.56e^-$ from Pt to PyH^+ and disruption of the aromaticity of

PyH^+. Consequently, the strong binding interaction of heterocyclic aromatic[49] PyH^+ with Pt (111) significantly lowers (becomes less negative) its heterogeneous reduction potential,[50] explaining the discrepancy between the experimentally measured heterogeneous E^0 and calculated homogeneous E^0 for PyH^+.

Keith *et al.* suggested that even if PyH^0 were formed it would not catalyze CO_2 reduction due to the difficulty in deprotonating the reduced species, based on their calculated pKa for PyH^0 of ~27.[43] Although we calculate a similar pKa for PyH^0 of ~31, we predict that PyH^0's pKa does not indicate the reactivity of PyH^0 towards CO_2 reduction because as we show, ET from PyH^0 to CO_2 precedes PT, which effectively lowers the pKa of the partially oxidized PyH^0 species; Our results demonstrate that the electrochemically produced PyH^0 reacts with CO_2 in the homogeneous phase to form the carbamate species $PyCOOH^0$, consistent with the EC' mechanism[50] previously proposed by Bocarsly *et al.*[40-41] Furthermore, our calculated enthalpic barrier agrees with Bocarsly's experimentally determined barrier of 16.5±2.4 kcal/mol.[41] We predict that two effects significantly lower the barrier for this process; 1) water molecules play a central role in facilitating $PyCOOH^0$ formation by solvent assisted proton coupled electron transfer (PCET) where ET precedes PT and 2) aromatic stabilization leads to the production of the low energy one e^- transfer product ($PyCOO^-$) to significantly lower the barrier for this process.

This contribution focuses on predicting a detailed mechanism of CO_2 reduction in the Py/p-GaP system with associated energetics and providing a thorough understanding of the intriguing effects that underlie the homogeneous reduction of CO_2 by PyH^0 to form $PyCOOH^0$. In particular, we attempt to answer several fundamental questions related to CO_2 reduction in this system. These include: i) Is CO_2 reduced through one e^- or two e^- transfers?; ii) If CO_2 reduction proceeds through one e^- transfers as proposed by Bocarsly *et al.*,[40] how does Py act as a catalyst to stabilize the high-energy CO_2^- anionic radical (E^0_{exp}=−2.18 V vs. SCE)?[51]; iii) Is ET and PT from PyH^0 to CO_2 stepwise or concurrent?; iv) If ET and PT occur sequentially, does ET precede PT or vice-versa?; and finally, v) Is CO_2 prebent to lower its reorganization energy for ET from PyH^0 and is prebending of CO_2 a general requirement for facile ET and thus an efficient reduction process?

Formation of the $PyCOOH^0$ carbamate species has been identified as an important intermediate and its production has been proposed to be the rate-determining step for the reduction of CO_2 to CH_3OH.[40-41] Scheme 1.1 shows two potential homogeneous routes to $PyCOOH^0$ formation.[40] Route 1 begins with the protonation of Py to form PyH^+. PyH^+ is then reduced at the p-GaP surface by a photoexcited electron to form PyH^0, which then diffuses into solution from the electrode. PyH^0 then reacts with CO_2 to form $PyCOOH^0$ in the homogeneous phase, which becomes further reduced into CH_3OH through a series of subsequent reduction steps. Route 2 is an alternative path that first involves the formation of the zwitterionic complex $Py{\bullet}CO_2$, which is then reduced and subsequently protonated. Bocarsly *et al.* determined that Route 2 does not contribute significantly to the overall reduction of CO_2 due to the presence of $Py{\bullet}CO_2$ at low concentration,[40] consistent with our calculated equilibrium constant of $1.0{\times}10^{-6}$ for $Py{\bullet}CO_2$ formation (See SI, section 2).

Scheme 1.1: Two potential routes for the formation of $PyCOOH^0$ in the homogeneous phase

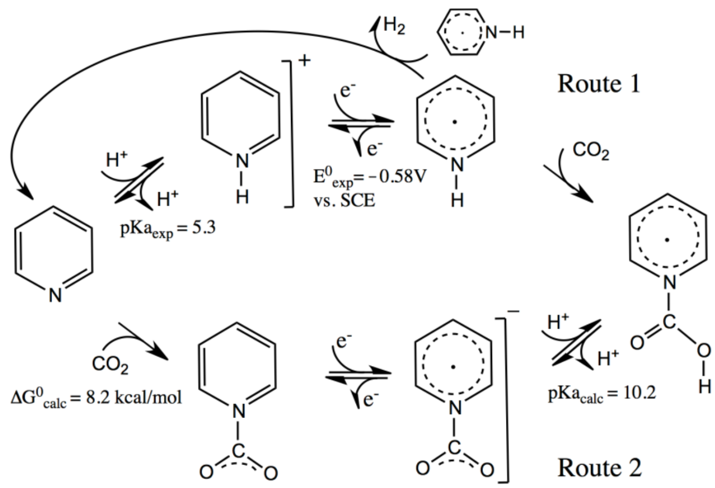

In contrast, experimental evidence suggests that $PyCOOH^0$ formation proceeds through Route 1. The pKa of Py is 5.3 and thus at a pH of 5.2 (slight acidic conditions due to the acid dissociation equilibrium of CO_2/Py species in aqueous solution) ~40% of Py is protonated in aqueous solution at equilibrium. Consequently, a considerable concentration of PyH^+ exists in the bulk solution, which can then be reduced to form PyH^0 either electrochemically[40, 42, 45] at various metal electrodes with different values of E^0 (see above) or photoelectrochemically by photoexcited p-GaP.[40] The reported −0.58 V (vs. SCE) E^0 of PyH^+ was measured on a Pt surface whereas E^0 at p-GaP is unknown. The PyH^0 formed by this reduction can then operate as an active species that is proposed to react with CO_2 to form $PyCOOH^0$ through inner-sphere ET.[40] Alternatively, as shown in Scheme 1.1, two PyH^0s can form H_2 as an unwanted side reaction[40, 42] through a self-quenching reaction at a rate constant of ~10^8 $M^{-1}s^{-1}$.[52] However, the concentration of PyH^0 derived from Bocarsly *et. al.*'s reported CV is only ~10^{-9} M.[40] At this low concentration, the bimolecular self-quenching rate is estimated to be only ~10^{-10} Ms^{-1}, consistent with the observed nearly reversible CV. In contrast, the concentration of CO_2 in the solution is ~30mM, more than ~10^7 times that of PyH^0. Therefore, the bimolecular collision probability between PyH^0 and CO_2 is much higher than for PyH^0 self-quenching.

While PyH^0 radical has been proposed as the active species catalyzing CO_2 reduction in this system, here we present a detailed mechanism with associated energetics for $PyCOOH^0$ formation from PyH^0 and CO_2 including kinetic barriers and TS structures and a specific description of Py's mechanism of activation. We calculate a high pKa for PyH^0 of ~31, in agreement with Keith *et al.*'s calculated pKa of ~27,[43] indicating that deprotonation of PyH^0 is thermodynamically unfavorable. Furthermore, Bocarsly *et al.* proposed that interaction between PyH^0 and the p-GaP surface may facilitate deprotonation or dissociation of the N−H bond of PyH^0.[41] Our results do not rule out active participation of p-GaP in activating $PyCOOH^0$ formation.[53] However, we do predict a pathway for homogeneous $PyCOOH^0$ formation with kinetics consistent with experiment[41] where the p-GaP[39] or other metal surfaces[40, 42, 45] only serve as the donor of a high-energy electron with sufficient energy to reduce PyH^+. We also show that the effects of proton shuttling and aromatic stabilization play key roles in the overall PCET process, catalyzing N−H bond dissociation and $PyCOOH^0$ formation, which have not been previously proposed.

The goals of this paper are: i) to identify a mechanism for homogeneous CO_2 reduction in this system, ii) to determine whether this mechanism is kinetically viable, iii) to elucidate the role of aqueous solvent in catalyzing $PyCOOH^0$ formation through prediction of the activation barriers of possible pathways, iv) to identify the properties of PyH^+/PyH^0 that enable it to perform as a $1e^-$ transfer mediator to facilitate CO_2 reduction, and v) to uncover the principles of CO_2 reduction at work in this system. We anticipate that the understanding our results provide will guide the catalyst community to discover additional systems similar to PyH^0 competent in reducing CO_2.

1.2 Computational details

The results we report were calculated using the unrestricted coupled-cluster method uCCSD(T)[54] combined with the cc-PVDZ, cc-PVTZ[55-56] and 6-311++G**[57] basis sets and the Restricted-Open Shell Moller-Plesset second order perturbation method[58] (roMP2) combined with the 6-31+G** basis set as implemented in the GAMESS[59-60] and Gaussian09[61] computational chemistry software packages. Computational details of the calculated adsorption energies discussed in the Introduction are provided in SI, section 1. roMP2 was chosen over the unrestricted uMP2 method largely because of its higher computational efficiency. The use of roMP2 was validated using both uCCSD(T) and uMP2 where roMP2/6-31+G** reproduces uCCSD(T)/cc-PVDZ enthalpic barriers evaluated at roMP2/6-31+G** geometries to within ~1.0 kcal/mol and uMP2/6-31+G** enthalpic barriers to within 2.5 kcal/mol (see Table 1.1). At the uCCSD(T) level of theory, the cc-PVDZ, cc-PVTZ and 6-311++G** basis sets result in similar enthalpic barriers (within ~2.5 kcal/mol) for PyH^0 + CO_2 (see footnote of Table 1.1).

We determined that the open-shell systems investigated are doublets and are not significantly multi-reference. Thus, they are well represented using a single Slater determinant by examining all stationary structures along the PyH^0 + CO_2 + $1H_2O$ (where a single H_2O acts as a proton relay) reaction pathway at the complete active space CASSCF (15,14) level of theory.[62] We found each structure to be dominantly composed (greater than 0.9 coefficient) of the ground state electronic configuration (see SI, section 3). Thus, the high-level uCCSD(T) method should provide a reliable benchmark for energies for this reaction (see Table 1.1). We found that various density functional theory (DFT) methods produced results with artifacts associated with DFT’s tendency to over stabilize zwitterionic charge transfer states, which arises from self-interaction and delocalization errors.[63-66] This is problematic when describing processes involving ET and aromaticity such as the PCET process catalyzed by PyH^0 examined here.

All reactant and product structures were verified to have real vibrational frequencies, meanwhile TSs were verified to have only one imaginary frequency corresponding to the reaction coordinate of interest as confirmed by both inspection of the normal mode and intrinsic reaction coordinate (IRC) calculations. Frequency calculations at the roMP2/6-31+G** level of theory were also employed for calculation of zero-point energies (ZPE), and thermal contributions to the enthalpy at 298 K and 1 atm.

All calculations employed the conductor-like polarizable continuum implicit solvent model (CPCM) to describe the effects of solvation,[67-68] where only electrostatic solute-solvent interactions were considered. We used the SMD solvent model[69] to calculate that neglect of non-electrostatic terms in CPCM leads to errors in the activation enthalpies of less than 2 kcal/mol. The details regarding these SMD calculations and the use of the CPCM model to describe the effects of solvation on enthalpic barriers are described in the SI, section 4. Because CPCM is less accurate in describing solvation of species with concentrated charges,[70-72] we also report energies where explicit H_2O molecules were added to explicitly solvate the system.

In the mechanism of CO_2 reduction catalyzed by PyH^0 we propose that H_2O actively participates in the PCET mechanism by undergoing O−H bond formation and dissociation to transfer protons. Consequently, we explicitly include these active H_2O's as part of the core reaction system. For example, in the PyH^0 + CO_2 + **3**H_2O + **10**H_2O(S) reaction, three H_2O molecules actively participate in the reaction while ten H_2O molecules are included to solvate the core reaction system and are labeled as H_2O(S) to indicate that they are *explicit* solvent. For each system, PyH^0 and CO_2 together with the active and solvating water molecules are embedded in a CPCM *implicit* solvent. All explicit H_2O molecules are treated quantum mechanically at the same level of theory as PyH^0 and CO_2. Using explicit solvent introduces challenges associated with particular solvent configurations producing different enthalpic reaction barriers.[73-74] One approach to examine how solvent dynamics leads to kinetic dispersion is to use molecular dynamics to sample the effect of solvent configurations on the reaction barrier.[73] On the other hand, CPCM implicit solvent empirically describes the contributions of solvent configurations to solvation energies in aqueous solutions in close agreement with explicit molecular dynamics.[73] We discuss the effects of solvent configurations on the reaction barrier below and in the SI, section 5.

Atomic charges were calculated using a Mulliken[75] population analysis and the CHELPG electrostatic potential derived charges method[76] at the roMP2/6-31+G**/CPCM-H_2O level of theory. In contrast, adiabatic electron affinity (EA) and E^0 calculations employed the high-level CBS-QB3/CPCM-H_2O compound method.[77] E^0s were calculated following the same procedure used by Winget *et al.* and Tossell;[44, 78] details describing this approach can be found in the SI, section 6. pKa calculations were performed using a similar approach to that used by Liptak *et al.*,[79] as described in the SI, section 6.

1.3 Results and Discussion

1.3.1 High barrier to formation of $PyCOOH^0$ for unmediated reaction between PyH^0 and CO_2. The PEC reduction of CO_2 to CH_3OH in the Py/p-GaP system has been observed to proceed at room temperature via a rate-limiting step with an effective activation barrier of 16.5±2.4 kcal/mol.[41] The rate-limiting step for this process has been proposed[41] to be the formation of $PyCOOH^0$ (see Figure 1.1) from PyH^0 and CO_2 where a proton is transferred from the nitrogen atom of PyH^0 to an oxygen atom of CO_2. Figure 1.1 shows the cis and trans isomers of $PyCOOH^0$ with the trans isomer being the more stable of the two by 6.1 kcal/mol. Our calculations predict a 45.7 kcal/mol enthalpic barrier for this step when it occurs in the homogeneous phase and is modeled as PyH^0 + CO_2 in an implicit aqueous solvent. The calculated ~46 kcal/mol barrier lies significantly higher than the experimentally determined barrier of ~17 kcal/mol. Furthermore, we obtained a similar barrier of 46.8 kcal/mol with the high-level uCCSD(T)/roMP2 method, confirming that this pathway is not active at 298 K. Figure 1.1 shows the optimized reactant, TS and product structures. In this reaction the less stable cis isomer of $PyCOOH^0$ (Figure 1.1c) is formed. We calculate an isomerization barrier of 1.6 kcal/mol to convert the cis isomer to the trans isomer (Figure 1.1d).

In the formation of $PyCOOH^0$ the reaction proceeds via nucleophilic attack where PyH^0 approaches CO_2 with its N lone pair directed towards the C atom of CO_2. Figure 1.2 presents a localized orbital representation to illustrate donation of electron density from the PyH^0 N lone pair into the π^* orbital of CO_2 along the reaction coordinate R_{N-C}. As R_{N-C} decreases, CO_2 first bends as a result of nucleophilic attack and subsequently a proton transfers from PyH^0 to CO_2, suggesting that ET precedes and is coupled to PT (*vide infra*).

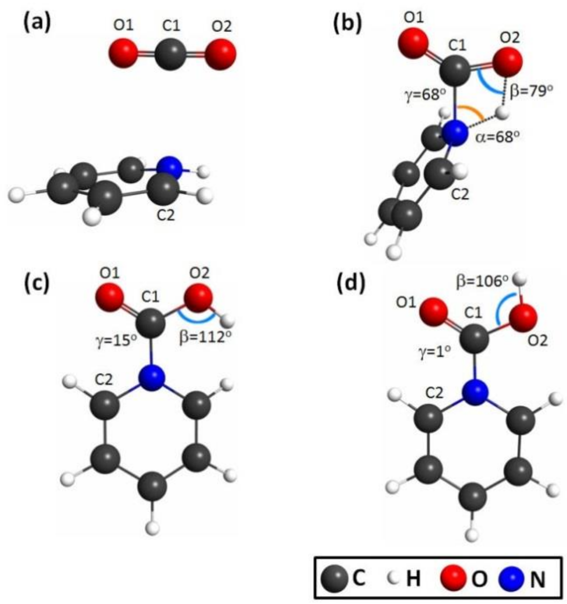

Figure 1.1: Formation of $PyCOOH^0$ by direct (unmediated) PT from PyH^0 to CO_2.
(a) Reactant complex, (b) TS for direct PT; RN−C = 1.61 Å, α is the C−N−H angle and β is the C−O−H angle, as shown, (c) cis isomer and (d) trans isomer products with γ indicating the dihedral angle O1−C1−N−C2.

Calculating the energetics of this PCET reaction step does not pose any particularly difficult challenges. For example, proper description of the electronic structure of the reacting system does not require a multi-reference method and should be well-described by reliable single Slater determinant *ab initio* methods. Consequently, the considerable disagreement between the barrier for the formation of $PyCOOH^0$ calculated using reliable quantum chemical methods and the experimentally determined barrier suggests that either a heterogeneous process involving the p-GaP electrode catalyzes $PyCOOH^0$ formation,[41] or that alternative lower barrier pathways occurring in the homogeneous phase may be active. However, a thorough search for alternative TSs for homogeneous formation of $PyCOOH^0$ by direct PT from PyH^0 to CO_2 (TS shown in Figure 1.1 b) yielded no low barrier pathways.

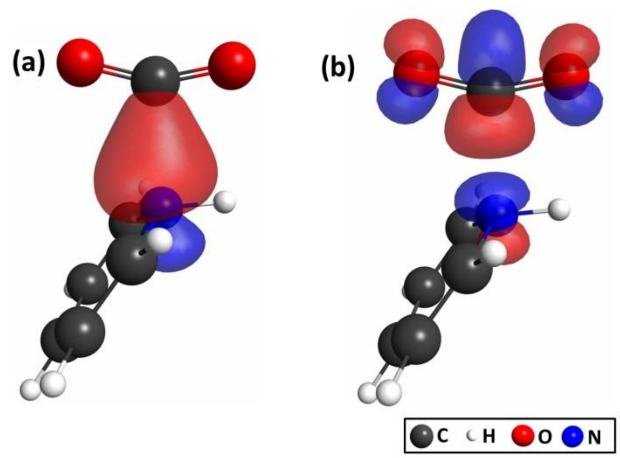

Figure 1.2: Localized orbitals.
(a) Localized representation of the N lone pair orbital of PyH^0 and (b) Localized representation of the π* orbital of C in CO_2 for a molecular structure along the IRC for $PyCOOH^0$ formation at R_{N-C}= 2.01 Å. The TS occurs at R_{N-C} = 1.61 Å.

After a comprehensive search did not identify alternative low barrier pathways for the homogeneous formation of $PyCOOH^0$ via direct PT from PyH^0 to CO_2, we hypothesized that H_2O molecules in the aqueous solvent act as proton relays to catalyze $PyCOOH^0$ formation. This supposition was based on thorough inspection of the TS structure for direct PT from PyH^0 to CO_2 (illustrated in Figure 1.1b), which exhibits considerable strain. The substantial strain present in the TS primarily arises from: i) bending of the C−O−H angle to 79° relative to its near tetrahedral strain-free angle of 112° in the product structure, ii) bending of the C−N−H angle to 68° relative to its nearly strain-free angle of between 109° and 120°, and iii) rotation of the dihedral angle between the Py and CO_2 planes to 68° relative to its angle of 15° in the product. We suggest that H_2O molecules in the aqueous solvent form a *proton shuttling network* that lowers the barrier to $PyCOOH^0$ formation by providing alternative, lower barrier paths for PT from PyH^0 to CO_2. Although PT from PyH^0 to CO_2 via proton shuttling mediated by water is indirect, the TSs involve substantially less strain and thus a considerably lower barrier than direct PT from PyH^0 to CO_2 (*vide infra*).

Although a proton relay has not been previously proposed for CO_2 reduction in the Py/p-GaP system, proton shuttling mechanisms have been proposed for a number of other processes.[80-90] While enthalpic barriers to reaction generally determine the kinetics of reactions, especially at low to moderate temperatures, entropic considerations should not be neglected. For example, because CO_2 reduction in the Py/p-GaP system occurs in aqueous solvent, pathways that involve specific solvent configurations may be entropically disfavored. However, if interactions in the solute-solvent system arrange the solvent into configurations that require little solvent reorganization to configure the solvent into the TS structure, a minimal entropic penalty will be required for solvent reorganization to configurations of the TS.

1.3.2 Proton relay composed of one to three waters. To determine whether a proton relay through water can indeed lower the barrier to $PyCOOH^0$ formation via mediated PT from PyH^0 to CO_2 we calculated the transition states for proton shuttling from PyH^0 to CO_2 through one, two, and three H_2O molecules. In each case, hydrogen bonding positioned the water molecules relative to PyH^0 and CO_2 with the hydrogen atoms of the water arranged to facilitate PT (see Figure 1.3); these configurations are stabilized by significant hydrogen bonding. In addition to the explicit inclusion of water molecules that actively participate in the reaction, the $PyH^0 + CO_2 + mH_2O$ core reaction system (with m=1 to 3) was solvated in implicit solvent. Figure 1.3a shows the TS for $PyCOOH^0$ formation via direct PT (repeat of Figure 1.1b for comparison). Figure 1.3b shows the TS for $PyCOOH^0$ formation where a single H_2O acts as a proton shuttle between PyH^0 and CO_2; the water molecule concomitantly accepts a proton from the N of PyH^0 and donates a different proton to an O atom of CO_2.

Remarkably, a single water molecule catalyzes $PyCOOH^0$ formation and lowers the barrier 16.2 kcal/mol from ΔH^0_{act} = 45.7 to 29.5 kcal/mol. The TS for $PyCOOH^0$ formation via proton shuttling through one H_2O molecule involves little strain; i) the C−O−H angle (β) in the TS is 109^o, similar to its angle of 112^o in the product; ii) the C−N−H angle (α) in the TS is 98^o, close to the strain-free angle between 109^o and 120^o and iii) the dihedral angle (γ) between the Py and CO_2 planes in the TS is 27^o, similar to its angle of 15^o in $PyCOOH^0$. Although these results predict that water catalyzes $PyCOOH^0$ formation and facilitates PT from the PyH^0 to CO_2 by shuttling protons, the predicted barrier of 29.5 kcal/mol is still significantly above the experimentally determined barrier of 16.5 kcal/mol for CO_2 reduction in this system. However, this pathway involves only a single water molecule acting as a proton shuttle.

While one water molecule can relay a proton, multiple water molecules can also be arranged to form a chain of proton shuttles where protons are relayed from one water molecule to the next. Figure 1.3c and d show proton relays composed of a chain of two and three water molecules. When two H_2O molecules are arranged to relay the proton from PyH^0 to CO_2, we calculate that the activation barrier (Figure 1.3c shows the TS) is lowered by an additional 9 kcal/mol to 20.4 kcal/mol. Similarly, arranging three water molecules into a proton shuttling sequence lowers the barrier to 18.5 kcal/mol (TS shown in Figure 1.3d). We also examined longer chains of H_2O molecules; however, each relaxed to a chain of three H_2O’s with the remaining waters solvating the chain. Like direct PT (Figure 1.3a), PT from PyH^0 to CO_2 mediated through one and two water molecules produces the higher energy cis isomer of $PyCOOH^0$, which is easily converted to the more stable trans isomer through a barrier of only 1.6 kcal/mol. In contrast, PT through the three H_2O molecule shuttle yields the more stable $PyCOOH^0$ trans isomer (Figure 1.1d).

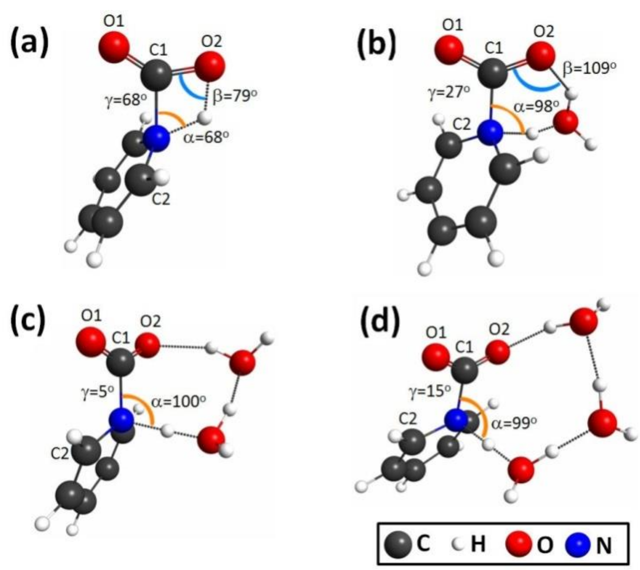

Figure 1.3: TS structures for the formation of $PyCOOH^0$ via proton shuttling through 0 to 3 H_2O molecules.
(a) Direct PT from PyH^0 to CO_2 (same as Figure 1.1b), (b) PT from PyH^0 to CO_2 mediated by a one water molecule proton relay, (c) PT mediated by a chain of two water molecules and (d) PT mediated by a chain of three water molecules. α refers to angle C−N−H, β to angle C−O−H and γ refers to the dihedral O1−C1−N−C2.

The ability of the three H_2O proton relay to form the more stable $PyCOOH^0$ trans isomer is illustrated in Figure 1.4. It shows the proton transfer from PyH^0 to CO_2 via a sequence of three H_2O molecules using several structures along the IRC of the reaction step $PyH^0 + CO_2 + 3H_2O$ −> $PyCOOH^0 + 3H_2O$. The reaction begins at reactant (a), followed by N−C bond formation through nucleophilic attack by the N of PyH^0 on the C of CO_2, similar to the direct PT case presented in Figure 1.2. The reaction then proceeds through (b), a TS for PT from $PyH^0 \bullet CO_2$ to the first water molecule in the shuttling chain, followed by (c) and (d), which show subsequent PTs from H_3O^+ to the next water in the chain and finally (e), PT from H_3O^+ to $PyCOO^-$ to form (f) $PyCOOH^0$ (trans). The ability of the three H_2O molecule proton relay to produce the more stable trans isomer further demonstrates the ability of the proton shuttle to lower the barrier to form $PyCOOH^0$. We summarize the enthalpic barriers (ΔH^0_{act}) and reaction enthalpies (ΔH^0_{rxn}) at standard conditions in Table 1.1 for $PyCOOH^0$ formation by various PT pathways involving proton relays formed by different numbers of H_2O molecules. Figure 1.5 depicts the stationary points along the PES for $PyCOOH^0$ formation from the data in Table 1.1 and emphasizes proton shuttling in lowering $PyCOOH^0$ formation barriers.

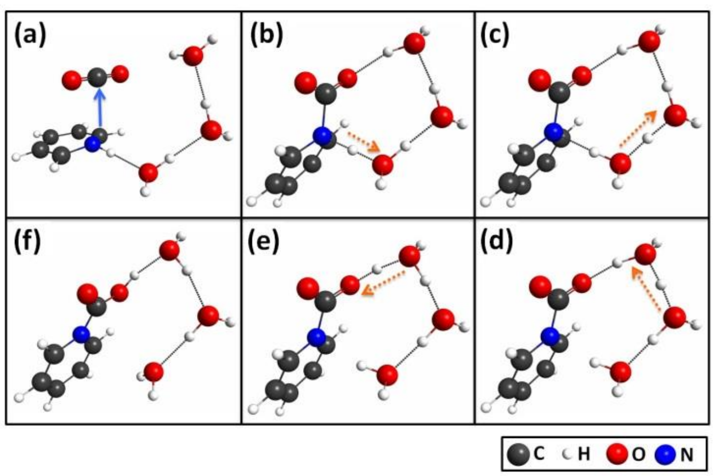

Figure 1.4: Structures along the IRC for the $PyH^0+CO_2+3H_2O$ reaction step of indirect proton transfer from PyH^0 to CO_2 via a proton relay comprised of a chain of three H_2O molecules.
(a) Reactants, (b) TS for $PyCOO^-$ formation by PT from PyH^0 to a H_2O, (c) and (d) PT from a H_3O^+ to a neighboring H_2O, (e) PT from H_3O^+ to $PyCOO^-$ and (f) the trans $PyCOOH^0$ product. The dashed orange arrows indicate the direction of PT and the blue arrow the nucleophilic attack on the C of CO_2.

The results shown above demonstrate that the 45.7 kcal/mol barrier to form $PyCOOH^0$ without the aid of the water proton relay is ~30 kcal/mol above the experimentally determined barrier of 16.5 kcal/mol. Furthermore, we predict that the barrier decreases to ~18 to 20 kcal/mol when multiple water molecules form a proton shuttling relay. As we discuss in detail below, the barrier declines further to between 13.6 to 16.5 kcal/mol when the TSs are calculated with explicit water molecules solvating the reaction complex (Table 1.1 cases **e**-**i** and Figure 1.5). We speculated that proton shuttling via water may partially lower the reaction barrier by alleviating strain in the TS in the: i) C−N−H angle, α ii) C−O−H angle, β and iii) the dihedral angle, γ, between the Py and CO_2 planes. Next, we analyze how proton shuttling via water reduces those strains.

1.3.3 Proton relay network reduces strain in the TS. Figure 1.1 shows the reactant, TS and product structures for $PyCOOH^0$ formation for direct PT from PyH^0 to CO_2. While the product has a C−O−H angle of 112°, this angle is 79° in the TS structure. This suggests that part of the activation barrier can be attributed to this angular strain. Although this analysis compares the TS structure to the product rather than the reactant to estimate the strain in the TS from the C−O−H angle, it still indicates a high-lying TS because this reaction step is relatively thermoneutral (see Table 1.1). If this reaction were significantly exothermic, this approach to analyzing the strain could be misleading because a reaction with a low barrier in the forward direction could still exhibit a large degree of strain between the TS and product.

Table 1.1: Enthalpic barriers and reaction enthalpies for the reaction of PyH^0+ CO_2+ mH2O + $nH_2O(S)$ to form $PyCOOH^0$ where m is the number of active H_2O's in the proton relay and n is the number of solvating H_2O's

System[a]	ΔH^0_{act}		ΔH^0_{rxn}	
	CCSD(T)[b]	MP2[c]	CCSD(T)[b]	MP2[c]
a) PyH^0+CO_2	46.8[d]	45.7	9.3[e]	8.9[e]
b) PyH^0+CO_2+H_2O	29.9	29.5[f]	5.7[e]	6.0[e]
c) PyH^0+CO_2+$2H_2O$	21.2	20.4	3.4[e]	3.3[e]

d) PyH^0+CO_2+3H_2O	18.6	18.5	−5.2	−3.2
e) PyH^0+CO_2+3H_2O+ H_2O(S)	–	16.5	–	−2.2
f) PyH^0+CO_2+3H_2O+ 4H_2O(S)	–	14.6	–	−4.0
g) PyH^0+CO_2+2H_2O+5H_2O(S)	–	14.6	–	0.6[e, g]
h) PyH^0+CO_2+3H_2O+6H_2O(S)	–	14.5[h]	–	−4.2
i) PyH^0+CO_2+3H_2O+10H_2O(S)	–	13.6	–	−5.8

[a]All enthalpies in kcal/mol at 298K and 1 atm where electrostatic solute-solvent interactions were treated using CPCM with aqueous solvent. In case **e**-**i**, explicit solvent was also employed to treat solvation. [b]Single-point uCCSD(T)/cc-PVDZ//roMP2/6-31+G** enthalpies. [c]roMP2/6-31+G**. [d]Reported barrier at cc-PVDZ (46.8 kcal/mol) basis set agrees with cc-PVTZ (44.5 kcal/mol) and 6-311++G** (46.9 kcal/mol). [e]Cis isomer of $PyCOOH^0$ was produced (Figure 1.1c). [f]uMP2/6-31+G** produced a similar barrier of 31.9 kcal/mol. [g]$PyCOOH^0$ (cis) product with partial PT from H_3O^+ to CO_2 (see SI, section 5). [h]15.3 kcal/mol barrier obtained with a different explicit H_2O configuration (see SI section 5).

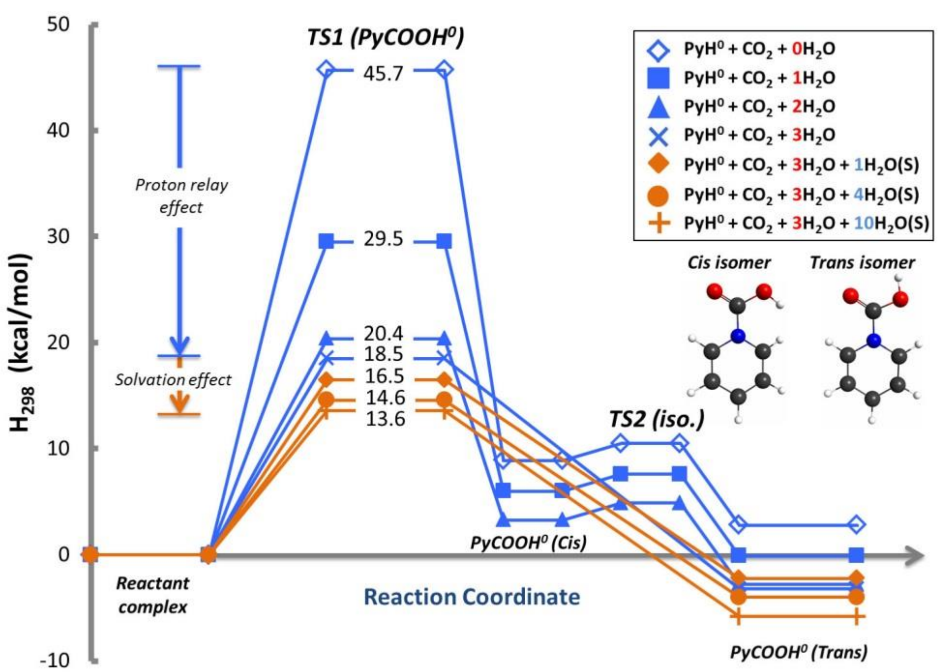

Figure 1.5: Stationary points along the potential energy surfaces for $PyCOOH^0$ formation via both direct and indirect (via the water proton relay) PT from PyH^0 to CO_2.

The $PyCOOH^0$ formation barrier (TS1) decreases with increasing number of water molecules **m** in the proton relay from 0 to 3 and by including explicit water (denoted by **S**) to solvate the reaction complex. TS2 is for cis-trans isomerization, which lies 1.6 kcal/mol above the cis isomer. Cases **g** and **h** reported in Table 1.1 have been omitted for clarity.

We estimate that strain in the C−O−H angle accounts for ~15 kcal/mol of the activation energy (see Figure 1.6a and the SI, section 7). In contrast, for the one water molecule proton relay (Figure 1.3b), the C−O−H angle in the TS is 109°, similar to its angle of 112° in the product, leading to a substantial reduction in strain and a decrease of 16.2 kcal/mol in the barrier (see Table 1.1). In the cases of the two (Figure 1.3c) and three (Figure 1.3d) water molecule proton relays, the TS involves PT to form a H_3O^+ intermediate. Consequently, the O−H bond of the product is not in the process of forming at the TS. Another potential source of strain is the C−N−H angle. In the event of direct PT (Figure 1.1b or Figure 1.3a), this angle is 68° compared to a strain-free angle between 109 and 120°; the proton relay partially alleviates this strain, leading to C−N−H angles in the TSs of 98° (one H_2O), 100° (two H_2O's) and 99° (three H_2O's).

Lastly, strain can also be attributed to the rotation of the dihedral angle between the PyH^0 and CO_2 planes, i.e. the dihedral angle is 68° at the TS versus 15° in the product $PyCOOH^0$. Using $PyCOO^-$ as a model system, we determined that this dihedral strain contributes ~10 kcal/mol to the activation barrier (see Figure 1.6b), which is consistent with the 16 kcal/mol barrier to internal rotation of this dihedral previously calculated by Han *et al.*[91] They explained that the barrier to rotation of this dihedral angle arises from the π character of the N−C bond,[91] which is supported by the N−C π orbital shown in Figure 1.6b.

1.3.4 Adding solvating waters to the $PyH^0 + CO_2 + 3H_2O$ system. Although CPCM generally calculates solute-solvent electrostatic interactions correctly, it describes solvation of solutes possessing concentrated charges less accurately.[70-72] For example, the negative charge of the $PyCOO^-$ complex at the TS is concentrated on CO_2 (discussed further below) and consequently, CPCM may not accurately describe solvation of this TS. Thus, to determine the effect of describing the solvation of species with concentrated charge, we also employed explicit H_2O to solvate the reacting system.[74, 92] To examine the significance of including explicit solvent, we added one, four, six and ten additional H_2O molecules to solvate the reaction core consisting of PyH^0, CO_2 and the H_2Os of the proton relay. These additional water molecules were treated at the same level of theory as the rest of the system. Similar to the previously discussed calculations, the $PyH^0 + CO_2 + 3H_2O + nH_2O(S)$ systems, consisting of the core reactive system and **n** explicit solvating water molecules, are embedded in a continuum polarizable solvent. The effect of additional explicit solvent is reflected in the results shown in Table 1.1 entries **e**-**i** and Figure 1.5. We find that adding one solvating water molecule to hydrogen bond with an O of CO_2 and a H of the neighboring H_2O of the proton relay included in the $PyH^0 + CO_2 + 3H_2O$ core reaction system (Figure 1.7a) decreases the barrier by 2 kcal/mol to 16.5 kcal/mol. Adding four and six solvating H_2O's (Figure 1.7b and c) only decreases the barrier by 4 kcal/mol to 14.6 and 14.5 kcal/mol. Finally, upon adding ten solvating H_2O's, the reaction barrier decreases to 13.6 kcal/mol, as shown in Figure 1.7d. In the SI, section 5, we show that the barrier calculated using four to ten explicit solvating H_2O's is converged within the accuracy of the methods employed.

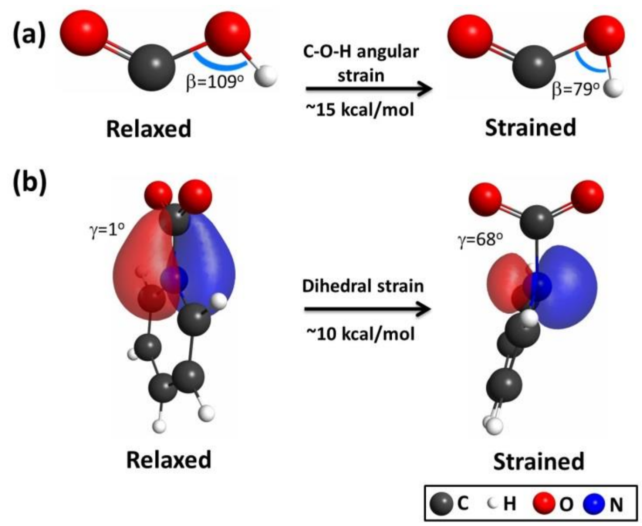

Figure 1.6: Strain energy contributions to the activation barrier for $PyCOOH^0$ formation.
Estimated using (a) $COOH^0$ as a model to estimate the angular strain in the C–O–H angle β and (b) $PyCOO^-$ as a model to estimate the dihedral strain between the Py and CO_2 planes, γ.

Adding multiple solvating H_2O molecules leads to stabilization of one of the shuttling protons such that a H_3O^+ intermediate results. Here, the 14.6, 14.5 and 13.6 kcal/mol barriers for four, six and ten solvating H_2O's, respectively, are the activation energies to form the $PyCOO^-$ ($PyCOO^-$•H_3O^+•$2H_2O$) intermediate rather than $PyCOOH^0$. In these three cases, the formation of $PyCOOH^0$ proceeds through a second TS where a proton is relayed from the H_3O^+•$2H_2O$ complex to $PyCOO^-$ with a negligible activation energy (less than 0.1 kcal/mol at 0K) which becomes barrierless upon addition of the ZPE and the thermal correction at 298K. Thus, the 14.6, 14.5 and 13.6 kcal/mol barriers to form the $PyCOO^-$•H_3O^+ intermediate are effectively the barriers to form $PyCOOH^0$ and this pathway contributes to the overall rate of $PyCOOH^0$ formation. We calculated a pKa of 10.2 for $PyCOO^-$/$PyCOOH^0$, thus $PyCOOH^0$ should dominate over $PyCOO^-$ at thermodynamic equilibrium. Our results demonstrate that inclusion of explicit H_2O molecules to solvate the active reaction complex lowers the reaction barrier. This effect is caused by additional solvent stabilization of the concentrated charges on CO_2 (in the $PyCOO^-$

complex) at the TS relative to the reactants than what is provided by the implicit CPCM solvent. However, the lowering of the activation barrier from 18.5 kcal/mol (CPCM only) to 13.6 kcal/mol (ten H_2O(S) case) is likely overestimated.

Inclusion of an explicit first solvation shell with no surrounding solvent can result in over polarization between the explicit solvent and the core reaction system[73] due to the absence of interactions with additional solvation shells. In the case of aqueous solvent and a TS more polar than the reactants, this may result in excessive lowering of the activation barrier. However, embedding of the explicit solvent in implicit solvent mitigates this effect through interactions of the infinite bath of implicit solvent with the first solvation shell. For example, the PCET barrier for PyH^0 + CO_2 + 3H_2O + 4H_2O(S) increased from 12.5 kcal/mol (gas phase) to 14.6 kcal/mol (CPCM) with addition of implicit solvent (see the SI, section 4). The extent to which CPCM alleviates the error of over polarization of the first solvation shell effect is unknown and beyond the scope of this study. However, for PyH^0 + CO_2 + 3H_2O, the results with explicit solvent (over polarization) and CPCM only (under polarization), respectively, set a lower and an upper bound to the barrier; thus, our results predict that the PCET barrier lies between 13.6 and 18.5 kcal/mol.

Introduction of explicit solvent can introduce additional challenges due to the large solvent configurational space. For example, particular solvent configurations stabilize the TS relative to the reactants more than others. These configurational variations introduce a distribution of enthalpic barriers.[73] For example, in Table 1.1, we report the barrier for PyH^0 + CO_2 + **3**H_2O + **6**H_2O(S) to be 14.6 and 15.3 kcal/mol in two possible solvent configurations (see

SI, section 5). Solvent reorganization due to thermal fluctuations introduces similar effects and consequently a distribution of enthalpic barriers such that the experimentally determined barrier corresponds to an ensemble average over many solvent configurations. The barriers involving explicit H_2O reported in Table 1.1 are calculated for only a few of the many possible configurations that can contribute to the ensemble averaged barrier. Moreover, configurations that result in proton relays composed of various numbers of H_2O can contribute to the ensemble averaged barrier. For instance, the barrier for PyH^0+CO_2+$2H_2O$+$5H_2O(S)$ in a two water proton relay is 14.6 kcal/mol (Table 1.1, entry **g**), similar to the barrier of the three water proton relay.

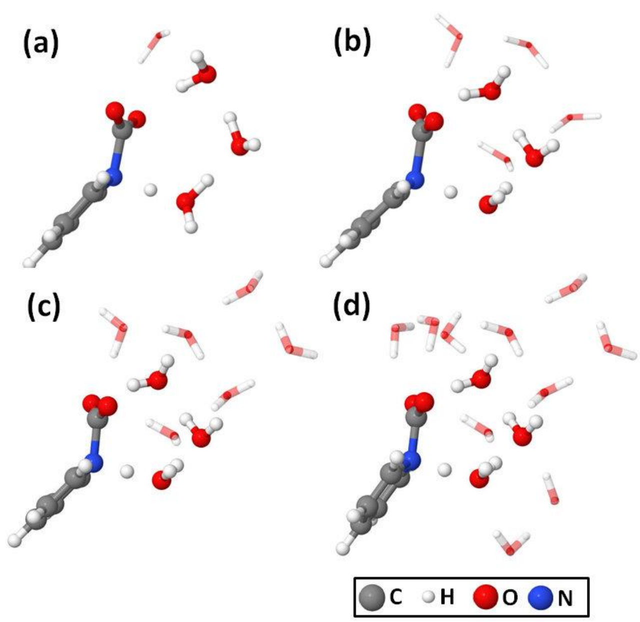

Figure 1.7: TS structures for PyCOOH0 formation via a proton shuttling network formed by three H2O molecules (illustrated using a ball-and-stick model) and (a) one, (b) four, (c) six and (d) ten solvating H2O's. Solvating H2O's are depicted by a stick model.

1.3.5 Comparison with the experimentally determined barrier. Our results demonstrate the central role of proton shuttling via water in catalyzing the formation of $PyCOOH^0$, where shuttling through the three water molecule relay lowers the reaction barrier by ~27 kcal/mol relative to direct PT. The 18.5 kcal/mol barrier for PyH^0 + CO_2 + **3**H_2O modeled in CPCM, confirmed by high-level CCSD(T) results, should provide a reliable baseline estimate for the activation barrier to form $PyCOOH^0$ from reaction of PyH^0 and CO_2 in the homogeneous phase because the continuum description of the solvent implicitly averages out the variations in the enthalpic barrier resulting from solvent fluctuations despite its limitation in describing solute with concentrated charges.[73, 93] To better describe interaction between the solvent and the solute with localized charges, four, six and ten solvating H_2O's were included. These models all predicted a barrier within 0.5 kcal/mol of 14.1 kcal/mol, which is well within the accuracy of roMP2. Thus, 14.1±0.5 kcal/mol provides our best estimate of the barrier for the three water proton relay configuration, assuming that CPCM alleviates most of the over polarization of the TS by the first solvation shell (see discussion above). This estimate does not explicitly consider how other solvent configurations might affect the barrier beyond demonstrating that it changes by less than 1 kcal/mol for four to ten explicit H_2O's and for two different solvent configurations for the case of six explicit solvating H_2O's, as shown in Table 1.1. Moreover, the two water proton relay also proves to be a viable pathway with a 14.6 kcal/mol barrier for PyH^0 + CO_2 + $2H_2O$ + $5H_2O(S)$ (see Table 1.1, case **g**).

We propose that the experimentally determined barrier of 16.5±2.4 kcal/mol is consistent with a weighted average of active pathways that consist of proton transfers through relays of one to three H_2O molecules where the ensemble averaged barrier depends on both the configurational and Boltzmann weight for each pathway. Although an exhaustive examination of all possible pathways and calculation of the configurational weights for the pathways we report is beyond the scope of this study, the ensemble average for the lowest energy pathways we report must lie within the range of 13.6 kcal/mol (two and three water proton relays) and 22.8 kcal/mol (one water proton relay, see SI, section 5 for estimation of this barrier). Because the barrier for reaction through the one H_2O shuttle is ~9 kcal/mol larger than the barrier for PCET through two and three H_2O's the configurational weight on the one H_2O shuttle must be at least ~10^6 times larger for it to contribute significantly to the reaction rate at 298K. For example, with relative configurational weights of 10^5 and 10^6 on the one H_2O shuttle pathway and configurational weights of one on each of the two and three H_2O shuttle pathways the average barriers are 13.9 and 14.9 kcal/mol, respectively. Consequently, although it is possible that other active pathways exist and we do not explicitly calculate the configurational weights required for evaluating the ensemble averaged barrier, we expect that ensemble averaging the pathways we report will result in a predicted barrier of between 13.6 to 15 kcal/mol.

These results predict that the homogeneous formation of $PyCOOH^0$ is viable, mediated by proton shuttling in aqueous solvent, and does not require the p-GaP electrode surface to play an active role in N−H bond cleavage of PyH^0. However, it is also possible that the experimentally measured barrier corresponds to thermally activated desorption of PyH^0 from the Pt electrode to the homogeneous phase. In the Py/Pt system the measured reduction potential for PyH^+ suggests that desorption of PyH^0 from Pt into the homogeneous phase requires at least 16.8 kcal/mol (see Introduction), a value that coincides with both the experimentally determined barrier and our calculated barrier for homogeneous reaction between PyH^0 and CO_2. Consequently, desorption of the reduced PyH^0 species from Pt may limit $PyCOOH^0$ formation. However, the observed first order dependence on both PyH^+ concentration and CO_2 concentration is indicative of a bimolecular homogeneous process.[41] We suggest that use of an electrode material with minimal surface effects on the reduction of PyH^+ (e.g. a Pb or dropping Hg electrode) should exhibit the homogeneous barrier for catalytic reduction of CO_2 by PyH^0. However, aqueous solvent should be used with caution because the homogeneous E^0 of PyH^+ (–1.31 V vs. SCE) is more negative than the reduction potential of H_2O, E^0=–1.07 V vs. SCE.

1.3.6 Charge analysis, pK_a and EA all show step-wise ET followed by PT. Next, we examine the interplay between ET and PT from PyH^0 to CO_2 to accomplish the chemical reduction of CO_2 through the formation of $PyCOOH^0$. Fundamental questions at the heart of pyridine-catalyzed reduction of CO_2 include: Do ET and PT occur concomitantly or sequentially? If sequentially, in what order do ET and PT occur? In this section, we focus on providing insight into these questions to understand the nature of CO_2 reduction in this system to reveal the role of the Py catalyst in CO_2 reduction. Figure 1.8 shows a plot of the net charges on PyH^0 and CO_2 as a function of the distance between the N of PyH^0 and the C of CO_2, which we define as $R_{N\text{–}C}$. The atomic charges were determined using the CHELPG method for several structures along the IRC of $PyCOOH^0$ product formation to delineate the details of the ET process. A charge analysis based on Mulliken populations shows the same qualitative trend as CHELPG derived atomic charges (see SI, section 8).

In particular, we examine the net charges on CO_2 and PyH^0 for two cases: $PyCOOH^0$ formation in the absence of the proton shuttling network (direct PT) and $PyCOOH^0$ formation mediated by proton shuttling through three water molecules. For both cases, the charge on CO_2 becomes negative while the charge on PyH^0 becomes more positive as the reaction proceeds from reactant towards the TS along the IRC (see Figure 1.8). This result demonstrates that ET from PyH^0 to CO_2 occurs as the N−C bond is formed and prior to PT. The charge transfer involves the donation of the N lone pair into a π* orbital of CO_2, as shown in Figure 1.2. For the case of no proton shuttle, the charge on CO_2 reaches a minimum of −0.60 e at R_{N-C} = 1.66 å and increases to −0.44 e at the TS (R_{N-C} = 1.61 Å) because the proton is now partially transferred to CO_2 along with its partial positive charge (see inset of Figure 1.8). These results predict that reduction of CO_2 through $PyCOOH^0$ formation occurs through a stepwise charge transfer mechanism where ET to reduce CO_2 precedes PT. Our calculations predict this same mechanism for the case of $PyCOOH^0$ formation through the three H_2O molecule proton relay. In this case, the charge decreases to a minimum of −0.86 e at R_{N-C} = 1.50 å, just after the TS at R_{N-C} = 1.57 Å, followed by the onset of PT to CO_2 at R_{N-C} = 1.45 Å (see inset of Figure 1.8 for the structure at R_{N-C} = 1.45Å).

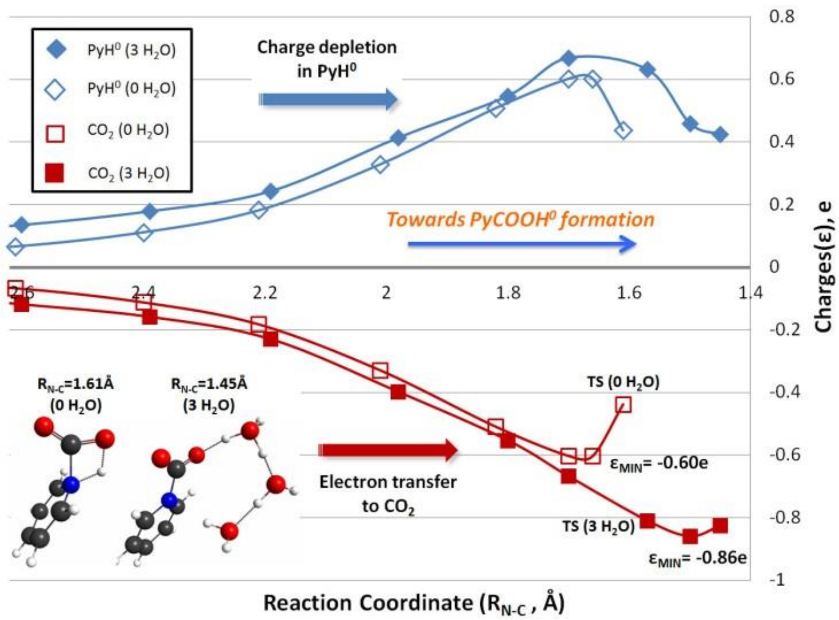

Figure 1.8: Charges on PyH0 (blue) and CO2 (red) along the IRC for PyCOOH0 formation from PyH^0 and CO_2.
(0 H_2O) and (3 H_2O) denote the cases of no proton relay (direct PT) and a three H_2O molecule proton relay. ET from PyH^0 to CO_2 is significant at C–N distances significantly longer than the TS (~1.6 Å). Charges determined using the CHELPG method at roMP2/6-31+G**.

An alternative mechanism might occur by PyH^0 first transferring its proton to CO_2, followed by ET to reduce CO_2. However, we calculate a pKa of 31 for PyH^0 in agreement with Keith *et al.*' s calculated pKa of ~27.[43] This suggests that direct PT from PyH^0 to CO_2 without ET first is highly thermodynamically unfavorable because it leads to the formation of the high-energy Py^- anionic radical. The energetic cost to form the Py^- anionic radical, either by direct PT from PyH^0 or ET to Py is also evident from the adiabatic electron affinity (EA) analysis summarized in Table 1.2, which also lists our calculated E^0 values for related Py and CO_2 species. We find that Py^- formation is even less favorable than formation of the high-energy CO_2^- anionic radical as demonstrated by our calculations showing that Py' s EA of 37.9 kcal/mol is less positive than CO_2' s EA of 47.4 kcal/mol. These calculated EAs are consistent with Tossell's CBS-QB3 thermochemical calculations for a number of reduced Py complexes.[44] This analysis based on the pKa of PyH^0 and the EA's of CO_2 and PyH^0 clearly demonstrates that if PyH^0 and CO_2 were to react, ET must precede PT to avoid the high energy cost of producing the Py^- anionic radical. This result explains and confirms the results of the charge analysis described above.

Table 1.2: Adiabatic electron affinities (EA) and homogeneous standard reduction potentials (E^0 vs. SCE).

System[a]	EA[b]	$E^{0(c)}$
a) $Py + CO_2 + e^- = Py^- + CO_2$	37.9	−2.90
b) $Py + CO_2 + e^- = Py + CO_2^-$	47.4	−2.34
c) $Py + CO_2 + e^- = PyCOO^-$	66.3	−2.05
d) $PyH^+ + e^- = PyH^0$	73.9	−1.31

[a]Calculations performed using CBS-QB3/CPCM-H_2O. [b]EA = $-\Delta H^0_{reduction}$ in aqueous solution in kcal/mol. [c]E^0 in aqueous solvent in V vs. SCE.

1.3.7 Formation of PyCOO– anionic complex provides a low-energy pathway for ET.

The calculated high pKa of PyH^0, low EA of Py and net charge versus IRC analysis all suggest that ET to CO_2 must precede PT in the formation of $PyCOOH^0$. If this is indeed the case, what then enables ET, especially given the fact that the anionic radical CO_2^- is high-energy? The answer lies in the unusual nature of the $PyCOO^-$ complex (Figure 1.6b, left) and it is this anionic complex that forms, not CO_2^-. As shown in Figure 1.9 and Table 1.2, the $PyCOO^-$ anionic complex is significantly more stable than the CO_2^- or Py^- anions as reflected by their EA's, consistent with Tossell's calculations.[44] It is this unusual stability of $PyCOO^-$ that provides a low energy pathway for ET from PyH^0 to CO_2 and which results in forming $PyCOO^-$. Formation of the $PyCOO^-$ anionic complex in the three H_2O proton shuttle case is evident in Figure 1.4 c-e, where $PyCOO^-$ is formed transiently after ET and during PT by proton shuttling through the three water molecule chain en route to $PyCOOH^0$ formation. Thus, the formation barriers for $PyCOOH^0$ shown in Figure 1.5 and schematically in Figure 1.9 are primarily the ET energy cost to form $PyCOO^-$ by this low energy pathway; $PyCOO^-$ is subsequently stabilized by protonation at a calculated pKa of 10.2. The existence and stability of the $PyCOO^-$ complex is also supported experimentally where Han and Kamrath *et al*. generated the $PyCOO^-$ complex through high-energy ionization,[91, 94] in contrast to the PEC reduction of CO_2, where $PyCOO^-$ is generated transiently through homogeneous reaction between PyH^0 and CO_2 mediated by the proton relay. These results prompt the question: What provides $PyCOO^-$ with its unusual stability?

1.3.8 Aromatic resonance stabilization stabilizes the PyCOO− complex. From the analysis above, we can deduce the role of the pyridine catalyst in the PEC reduction of CO_2. Py acts as a catalyst by stabilizing the high-energy anionic radical of CO_2^- by forming the stable $PyCOO^-$ complex, thus providing a low energy pathway for $PyCOOH^0$ formation. *What makes $PyCOO^-$ unusually stable? Aromatic resonance stabilization.*[95-96] Reduction of PyH^+ to PyH^0 increases the number of π electrons of from six to seven, resulting in a loss of aromaticity and PyH^+' s large negative reduction potential (Figure 1.10). The drive to regain the aromaticity lost upon PyH^+ reduction compels ET from PyH^0 to CO_2 to transiently form $PyCOO^-$. The resulting negative charge localized on CO2 then drives PT from PyH to CO2 through the water proton relay to ultimately form $PyCOOH^0$. Six electrons remain in the π system of Py after ET, thus making both $PyCOO^-$ and $PyCOOH^0$ aromatic and lowering their energy. This stabilizes the TS to lower the PCET barrier, as described by the Evans-Polanyi principle.[97]

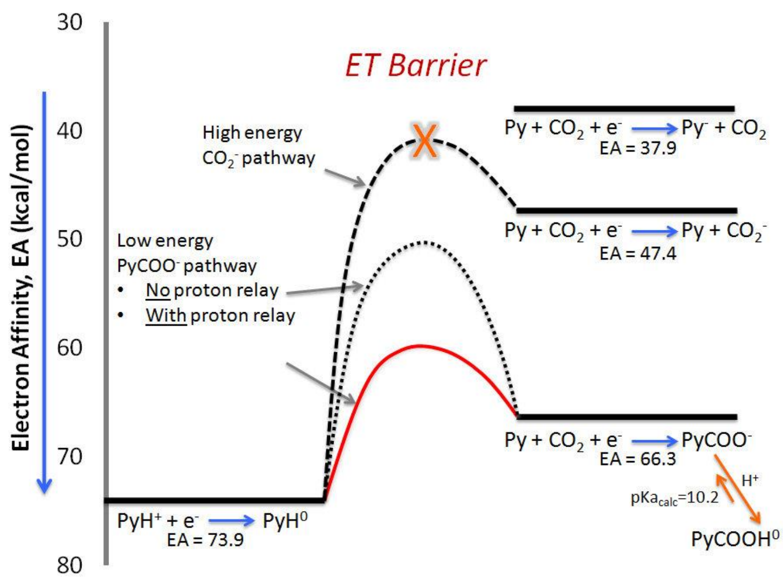

Figure 1.9: Formation of the PyCOO− anionic complex mediated by the proton relay provides a low energy pathway for ET en route to formation of the $PyCOOH^0$ carbamate species. The ET barriers are shown schematically.

Without aromatic stabilization one electron reduction of CO_2 or PT from PyH^0 leading to the one electron reduction of Py to Py^- are both prohibitively high in energy (see Figure 1.9). We test this suggestion using protonated 1,4-azaborinine (AB). Because the transferred electron is added to and removed from the sp^2 orbital localized on B, AB maintains its aromaticity on being reduced and during reduction of CO_2 via PCET. For reduction of CO_2 by PCET from AB we calculate an enthalpic barrier of 33.8 kcal/mol at the MP2 level of theory compared to 18.5 kcal/mol for PyH^0 where three waters act as a proton relay for both cases. The high barrier for AB catalyzed CO_2 reduction is a consequence of AB maintaining it aromaticity throughout PCET, thus providing no driving force for ET. Our results provide direct evidence and a detailed and fundamental explanation in support of Bocarsly *et al.*'s suggestion that Py-catalyzed CO_2 reduction proceeds through one electron reduction of CO_2.[40] The inverse view in which CO_2 stabilizes the high energy Py^- anionic radical is an equally valid alternative picture of this process. While both views are correct, a more complete analysis demonstrates that Py and CO_2 stabilize each other's anionic radical in the form of the $PyCOO^-$ complex.

1.3.9 Proton shuttling reduces the radical character of Py anionic radical. We emphasize again that ET precedes PT for cases of direct PT and for PT through the H_2O molecule relay, as shown in Figure 1.8. However, the proton relay offers the advantage of more extensive ET to CO_2 prior to PT; Figure 1.8 shows the minimum charge on CO_2 for the case of the three H_2O molecule relay to be −0.86 e compared to −0.60 e for direct PT in the absence of the relay. The more complete ET to CO_2 prior to PT enables Py to approach its low-energy neutral closed-shell state, reducing its high energy Py^- anionic radical character and consequently lowering the barrier to $PyCOOH^0$ formation. In other words, we propose that the high 45.7 kcal/mol barrier for direct PT is partially due to the larger Py^- anionic radical character of Py that results from less charge transfer to CO_2 prior to PT. Thus, the proton relay provides an additional important effect to catalyze CO_2 reduction; In addition to providing a pathway that lowers the strain in the TS, it also provides a favorable configuration that facilitates more complete ET to CO_2 during the formation of the $PyCOO^-$ complex to reduce the high-energy anion radical character of Py^- prior to PT. This effect is also consistent with the lowering of the reaction barrier by the proton relay as shown in Figure 1.5.

1.3.10 Is CO_2 prebent to facilitate reduction? The result that ET precedes PT introduces the question of whether CO_2 must be prebent to prepare it for reduction where bending CO_2 may lower the reorganization energy required for ET. The case where PT is mediated through the three water proton shuttle solvated by ten quantum solvating waters (as shown in Figure 1.5) exhibits the most extensive ET to CO_2 and a barrier of 13.6 kcal/mol for $PyCOOH^0$ formation. At the TS ET is mostly complete, and as seen in Figure 1.7d, CO_2 is not bent prior to ET, but is in fact bent as a result of ET. This shows that CO_2 prebending is not a generally required condition to effect low barrier CO_2 reduction.

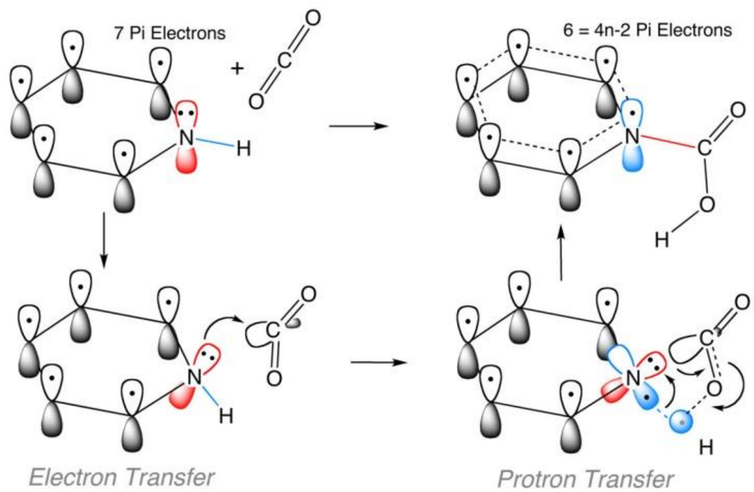

Figure 1.10: Stabilization of the PyCOO− complex through aromatic resonance stabilization.
PyH^0 possesses seven electrons in its π system. Nucleophilic attack at the C of CO_2 by the N of PyH^0 transfers electron density to CO_2 to reduce it while recovering the aromaticity of PyH^+ and facilitate proton transfer to form $PyCOOH^0$.

1.4 Conclusion

We have performed *ab initio* quantum chemical calculations on proposed pathways for homogeneous $PyCOOH^0$ formation to examine how Py catalyzes the PEC reduction of CO_2 in the Py/p-GaP system. We predict that the barrier to homogeneous $PyCOOH^0$ formation lies between 13.6 and 18.5 kcal/mol where PCET proceeds through a proton relay of three H_2O’s and the solvent is modeled using mixed implicit/explicit and only implicit solvation, respectively. A weighted average of PCET’s through one to three H_2O relays also falls within this range for weights of the higher barrier one H_2O relay path as large as $\sim 10^6$ times the weights on the two and three H_2O relays. Furthermore, this range is consistent with the experimentally determined barrier of 16.5±2.4 kcal/mol. In contrast, in the absence of the proton relay we predict a barrier for direct PT from PyH^0 to CO_2 of ~46 kcal/mol. The predicted solvent assisted PCET suggests a favorable pathway to CO_2 reduction through $PyCOOH^0$ formation in the homogeneous phase where the purpose of the p-GaP surface is the PEC reduction of PyH^+ to produce active PyH^0 species and may not be an active heterogeneous catalyst for CO_2 reduction. The water proton shuttling network has multiple effects: a) it reduces the strain in the TS, b) it produces the more stable $PyCOOH^0$ trans isomer and c) it reduces the radical character of the Py^- anion prior to PT. However, it is also possible that the experimentally measured barrier corresponds to endothermic desorption of PyH^0 from the Pt electrode to the homogeneous phase, which requires at least 16.8 kcal/mol of thermal energy, a value that coincides with both the experimentally determined barrier and our calculated barrier for homogeneous reaction between PyH^0 and CO_2.

We determine that Py facilitates the PEC reduction of CO_2 by avoiding the formation of high-energy Py^- and CO_2^- anionic radicals. A population analysis to describe details of charge transfer indicates that $PyCOOH^0$ formation occurs by a stepwise charge transfer mechanism where ET precedes PT. Consequently, the pKa of PyH^0 is irrelevant in predicting PyH^0's ability to transfer a proton to CO_2. Furthermore, our calculated pKa of 31 for PyH^0 predicts that PT from PyH^0 does not occur before ET. This is also supported by the calculated EA's of CO_2, Py and Py •CO_2 which show that the one-electron reductions of CO_2 and Py are prohibitively high in energy, whereas $PyCOO^-$ is a low energy one-electron reduced state with little radical character. Although the one electron reduced states of Py and CO_2 are high energy, aromatic resonance stabilization reduces the energies of the transiently formed $PyCOO^-$ anionic complex and $PyCOOH^0$ to lower the barrier to $PyCOOH^0$ formation. We demonstrate that prebending of CO_2 is not a requirement in achieving a low barrier to CO_2 reduction.

2 Reduction of CO_2 to Methanol Catalyzed by a Biomimetic Organo-Hydride Produced from Pyridine

Chern-Hooi Lim[1], Aaron M. Holder[1,2], James T. Hynes[2,3], and Charles B. Musgrave[1,2]*

[1]Department of Chemical and Biological Engineering and [2]Department of Chemistry and Biochemistry, University of Colorado, Boulder, Colorado 80309. [3]Chemistry Department, Ecole Normale Supérieure, UMR ENS-CNRS-UPMC 8640, 24 rue Lhomond, 75005 Paris, France

Journal of American Chemistry Society: dx.doi.org/10.1021/ja510131a

Abstract:

We use quantum chemical calculations to elucidate a viable mechanism for pyridine-catalyzed reduction of CO_2 to methanol involving homogeneous catalytic steps. The first phase of the catalytic cycle involves generation of the key catalytic agent, 1,2-dihydropyridine (**PyH_2**). First, pyridine (Py) undergoes a H^+ transfer (PT) to form pyridinium (PyH^+), followed by an e^- transfer (ET) to produce pyridinium radical (PyH^0). Examples of systems to effect this ET to populate PyH^+'s LUMO (E^0_{calc} ~ -1.3V vs. SCE) to form the solution phase PyH^0 via highly reducing electrons include the photo-electrochemical p-GaP system (E_{CBM} ~ -1.5V vs. SCE at pH= 5) and the photochemical $[Ru(phen)_3]^{2+}$/ascorbate system. We predict that PyH^0 undergoes further PT-ET steps to form the key closed-shell, dearomatized (**PyH_2**) species (with the PT capable of being assisted by a negatively biased cathode). Our proposed sequential PT-ET-PT-ET mechanism transforming Py into **PyH_2** is analogous to that described in the formation of related dihydropyridines. Because it is driven by its proclivity to regain aromaticity, **PyH_2** is a potent recyclable organo-hydride donor that mimics important aspects of the role of NADPH in the

formation of C-H bonds in the photosynthetic CO_2 reduction process. In particular, in the second phase of the catalytic cycle, which involves three separate reduction steps, we predict that the **PyH_2**/Py redox couple is kinetically and thermodynamically competent in catalytically effecting hydride and proton transfers (the latter often mediated by a proton relay chain) to CO_2 and its two succeeding intermediates, namely formic acid and formaldehyde, to ultimately form CH_3OH. The hydride and proton transfers for the first of these reduction steps, the homogeneous reduction of CO_2, are sequential in nature (in which the formate to formic acid protonation can be assisted by a negatively biased cathode). In contrast, these transfers are coupled in each of the two subsequent homogeneous hydride and proton transfer steps to reduce formic acid and formaldehyde.

2.1 Introduction

Conversion of carbon dioxide (CO_2) to fuels enabling a closed-carbon cycle powered by renewable energy has the potential to dramatically impact the energy and environmental fields.[1-3, 9-13, 17, 25] However, the chemical reduction of CO_2 to highly reduced products such as methanol (CH_3OH) remains a daunting task. The groups of Fujita,[35, 98-99] Kubiak,[25, 100] Meyer,[29, 101-102] Savéant[27, 103-104] and others[15-16, 18, 20, 26, 30, 39, 42, 105-108] have made significant contributions to this field, particularly in the fundamental understanding of using transition-metal complexes to catalyze CO_2's transformation. Despite these advances, many challenges remain: for example, CO_2 reduction has largely been confined to $2e^-$ products such as CO and formate, and in many cases large overpotentials are required to drive these reactions.[35, 100, 103, 105]

Recently, Bocarsly and coworkers[39-40] employed pyridine (Py) in a photo-electrochemical system using a p-type GaP cathode to efficiently convert CO_2 to CH_3OH at 96% Faradaic efficiency and 300 mV of underpotential;[39] it is notable that although semiconductor cathodes, such as n-GaAs, p-GaAs and p-InP, have been shown to convert CO_2 to CH_3OH without Py when biased to potentials more negative than -1 V vs. SCE,[109-110] on a p-GaP cathode under illumination and biased to only ~ -0.2V vs. SCE,[39] CH_3OH is only produced in the presence of Py; thus Py evidently plays a key role in catalyzing the formation of CH_3OH from CO_2. Clearly, thorough understanding of any Py-catalyzed CO_2 reduction is required not only to elucidate Py's catalytic role in general, but also to develop related catalysts that exploit the fundamental phenomena at play in such a reduction. In this contribution, we use quantum chemical calculations to discover that the key to Py's catalytic behavior lies in the homogeneous chemistry of the 1,2-dihydropyridine/pyridine redox couple, driven by a dearomatization-aromatization process, in which 1,2-dihydropyridine (**PyH_2**) acts as a recyclable organo-hydride that reduces CO_2 to CH_3OH via three hydride and proton transfer (HTPT) steps (see Scheme 2.1).

We pause to stress that while the fundamental reduction mechanism we develop --- the generation of **PyH_2** and three catalytic steps to reduce CO_2 progressively to CH_3OH --- can operate under homogeneous conditions (although probably with low CH_3OH yield at typically employed pH values; *vide infra*), we do find that the mechanism can be assisted at two stages by the influence of the double layer adjoining the negatively biased cathode. These involve a step in the **PyH_2** formation and the formate-formic acid conversion preparatory to formic acid reduction. Even with these assisting heterogeneous aspects, the overall process is predominantly homogeneous and is active in their absence. We will use 'homogeneous' as a descriptor for reaction steps where appropriate, and will explicitly indicate the two junctures where cathode heterogeneous effects assist the mechanism.

Hydride transfer (HT) reactions --- which are formally equivalent to $2e^-/H^+$ reductions --- have been proven adept in forming C-H bonds, converting CO_2 to CH_3OH at mild conditions.[16, 20, 108] For example, we have shown how ammonia borane ($H_3N\text{-}BH_3$)[111] accomplishes hydride (H^-) and proton (H^+) transfers to CO_2 that ultimately lead to CH_3OH.[21, 112] The particular relevance of this example is that **PyH_2**, the hydride reagent of special focus in this article, is similar to ammonia borane in that both involve a protic hydrogen on N which has neighboring hydridic hydrogens, on the ortho-C of 1,2-dihydropyridine and on the B of ammonia borane. However, **PyH_2** is unique in the critical sense that it is a catalytic hydride donor (*vide infra*), similar to NADPH in photosynthesis (as discussed within), rather than a stoichiometric hydride reagent (such as ammonia borane and silanes).

Scheme 2.1: Homogeneous reduction of CO_2 to methanol by 1,2-dihydropyridine via hydride and proton transfer steps

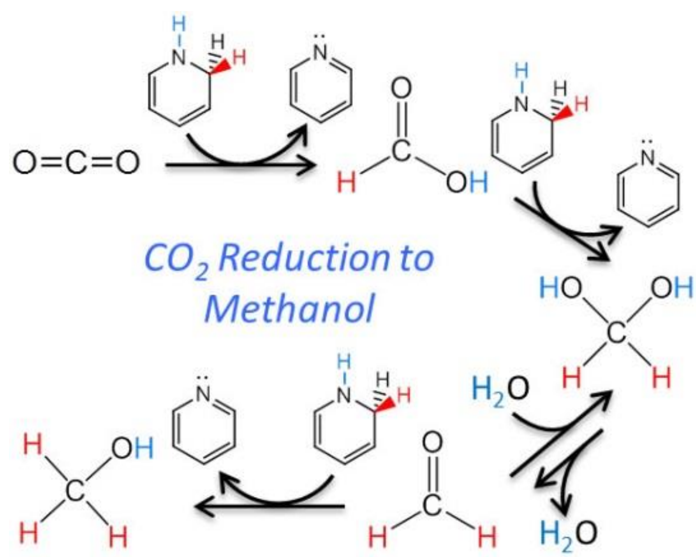

The outline of the remainder of this paper is as follows. Using quantum chemical calculations whose methodology is outlined in section 2.2, we will: 1) demonstrate how Py is transformed into the recyclable organo-hydride **PyH_2**, via a sequential PT-ET-PT-ET process (sections 2.3.1 and 2.3.2). **PyH_2** is a $2H^+/2e^-$ transfer product of pyridine (Py).[113-116] We note that the formation of related dihydropyridines proceeds via sequential PT and ET steps.[117-119] 2) establish the hydride nucleophilicity of **PyH_2** and related dihydropyridines (section 2.3.3); 3) calculate key transition states and reaction free energies to demonstrate that **PyH_2** is both kinetically and thermodynamically proficient in reducing CO_2 to CH_3OH through three successive homogeneous HTPT steps (sections 2.3.4-2.3.7); and 4) show that the catalytic hydride transfer reaction by the **PyH_2**/Py redox couple is driven by a dearomatization-aromatization process (section 2.3.8).[120] Concluding remarks are given in section 2.4.

2.2 Computational methods

We compute stationary geometries (reactants, transition states and products) for all systems studied using density functional theory based on the M06 density functional[121] and 6-31+G** basis set[57] and a water solvent model described below. The M06 functional was chosen because it has been parameterized with experimental thermodynamic data, should provide a reliable description of the molecular structures for the reactions of interest.[121] To further improve the reported energies, we performed single point energy calculations at the M06/6-31+G** geometries using 2nd order Møller-Plesset perturbation theory (MP2)[58] with the extensive aug-ccPVTZ basis sets.[56] We previously found that MP2 accurately reproduces the CCSD(T) reaction and transition state (TS) energies for reactions between pyridine (Py) and

CO_2,[120] and have further benchmarked this method against CCSD(T) for reactions involving HT to CO_2, as summarized in Table S1 of the Supporting Information (SI), section 1.

An adequate treatment of solvent is crucial to correctly describe reactions involving a polar TS, such as those involving electron, proton, or hydride transfers which are of particular interest here. Therefore, we employed the implicit polarized continuum solvation model (CPCM) in all calculations to treat the solute-solvent electrostatic interactions in aqueous solvent.[67-68] In addition to the CPCM-description, in the direct hydride transfer models DHT-1H_2O and DHT-2H_2O of section 2.3.3, we explicitly included one and two water molecules to quantum mechanically model the solvent polarization essential for correctly describing the ionic HT TS. In addition to stabilizing the TS, these water molecules also intimately participate in the reaction by acting as a proton relay chain during the proton transfer event.[80-81, 83-84, 86, 89, 120, 122-129] The treatment of explicit waters is discussed in greater detail in SI, section 1d.

We calculate vibrational force constants at the M06/6-31+G** level of theory to: 1) verify that the reactant and product structures have only positive vibrational modes, 2) confirm that each TS has only one imaginary mode and that it connects the desired reactant and product structures via Intrinsic Reaction Coordinate (IRC) calculations, and 3) compute entropies, zero-point energies (ZPE) and thermal corrections included in the reported free energies at 298K.

For the activation and reaction enthalpies, entropies and free energies for each of the various reactions examined within, we define the reference state as the separated reactants in solution, as is appropriate for solution phase bimolecular reactions.[130] It is important to recognize that commonly employed entropy evaluations within the rigid rotor, harmonic oscillator and ideal gas approximations normally overestimate the entropic cost for reactions occurring in solution phase, because ideal gas partition functions do not explicitly take into account hindered translation, rotation and vibration of the solute surrounded by solvent molecules.[18, 131-136] For example, Huang and coworkers observed that the calculated standard activation entropy values ($-T\Delta S^{\ddagger}_{calc}$) consistently overestimate the experimental $-T\Delta S^{\ddagger}_{exp}$ values by ~4-5 kcal/mol at 298K.[133-134] Liang and coworkers also observed that $-T\Delta S^{\ddagger}_{exp}$ values are 50-60% of the computed $-T\Delta S^{\ddagger}_{calc}$, and in some cases activation entropic costs $-T\Delta S^{\ddagger}_{exp}$ are overestimated by ~11 kcal/mol.[132] In SI, section 2, we show that $-T\Delta S^{\ddagger}_{calc}$ overestimates $-T\Delta S^{\ddagger}_{exp}$ by ~12 kcal/mol for the analogous HT reaction from the **PyH_2**-related dihydropyridine 1-benzyl-1,4-dihydronicotinamide (in eq. 1). Clearly, ideal gas-based calculated $-T\Delta S^{\ddagger}_{calc}$ values can have significant errors.

While various empirical correction factors for $-T\Delta S^{\ddagger}_{calc}$ values have been proposed,[18, 131, 136-137] all of which significantly lower $-T\Delta S^{\ddagger}_{calc}$, our approach to better estimate $-T\Delta S^{\ddagger}$ is to employ the experimentally obtained $-T\Delta S^{\ddagger}_{exp}$ value for an analogous HT reaction; as we discuss later, the transition states for all three steps in reduction of CO_2 to CH_3OH are of HT character. This $-T\Delta S^{\ddagger}_{exp}$ value is then added to our calculated $\Delta H^{\ddagger}_{HT}$ in order to obtain more accurate estimates to the activation free energy $\Delta G^{\ddagger}_{HT}$. In particular, the homogeneous HT from the **PyH_2**-related dihydropyridine 1-benzyl-1,4-dihydronicotinamide to Δ^1-pyrroline-2-carboxylic acid (zwitterionic form) in aqueous methanol (eq. 1)[138] is analogous to each of the three HTs from **PyH_2** of interest here: to CO_2, formic acid (HCOOH) and formaldehyde (OCH_2). We thus add the $-T\Delta S^{\ddagger}_{exp}$ of 2.3 kcal/mol (298 K) determined experimentally for eq. 1[138] to the calculated $\Delta H^{\ddagger}_{HT}$ values in Table 2.1 to obtain our estimates for $\Delta G^{\ddagger}_{HT}$. This procedure is further discussed in section 2.3.5. As comparison, we also employed the approach of Morokuma and coworkers[139] to omit the translational contribution from computed gas phase entropies. We obtained $-T\Delta S^{\ddagger}_{calc}$ = 3.0, 2.2, and 2.7 kcal/mol for the reduction of CO_2, formic acid and formaldehyde, respectively, (via the DHT-1H_2O model defined in section 2.3.3); these values are similar to the experimental $-T\Delta S^{\ddagger}_{exp}$ of 2.3 kcal/mol for eq. 1 that we have employed. See SI, section 2 for details.

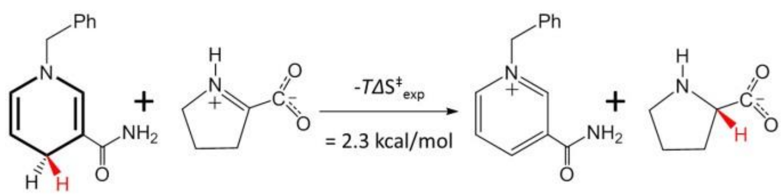

(1)

Finally, reaction free energies (ΔG^{0}_{rxn}) are reported by adding ΔH^{0}_{rxn} to $-T\Delta S^{0}_{rxn}$ in Table 2.1. Because the number of species remains constant on going from reactants to products in the HTPT reactions described here, the overestimation issue for the calculated $-T\Delta S^{0}_{rxn}$ is less severe. All reported energies were referenced to separated reactants in solution (as noted above) and calculations were performed using the GAUSSIAN 09[61] and GAMESS[59] computational software packages. Often, reported bimolecular reaction activation and thermodynamic quantities in the literature are referenced to reactants within a reactant complex rather than to the separated reactants. Thermodynamic quantities with the former reference are given for comparison in SI, section 3.

2.3 Results and Discussion

2.3.1 Formation of PyH^0 from Py via $1H^+/1e^-$ transfers. We begin with the key issue of the generation of PyH^0 from Py via sequential PT-ET steps. In Scheme 2.2, route **I**, Py first undergoes protonation to form pyridinium (PyH^+; pK_a= 5.3) in a pH= 5 solution. Subsequent $1e^-$ reduction (route **II**) produces PyH^0. Experimentally, photo-excited electrons of the p-GaP semiconductor are sufficiently reducing to populate PyH^+'s LUMO (E^0_{calc}~ -1.3 V vs. SCE)[43-44, 120] via $1e^-$ transfer to form solution phase PyH^0.[140] For example, at a pH of 5 the conduction band minimum of p-GaP (E_{CBM})[141-142] lies at approximately -1.5 V vs. SCE,[143-144] a more negative potential than PyH^+'s LUMO. Furthermore, the p-GaP electrode is electrochemically biased by -0.2 to -0.7 V,[39] which further increases the reducing ability of the transferring electron.

Scheme 2.2: Formation of pyridinium radical (PyH^0)

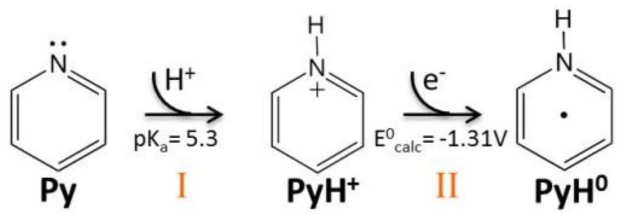

We pause to consider other PyH^0 generation routes. PyH^0 can also be produced electrochemically at inert electrodes. For instance, a glassy carbon electrode[145-147] has been used to electrochemically produce similar neutral radicals from the Py-related species nicotinamide and acridines.[117-119] In another case, photochemical production of PyH^0 driven by visible light was recently demonstrated by MacDonnell and coworkers using a surface-free photochemical process in which Ru(II) trisphenanthroline (chromophore) and ascorbate (reductant) act in concert to reduce PyH^+ to PyH^0 via $1e^-$ transfer. The produced PyH^0 radical is actively involved in the observed homogeneous reduction of CO_2 to CH_3OH (albeit at low yield),[148-150] an observation in contrast with recent studies focused on the specific case using a Pt cathode[43, 145, 151-155] that rule out participation of homogenous PyH^0 in Py-catalyzed CO_2 reduction. We stress that we consider a Pt electrode to be a special case. There, $1e^-$ reduction of PyH^+ is favored to form adsorbed H-atoms (Pt-H*)[45, 153-156] such that its use introduces additional routes (e.g. H_2 formation) which likely outcompete any processes catalyzed by Py. Therefore, surface pathways[152, 154] for CO_2 reduction on Pt may predominate such that the homogeneous mechanism discussed in the text requiring the production of PyH^0 becomes a minor pathway. Nonetheless, the mechanism we elucidate involving hydride and proton transfers by dihydropyridines may provide useful insights into any presumably minority surface-mediated pathways that may occur on (including Pt) active cathodes.

The conversion of the produced solution phase PyH^0 to the desired intermediate $\mathbf{PyH_2}$ will be taken up in section 2.3.2. Here we pause to discuss some competing routes. The first of these arises because PyH^0 is a dearomatized species driven to donate an electron in order to recover its aromaticity.[120, 157] For example, Bocarsly and coworkers[40-41] proposed that PyH^0 reacts with CO_2 to form a pyridine-carbamate ($PyCOOH^0$) intermediate (Scheme 2.3, route **III**) prior to CH_3OH formation.[40] $PyCOOH^0$ formation by this route is supported by our recent computational study,[120] and spectroscopic measurements.[94] In particular, using a hybrid explicit/implicit solvent model, we calculated low enthalpic barriers with respect to the complexed reactants of 13.6-18.5 kcal/mol (depending on the number of solvating waters) for $PyCOOH^0$ formation via a proton relay mechanism; the importance of proton relays have been extensively described in assorted chemical reactions.[80-81, 83-84, 86, 89, 122-127] Charge analysis on CO_2 and PyH^0 along the reaction coordinate reveals that PyH^0's propensity to recover its aromaticity drives the sequence of ET to CO_2 followed by PT (mediated by a proton relay) to ultimately form $PyCOOH^0$.[120, 158] While this particular reaction is not of direct interest in the present work (see the end of section 2.3.2), we will see that the themes of aromaticity recovery and proton relay mechanisms also prove to be important for our three HTPT step reduction of CO_2 to CH_3OH.

Another oxidation channel for PyH^0 is via radical self-quenching, shown in route **IV**. PyH^0 undergoes self-quenching[52] to form either H_2 + 2Py or a 4,4' coupled dimer;[45, 159] the recovery of Py catalyst from the 4,4' coupled dimer is demonstrated in SI, section 4. Interestingly, the PyH^0 self-quenching can also lead to a productive outcome: disproportionation[160] of two PyH^0 radicals leads to Py and the desired **PyH_2** species.[161] However, we consider the main route to **PyH_2** is not this, but instead a successive PT and ET to PyH^0,[162-163] now described.

Scheme 2.3: 1e- reduction of CO_2 by PyH^0 to form $PyCOOH^0$ and self-radical quenching reactions of PyH^0

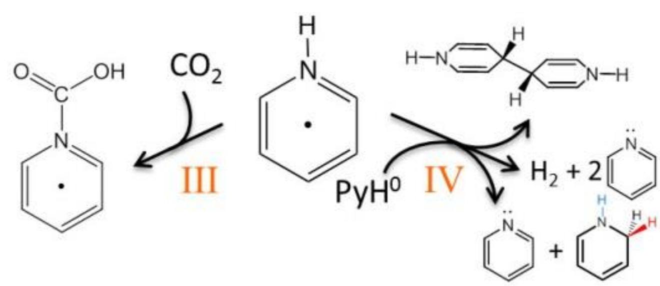

2.3.2 Formation of 1,2-dihydropyridine (PyH_2) from PyH^0 via successive $1H^+/1e^-$ transfers. We now discuss production of **PyH_2** from PyH^0 via routes **V** and **VI** of Scheme 2.4 in which PyH^0 undergoes further $1H^+$ and $1e^-$ transfers to form closed-shell solution phase **PyH_2**. We propose that these routes are competitive with, if not predominant over, Scheme 2.3's quenching routes **III** and **IV**. In particular, given that quenching routes are second-order in [PyH^0] and that routes **III** and **V** are first-order in [PyH^0], it is likely that quenching would prevent the concentration of PyH^0 from reaching a level at which the second-order process dominates. Furthermore, a significant fraction of any self-quenching of PyH^0 that does occur could lead to the desired **PyH_2** species, as observed experimentally for quenching of the related 3,6-diaminoacridinium radical to form the corresponding dihydropyridine species (3,6-diaminoacridan).[160-161]

The protonation of PyH^0 by our proposed route **V** depends on the rate of PT to PyH^0, which we now address in some detail. The pK_a of $PyH_2^{+\cdot}$ is calculated to be 4.1 (at the C_2 carbon),[164-166] indicating that at a pH of 5, ~13% of PyH^0 is protonated in the bulk solution. However, in the case of photo-electrochemical reduction on a p-GaP cathode, PyH^0 is produced by reduction of PyH^+ at the cathode near the double layer region where the lower pH facilitates its protonation to form $PyH_2^{+\cdot}$. The key here is that near the double layer region, the electric field created by the applied negative bias at the cathode concentrates cationic PyH^+ and H_3O^+ species according to a Poisson-Boltzmann distribution,[167-169] lowering the pH near the cathode surface. For example, in SI section 5, we use a linearized Poisson-Boltzmann model to show that the concentrations of cation acids, e.g. H_3O^+ and PyH^+, increase considerably as they approach the negatively biased cathode. While these calculations are certainly not quantitative very near the cathode**,** our estimate at ~5 Å of a factor of ~10 increase in $[H_3O^+]$ and $[PyH^+]$ from their bulk values is reasonable. A decrease of the effective pH by one unit to a pH of 4 raises the percentage of PyH^0 protonated by PyH^+ or H_3O^+ from ~13% to ~50%. Thus, protonation of PyH^0 by PyH^+ or H_3O^+ near the cathode double layer to form the desired radical cation $PyH_2^{+\cdot}$ becomes a quite probable event with a much higher probability than radical self-quenching via route **IV** because [cation acids]>>$[PyH^0]$.

Scheme 2.4: Formation of 1,2-dihydropyridine (PyH_2)

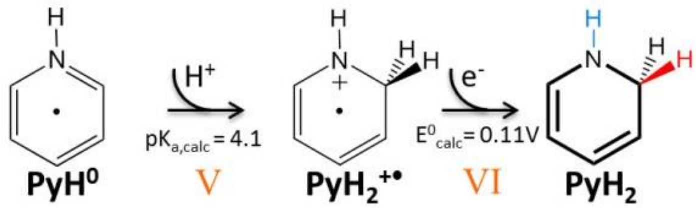

It is noteworthy that the lack of any negative cathode double layer assistance in the surface-free Ru(II)/ascorbate photochemical system mentioned in section 2.3.1 is consistent with the observation that high PyH^+/Ru(II) ratios of ~100 were required to produce CH_3OH, which we suggest is required to drive protonation of PyH^0 in a cathode's absence.[148]

Finally, **PyH_2** is produced by reduction of $PyH_2^{+\cdot}$ in proposed route **VI** in Scheme 2.4; our calculated positive reduction potential for $PyH_2^{+\cdot}$ of E^0_{calc}= 0.11 V vs. SCE indicates that $PyH_2^{+\cdot}$ reduction is facile and consequently that $1e^-$ transfer (from PyH^0 or via a photoexcited electron) to $PyH_2^{+\cdot}$ to form **PyH_2** is realized on p-GaP and in the homogeneous Ru(II)/ascorbate photochemical system. We note that in the presence of an electrode (e.g. p-GaP), $1e^-$ reduction of $PyH_2^{+\cdot}$ occurs near the double layer to form **PyH_2**, although diffusion of the neutral **PyH_2** into the reaction layer and bulk solution allows catalytic homogeneous HT reaction to occur.

Our suggested sequential PT-ET-PT-ET sequence (Scheme 2.2 and Scheme 2.4, route **I**-**II**-**V**-**VI**) to form **PyH_2** from Py is strongly supported by the fact that an analogous process has been observed for the conversion of the Py-related species nicotinamide,[117, 170] acridine,[118, 171] and 3,6-diaminoacridine (proflavine)[119] to their related dihydropyridine species. We point out that we propose the formation of 1,2-dihydropyridine as the kinetic product[113] because protonation of the PyH^0's C_2 carbon is more facile than protonation at the C_4 position,[164] analogous to protonation of nicotinamide where the related 1,2-dihydropyridine is formed.[117] However, 1,4-dihydropyridine can also be produced, although at a slower rate.[113] In SI, section 6, we show both dihydropyridine species to be capable of direct HT, with 1,2-dihydropyridine being the slightly more reactive species. We also note that acid-catalyzed hydration of both 1,2-dihydropyridine and 1,4-dihydropyridine may generate undesirable side products.[172-173]

The focus of this work is to demonstrate the formation of **PyH_2** and its subsequent hydride transfer reactions to form methanol (Scheme 2.1). Routes **III** ($PyCOOH^0$ formation), **IV** (radical quenching), and **V** (PT to PyH^0) are all bimolecular reactions with corresponding rate constants of ~10^0 $M^{-1}s^{-1}$,[120] ~10^9 $M^{-1}s^{-1}$,[52] and ~10^4-10^9 $M^{-1}s^{-1}$,[162] respectively. At the commonly employed experimental conditions/ concentrations, the rates of routes **IV** and **V** are both expected to be concentration dependent whereas the rate of route **III** is activation dependent. Therefore, we expect the contribution of route **III** to be minor under these conditions, but we note that insufficient evidence exists to conclude the fate of $PyCOOH^0$ species; thus far there is also no experimental verification for the existence of $PyCOOH^0$ species (as well as several intermediates leading to methanol production) produced under electrochemical/ photoelectrochemical conditions.

We have thus far described likely steps that transform Py into **PyH_2**, a species which we now show to be competent in performing catalytic direct HT to carbonyls.

2.3.3 Establishing the hydride nucleophilicity of PyH_2 and related dihydropyridines.

First, it is noteworthy that **PyH_2** chemically resembles the NADPH dihydropyridine species found in nature (see Scheme 2.5a and caption) that acts in the NADPH/$NADP^+$ redox cycle of photosynthesis to produce sugars from CO_2 by hydride transfers.[174-175] In particular, NADPH creates a C-H bond by HT to a carbonyl group --- not in CO_2 --- in a key reduction in the multi-step photosynthetic process. Although HT from NADPH is catalyzed by enzymes, both NADPH and **PyH₂** share the same dihydropyridine core, the $2e^-/1H^+$ redox cycle that produces the dihydropyridines and the subsequent HT chemistry. More generally, since the discovery of NADPH in the 1930's, related dihydropyridine compounds have been studied, especially in connection with their HT to various substrates containing C=C, C=N and C=O groups.[113-116] HT to carbonyls is obviously of particular interest here: the reactant CO_2 and its reduced intermediates formic acid (HCOOH) and formaldehyde (OCH_2) leading to CH_3OH formation all contain C=O groups susceptible to HT.

Here we mention two examples of related recyclable dihydropyridines performing HT to the C=O and C=N groups. Tanaka and coworkers demonstrated[176] (Scheme 2.5b) that the electrochemical reduction of $Ru(bpy)_2(pbn)^{2+}$ forms the NADPH-like $\mathbf{Ru(bpy)_2(pbnH_2)^{2+}}$, where the pbn ligand has undergone $2H^+/2e^-$ transfer to form a dihydropyridine-like hydride donor.[177] Association of $\mathbf{Ru(bpy)_2(pbnH_2)^{2+}}$ with a benzoate base ($PhCOO^-$) then activates its hydride donation to CO_2 to form $HCOO^-$ and PhCOOH and to concomitantly regenerate $Ru(bpy)_2(pbn)^{2+}$.[107] An H/D kinetic isotope effect of 4.5 further supports the direct hydride transfer mechanism to CO_2 to form $HCOO^-$.[107] Similarly, Zhou *et al.'s* dihydrophenanthridine (**$\mathbf{PhenH_2}$**), a **$\mathbf{PyH_2}$** analog, catalytically transfers both its hydride and proton to benzoxazinone and regenerates the phenanthridine catalyst (Scheme 2.5c), further demonstrating the competence of dihydropyridine species as recyclable hydride donors.[178]

Scheme 2.5: Reductions via direct hydride transfers from related dihydropyridine species

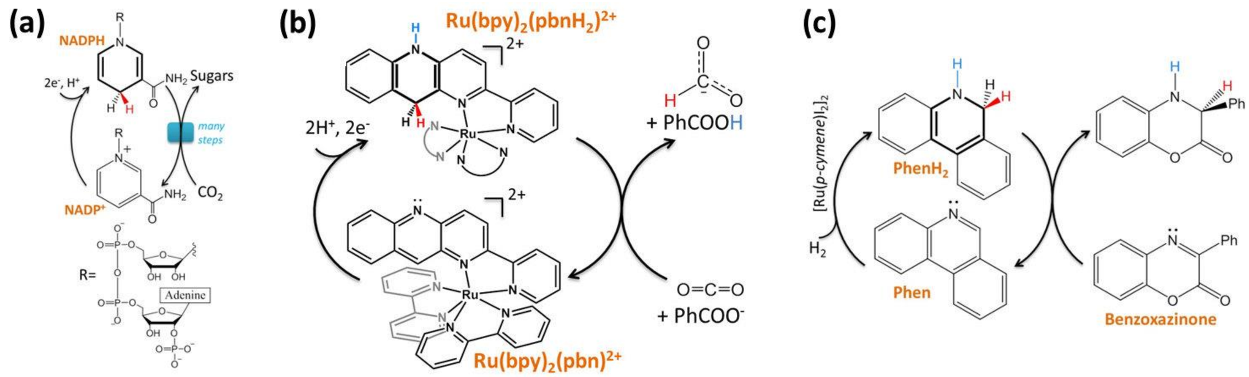

(**a**) NADPH/NADP$^+$ redox cycle of photosynthesis to produce sugars from CO_2 by hydride transfers. NADPH creates a C-H bond by HT to a carbonyl group --- not in CO_2 --- in a key reduction in the multi-step photosynthetic process. (**b**) Catalytic reduction of CO_2 to formate via HT involving Tanaka's Ru-based dihydropyridine species (**Ru(bpy)$_2$(pbnH$_2$)$^{2+}$**); bpy= 2,2'-bipyridine, pbn= 2-(pyridin-2-yl)benzo[b][1,5]naphthyridine).[107, 176] (**c**) Catalytic hydrogenation (via hydride and proton transfer) of benzoxazinone by Zhou's dihydrophenanthridine species (**PhenH$_2$**).[178]

We have thus far argued that the HT reactivity of related dihydropyridine hydrides **NADPH**, **Ru(bpy)$_2$(pbnH$_2$)$^{2+}$** and **PhenH$_2$** --- especially the extraordinary ability of **Ru(bpy)$_2$(pbnH$_2$)$^{2+}$** to effect CO_2 reduction --- strongly implicates **PyH$_2$** as a robust hydride donor in Py-catalyzed CO_2 reduction. The next step is to quantify **PyH$_2$**'s ability as a hydride donor, i.e. its hydride nucleophilicity. Figure 2.1 shows the quantification of this aspect of hydride donors using Mayr and coworkers' Nucleophilicity (N) values,[179-180] where large N values indicate strong hydride donor ability. Note that the N scale is a kinetic parameter quantifying the HT rate, whereas the often-employed hydricity is a thermodynamic parameter.[181-183] In order to place the N values of **PyH$_2$** and Zhou's **PhenH$_2$** in perspective relative to established values for dihydropyridines and $NaBH_4$, we calculate activation free energies for HT ($\Delta G^{\ddagger}_{HT}$) from these donors to CO_2 to reduce it to formate ($HCOO^-$) via the Direct-Hydride-Transfer (DHT) model illustrated in Figure 2.2a.

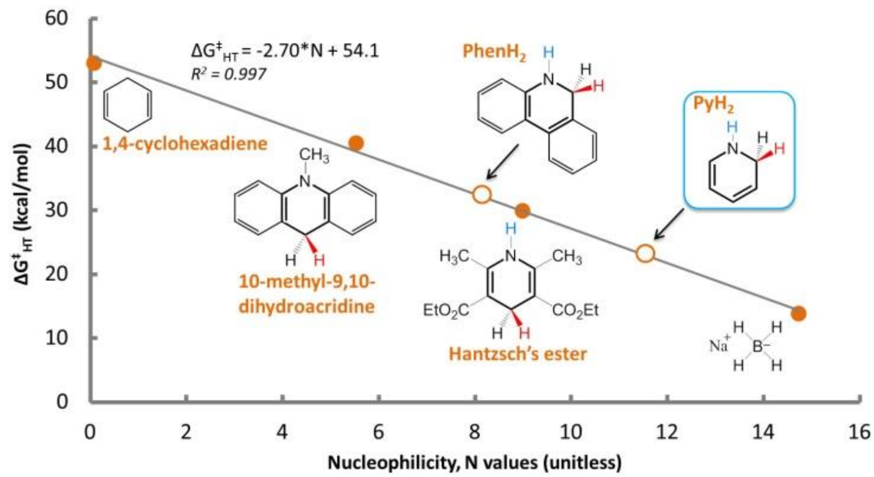

Figure 2.1: The activation free energy of hydride transfer to CO_2 varies linearly with hydride nucleophilicity. $\Delta G^{\ddagger}_{HT}$ (kcal/mol) is our calculated activation free energy for direct HT to CO_2 to form $HCOO^-$. $\Delta G^{\ddagger}_{HT}$ is obtained by adding our calculated $\Delta H^{\ddagger}_{HT}$ to the experimental $-T\Delta S^{\ddagger}_{exp}$ = 2.3 kcal/mol for the analogous HT reaction eq. 1, with all quantities referenced to the separated reactants (see section 2.2). Nucleophilicity (N) values quantify the strength of hydride donors.[179-180] The equation log k(20°C) = s(N+E) was used to obtain N and s (the slope factor) values in order to generalize various classes of hydride donors, including dihydropyridines and borohydrides. HT rate constants k are measured at 20°C for HT to acceptors with known E (Electrophilicity) values. Our calculated $\Delta G^{\ddagger}_{HT}$ values are used to estimate k, and thus N values of **PyH_2** and Zhou's **$PhenH_2$** relative to established N values for dihydropyridines and $NaBH_4$. These $\Delta G^{\ddagger}_{HT}$ values are obtained with CO_2 acting as the hydride acceptor; CO_2's E value is unknown but this is immaterial to the estimation of **PyH_2** and **$PhenH_2$**'s N values.[184] The comparatively low $\Delta G^{\ddagger}_{HT}$ and high hydride nucleophilicity of **PyH_2** are apparent in this Figure.

In Figure 2.1, we use the experimental N and our calculated $\Delta G^{\ddagger}_{HT}$ values (in kcal/mol) of 1,4-cyclohexadiene (0.09, 53.0), 10-methyl-9,10-dihydroacridine (5.54, 40.5), Hantzsch's ester (9.00, 29.9), and $NaBH_4$ (14.74, 13.8) to obtain a nearly linear relationship between $\Delta G^{\ddagger}_{HT}$ and N: $\Delta G^{\ddagger}_{HT} = -2.70*N + 54.1$.[185] We then use this linear relation together with our calculated $\Delta G^{\ddagger}_{HT}$ barriers to estimate that the N values of **$PhenH_2$** and **PyH_2** are 8.1 and 11.4, respectively. Although **PyH_2** is a less capable hydride donor than the well-known strong donor $NaBH_4$, it is the most reactive dihydropyridine, reducing CO_2 to $HCOO^-$ at $\Delta G^{\ddagger}_{HT}$ = 23.2 kcal/mol by the DHT model. The hydricity of **PyH_2** was also calculated according to Muckerman *et al.*'s approach;[183] we obtained 41.5 kcal/mol (< 43 kcal/mol of $HCOO^-$), which supports that HT from **PyH_2** to CO_2 is thermodynamically favorable.[186] We note that although cyclic voltammetry shows that the oxidation of **PyH_2**-related dihydronicotinamide by ET-PT-ET-PT is irreversible and indicates that it is a poor electron transfer catalyst,[170] this does not preclude dihydronicotinamide or dihydropyridines in general from being competent hydride transfer catalysts.

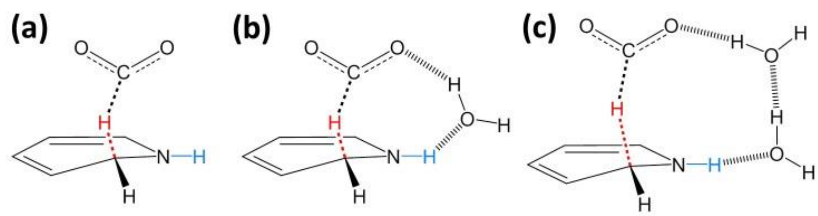

Figure 2.2: HT to CO_2 can occur through various direct HT configurations.
Here, we model three possible HT configurations, without (a) and with (b and c) the active participation of H_2O, which we demonstrate are kinetically and thermodynamically favorable towards reducing CO_2: (a) Direct-Hydride-Transfer (DHT) model, (b) DHT-1H_2O model where one H_2O acts as a proton relay and (c) DHT-2H_2O model where two H_2O's act as a proton relay. Details of these relays are discussed subsequently.

With these important preliminaries concerning **PyH_2**'s generation and HT ability concluded, we now turn to the three HTPT steps in the reduction of CO_2 to methanol.

2.3.4 First HTPT step: $PyH_2 + CO_2 \rightarrow Py + HCOOH$. We now elaborate the first HTPT step in CO_2's conversion to CH_3OH: HT to CO_2 by **PyH_2** to form formic acid (HCOOH). This step is illustrated in Scheme 2.6, route **VII**, although as we will see, there are two sequential steps involved, namely first formate ion $HCOO^-$ production followed by formic acid generation.[187] $\Delta G^{\ddagger}_{HT}$ for this step without the electrostatic effects and active participation of the proton relay (predicted using the DHT model in Figure 2.2a) is 23.2 kcal/mol. This shows that even without the effects described by explicit water, HT is kinetically viable.

Scheme 2.6: Reduction of CO_2 to formic acid by PyH_2.

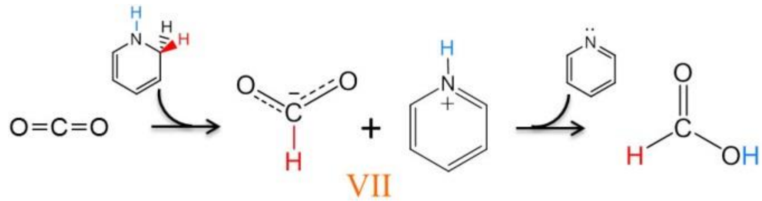

In an attempt to improve the description beyond the DHT model, we have considered two likely elaborations in aqueous solution. We added one and two solvating water molecules (DHT-1H_2O and DHT-2H_2O, Figure 2.2b and c) to polarize the reactive complex beyond the polarization afforded by implicit solvent, and thus stabilize the ionic TS relative to the neutral reactants. As will be seen, in the formic acid and formaldehyde reductions, the solvating water molecule(s) play an additional, more active role; they act as a proton relay, for which this mixed explicit/implicit solvation approach[73, 123-124] is especially important for an accurate description.[80-81, 83-84, 120] For the DHT-1H_2O and DHT-2H_2O models, we obtain the barriers of $\Delta G^{\ddagger}_{HT}$ = 17.1 and 14.3 kcal/mol for the CO_2 reduction to $HCOO^-$, ~6 and 9 kcal/mol lower than for the DHT model, reflecting the importance of quantum mechanically described water polarization (see Table 2.1).

Analysis of the reaction path using an IRC calculation shows that the TS is of HT character, such that the use of the experimental HT activation entropy discussed at the end of section 2.2 is appropriate.[188] The IRC analysis also shows that the product complex consists of the formate anion $HCOO^-$ and PyH^+; the reaction is pure HT without any PT, even with a proton relay chain of one or more explicit water molecules included. Because HCOOH's pK_a of 3.8 is relatively low, the carbonyl of $HCOO^-$ is not basic enough to abstract a proton from its neighboring H-bonded water to initiate a proton relay that would effectively transfer the proton from PyH^+ to $HCOO^-$. In contrast, in sections 2.3.5 and 2.3.6, we will show that the HT intermediary products of formic acid (hydroxymethanolate $(HCOOH)H^-$) and formaldehyde (methoxide, OCH_3^-) are highly basic and do initiate a proton relay; PyH^+'s proton is effectively transferred to these species through the proton relay to form methanediol and methanol, respectively.

Table 2.1: Activation and reaction free energies and enthalpies for HTPT steps from PyH_2 to CO_2, HCOOH and OCH_2 via various HT models in Figure 2.2.

Model[a]	CO_2[b]		HCOOH[c]		OCH_2[d]	
	$\Delta G^{\ddagger}_{HT}$ ($\Delta H^{\ddagger}_{HT}$)	ΔG^0_{rxn} (ΔH^0_{rxn})	$\Delta G^{\ddagger}_{HT}$ ($\Delta H^{\ddagger}_{HT}$)	ΔG^0_{rxn} (ΔH^0_{rxn})	$\Delta G^{\ddagger}_{HT}$ ($\Delta H^{\ddagger}_{HT}$)	ΔG^0_{rxn} (ΔH^0_{rxn})
DHT	23.2 (20.9)	-9.2 (-5.5)	25.6 (23.3)	-12.8 (-12.8)	14.5 (12.2)	-31.3 (-31.4)
DHT-1H_2O	17.1 (14.8)	-8.3 (-10.8)	23.4 (21.1)	-10.6 (-10.8)	8.9 (6.6)	-31.9 (-31.8)
DHT-2H_2O	14.3 (12.0)	-5.6 (-9.8)	18.7 (16.4)	-11.9 (-12.2)	6.0 (3.7)	-30.8 (-31.9)

[a]All free energies and enthalpies, referenced to separated reactants in solution, are reported in kcal/mol at 298K and 1 atm. $2e^-/2H^+$ transfer products: [b]formic acid, [c]methanediol and [d]methanol. The CO_2 pathway involves a sequential HT (to produce formate) followed by cathode-assisted PT (to produce formic acid); the activation barriers displayed refer to the HT portion of the reaction. The formic acid and formaldehyde reduction pathways both involve a coupled HTPT process, where **PyH_2** transfers both its hydridic and protic hydrogens to HCOOH and OCH_2, respectively: each case involves a single TS of HT character, with the PT following at a slightly later time, without a separate TS. The formaldehyde reduction step is preceded by the dehydration of methanediol to formaldehyde (K_{eq} = ~5×10^{-4}); see Figure 2.3 and section 2.3.6. Calculated imaginary frequencies corresponding to the transition state structures are reported in the SI, section 8.

Thus, with all three models, the formate product remains unprotonated. However, for the next HTPT step to proceed, $HCOO^-$ must first be protonated to form formic acid (HCOOH). HCOOH's pK_a of 3.8 indicates that at equilibrium, 298K and a pH = 5, only ~1/16 of $HCOO^-$ is protonated to produce HCOOH; such a low [HCOOH] combined with its high reduction barrier (*vide infra*) leads to the observed formate accumulation in the homogeneous Ru(II)/ascorbate photochemical system.[148] However, heterogeneous assistance (not shown explicitly in Scheme 2.6) can be provided by a cathode, as described in section 2.3.2; the enhanced concentrations of H_3O^+ and PyH^+ near the cathode (e.g. p-GaP)[40, 167] increases the concentration of HCOOH in equilibrium with $HCOO^-$ which increases the reduction rate in the reaction layer.

Thus, the first HTPT step to reduce CO_2 is sequential, with HT (to produce a relatively stable $HCOO^-$ intermediate corresponding to a minimum on the HT potential energy surface) followed by a subsequent cathode-assisted PT (to produce HCOOH), which we write collectively as $\mathbf{PyH_2} + CO_2 \rightarrow Py + HCOOH$. We could also term this step-wise HTPT as *uncoupled* HTPT.

Py and HCOOH formation by $\mathbf{PyH_2} + CO_2 \rightarrow Py + HCOOH$ with all three DHT models have negative reaction free energies ΔG^0_{rxn} of ~ -9 to -6 kcal/mol as shown in Table 2.1. This demonstrates that **PyH₂** is both kinetically and thermodynamically competent in catalytically reducing CO_2, at least for the first HTPT step. We will show that this catalytic ability also holds for the remaining two HTPT steps to attain methanol. The schematic free energy surface for this first HTPT step to transform CO_2 into HCOOH is shown in Figure 2.3, which also illustrates the free energies of the two subsequent HTPT steps described in sections 2.3.5 and 2.3.6.

We close the discussion of this first CO_2 reduction step with two remarks. First, although we have considered only three models (Figure 2.2a-c) for HT from $\mathbf{PyH_2}$ to CO_2, other configurations --- such as DHT-K^+ and DHT-PyH^+ where a potassium cation (present as an electrolyte) and the pyridinium cation act as a Lewis acid and a Brønsted acid, respectively, to activate and stabilize HT[189] to CO_2 --- can also lead to the desired HCOOH and Py products.

Furthermore, because the reaction is carried out in aqueous solvent, we propose that DHT-1H_2O, DHT-2H_2O and other likely DHT models with somewhat longer water proton relay chains contribute significantly to the ensemble-weighted average $\Delta G^{\ddagger}_{HT}$. Secondly, all reported $\Delta G^{\ddagger}_{HT}$ values in Table 2.1 (including $\Delta G^{\ddagger}_{HT}$ for the first HTPT step to form HCOOH and Py) are derived by adding our calculated $\Delta H^{\ddagger}_{HT}$ to the experimentally obtained $-T\Delta S^{\ddagger}_{exp}$ = 2.3 kcal/mol for an analogous HT reaction eq. 1 (again, all quantities are referenced to separated reactants). This is a significantly more reliable estimate for solution phase HT from **PyH_2** than a calculated $-T\Delta S^{\ddagger}_{calc}$ based on ideal gas assumptions, which can severely overestimate the entropic contribution to $\Delta G^{\ddagger}$;[18, 131-136] see section 2.2.

2.3.5 Second HTPT step: PyH_2 + HCOOH → Py + $CH_2(OH)_2$. We now turn to the second HTPT step: the homogeneous reduction of formic acid to methanediol ($CH_2(OH)_2$), as illustrated in Scheme 2.7, route **VIII**. HCOOH's reduction is actually more challenging than that of CO_2, a feature implied by the fact that most CO_2 reduction catalysts produce $HCOO^-$/HCOOH, but fail to convert HCOOH to more reduced products.[35, 100, 103] A further indication is provided by the observations of MacDonnell and coworkers, who found a significant build-up of $HCOO^-$ in their photochemical CO_2 reduction study referred to earlier, reflecting the challenge of HCOOH reduction.[148] The key characteristic of HCOOH that makes it difficult to reduce is its highly negative electron affinity (EA); we calculated the gas phase adiabatic EA of HCOOH to be -1.22 eV, which is significantly more negative than the -0.60 eV EA of CO_2 (see SI, section 1c) and indicates that, as noted above, formic acid is even more challenging to reduce than CO_2.[190-191] We now examine **PyH_2**'s ability to reduce HCOOH.

Table 2.1 summarizes both $\Delta G^{\ddagger}_{HT}$ and ΔG^{0}_{rxn} for the second HTPT step: **PyH_2** + HCOOH → Py + $CH_2(OH)_2$ via the three HT models shown in Figure 2.2a-c; note that the CO_2 $4e^-$ reduction product methanediol is formed along with the recovery of the Py catalyst. The $\Delta G^{\ddagger}_{HT}$ of 23.4 kcal/mol for the DHT-1H_2O case is ~2 kcal/mol lower than the DHT barrier (25.6 kcal/mol), while the DHT-2H_2O model reaction results in a further lowering of $\Delta G^{\ddagger}_{HT}$ to 18.7 kcal/mol (see Figure 2.3 for the computed TSs for the DHT-2H_2O model). As we will soon see, this reduction only involves a single TS and is thus a *coupled* HTPT process. The character of the TS is primarily that of HT, with PT occurring subsequently without its own TS (as implied in Figure 2.4, to be discussed). This supports our use of the HT activation entropy factor of section 2.2. In fact, because the PT occurs along the exit channel ~12 kcal/mol below the TS, even an unusually large $-T\Delta S^{\ddagger}$ for PT would not limit the rate of HTPT.

The DHT model results with one and two explicit waters show that HCOOH reduction to generate $CH_2(OH)_2$ is aided by a proton relay chain involving explicit water. Such chains of course stabilize the ionic TS, but they also facilitate PT by reducing strain in the TS and in addition, the PT from the H_2O H-bonded to HCOOH (see Figure 2.4) stabilizes the partially reduced product as negative charge accumulates on HCOOH. Consequently, the coupled PT helps to overcome the reduction challenges associated with HCOOH's low EA.

This PT and subsequent PTs in the relay chain occur after the HT barrier (see Figure 2.4a) and of course before the stable products are formed (see Figure 2.4 for the DHT-1H_2O case). Only a very modest activation entropy effect is anticipated here because in the coupled HTPT process, the PT step(s) is (are) considerably delayed relative to the HT such that any entropic penalties due to PT contribute to the free energies of structures well past the TS. This view is also supported by the prior configuration of the water molecules in the aqueous solution solvating the reactant complex and the widespread occurrence of proton relays in other processes,[80-81, 83, 86, 123-124, 127-129] including water oxidation[84, 122] and enzymatic reactions.[89, 125-126] In any event, the $\Delta G^{\ddagger}_{HT}$'s reported in Table 2.1 show that the homogeneous reaction is viable even without involvement of any proton relay chain.

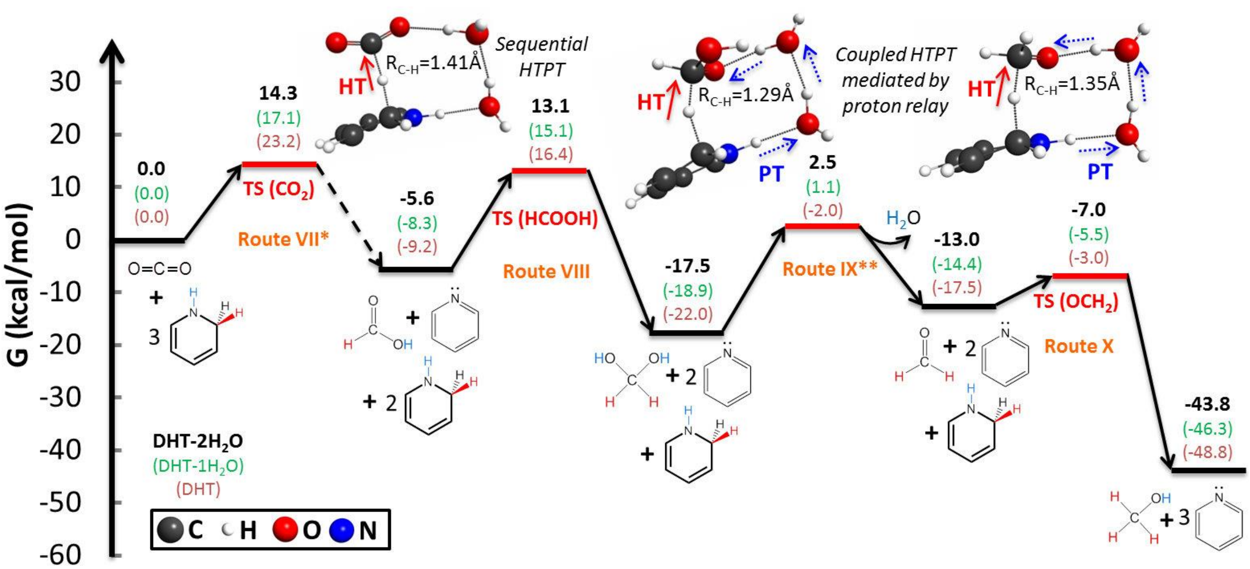

Figure 2.3: Conversion of CO_2 to CH_3OH and H_2O by PyH_2 proceeds through three hydride and proton transfer steps.

The reported free energies correspond to stationary points along the reaction potential energy surface using the DHT-2H_2O (Black), DHT-1H_2O (Green) and DHT (Orange) models, catalyzed by HTPT reactions of the **PyH_2**/Py redox couple. The 1st HTPT step (Scheme 2.6, route **VII**) is sequential where HT from **PyH_2** to CO_2 forms stable formate ($HCOO^-$), with a single TS of HT character, and subsequent PT follows to produce formic acid (HCOOH); (*the dashed line indicates that the product of HT to CO_2 is formate where a separate cathode-enhanced protonation step forms formic acid.) In the 2nd HTPT step (Scheme 2.7, route **VIII**), homogeneous coupled HTPT occurs with a single TS: HT from **PyH_2** to HCOOH, which dominates the barrier and is followed by PT without an additional TS (from oxidized **PyH_2**, essentially a PyH^+), is mediated by a proton relay involving water molecules, ultimately producing methanediol ($CH_2(OH)_2$). Prior to the next reduction step, $CH_2(OH)_2$ is dehydrated to form the reactive formaldehyde (OCH_2) species at K_{eq} ~5×10^{-4} (Scheme 2.8, route **IX**); thus this constitutes an additional free energy activation cost of ~4.5 kcal/mol for OCH_2 reduction. (**The rate constant for the dehydration of $CH_2(OH)_2$ to OCH_2 at 298K and pH of 6-7.8 is ~5×10^{-3} s^{-1} or equivalently the estimated $\Delta G^{\ddagger}_{dehyd}$ is ~20 kcal/mol.[192-193] Consequently, the effective rate constant for transformation of $CH_2(OH)_2$ to CH_3OH is that of $CH_2(OH)_2$ dehydration.) In the 3rd and final, homogeneous, HTPT step (Scheme 2.8, route **X**), which is similar to HCOOH reduction, coupled HTPT occurs where HT from **PyH_2** to OCH_2, involves a single TS of HT character, and is followed by a proton relay-mediated PT without an additional TS to ultimately form methanol (CH_3OH). During each reaction step, the Py catalyst is recovered, thus confirming **PyH_2** as a recyclable organo-hydride. TS structures for the HTPT steps from **PyH_2** to CO_2, HCOOH and OCH_2 are shown for the DHT-$2H_2O$ model. (Coordinates for the TS structures for all three DHT models are reported in SI, section 9.) All TS structures are HT in character.

Scheme 2.7: Reduction of formic acid to methanediol by PyH_2.

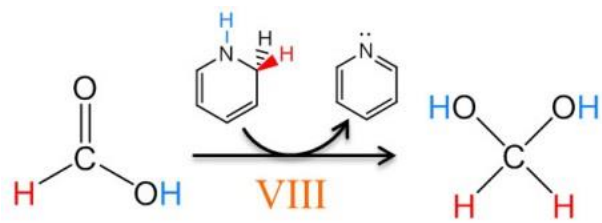

To better understand how coupled HT and PT enables **PyH_2** to reduce formic acid and indeed to further support our statements above concerning its coupled character, we analyze HCOOH's reduction by **PyH_2** and its proton relay process in greater detail. In Figure 2.4a we show how DHT-$1H_2O$'s energy (the internal energy E_{0k} calculated at 0K and not ZPE-corrected) changes from the reactant complex (R), through the TS and structures (i, ii, and iii) energetically downhill from the TS, before ultimately reaching the product complex (P) along the computed reaction coordinate. Along the same coordinate reaction we plot the change of key bond lengths (Figure 2.4b). This analysis shows that the transformation from the reactant to the TS is dominated by HT. That is, $R_{C\text{-}H}$ (defined in Figure 2.4a) shortens from 2.82Å at R to 1.29Å at the TS while $R_{O\text{-}H}$ and $R_{N\text{-}H}$ do not change appreciably. Consequently, PT either to HCOOH or from oxidized **PyH_2** does not occur until well past the TS. There is no TS associated with either of these PTs, although PT does produce a shoulder in the potential energy surface ~12 kcal/mol below the TS caused by HT.

Despite the important distinction between the first two HTPT reduction steps just emphasized, the character of HCOOH's reduction by **PyH_2** is similar to that of the reduction of CO_2 in the sense that HT dominates the energetics leading to the TS for both reactions; thus, as commented upon in the caption of Figure 2.4, the experimental -T$\Delta S^{\ddagger}_{exp}$ value of 2.3 kcal/mol for HT from the related dihydropyridine HT reaction (eq. 1) is also a reasonable -T$\Delta S^{\ddagger}_{HT}$ estimate for HT to HCOOH by **PyH_2**.

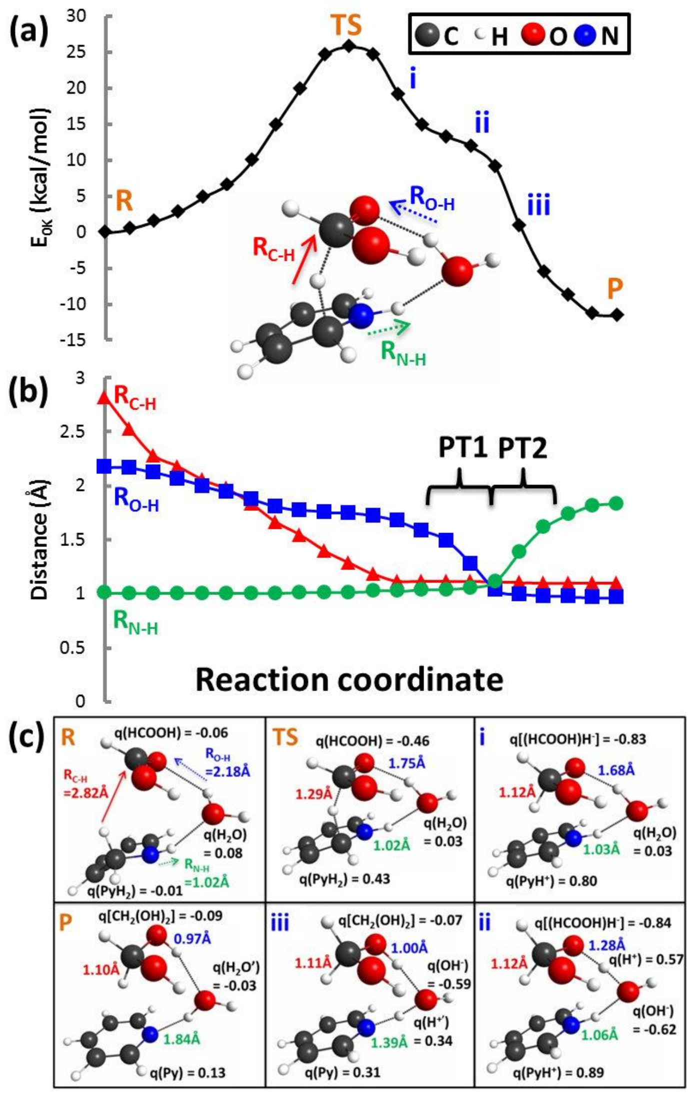

Figure 2.4: Analysis of the coupled homogeneous HTPT process between PyH_2 and HCOOH to form Py and $CH_2(OH)_2$ via the DHT-1H_2O model.

Similar results are found for HTPT to formaldehyde. Panels: (a) energy (E_{0K}, not ZPE-corrected); R denotes the reactant complex, TS the transition state, i, ii, and iii are structures in the exit channel, and P, the product complex, (b) bond length, and (c) structures and charges q (calculated with the CHELPG method[76] and in the units of e) of important moieties along the reaction coordinate (corresponding to structures in (a)). Both bond length and charge analyses show that the TS is dominated by HT (which is similar to the case of CO_2 reduction by **PyH_2**). Thus, the experimentally obtained -T$\Delta S^{\ddagger}_{exp}$ = 2.3 kcal/mol for a related HT reaction (eq. 1) is a good estimate for the -T$\Delta S^{\ddagger}_{HT}$ of the HCOOH reduction, despite the involvement of PT because PT occurs well after the HT TS, though well before the product is formed. Here, PT occurs via proton relay ~12 kcal/mol below (after) HCOOH's TS. This feature, as well as the absence of a TS for the PT, confirms the coupled character of the HTPT reaction. Because the HT and PT reactions occur in a process characterized by a single free energy TS,[194-198] we have characterized this HTPT process as *coupled*.[199] It is so distinguished from the *uncoupled* HTPT reduction of CO_2 to ultimately produce HCOOH, where first HT involving a single TS produces the $HCOO^-$ intermediate, and subsequently PT to $HCOO^-$ occurs independently to produce HCOOH.

On the other hand, the HCOOH reduction is different from that of CO_2 in that --- as we noted above --- HCOOH's HT reaction is followed by coupled PT along the reaction coordinate, mediated by a proton relay via H-bonded water molecule(s). The first PT occurs along the exit channel ~12 kcal/mol downhill from the TS (Figure 2.4a and b), where the C=O oxygen of the hydroxymethanolate anion ($(HCOOH)H^-$ product of HT to HCOOH) abstracts a H^+ from its H-bonded H_2O to form methanediol and a hydroxide (OH^-)-like moiety (characterized further below). In contrast to CO_2 reduction where the produced $HCOO^-$ is not basic enough to initiate a proton relay, the HT intermediary product of formic acid, $(HCOOH)H^-$, is sufficiently basic (pK_a of methanediol is ~13)[200-201] to commence a proton relay by abstracting a H^+ from the neighboring H-bonded water.

This first PT event (PT1) is marked by the shortening of R_{O-H} from ~1.6 to ~1.0 Å. Immediately following PT1, the second PT event (PT2) occurs where the just-formed OH^--like moiety now abstracts a H^+ from its H-bonded partner PyH^+ (formed by HT from $\mathbf{PyH_2}$) to form H_2O and more importantly, to recover the Py catalyst. This aspect of the proton relay process is marked by the lengthening of R_{N-H} from ~1.0 to ~1.8 Å. This analysis clearly shows the cooperative nature of the HT and PT and that although PTs occur well into the exit channel, they act to stabilize the HT TS without participating in the TS's configuration.

Finally, we analyze how the charges on various moieties change along the reaction coordinate. In Figure 2.4c it is apparent that as the reaction proceeds from R to TS the charge of **PyH_2** becomes increasingly positive (q= 0.43e), while HCOOH becomes increasingly negative (q= -0.46e); this is consistent with a HT reaction and correlates with the motions along the reaction coordinate in Figure 2.4b. As the hydride transfer from **PyH_2** to the HCOOH carbon becomes more complete (structure i), the $(HCOOH)H^-$ moiety becomes increasingly basic (q= -0.83e) such that its carbonyl oxygen begins to abstract a proton from the H-bonded water molecule (structure ii) to form an intermediate hydroxide OH^- type moiety (q= -0.62e). Structure iii shows that this basic species then abstracts a proton from PyH^+, completing the proton relay to ultimately produce $CH_2(OH)_2$, while recovering the Py catalyst in the product P; H_2O' denotes a newly formed water as a result of proton relay. Figure 2.4 shows that **PyH_2** contains both hydridic (C_2-H) and protic (N-H) hydrogens; this is analogous to the situation for ammonia borane, which we previously showed reduces CO_2 by HTPT.[21, 112]

2.3.6 Third HTPT step: $PyH_2 + OCH_2 \rightarrow Py + CH_3OH$. We now address the third and final reduction step to produce the desired product, CH_3OH. This homogeneous step follows the formation of $CH_2(OH)_2$, which is a hydrated formaldehyde (OCH_2). To effect further reduction, the sp^3-hybridized $CH_2(OH)_2$ produced by the second HTPT must first be dehydrated to form the sp^2-hybridized species OCH_2 at K_{eq} ~$5x10^{-4}$ (Scheme 2.8, route **IX**).[202] While equilibrium strongly favors the diol species, OCH_2 is significantly more reactive to HT, producing methanol via **PyH_2** + $OCH_2 \rightarrow Py + CH_3OH$ (route **X**) at low barrier, e.g. $\Delta G^{\ddagger}_{HT}$ = 6.0 kcal/mol calculated for the DHT-$2H_2O$ model (see Table 2.1 for $\Delta G^{\ddagger}_{HT}$ values and Figure 2.3 for TSs). This low $\Delta G^{\ddagger}_{HT}$ value suggests that the slowest step from $CH_2(OH)_2$ to CH_3OH is in fact likely to be the dehydration of

$CH_2(OH)_2$ to OCH_2. The rate constant for the dehydration of $CH_2(OH)_2$ to OCH_2 at ambient conditions[192-193] is ~5x10^{-3} s^{-1} (obtained in the pH range 6.0-7.8) or equivalently the estimated free energy barrier $\Delta G^{\ddagger}_{dehyd}$ is ~20 kcal/mol. Consequently, the effective rate constant for transformation of $CH_2(OH)_2$ to CH_3OH is that of $CH_2(OH)_2$ dehydration (for all three of our models; see Table 2.1 and Figure 2.3).[203]

In a fashion similar to the HCOOH reduction, the reduction of OCH_2 proceeds homogeneously via a *coupled* HTPT step, which we illustrate using structures determined via IRC calculations. Figure 2.5 shows the reactant complex R involving **PyH_2**, OCH_2 and H_2O for the DHT-1H_2O model. In this complex, the C of OCH_2 is still far from the hydridic H of **PyH_2** (e.g. $R_{C\text{-}H}$ = 2.39 Å) and all moieties are approximately charge neutral (e.g. HT has not yet commenced and all species have q ~ 0). At the TS, OCH_2 is in the process of accepting a hydride from **PyH_2** and importantly, there is no significant PT, as evidenced by the relatively large $R_{O\text{-}H}$= 1.73 Å value relative to the $R_{O\text{-}H}$ value 0.98 Å of the product. Thus, the TS consists of HT character, again justifying our use of the experimental HT activation entropy factor proposed in section 2.2.

Scheme 2.8: Dehydration of methanediol to form formaldehyde and the subsequent reduction to methanol by PyH_2.

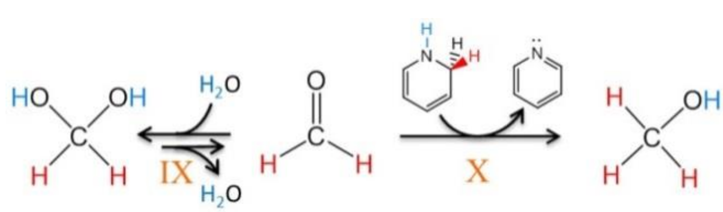

As the reaction progresses energetically downhill from the TS towards the product, HT completes, transiently forming the methoxide (OCH_3^-) anion-type moiety, displayed in structure i of Figure 2.5. In analogy to the second HTPT step, the PT occurs well into the exit channel after the HT TS and involves no TS on the way to the reaction product. Thus, the HT and PT are *coupled* in this HTPT process. The PT aspect of the reaction involves a proton relay chain for the one and two H_2O DHT model cases. The newly formed methoxide anion-like moiety is negatively charged [$q(OCH_3^-)$ = -0.76e] and possesses a sufficiently basic carbonyl (pK_a of methanol is ~16)[204] that it abstracts a proton from a neighboring hydrogen-bonded H_2O (structure ii) to initiate a proton relay cascade: a transient hydroxide anion-like moiety is produced (structure ii), which then abstracts an H^+ from PyH^+ (the oxidized **PyH₂** which has earlier resulted from HT) as CH_3OH formation is completed (structure iii), to finally form Py together with H_2O' and CH_3OH in the product complex, P. The HTPT activation free energies for the three cases are reported in Table 2.1. Our earlier remark about a minor activation entropy effect for the proton relay aspects of the second step also applies here.

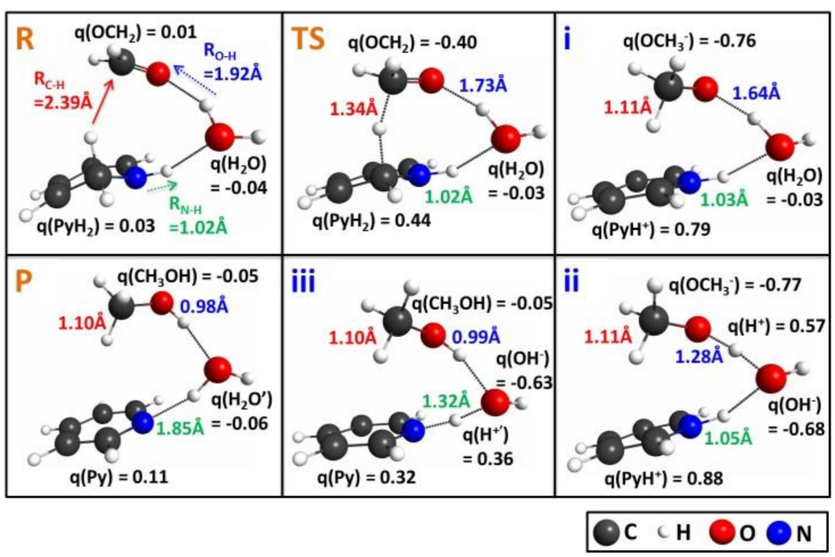

Figure 2.5: Reduction of formaldehyde by PyH_2 to methanol (via the DHT-1H_2O model) in a coupled HTPT step.
In the reactant complex R, all moieties (**PyH₂**, OCH_2, and H_2O) are approximately neutral (e.g. q ~ 0, in electronic charge units, e) and the HT reaction from **PyH₂** to OCH_2 has not commenced (e.g. $R_{C\text{-}H}$ = 2.39 Å). The reaction then proceeds to the TS, which is of HT character: OCH_2 becomes more negatively charged [$q(OCH_2)$ = -0.40e] on the

way to full HT, while **PyH₂** becomes more positive [q(**PyH₂**) = 0.44e], without any significant PT (e.g. $R_{O\text{-}H}$ = 1.73 Å). As the reaction progresses energetically downhill from the TS towards the product, the HT completes and methoxide anion (OCH_3^-) is formed in structure i. The basic methoxide [q(OCH_3^-) = -0.77e] now begins to abstract a proton from the neighboring H_2O in structure ii to form methanol (CH_3OH) in structure iii. The proton relay continues as the first PT-produced transient hydroxide anion-like OH^- now abstracts a proton from PyH^+ to finally form the product complex P of Py, CH_3OH and H_2O', where ′ denotes the water molecule newly formed in the proton relay.

It is noteworthy that HT from a related dihydropyridine species to an aldehyde has been observed.[205-206] In eq. 2, 10-methyl-9,10-dihydroacidine transfers its hydride to benzaldehyde to form benzyl alcohol in the presence of perchloric acid ($HClO_4$), which acts as the H^+ donor.[205] The HTPT reaction between **PyH₂** and OCH_2 to form methanol (Scheme 2.8, route **X**) is analogous to eq. 2; however route **X** differs slightly because **PyH₂** acts as both the hydride and proton donor.

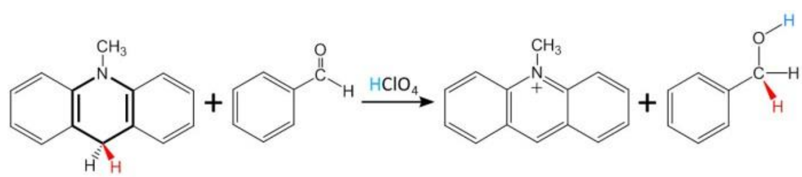

(2)

2.3.7 Commentary on the homogeneous mechanism for CO_2 reduction to CH_3OH catalyzed by pyridine. The preceding results in this section allow us to map out a complete mechanism of Py-catalyzed CO_2 reduction to CH_3OH via three HTPT steps (Scheme 2.9) where the first HTPT to CO_2 is uncoupled, and PT may be cathode-assisted, and sequential and the final two HTPT steps are coupled in character and homogeneous. These results are summarized in Table 2.1 and Figure 2.3. Examination of Table 2.1 and Figure 2.3 shows that the second HTPT step, that of HCOOH reduction, is the highest HTPT free energy barrier step for the reduction of CO_2 to CH_3OH by **PyH₂** in all cases. However, in the DHT-2H_2O case, the second HTPT barrier $\Delta G^{\ddagger}_{HT}$= 18.7 kcal/mol is lower than the methanediol dehydration barrier $\Delta G^{\ddagger}_{dehyd}$ of ~20 kcal/mol (see section 2.3.6 and Figure 2.3). In this connection, it is noteworthy that substrate and/or hydride donor activation[107, 189, 205, 207] can act to further lower $\Delta G^{\ddagger}_{HT}$. For example, K^+ and PyH^+ in solution can activate the carbonyls for HT (see discussion at end of section 2.3.4). However, even without this additional activation, the $\mathbf{PyH_2}$-catalyzed reduction of CO_2 to CH_3OH is kinetically facile. Moreover, we have found that for the second and third reduction steps, a proton relay chain can noticeably reduce the reaction barriers. However, even without these proton relays, Table 2.1 --- and the methanediol dehydration barrier $\Delta G^{\ddagger}_{dehyd}$ of ~20 kcal/mol --- indicate that these reactions remain viable in activation free energy terms.

For completeness, we have also considered a potential side reaction that might significantly impact the Faradaic yield for the overall $\mathbf{PyH_2}$-catalyzed CO_2 reduction to CH_3OH: HT from $\mathbf{PyH_2}$ to a proton donor such as PyH^+ to evolve H_2 ($\mathbf{PyH_2}$ + PyH^+ = PyH^+ + Py + H_2). We have calculated that this route involves a $\Delta G^{\ddagger}_{HT}$ of 24.0 kcal/mol, which demonstrates that such unproductive heterolytic quenching to form H_2 is dominated by the $\mathbf{PyH_2}$-catalyzed HT to CO_2, HCOOH, and OCH_2, as well as the methanediol dehydration. The higher barrier for H_2 production is supported by the fact that the HT reaction by the corresponding dihydropyridine species in eq. 2a can be carried out in acidic conditions without appreciable H_2 production.[205] The very high (96%) Faradaic yield of the p-GaP system[39] is also consistent with the unfavorable heterolytic quenching to form H_2.

We recognize that homogeneous components of a pathway for a pyridine-mediated CO_2 reduction to CH_3OH have been argued to be ruled out in several recent theoretical studies,[43, 151] and we briefly address this here. One key premise raised by the studies' authors is that $1e^-$

reduction of PyH^+ to PyH^0 cannot occur at experimental conditions.[43] But this statement is not supported by the fact that highly reducing electrons are present in both the photo-electrochemical p-GaP system (E_{CBM} ~ -1.5V vs. SCE at pH= 5)[74,75] and the photochemical $[Ru(phen)_3]^{2+}$/ascorbate system[148] to populate PyH^+'s LUMO (E^0_{calc} ~ -1.3V vs. SCE) to form the solution phase PyH^0 (see the discussion in section 2.3.1). Another premise is that radical self-quenching will render PyH^0 inactive.[151] We have already pointed out in section 2.3.1 that radical self-quenching of PyH^0 can actually yield the productive $\mathbf{PyH_2}$ via disproportionation.[160] In addition, it is relevant to note that Py-related neutral radicals of nicotinamide,[117] acridine,[118] and 3,6-diaminoacridine[119] have been experimentally observed and are key intermediate species en route to forming the related dihydropyridine species.

Scheme 2.9: Homogeneous mechanism of Py-catalyzed CO_2 reduction to CH_3OH via PyH_2/Py HTPT processes.

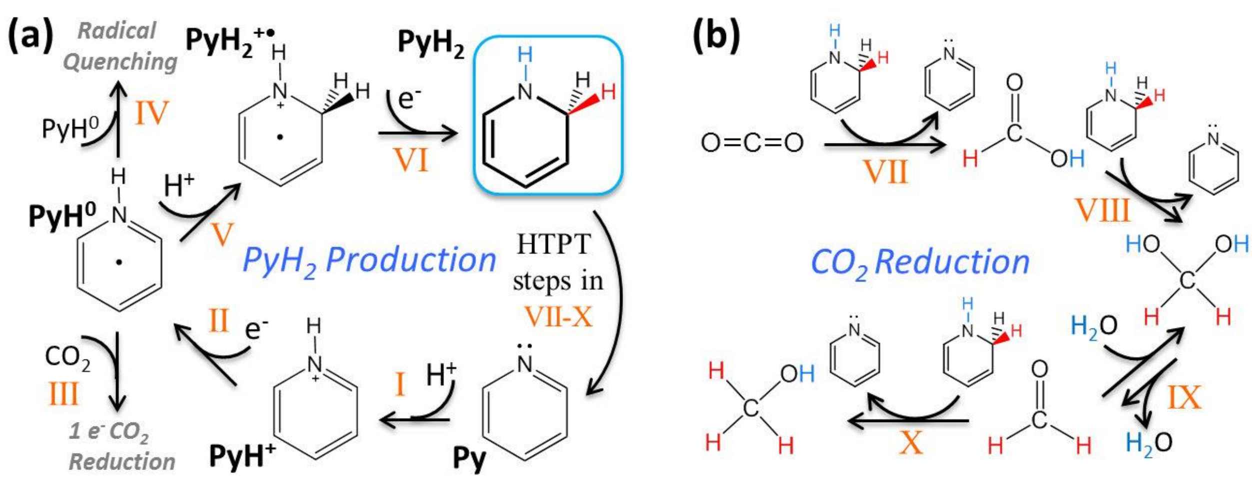

(a) $\mathbf{PyH_2}$ formation issues. In routes **I** and **II**,[120] Py accepts an H^+ to form PyH^+ and then an e^- to form the PyH^0 neutral radical, which then either reduces CO_2 by 1 e^- reduction to form $PyCOOH^0$ (route **III**)[120] or undergoes radical self-quenching (route **IV**) to produce H_2 + 2Py, a 4,4' coupled dimer or Py + $\mathbf{PyH_2}$. Alternatively, and of most importance in the present work, in routes **V** and **VI**, PyH^0 accepts a second H^+ and then a second e^- to form the potent recyclable organo-hydride $\mathbf{PyH_2}$. (b) CO_2 reduction to methanol. In routes **VII-X**, the produced $\mathbf{PyH_2}$ then participates in each of three catalytic HTPT steps to reduce CO_2 to CH_3OH and H_2O, while recovering the Py catalyst.

Finally, and in contrast to the present identification of **PyH_2** as the important catalytic agent in homogeneous and cathode-assisted Py-mediated CO_2 reduction, it has been suggested that a surface-adsorbed dihydropyridine reduces CO_2 by HT from its N-H bond.[151-152] We already noted that a solution phase dihydropyridine is normally involved in observed HT reactions such as those in eq. 1 and 2. In any event, in our view, the proposed reduction through the surface-adsorbed species does not provide a viable HT mechanism.[208] A key issue is that the adsorbed dihydropyridine's N-H bond is proposed to act as a hydride donor.[152] However, the N-H hydrogen is protic, not hydridic; accordingly, this suggestion is inconsistent with the extensive literature concerning HT from dihydropyridines,[107, 113-114, 116, 138, 176, 178-180, 182, 205-206] including the present work, which uniformly shows that the hydride transfers from the hydridic hydrogen of the C-H bond and not from N-H.[209]

2.3.8 Recovery of aromaticity drives hydride transfer from PyH_2. We have shown that CO_2 reduction to CH_3OH is accomplished via three successive HTPT steps by **PyH_2**. We now describe the principle that makes **PyH_2** an effective HT agent. In fact, **PyH_2**'s strong hydride nucleophilicity could be regarded in a certain sense as rather surprising; it is an organo-hydride where the hydridic H is provided by a C-H bond. Consequently, **PyH_2** differs significantly from conventional transition-metal hydrides (M-H)[105-106, 181, 183] in that C is more electronegative than the transition metals (M), e.g., Co, Ni and Pt. We suggest that the origin of the hydride nucleophilicity of the hydridic C-H bonds of **PyH_2** lies in the energetics of dearomatization and aromatization of PyH^+,[120] a concept similar to one applied to metal-ligand cooperation in catalysis involving transition-metal complexes.[210-211] During the formation of **PyH_2**, the first reduction of PyH^+ to PyH^0 dearomatizes PyH^+'s ring (Scheme 2.9a, route **II**), a destabilization consistent with PyH^{+}'s highly negative E^0 of ~ -1.3V vs. SCE. PyH^{+}'s proclivity to regain its aromaticity drives HT from the hydridic C-H bond of **PyH_2** to the carbon atoms of CO_2, HCOOH and OCH_2 to form reduced products and to recover the aromatic PyH^+ (or Py) catalyst. This mirrors the aromatization driving force several of us previously described in $PyCOOH^0$ formation via a $1e^-$ process.[120]

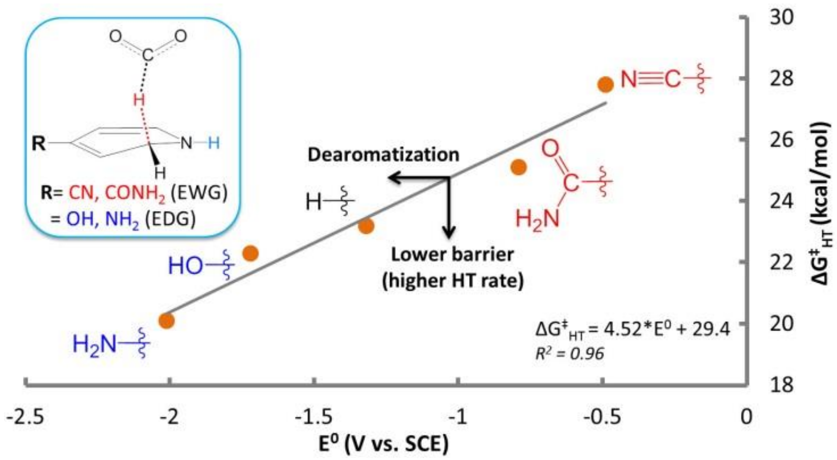

Figure 2.6: The calculated standard activation free energy 'barrier' $\Delta G^{\ddagger}_{HT}$ (kcal/mol) to hydride transfer to CO_2 correlates linearly with the degree of dearomatization of the hydride donor.

$\Delta G^{\ddagger}_{HT}$ (kcal/mol) is calculated for hydride transfer to CO_2 to form $HCOO^-$ using the DHT model of Figure 2.2a (also shown here in the inset). E^0 measures the energy required to dearomatize PyH^+ and related protonated aromatic amines and thus serves as a quantitative measure of the degree of dearomatization. E^0 (V vs. SCE) is our calculated standard reduction potential for the protonated pyridine species indicated in Scheme 2.9a, route **II**, e.g. $PyH^+ + e^- = PyH^0$ (see SI, section 1b for details of E^0 calculations). We substitute **PyH_2** with electron-withdrawing (R= CN, $CONH_2$) and electron-donating (R= OH, NH_2) groups in the para position of the ring to establish a wide range of E^0, spanning from -0.49 to -2.10V vs. SCE, and thus a broad degree of dearomatization.

Figure 2.6 confirms the dearomatization-aromatization principle by demonstrating that the free energy barrier for HT to CO_2, $\Delta G^{\ddagger}_{HT}$, decreases with increasing cost of dearomatization as measured by the standard reduction potential E^0 defined in Scheme 2.9a, route **II**. We obtain a wide range of E^0 spanning from -0.49 to -2.10V vs. SCE by substituting electron-withdrawing (e.g. CN, $CONH_2$) and electron-donating (e.g. OH, NH_2) groups at **PyH_2**'s para position. We contend that as the E^0 of an aromatic species becomes increasingly negative, more energy is required to dearomatize that species by populating its LUMO (a benzene-like π^* orbital);[96] thus E^0 is a quantitative measure of the energetic cost of dearomatization. The linear trend established in Figure 2.6 has a firm physical basis: as E^0 becomes more negative, the driving force to recover aromaticity increases accordingly, which in turn results in lower $\Delta G^{\ddagger}_{HT}$ and consequently a higher hydride transfer rate. Figure 2.6 shows that the effect of dearomatization/aromatization on $\Delta G^{\ddagger}_{HT}$ enables **PyH_2** to act in its unique role as a potent hydride donor, here one that catalyzes the reduction of CO_2 to CH_3OH through three HTPT steps and which is regenerated through the **PyH_2**/Py redox couple (Scheme 2.9a, route **I**-**II**-**V**-**VI**).

2.4 Concluding Remarks

In summary**,** we have elucidated a kinetically and thermodynamically viable mechanism for the reduction of CO_2 to CH_3OH by 1,2-dihydropyridine, **PyH_2**, via primarily homogeneous steps with some heterogeneous cathode assistance.[212] Our proposed sequential PT-ET-PT-ET process of alternating proton and electron transfers (Scheme 2.9a, routes **I**-**II**-**V**-**VI**) that initially transforms Py into the catalytic species **PyH_2** is supported by the observation of a similar process occurring in Py-related species, e.g. nicotinamide and acridines,[117-119] where the aromatic PyH^+ is dearomatized during the process. Subsequently, driven by the proclivity to recover aromaticity, **PyH_2** transfers its hydridic hydrogen in three successive steps to CO_2, HCOOH and OCH_2 to ultimately form CH_3OH (Scheme 2.9b, routes **VII**-**X**). The initial reduction of CO_2 is mediated by an uncoupled, sequential HTPT process; for the subsequent HCOOH and OCH_2 reductions, coupled HTPT occurs, in which PT is mediated by a proton relay via one or two water molecules.

We stress that while we have theoretically demonstrated CO_2 reduction proceeding primarily homogeneously after **PyH_2** formation, we do not rule out possible intrinsically surface-catalyzed events, most especially on a Pt electrode (see section 2.3.1). On the other hand, we suggest that both Bocarsly's p-GaP[39] (modulo the two cathode-assisted aspects we have described within) and MacDonnell's surface-free Ru(II)/ascorbate[148] systems are homogeneous processes mediated by our proposed recyclable **PyH_2**/Py redox couple. This suggestion is reinforced by Tanaka's demonstration that the related dihydropyridine (**$Ru(bpy)_2(pbnH_2)^{2+}$**) species homogeneously reduces CO_2 to $HCOO^-$ by hydride transfer;[107] in addition, the related 10-methyl-9,10-dihydroacidine has been demonstrated to convert benzaldehyde into benzyl alcohol via a HTPT step.[205] We thus theoretically predict that pyridine's intriguing catalytic behavior lies in the fundamentally homogeneous HT chemistry of the **PyH_2**/Py redox couple, whose production (Scheme 2.9a) is driven by a dearomatization-aromatization process, as argued in connection with Figure 2.6.

It is noteworthy that the **PyH_2**/Py redox couple --- by its hydride transfer to carbonyl for C-H bond formation --- closely imitates the NADPH/$NADP^+$ catalyzed reduction step in photosynthesis (see Scheme 2.5a). Our results thus suggest that the NADPH/$NADP^+$ couple is similar to the **PyH_2**/Py couple in that dearomatization is used to store energy that is subsequently used to drive HT while regaining aromaticity. Finally, we propose that the advantage of the recyclable **PyH_2**/Py redox couple extends beyond the mechanism of CO_2 reduction described within to provide inexpensive and green alternatives to commonly used hydride donors in organic synthesis.

3 Roles of the Lewis Acid and Base in the Chemical Reduction of CO_2 Catalyzed by Frustrated Lewis Pairs

Chern-Hooi Lim,[†] Aaron M. Holder,[†,‡] James T. Hynes,[‡,§] and Charles B. Musgrave[*,†,‡]

[†]Department of Chemical and Biological Engineering and [‡]Department of Chemistry and Biochemistry, University of Colorado, Boulder, Colorado 80309, United States [§]Department of Chemistry, UMR ENS-CNRS-UPMC-8640, Ecole Normale Supérieure, Paris 75005, France

Inorganic Chemistry: dx.doi.org/10.1021/ic4013729

Abstract:

We employ quantum chemical calculations to discover how frustrated Lewis pairs (FLP) catalyze the reduction of CO_2 by ammonia borane (AB); specifically, we examine how the Lewis acid (LA) and Lewis base (LB) of an FLP activate CO_2 for reduction. We find that the LA (trichloroaluminum, $AlCl_3$) alone catalyzes hydride transfer (HT) to CO_2 while the LB (trimesitylenephosphine, $PMes_3$) actually hinders HT; inclusion of the LB increases the HT barrier by ~8 kcal/mol relative to the reaction catalyzed by LAs only. The LB hinders HT by donating its lone pair to the LUMO of CO_2, increasing the electron density on the C atom and thus lowering its hydride affinity. Although the LB hinders HT, it nonetheless plays a crucial role by stabilizing the active FLP•CO_2 complex relative to the LA dimer, free CO_2 and free LB. This greatly increases the concentration of the reactive complex in the form FLP•CO_2 and thus increases the rate of reaction. We expect that the principles we describe will aid in understanding of other catalytic CO_2 reductions.

3.1 Introduction

The rising concentration of atmospheric carbon dioxide (CO_2) and its potential to impact global climate has motivated a growing effort to lower atmospheric CO_2 levels.[9] One approach that has gained significant attention is the capture and sequestration of CO_2. However, among the many obstacles to this approach is the significant challenge of long-term, stable storage of CO_2 in vast quantities.[213] An alternative approach that has received less attention and avoids the issue of long-term CO_2 sequestration is the chemical reduction of CO_2 into valuable materials such as methanol (CH_3OH) or its dehydrated form dimethyl ether[10] or possibly C_n ($n \geq 2$) products. The conversion of CO_2 into CH_3OH or other fuels using renewable energy input would enable a carbon-neutral energy cycle that could have a dramatic effect on atmospheric CO_2 levels. The successful conversion of CO_2 to CH_3OH by various homogeneous catalysts and reducing agents has been reported elsewhere;[15, 18-19, 108, 214] here we use quantum chemistry to discover the underlying principles that govern CO_2 conversion by frustrated Lewis pairs (FLP) catalysts.

Experimentally, an FLP was first used to activate CO_2 by irreversibly complexing with it to catalyze CO_2 reduction via hydride transfer (HT) from ammonia borane (NH_3BH_3, AB), which acts as a sacrificial hydride donor;[20, 215] each HT is equivalent to a two-electron reduction. 37-51% yield of CH_3OH was observed after 15 min. at ambient conditions. The FLP consists of a Lewis acid (LA) and a Lewis base (LB) with bulky ligands that prevent these species from neutralizing each other.[216] In particular, the FLP used to activate CO_2 for reduction (and our focus in this work) consists of two trichloro-aluminum ($AlCl_3$) LAs and the trimesitylenephosphine ($PMes_3$, Mes = 2,4,6-$C_6H_2Me_3$) LB, where the LAs and LB datively bond to the oxygens and carbon of CO_2, respectively, to form an FLP•CO_2 complex (Figure 3.1b).

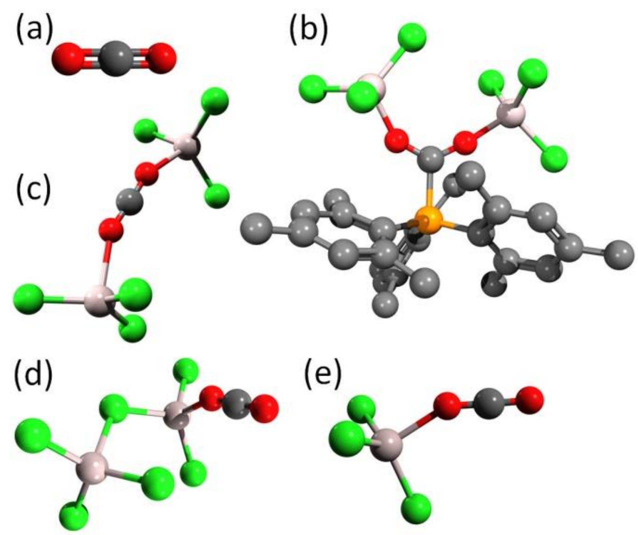

Figure 3.1: Reactive complexes of CO_2 considered.
(a) Free CO_2 molecule, (b) FLP•CO_2, composed of CO_2, two LAs and one LB, (c) LA-O=C=O-LA, (d) CO_2•$(LA)_2$, and (e) CO_2•(LA). H atoms in (b) omitted for clarity. Al, light gray; C, gray; Cl, green; O, red; and P, orange.

Recent experimental efforts have aimed at modifying the original $AlCl_3$-$PMes_3$ FLP system,[217-218] e.g. by varying the LA bound to CO_2[219] and employing geminal P/Al-based FLPs,[220] but those systems afforded weaker complexation to CO_2 than the $AlCl_3$-$PMes_3$ FLP. Additionally, recent theoretical studies identify the mechanistic steps for conversion of CO_2 to CH_3OH catalyzed by the FLP[221] and provide insights into the effect of explicit C_6H_5Br solvent in FLP•CO_2 formation.[222] However, these experimental and theoretical efforts have not examined several key issues of CO_2 reduction by FLPs, namely, the mode of CO_2 activation, the roles of the LA and LB in CO_2 reduction, the effect of LA dimerization, and the possible need for pre-bending CO_2 prior to its reduction. The use of an expensive FLP and AB as a sacrificial hydride source will unlikely be pragmatic for CO_2 reduction, however we examine the basic aspects of CO_2

reduction by FLPs and LAs to further the fundamental understanding of CO_2 activation that may provide insight into developing improved CO_2 reduction catalysts.

3.2 Computational Details

See supporting information attached in the appendices.

3.3 Results and Discussion

3.3.1 LB hinders HT: an anti-catalytic role. One might expect both members of the FLP to assist in catalysis. However, close inspection of the FLP•CO_2 complex shown in Figure 3.1b reveals a striking chemical contradiction in the role of the LB in FLP activation of CO_2 for its chemical reduction; in the complex, the LB donates its lone pair to the carbon of CO_2, which should decrease the electrophilicity of the CO_2 carbon and hence lower its tendency to accept a hydride. We thus hypothesize that: 1) the LB in FLP•CO_2 actually hinders HT, and consequently 2) the LA must act as the catalyst that both activates CO_2 for reduction and overcomes the hindrance to HT caused by the LB.

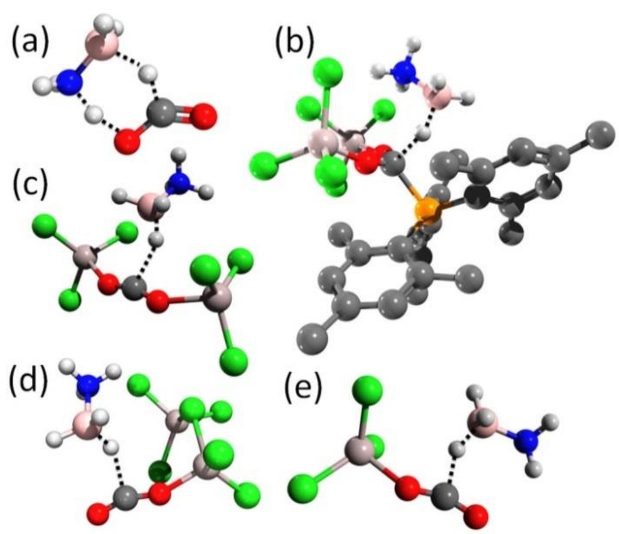

Figure 3.2: Transition state structures of CO_2 complexes with AB.

(a) CO_2 + AB, (b) FLP•CO_2 + AB, (c) LA-O=C=O-LA + AB, (d) CO_2•(LA)$_2$ + AB and (e) CO_2•(LA) + AB. The H atoms of $PMes_3$ ligands in (b) are omitted for clarity. Al, light gray; B, pink; C, gray; Cl, green; H, white; N, blue; O, red; P, orange.

To test these hypotheses, we have calculated the reaction barrier (activation enthalpy, $\Delta H^{\ddagger}_{hydride}$) for HT from AB to CO_2 using $AlCl_3$ as the LA and $PMes_3$ as the LB for the following five cases: a) the reference uncatalyzed reduction (Figure 3.2a) where AB reduces CO_2 in the absence of the FLP, b) catalyzed reduction by the FLP (Figure 3.2b), c) and d) catalyzed reduction by two LAs (isomer 1, Figure 3.2c and isomer 2, Figure 3.2d) and e) catalyzed reduction by a single LA (Figure 3.2e). Cases **c**-**e** involve only LAs and thus allow us to determine whether LAs alone catalyze CO_2 reduction and if so, which arrangement is most effective, and by comparison with the FLP catalyzed reaction (case **b)**, whether the LB hinders HT.

One of us previously published a detailed mechanistic study using the accurate CCSD(T) method for the uncatalyzed conversion of CO_2 to CH_3OH by AB where complete conversion to CH_3OH requires three HTs.[21] Here, we instead examine the first catalyzed HT in order to focus on the roles of the LA and LB in CO_2 activation. It is important to note in this connection that in the uncatalyzed case **a**, the hydride and proton transfer concomitantly react to produce formic acid,[21] whereas in the catalyzed (vide infra) cases **b-e** our calculations predict HT occurs to produce (complexed) formate ($HCOO^-$). Table 3.1 reports the predicted $\Delta H^{\ddagger}_{hydride}$ for the aforementioned five cases in C_6H_5Cl solvent, described by the implicit polarizable continuum model (CPCM).[68, 223]

Before discussing the results in Table 3.1, an important computation issue requires comment. The FLP system involves significant dispersion interactions that affect complexation energies and thus HT barriers. Therefore, we employed the B97-D exchange-correlation functional to obtain TS and equilibrium geometries as this method accounts for dispersion effects important in complex formation.[224] Grimme *et al*. previously used this functional to describe the heterolytic cleavage of H_2 by an FLP catalyst for which the popular B3LYP functional gave erroneous results due to its neglect of dispersion.[225] For accurate energies, we performed MP2 single-point energy calculations at the B97-D identified stationary point geometries, which we found differ from high-level CCSD(T)//MP2 energies by less than 1 kcal/mol for both HT barriers and complexation energies (see Supporting Information for additional computational details).

Table 3.1: HT barrier ($\Delta H^{\ddagger}_{hydride}$) and hydride affinity (HA) of CO_2 complexes at T=298K and P=1atm.

System	$\Delta H^{\ddagger}_{hydride}$ [a]	HA [b]
a) CO_2	25.3	40.5
b) FLP•CO_2	7.9	79.9
c) LA-O=C=O-LA	–0.2	131.9
d) CO_2•$(LA)_2$	4.1	99.1
e) CO_2•(LA)	3.8	91.7

[a]HT (from AB) enthalpic barriers, in kcal/mol, referenced to the reactant complex. [b]Hydride affinity, in kcal/mol. All calculations performed using MP2/6-311++G(d,p)//B97-D/6-311G(d,p) [MP2//B97-D], except $\Delta H^{\ddagger}_{hydride}$ of case **c**, which was calculated using CCSD(T)/6-311++G(d,p)//MP2/6-311G(d,p) [CCSD(T)//MP2]. All enthalpies include zero-point energies (ZPE) and thermal corrections at 298 K. Solvation in C_6H_5Cl was treated with the CPCM solvent model.

3.3.2 Hydride transfer barriers and affinities reveal the catalytic role of the LA. We now return to the main focus of this paper and observe that the $\Delta H^{\ddagger}_{hydride}$ values reported in Table 3.1 indicate that although the FLP does indeed catalyze CO_2 reduction by lowering $\Delta H^{\ddagger}_{hydride}$ from 25.3 kcal/mol for the uncatalyzed case **a** to 7.9 kcal/mol for the FLP catalyzed case **b**, the barriers are even lower for cases **c**-**e** that exclude the LB and only involve the LAs. This confirms our hypothesis that the LB impedes HT and that the LAs alone activate CO_2 for reduction (see SI, Section 3 for additional TS properties). The previously reported $\Delta H^{\ddagger}_{hydride}$ using B3LYP for case **b** is ~7 kcal/mol higher than our calculated barrier,[221] which we attribute to B3LYP's neglect of dispersion (see SI, Section 4). Furthermore, in contradiction to the suggestion that "pre-bending" of CO_2 is necessary to assist its reduction, we show that LAs catalyze the reduction of the linear form of CO_2 resulting in low HT barriers (see Figure 3.1c-e). For example, at the transition state (TS) for case **c** $\angle$O-C-O is 178^{o} (Figure 3.1c) and HT is barrierless. In addition, in case **b** where CO_2 is pre-bent (Figure 3.1b, $\angle$O-C-O= 126^{o}), the LB raises $\Delta H^{\ddagger}_{hydride}$ by ~8 kcal/mol compared to case **c**; this is due to the nucleophilic competition between the donating lone pairs of the LB and the transferring hydride from AB to the LUMO of CO_2.

We now examine the relative roles of the LB and LA moieties in further detail. We start with the case of two LAs (case **c)**, obtained by elimination of the $PMes_3$ LB from the FLP case **b**. We could not locate a TS for this step with B97-D, but were able to determine a TS using MP2 (single imaginary frequency of 182*i* cm^{-1}). A CCSD(T) energy at the MP2 TS geometry predicts a barrierless reaction after addition of ZPE and thermal contributions. Thus, the two LAs catalyze CO_2 reduction and adding the LB increases the barrier. With the catalytic importance of the two LAs of case **c** thus established, we ask if a different arrangement of the LAs would be more effective. The alternate arrangement $CO_2\bullet(AlCl_3)_2$ was suggested by Olah *et al*. as one of the reactive complexes in the addition of CO_2 to C_6H_6 to produce benzoic acid.[226] We examine this type of complex involving a $(LA)_2$ dimer in case **d**. We find that $\Delta H^{\ddagger}_{hydride}$= 4.1 kcal/mol, showing that this dimer also catalyzes HT to CO_2. These results suggest examination of the single LA (case **e**). And here we calculate a HT barrier of 3.8 kcal/mol. Thus, as we have previously noted, all three LA configurations **c**-**e** have HT barriers substantially below that of the FLP case **b** involving two LAs and the LB.

What is the key property of the LAs for catalytic CO_2 reduction efficacy? For Friedel-Crafts acylation where CO_2 adds to C_6H_6 to produce benzoic acid, Olah *et al*. concluded that the reaction was catalyzed by $AlCl_3$'s superelectrophilic activation of CO_2.[226] Also, Ren *et al*. observed a notable increase in the electrophilicity of simple aldehydes and ketones (carbonyl-containing species, like CO_2) when complexed to the LA BF_3.[227] These observations are consistent with our results, which show that the LAs lower the HT barriers by electrophilic activation of CO_2. We elaborate upon this explanation via hydride affinity (HA) calculations, reported in Table 3.1. HA is here defined as the negative of the change of enthalpy when CO_2's carbon (in complexes **a**-**e**) accepts a hydride. HA quantifies the electrophilicity of the carbon of CO_2 to accept a hydride, and as we now discuss, the fact that complexes **a**-**e** are more electrophilic with increasing HA is key for understanding the trends in Table 3.1's HT barriers.

As can be seen in Table 3.1, the FLP catalyst increases the HA of CO_2 from 40.5 (**a**) to 79.9 kcal/mol (**b**), a result consistent with the increase in CO_2 electrophilicity and thus the lowering of the HT barrier from 25.3 to 7.9 kcal/mol. When CO_2 is complexed with LAs only, as in cases **c**-**e**, the HA markedly increases to greater than 90 kcal/mol, consistent with the low HT barriers of **c**-**e**. This is especially true for **c**, where the HA is 131.9 kcal/mol and HT is barrierless. Thus, the role of the LAs is to render CO_2 more electrophilic (high HA), and as a result lower the barrier to HT. These results also support Stephan *et al.*'s very recent proposal that coordination of LAs to the oxygens of formate promotes HT.[228] The hindering role of the LB that we have emphasized is evident when the HAs of cases **b** and **c** are compared: removing the LB from (**b**) to create (**c**) results in a significant increase in HA from 79.9 to 131.9 kcal/mol.

Table 3.2: Thermodynamics of complex formation relative to the reactants two free CO_2, $(LA)_2$ dimer, two free LB and two free AB at T=298 K and P=1 atm.

Complexes	ΔH^a	$T\Delta S^a$	$K_{eq}{}^b$
1) $2CO_2 + (LA)_2$ + 2LB + 2AB	0.0	0.0	1.0
2) **FLP•CO_2** + CO_2 + LB + 2AB	-49.0	-26.5	2.8×10^{16}
3) **LA-O=C=O-LA** + CO_2 + 2LB + 2AB	12.9	-5.1	7.3×10^{-14}
4) **CO_2•$(LA)_2$** + CO_2 + 2LB + 2AB	0.8	-9.1	5.4×10^{-8}
5) 2[**CO_2•(LA)**] + 2LB + 2AB	4.9	-5.6	2.1×10^{-8}
6) **CO_2•(LA)** + CO_2 + **LA•LB** + LB + 2AB	-20.9	-12.6	1.2×10^{6}
7) **CO_2•(LA)** + CO_2 + **LA•AB** + 2LB + AB	-9.8	-8.0	2.1×10^{1}
8) **CO_2•$NH_3BH_2^+$** + **$AlCl_3H^-$** + CO_2 + **LA•AB** + 2LB	24.3	-7.5	4.7×10^{-24}
9) $2CO_2$ + 2[**LA•LB**] + 2AB	-46.7	-19.6	7.1×10^{19}
10) $2CO_2$ + 2[**LA•AB**] + 2LB	-24.5	-10.4	2.1×10^{10}
11) $2CO_2$ + **LA•LB** + **LA•AB** + LB + AB	-35.6	-15.0	1.21×10^{15}

[a]ΔH and TΔS in kcal/mol referenced to two free CO_2, $(LA)_2$ dimer, two free LB and two free AB of case 1 (see eq. 1 below). [b]Equilibrium constant of the complexes (unitless), defined as $K_{eq} = \exp(-\Delta G/RT)$. Calculations were performed using MP2//B97-D in CPCM modeled C_6H_5Cl solvent.

3.3.3 Positive role of the LB: establishing high concentrations of reactive CO_2 complexes.

We have already established that the role of the LB in the key CO_2 reduction step is a negative one – to hinder HT. We now ask if the LB might play any positive role in the FLP activation of CO_2; we will find that the answer is yes, but its origin lies in the formation of reactive CO_2 complexes rather than in their activation for reduction. Table 3.2 shows the calculated thermochemistry for several complexes (shown in bold and defined in equation 1; see SI, section 5) referenced to the starting reactants in case 1; two free CO_2, $(LA)_2$ dimer [$(AlCl_3)_2$], two free LB ($PMes_3$), and two free AB. Ammonia borane has been included here because, even though it was added to function as a reducing agent, it also complexes with the electrophilic LA through its hydridic hydrogens.[228] Dimeric $(AlCl_3)_2$ was chosen as the reference for Table 3.2 because $AlCl_3$ is known to predominantly form dimers[226] at various conditions;[229-231] the dimerization enthalpy of the LAs must be considered in determining the relative concentrations of reactive CO_2 complexes (vide infra).

$$2CO_2 + (LA)_2 + 2LB + 2AB \xleftrightarrow{\Delta H;\, T\Delta S;\, Keq} \text{Complexes 1 to 11} \quad (\textbf{eq. 1})$$

The thermodynamic variables reported in Table 3.2 allow us to predict the relative concentrations of a number of reactive CO_2 complexes. We calculate that K_{eq} for LA-O=C=O-LA (**3**) formation is 7.3×10^{-14}. This exceptionally low equilibrium constant is due to both the enthalpic and entropic costs of forming the complex from the $(AlCl_3)_2$ dimer and CO_2. The CO_2•$(LA)_2$ complex (**4**), where the LA dimer complexes with CO_2, initially looks more promising. K_{eq} for this case is 5.4×10^{-8}, ~6 orders of magnitude higher than for LA-O=C=O-LA. But this is still low, mainly due to the entropic cost of complex formation, which for this case is approximately enthalpically neutral. This CO_2•$(LA)_2$ complex should attain its equilibrium concentration with CO_2 and $(LA)_2$ dimer in the absence of LB and AB because the barriers for its formation (10.6 kcal/mol) from and dissociation (9.9 kcal/mol) to CO_2 + $(LA)_2$ are thermally accessible at room temperature (see SI section 3b). However its low K_{eq} suggests that it will not in fact be present in significant concentration. Thus, although complexes LA-O=C=O-LA and CO_2•$(LA)_2$ both have low barriers to HT (Table 3.1, cases **c** and **d**), their equilibrium concentrations are too low to have a significant reaction rate in reducing CO_2.

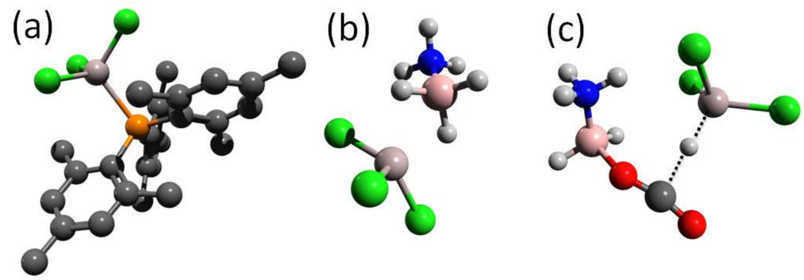

Figure 3.3: Various complexes.
(a) LA•LB complex, (b) LA•AB complex and (c) TS structure of CO_2•$NH_3BH_2^+$ + $AlCl_3H^-$, calculated at MP2//B97-D. LA = $AlCl_3$, LB = $PMes_3$, and AB = NH_3BH_3. The H atoms in (a) are omitted for clarity. Al, light gray; B, pink; C, gray; Cl, green; H, white; N, blue; O, red; and P, orange.

We next analyze reactive CO_2 complexes involving monomeric LA (Table 3.2, cases **5-7)**. Case **5** results from dissociation of the $AlCl_3$ dimer to form two CO_2•(LA) complexes. Its K_{eq} is low (2.1 x 10^{-8}) because CO_2•(LA) complexation is less exothermic than $AlCl_3$ dimerization. However, this dimerization is suppressed and an effective concentration of CO_2•(LA) established when LB or AB dissociate the $AlCl_3$ dimer by forming LA•LB (Figure 3.3a) or LA•AB (Figure 3.3b) complexes, Table 3.2 cases **6** and **7**, where K_{eq} is 1.2 x 10^6 and 2.1 x 10^1, respectively. Thus, in addition to its key role as a hydride donor, AB complexes with the LA via its hydridic H and promotes LA•AB adduct formation that increases CO_2•(LA) concentration. Given that CO_2•(LA) forms in non-vanishing concentrations relative to the dominant cases (Table 3.2, **2** and **9**), combined with the low HT barrier of 3.8 kcal/mol (Table 3.1, case **e**), CO_2 reduction via reactive CO_2•(LA) contributes to the CO_2 reduction rate. Case **8** in Table 3.2 is similar to CO_2 activation by one LA (Table 3.1, case **e**). Here, borenium cation $NH_3BH_2^+$ acts as a LA that activates CO_2 for HT from the $AlCl_3H^-$ counter ion. Figure 3.3c shows the TS for this HT where $\Delta H^{\ddagger}_{hydride}$ = 3.0 kcal/mol. But despite the low HT barrier, the endothermic formation of CO_2•$NH_3BH_2^+$ and $AlCl_3H^-$ results in a vanishingly low K_{eq} value of 4.7 x 10^{-24}, thus making this pathway inactive.

The single case that exhibits a positive role for LB is case **2** of Table 3.2 in which CO_2 is activated in the FLP•CO_2 complex. FLP•CO_2 proves to be one of the most readily formed CO_2 complexes. The large formation constant of K_{eq} = 2.8 x 10^{16} results from a favorable -49.0 kcal/mol enthalpy of formation relative to the $(LA)_2$ dimer, free CO_2 and free LB; this enthalpic contribution is nearly double the unfavorable entropic contribution (see Table 3.2). We conclude that the role of the LB in FLP-catalyzed reduction of CO_2 by AB is to provide a sufficient enthalpic driving force for the formation of the reactive FLP•CO_2 complex. Thus, we predict that, given its large K_{eq} and relatively low 7.9 kcal/mol HT barrier (Table 3.1, case **b**), FLP-catalyzed CO_2 reduction via FLP•CO_2 complex will dominate the HT rate, with minor contributions from CO_2•(LA) formed through Table 3.2 cases **6** and **7**.

In view of the above predictions, we now discuss the recent proposal by Stephan *et al.*[228] that in the presence of AB, the FLP•CO_2 complex first dissociates to produce different reactive CO_2 complexes that can dominate the HT rate. For the specific LA and LB choices considered here, our results we discussed above indicate that the dominant HT pathway proceeds through the undissociated FLP•CO_2 complex, with only minor contributions involving the AB-induced FLP•CO_2 dissociation product CO_2•(LA) (Table 3.2, case **7**). On the other hand, when LA = $Al(C_6F_5)_3$, and LB = P(*o*-tol)$_3$, where *o*-tol= 2-C_6H_4Me and AB = NMe_3BH_3,[228] the equilibrium of the analogues of **6** and **7** relative to **2** in Table 3.2 will be shifted due to the steric effects introduced by $Al(C_6F_5)_3$. This effect may increase the contribution to the HT rate by CO_2•(LA) in Table 3.2 cases **6** and **7** as proposed by Stephan *et al*.

In Table 3.2 cases **9-11**, favorable LA•LB and LA•AB interactions lead to CO_2 not being complexed and thus not activated. In case **9**, LA•LB exists in equilibrium (K_{eq} = 7.1 x 10^{19}) with FLP•CO_2 (K_{eq} = 2.8 x 10^{16}). In fact, LA•LB was isolated experimentally in the absence of CO_2. In contrast, FLP•CO_2 was isolated (as a solid) when the solvent was evaporated from mixtures containing LA, LB and CO_2.[20] In the solid-state structure, the enthalpy of formation dominates K_{eq}, thus FLP•CO_2 (ΔH= -49.0 kcal/mol) is predicted to exist in greater abundance than LA•LB (ΔH= -46.7 kcal/mol). In the presence of LB, **9** likely dominates over **10**, although LA•AB can still coexist with LA•LB through **11**. Interactions of the LB and AB with the LA in LA•LB and LA•AB complexes significantly shift the equilibrium concentrations and are key factors to consider in optimizing concentrations of reactive CO_2 complexes.

3.3.4 Reactive CO_2 complexes formed in the absence of LB. In addition to revealing the roles of the LAs and LB in the FLP-catalyzed reaction, our results suggest an alternate approach to CO_2 reduction using only LAs. None of the cases **1**, **3**, **4**, **5**, **7**, **8**, and **10** in Table 3.2 involve the LB and are thus relevant for the LB-free situation. The comparison of their equilibrium constant values indicates that when LB is absent, the equilibrium established by **10** dominates in which AB dissociates the $AlCl_3$ LA dimer to form LA•AB in abundance. This conclusion agrees with the reported isolation of analogous LA•AB complexes (LA= $Al(C_6F_5)_3$ and AB= NMe_3BH_3) in high yield.[228] But, CO_2 is not activated by LA•AB. Our results suggest that reactive CO_2 species are instead formed as CO_2•(LA) by reaction **7** in equilibrium with **10**. This proposal that CO2 is activated in the CO_2•(LA) form is supported by isolation of $Al(C_6F_5)_3(HCO_2)H_2BNMe_3$ formate species in the absence of LB;[228] the observed formate species is analogous to the HT product of the reaction of CO_2•(LA) with AB (Table 3.1, case **e**). We suggest that in the absence of LB, the relative K_{eq} values for cases **1**, **7**, and **10** must be considered to optimize the concentration of CO_2•(LA) in order to lead to rapid CO_2 reduction. Ideally, the K_{eq} value for **7** should be high[232] relative to **1** and **10**. In other words, a relatively high CO_2•(LA) complexation enthalpy and low binding affinities for LA•LA (dimer) and LA•AB formation will lead to significant concentrations of activated CO_2 complexes for CO_2 reduction. We propose that this can be achieved by employing LA and AB with bulky ligands[233-234] to weaken LA•LA and LA•AB interactions relative to CO_2•(LA).

3.4 Conclusion

In summary, we have determined a number of the underlying principles that govern CO_2 conversion by FLP catalysts. It is the LAs of the FLP that act as the catalyst by polarizing CO_2 to render it more electrophilic to accept a hydride at low barriers, which are strongly correlated with the hydride affinity of CO_2 in the complex. Furthermore, the LAs catalyze HT to CO_2 without pre-bending it from its linear geometry. Although we find that the LB hinders HT within the FLP•CO_2 complex by lowering the hydride affinity of CO_2, its role is to stabilize that complex relative to the $(LA)_2$ dimer, free CO_2 and free LB. This results in a high HT rate due to the high concentration of reactive CO_2 species in the FLP•CO_2 complex and a low HT barrier. In the presence of LB, and for the LA and LB considered here, we predict that the reactive CO_2 complex CO_2•(LA) is a minor pathway to HT relative to CO_2 reduction via the FLP•CO_2 complex. However, in the absence of LB, we predict that instead CO_2•(LA) will be the dominant reactive CO_2 complex responsible for forming HT products[228] such as formate and methoxide. We anticipate that the principles found here should prove useful in the understanding and discovery of other catalytic CO_2 reductions.

4 A Benzimidazole-Based Organo-Hydride for the Reduction of CO_2

Chern-Hooi Lim[1]*, Brady T. Worrell[1], Samuel S. Bacon[1], Christopher N. Bowman[1,2,3], James T. Hynes[2,4], and Charles B. Musgrave[1,2,3]*

[1]Department of Chemical and Biological Engineering and [2]Department of Chemistry and Biochemistry, [3]Materials Science and Engineering Program, University of Colorado, Boulder, Colorado 80309, United States. [4]Chemistry Department, Ecole Normale Supérieure-PSL Research University, Sorbonne Universités-UPMC University Paris 06, CNRS UMR 8640 Pasteur, 24 rue Lhomond, 75005 Paris, France

Abstract:

We report the metal-free reduction of CO_2 to the formate anion by a benzimidazole-based organo-hydride guided by quantum chemical calculations. The formate product was characterized and confirmed by ^{1}H-NMR, ^{13}C-NMR, and ESI-MS. We obtained the highest formate yield in the presence of potassium bromide under mild conditions; the proposed role of exogenous salt additives in this reaction is to stabilize and shift the equilibrium towards the ionic products. Such benzimidazole-based organo-hydrides rival the hydride donating abilities of noble metal-based hydrides, such as $[Ru(tpy)(bpy)H]^+$ and $[Pt(depe)_2H]^+$, demonstrating that these organo-hydrides stand as powerful, renewable, and inexpensive hydride transfer catalyst alternatives. We envision a catalytic cycle wherein benzimidazole-based organo-hydrides reduce CO_2 to fuels and their regeneration is driven by renewable energy, thereby catalytically and sustainably producing usable fuel from CO_2.

4.1 Introduction

The chemical reduction of gaseous carbon dioxide (CO_2) to liquid fuels (e.g. methanol) powered by renewable energy could revolutionize the future landscape of energy.[235-236] Although such a technology could effectively close the carbon cycle and despite much progress in the conversion of CO_2 to utilizable fuels, no process has effectively met the requirements for the practical conversion of CO_2 to fuels nor has the scientific community yet reached a consensus on a general approach.

The reduction of CO_2 via hydride (H^-) transfers stands as one of the most promising approaches to CO_2 conversion,[179-180, 237] with several reports describing progress towards implementation of such a system.[106-107, 238] Naturally, CO_2 cannot proceed directly to methanol by a reductive pathway; rather it undergoes a series of three reductions followed by protonations; first, to formic acid (HCOOH), second to methanediol, which converts to formaldehyde (CH_2O) with loss of water, and finally to methanol (CH_3OH).[239] Overall, this exergonic process requires the addition of three hydrides and three protons.

Transition metal hydrides have been studied and proven effective for such reductions, with some efforts focused on determining their relative hydricities: the thermodynamic property which quantifies their potency as hydride (H^-) donors.[181, 183, 240] Strong transition metal hydrides normally involve noble metals, such as $[Ru(tpy)(bpy)H]^+$ and $[Pt(depe)_2H]^+$;[240] however, recent advances using non-precious metal species, such as $Co(dmpe)_2H$, were developed to reduce CO_2 to $HCOO^-$, however this requires a strong sacrificial base to form the requisite reducing complex *in situ*.[106] Beyond the realm of transition metal catalyzed processes, only one example of an organo-hydride has been shown to reduce CO_2 to $HCOO^-$.[107] However, the intermediacy of a Ru metal center was still required in this case where the dihydropyridine organo-hydride is part of the pbn (2-(pyridin-2-yl)benzo[b][1,5]naphthyridine)) ligand of the $Ru(bpy)_2(pbnH_2)^{2+}$ complex. Moreover, a stoichiometric quantity of Brønsted base is required to activate the H^- transfer from the pbn ligand of the Ru complex.[241] Although many of these transition metal catalyzed and coupled complexes can effectively reduce CO_2 to the formate ion and beyond, the high cost of homogeneous noble metal catalysts effectively hampers the development of economical processes for production of utilizable fuels from CO_2.

Scheme 4.1: Reduction of CO_2 to formate anion by Benzimidazole-based organo-hydride

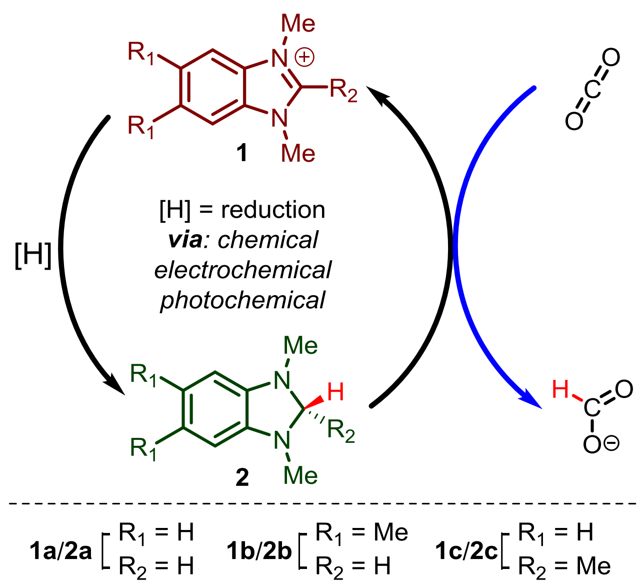

Directed by computational designs, we herein report benzimidazole-based organo-hydrides for the reduction of CO_2 to $HCOO^-$ (Scheme 4.1). To the best of our knowledge this is the first report of a non-sacrificial (*vide infra*) metal-free organo-hydride that reduces CO_2 to $HCOO^-$; moreover, it is worth noting that the CO_2 reduction illustrated in Scheme 4.1 proceeds in the absence of biological enzymes,[174] a sacrificial Lewis acid, or a base to activate the substrate or reductant.[20, 112] Specifically, as detailed in Scheme 4.1, we chemically transformed benzimidazolium cations (1,3-dimethyl-1H-benzimidazol-3-ium derivatives, species **1a-c**) into their corresponding dihydrobenzimidazole organo-hydrides (1,3-dimethyl-2,3-dihydro-1H-benzimidazole derivatives, species **2a-c**), which, as reported here, are capable of efficiently reducing gaseous CO_2 to $HCOO^-$. This demonstrates possible routes for the transformation of species **1** to **2** via electrochemical, photochemical, or photoelectrochemical pathways powered by renewable energy, thereby, closing the catalytic cycle for $HCOO^-$ generation. We envision that with the introduction of an appropriate H^+ source, exhaustive reduction of $HCOO^-$ to methanol via species **2** would be possible. We also foresee that metal-free organo-hydrides[114, 242] provide an exciting new direction as low-cost, versatile, and tunable catalysts for future CO_2 reduction research.

4.2 Results and Discussions

4.2.1 Benzimidazole-based organo-hydrides as strong hydride donors.

A number of previously reported studies have suggested that benzimidazole-based organo-hydrides are potential strong hydride donors.[179, 240, 243] Using density functional theory (DFT) calculations, we predicted the thermochemical properties of CO_2 reduction by benzimidazole-based organo-hydrides (**2a**-**c**) to determine if such hydrides were capable of reducing CO_2 to $HCOO^-$. As shown in Table 4.1, species **2a** (the most simplified system, where R_1=H and R_2=H) was predicted to reduce CO_2 to $HCOO^-$ with reaction free energy of ΔG^0_{rxn} = 4.2 kcal/mol, while regenerating species **1a**. Species **2b**, where R_1 = CH_3 and R_2 = H, was predicted to be a stronger hydride donor (when compared to our base case); the ΔG^0_{rxn},is now improved to 2.0 kcal/mol. Finally, our results predict that substitution of CH_3 at R_2 has a considerably larger effect towards the strengthening the hydricity, improving the hydride strength of **2c** such that ΔG^0_{rxn}= 0.7

kcal/mol. Our experimental results have corroborated these predictions. As noted in Table 4.1, the strongest hydride donor **2c** produced the correspondingly highest yield of $HCOO^-$ (59%) relative to complexes **2b** and **2a** (4% and 5%, respectively). We note here that these reactions were performed under mild conditions (T= 50°C and P_{CO2}= 30 psig) in DMSO-d_6 for 24 hours or less; the addition of salts, such as KBr, was empirically discovered to significantly increase the yield of the formate anion (*vide infra*).

Table 4.1: Predicted thermochemical properties of CO_2 reduction by reductants 2a-c with their corresponding experimental formate yields.

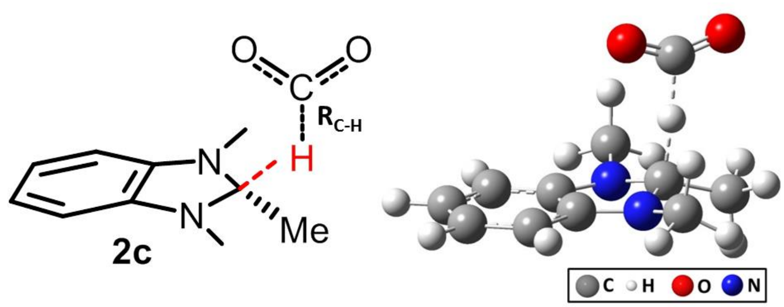

Reductant[a]	Formate yield (%)[b]	$\Delta G^{\ddagger}_{HT}$ (kcal/mol)[c]	ΔG^{0}_{rxn} (kcal/mol)[c]	R_{C-H} (Å)[d]
2a	5	23.1	4.2	1.37
2b	4	22.1	2.0	1.39
2c	59	20.6	-1.2	1.38

[a]Reaction conditions: 0.50 ml DMSO-d_6, [reductant] = 0.10M, [KBr] = 0.50M, P_{CO2} = 30 psig, T = 50°C and t = 24hr (except t = 11hr for 2c). [b]Determined from ^{1}H-NMR using 0.05M of 1,3,5-trimethoxybenzene as internal standard. [c]Activation free energy ($\Delta G^{\ddagger}_{HT}$) and reaction free energy (ΔG^{0}_{rxn}) at standard conditions were computed at rM06/6-31+G(d,p)/CPCM-DMSO level of theory. [d]Transition state bond distance between the transferring hydride (H) and the carbon (C) of CO_2.

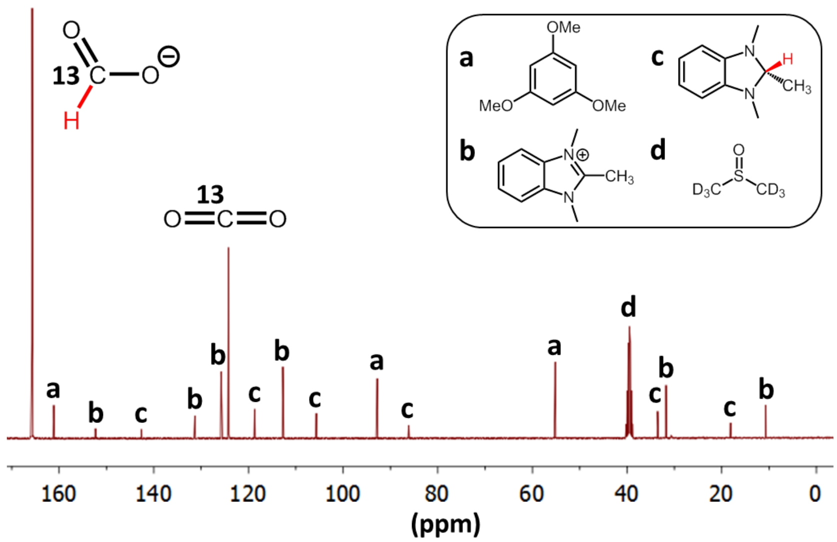

Figure 4.1: ^{13}C-NMR spectra of species 2c reacted with $^{13}CO_2$ in DMSO-d_6
Reaction conditions: [**2c**] = 0.10M, [KBr] = 0.20M, P_{CO2} = ~20 psig, T = 50^{o}C and t = 16hr. 0.05M 1,3,5-trimethoxybenzene was introduced as internal standard. ^{13}C-formate appeared at 165.70 ppm; dissolved $^{13}CO_2$ appeared at 124.18 ppm.[244]

4.2.2 Formation of ^{13}C-formate from $^{13}CO_2$.

To confirm the formation of the presumed formate anion in our reaction we have sought to detect its presence under synthetically relevant conditions via ^{1}H-NMR and electrospray ionization mass spectrometry (ESI-MS). The ^{1}H-NMR spectra obtained after completion of the reaction exhibited a peak at 8.46 ppm, which was confirmed to be the formate anion by comparison to the authentic sample (see supporting information S3 for experimental details). To further confirm the presence of the formate anion, ESI-MS (negative ion mode) was employed. The formate anion was observed to form complexes with the added salts: for example, in S4, we detected the presence of the KBr·HCOO$^-$ complex with m/z = 162.9, 164.9, and 166.9 in the correct isotopic ratios. Thus, these two analytical methods have unambiguously confirmed the presence of the formate anion in our product solution.

To further validate our proposed mechanism of reduction, we conducted experiments with isotopically enriched $^{13}CO_2$ gas (99 atom % ^{13}C). Figure 4.1 confirms the presence of $H^{13}COO^-$ (appearing at 165.70 ppm; see S5 for comparison to the authentic sample) in the product solution after $^{13}CO_2$ is reacted with the hydride species **2c**. The significant enhancement of $H^{13}COO^-$'s ^{13}C-NMR signal relative to other species in the solution (peaks a-d) is apparent in Figure 4.1. In addition, in S5, we show that the ^{13}C nuclear spin splits the ^{1}H-NMR peak of $H^{13}COO^-$ into a doublet (at 8.27 and 8.72 ppm), further corroborating the presence of isotopically enriched $H^{13}COO^-$. These results conclusively prove that the formate anion detected in the reaction mixture is derived from the chemical reduction of carbon dioxide introduced to our solution.

Table 4.2: Reaction of species 2c with CO_2 at various experimental conditions.

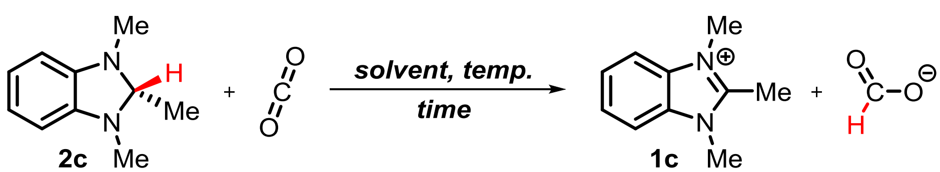

Entries[a]	Salts	[Salts] (M)	Solvent[b]	Temp. (°C)	Time (hr)	Consumption of 2c (%)[c]	Formation of 1c (%)[c]	Formate Yield (%)[c]
1	-	-	DMSO-d_6	50	24	69	69	5
2	KBr	0.20	DMSO-d_6	25	24	52	51	27
3	KBr	0.50	DMSO-d_6	25	24	79	77	33
4	KBr	0.20	DMSO-d_6	50	11	86	86	40
5	KBr	0.50	DMSO-d_6	50	11	92	91	59[d]
6	KI	0.50	DMSO-d_6	50	11	82	82	40[d]
7	LiBr	0.50	DMSO-d_6	50	11	95	94	36[d]
8	NaI	0.50	DMSO-d_6	50	11	87	86	25[d]

[a][species 2c]= 0.10M, P_{CO2} = 30 psig [b]Deuterated solvents at 0.50 ml; in DMSO-*d₆*, the solution appeared slightly cloudy after reactions were completed, 0.20 ml methanol-D[4] was added to the solution to improve solubility prior to acquiring NMR spectrums. [c]Determined from ^{1}H-NMR using 0.05M of 1,3,5-trimethoxybenzene as internal standard. [d]formate yield was determined from the average of three runs with reproducibility of ±5%.

4.2.3 Effects of salts on formate yield.

During the course of these studies we have empirically discovered that the addition of various salts to the reaction mixture greatly enhanced the observed formation of the formate anion. As noted in Table 4.2, it is apparent that without any salts the $HCOO^-$ yield was nearly undetectable (5%, entry 1). Alternatively, under various reaction conditions, the presence of salts (e.g. KBr, KI, LiBr and NaI) resulted in markedly higher yields of the reduced product (25-59%, entries 2-8); of which KBr gave the highest formate yield (59%, entry 3) in comparison to others salts under the same conditions. To explain the effect of such additives in this reaction we propose that salts increase the ionic strength of the solution, which in turn creates a more polar environment that stabilizes the ionic products (species **1c** and $HCOO^-$) and corresponding intermediates leading to their formation; this thus biases the equilibrium towards ionic product formation (e.g. $HCOO^-$).

Although we have, to this point, performed the reductions of CO_2 at slightly elevated temperatures (50^{o}C, entries 1-6), we anticipated that species **2c** could be capable of reducing CO_2 to $HCOO^-$ at room temperature (T = 25^{o}C), corroborating the low free energy activation barrier $\Delta G^{\ddagger}_{HT}$ = 20.6 kcal/mol as predicted in Table 4.1. Indeed, species **2c** was effective as a reductant under ambient conditions; however, lower yields of the formate anion were obtained (27-33%, entries 7-8). We also examined this reduction in different solvents including MeOH-d_4 and MeCN-d_3. However, essentially no formate anion was measured in either case. Taken together, we propose that the observed lapsed activity in these solvents (MeOH-d_4 and MeCN-

d_3) can be attributed to their lower polarity, as evidenced by their polarity index values of 5.1 and 5.8, respectively, in comparison to 7.2 for DMSO-d_6. Following the same argument as the previously discussed effect of salt in this reaction, lower solvent polarity disfavors ionic product formation, thus leading to lower yields of our reduced product.

The data reported in Table 4.2 shows that despite introducing CO_2 in great excess, in the best case only 59% of the hydride of **2c** is productively consumed to form the formate anion (Table 4.2, entry 3), while the remainder is presumably consumed by side reactions. We have identified two potential channels for the non-productive hydride consumption of species **2c**. First, we anticipate that the H^- can react with trace water in DMSO (due to its hygroscopic nature) to form H_2 and hydroxide (OH^-).[245] Second, the hydride form of **2c** could also non-productively react with DMSO to form dimethyl sulfide and hydroxide. The hydroxide generated from these two sources (trace water and DMSO) can balance with potassium cations available in the solution to form insoluble KOH salts, potentially explaining the slight cloudiness of the solution after completion of the reaction.

We propose that a dearomatization-aromatization process is at play to create the driving force for CO_2 reduction by this hydride, similar to the pyridine system[39] we examined previously.[239] As species **1** is aromatic and becomes dearomatized upon its reduction to compound **2**, the proclivity of this species to recover aromaticity drives **2** to transfer its H^- to CO_2, forming the reduced product while recovering the aromatic species **1**. Further elaboration of the general structure of species **1** based on such mechanistic investigations is currently underway in an attempt to maximize yield, stability, and reduction potential.

4.3 Conclusion

In conclusion, we have demonstrated the use of non-sacrificial and metal-free benzimidazole-based organo-hydrides (**2**) for the reduction of CO_2 to the formate anion. The quantitative recovery of benzimidazolium cations (**1**) from species **2** after hydride transfer to CO_2 establishes that a redox couple (**2**/**1**) could function effectively in CO_2 reduction. This not only shows the possibility of utilizing organically derived hydride sources to efficiently reduce CO2 to usable fuels, but also opens the door for future development of reducing species **1** to **2** electrochemically, photochemically or photoelectrochemically powered by renewable energy, thereby closing the carbon cycle. We envision this work will inspire future research that incorporates an appropriate proton source into our proposed catalytic cycle to affect the exhaustive reduction of CO_2 to methanol.

5 Visible-light organic photocatalysis for latent radical-initiated polymerization via $2e^-/1H^+$ transfers: Initiation with parallels to photosynthesis

Alan Aguirre-Soto[†], Chern-Hooi Lim[†], Albert T. Hwang[†], Charles B. Musgrave[†], Jeffrey W. Stansbury[*†,¥]

[†]Department of Chemical and Biological Engineering, University of Colorado Boulder, 3415 Colorado Ave., Boulder, Colorado 80303, USA.

[¥]Department of Craniofacial Biology, School of Dental Medicine, University of Colorado, 12800 East 19th Ave., Aurora, Colorado 80045, USA.

Journal of American Chemistry Society: dx.doi.org/10.1021/ja502441d

Abstract:

We report the latent production of free radicals from energy stored in a redox potential through a $2e^-/1H^+$ transfer process, analogous to energy harvesting in photosynthesis, using visible-light organic photoredox catalysis (photocatalysis) of methylene blue chromophore with a sacrificial sterically-hindered amine reductant and an onium salt oxidant. This enables light-initiated free-radical polymerization to continue over extended time intervals (hours) in the dark after brief (seconds) low-intensity illumination, and beyond the spatial reach of light by diffusion of the meta-stable leuco-methylene blue photoproduct. The present organic photoredox catalysis system functions via a $2e^-/1H^+$ shuttle mechanism, as opposed to the $1e^-$ transfer process typical of organometallic-based and conventional organic multi-component photoinitiator formulations. This prevents immediate formation of open-shell (radical) intermediates from the amine upon light-absorption, and enables the 'storage' of light-energy

without spontaneous initiation of the polymerization. Latent energy-release and radical production are then controlled by the subsequent light-independent reaction (analogous to the Calvin cycle) between leuco-methylene blue and the onium salt oxidant that is responsible for regeneration of the organic methylene blue photocatalyst. This robust approach for photocatalysis-based energy harvesting and extended release in the dark enables temporally-controlled redox initiation of polymer syntheses under low-intensity short exposure conditions, and permits visible-light-mediated synthesis of polymers at least one order of magnitude thicker than achievable with conventional photoinitiated formulations and irradiation regimes.

5.1 Introduction

Free radicals (radicals) participate in a wide variety of organic synthetic[246] and polymerization reactions,[247] e.g., vinyl homo- and co-polymerizations,[248] thiol-ene click chemistry,[249] Cu-catalyzed azide-alkyne cycloadditions,[250] Atom Transfer Radical Additions,[251-252] and alcohol to halide conversions.[253] Radical production by light activation provides unique temporal control of reactions. However, radicals must be produced continuously by large irradiation doses to sustain the balance between competing creation and termination of radicals. As a result, radical-initiated reactions characteristically halt quickly due to efficient radical termination when the external energy supply (light) is extinguished. Persistent or trapped radicals in dense polymer networks allow a limited degree of polymerization after light-cessation.[248, 254] Whereas in Controlled or 'Living' Polymerization, the termination process is altered through an equilibrium that favors radicals in a dormant state so active radical concentrations remain low and essentially constant.[255-256] However, living radical photopolymerization is usually slow and still requires continued irradiation.[255] Furthermore, no scheme has yet been devised to sustain radical production after the energy supply is extinguished without altering the radical termination process. Here, we report the first use of organic photoredox catalysis to continue radical production for extended time intervals in the dark after a brief initial low-intensity light-exposure, opening new opportunities in photo-activated polymer and possibly organic synthesis.[257]

Conventionally, light-activated radical-based polymer synthesis entails radical production via photolytic bond-cleavage, e.g. phosphine oxides or acetophenones,[258] or by light-mediated electron transfer or exchange between a chromophore, such as camphorquinone, and either a reductant or an oxidant.[259] In principle, radical generation in both of these approaches is restricted to where the excited molecules reside, i.e. within the imprint and penetration depth of photons. Examples of applications that rely on spatiotemporal controlled processing include the creation of patterned materials for nano- and micro-scale devices, metamaterials, laser imaging and holography.[260-263] However, in optically thick materials, light absorption, scattering and reflection limit light penetration and thus polymerization to mere millimeters, or often, to just tens to hundreds of micrometers from the irradiated surface while requiring high irradiation intensities or extended photocuring intervals.[264-265] As a result, through-plane polymerization is severely limited, which is detrimental in applications such as dental and orthopedic composites, irregular surface coatings, photolithographic resists, and cell-encapsulation hydrogels,[263, 266-268] where unintentional property gradients and residual monomer beyond the light penetration depth limit is generally unacceptable. Ultimately, layer-by-layer polymerization is thus required if conventional free-radical photopolymer initiators are to be used for optically thick materials.

In contrast, radical generation through chemically-activated redox initiation, such as with peroxide/amine combinations, allows synthesis of thick polymeric materials under ambient conditions upon *in-situ* mixing of two-part formulations, as in bone cements.[269] However, this redox approach lacks temporal control of the initiation reaction beyond the mixing process. In other instances 'dual-cure' systems require post-irradiation heating or moisture cure.[270] 'Dual-cure' systems, in which photo- and redox-activated chemistries work more or less simultaneously, introduce some temporal control. However, the two initiation modes work relatively independently and mixing immediately prior to use is still required; thus, imposing similar temporal control limitations as redox systems.[271]

Frontal polymerization has been reported to allow deep shadow cure in free-radically and cationically initiated thick (centimeter scale) or opaque samples upon UV exposure.[272] Despite its attractive simplicity, limited storage stability of the peroxides-containing formulations and its inherent dependence on the self-propagated (by polymerization exothermicity) temperature wave front (over 100 ˚C) have precluded the use of this technique in most applications.[273-275] No reports were found of free-radical photopolymerization of (meth)acrylates in which initiation extends beyond the irradiation space and time under ambient conditions without depending on the polymerization exotherm to sustain initiation in the dark.

In this contribution, we introduce the concept of organic photoredox catalysis as a novel approach to combine the temporal onset control of conventional photo-activation with the spatial reach of redox-activated radical production. We demonstrate that the combination of these phenomena extends the capabilities of prevailing photoinitiated processes and enables the practical synthesis of initially optically thick, centimeter-scale vinyl photopolymers at ambient conditions.

In recent years, photoredox catalysis has gained attention as an alternative to achieve faster rates of radical-initiated polymerization upon low-intensity visible-light irradiation.[276] Almost all of the reported mechanisms, including those for similar methylene blue (MB^+)/amine/onium salt formulations, rely on sequential $1e^-$ transfers to and from the photocatalyst, as is characteristic of ruthenium and iridium complexes.[276-283] In these mechanisms, transfer of a single electron allows production of (open-shell) radicals from the photo-induced electron transfer (PET) step and essentially initiates the polymerization process immediately after the light-absorption event. Then, the consecutive $1e^-$ transfer step(s), responsible for the regeneration of the photocatalyst, occur(s) so fast that light-energy 'stored' in the photocatalyst as chemical energy is used shortly (less than a few seconds) after the PET step; thus these radical production approaches are incapable of sustaining the polymer synthesis for prolonged periods (hours) following light cessation.[255, 281]

To the best of our knowledge, we report the first energy-harvesting approach using organic photocatalysis for latent light-induced radical-initiated polymer synthesis that relies on a two-electron/one-proton ($2e^-/1H^+$) transfer mechanism. Using a sterically-hindered amine (N,N-diisopropylethylamine, DIPEA) as a sacrificial donor that induces a $2e^-/1H^+$ transfer to the organic photocatalyst MB^+ in a 1-to-1 fashion, we prevent immediate free-radical initiation of polymer synthesis of (meth)acrylate monomers upon light absorption, and enable visible-light energy storage as chemical energy in a metastable closed-shell species: leuco-methylene blue (LMB). The stored energy is subsequently utilized to generate two initiating phenyl radicals per photocatalytic cycle from the ground-state redox reaction between the metastable LMB and the oxidizer (diphenyliodonium, DPI^+) for extended time intervals (hours) after short, low-intensity irradiation.

Using photocatalysis to store light-energy in a metastable species (via a $2e^-/1H^+$ transfer mechanism) in order to sustain ground-state reactions (e.g. radical generation that initiates polymer synthesis) for extended periods (hours) after a brief light-activation is the basis of the approach presented herein. Similar PET-based mechanisms have been envisioned as the basis for 'molecular circuits' and 'molecular computing devices',[284-285] but we present the first example of a PET-based scheme for light harvesting analogous to photosynthesis that allows photopolymerization be extended well beyond irradiation. In this paper, we: 1) describe coupled experimental and quantum chemical studies that support the photo-induced redox radical formation via the $2e^-/1H^+$ transfer mechanism and 2) demonstrate the capabilities of this new radical production approach within the scope of radical chain-growth polymer synthesis.

5.2 Results and discussion

5.2.1 Fast radical production in MB^+/DIPEA/DPI^+ formulations. Radical production was analyzed by monitoring the disappearance of the infrared absorption corresponding to the vinyl group ($=CH_2$) of the monomer with Fourier transform near-infrared spectroscopy (FT-NIR).[286] The extent of vinyl group consumption indicates monomer conversion due to polymerization, which correlates with radical production. Under continuous, low-intensity visible-light irradiation, monomer solution (e.g. 2-hydroxyethyl methacrylate; HEMA) containing methylene blue (MB^+, **1**), N,N-diisopropylethylamine (DIPEA, **2**), and diphenyliodonium cation (DPI^+, **3**) reaches a vitrification-limited 85 % conversion in 500 s (Figure 5.1a). Under the same conditions, formulations where either or both DIPEA and DPI^+ are absent (MB^+/DIPEA; MB^+/DPI^+; or MB^+) exhibit less than 2 % monomer consumption.

To further probe the initiation process, the concentration of MB^+ was analyzed via real-time ultraviolet-visible (UV-Vis) spectroscopy. MB^+ is consumed efficiently (Figure 5.1b) in the presence of DIPEA with or without DPI^+. However, the MB^+/DIPEA formulation is ineffectual towards initiating polymerization, whereas the MB^+/DIPEA/DPI^+ formulation leads to a significant radical production rate, as demonstrated by HEMA conversion, that is comparable to the reaction kinetics and conversion achieved with a conventional visible-light initiator composed of camphorquinone (CQ) and ethyl 4-dimethylaminobenzoate (EDMAB), for which equivalent amounts of photons are absorbed (Figure 5.1a- see experimental section). Hence, direct radical production from MB^+ consumption by DIPEA is negligible. This indicates that MB^+ consumption and radical production involve separate reaction steps (described in detail in following sections); while MB^+ consumption is primarily dependent on the presence of DIPEA; the oxidant (DPI^+) plays the main role in radical production.

5.2.2 PET reaction of MB^+/DIPEA generates the colorless LMB. Now, we reevaluate the MB^+/DIPEA system to establish the connection between photoreduction of MB^+ and the subsequent radical generation that necessitates the presence of DPI^+. In general, the reduction of MB^+ has been proposed to proceed via a $2e^-/1H^+$ process to produce the leuco product LMB in a reducing environment,[287-288] as represented in reaction (1).

$$MB^+ + 2e^- + 1H^+ = LMB \qquad (1)$$

a

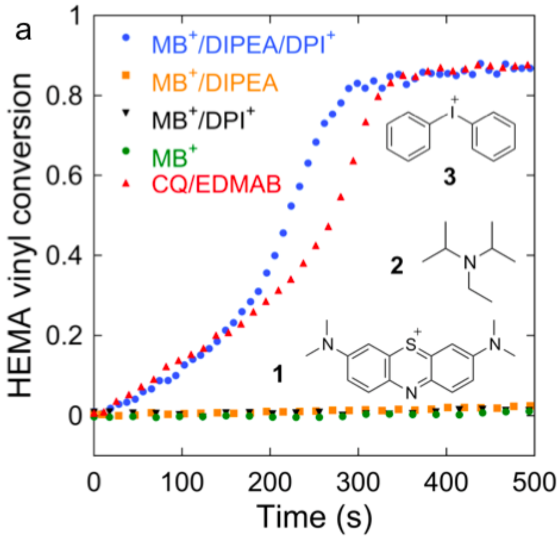

b

	R_{po} (mol/L•s)	Initial rate of MB^+ consumption (mol/L•s)
MB^+	2.2 x 10^{-4}	-
MB^+/DPI^+	1.6 x 10^{-4}	-
MB^+/DIPEA	3.4 x 10^{-4}	2.1 x 10^{-5}
$MB^+/DIPEA/DPI^+$	38.0 x 10^{-4}	2.7 x 10^{-5}

c

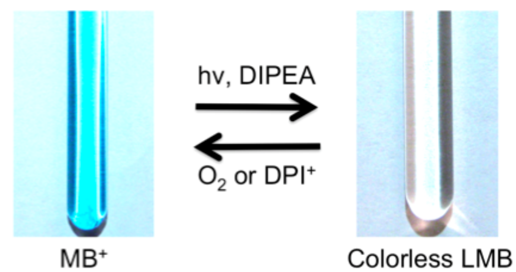

Figure 5.1: Evidence of radical production via photoredox catalysis of methylene blue (MB^+).
a, Conversion of vinyl group (polymerization) of 2-hydroxyethyl methacrylate (HEMA) during continuous irradiation of 1 mm thick samples. MB^+ (**1**)/DIPEA (**2**)/DPI^+ (**3**) are required for polymerization at a rate comparable to the conventional CQ/EDMAB formulation with the same amount of photons absorbed (~13 and 22 mW/cm^2, respectively). **b,** Initial rates of polymerization (R_{p0} from numerical differentiation of FT-IR data- see SI section 4) and initial rates of MB^+ bleaching (with UV-Vis spectroscopy at ~60 mW/cm^2). MB^+/DIPEA leads to efficient consumption of MB^+ (2.1*10^{-5} M/s) but no radical production (which correlates to the vinyl group conversion and R_{p0}), whereas $MB^+/DIEPA/DPI^+$ increases radical production rate dramatically (~100-fold based on R_{p0}) with no significant improvement on MB^+ consumption rate (2.7*10^{-5} M/s). Rates of bleaching without DIPEA are negligible. This indicates that DIPEA does not produce radicals efficiently (shows negligible polymerization). Thus, DPI^+ should play the main role in term of radical production. **c,** Photoredox cycle in methanol with DIPEA and O_2 or DPI^+. MB^+ in methanol is bleached, photoreduced to colorless LMB, and regenerated by an oxidant. The process can be repeated as MB^+ is regenerated after each cycle, i.e. photocatalysis cycle.

Under irradiation, the $2e^-/1H^+$ transfer process (1) is driven by light and is referred to as photo-induced electron transfer (PET).[289-290] The PET of specific interest here is the reduction of MB^+ to the colorless LMB in the presence of DIPEA (reductant). For example, in Figure 5.1b, we see that the rates of MB^+ consumption for the MB^+/DIPEA and $MB^+/DIPEA/DPI^+$ formulations are 2.1*10^{-5} and 2.7*10^{-5} M/s, respectively. Reduction of MB^+ to LMB is identified by the decrease of the ~650 nm-centered peak and appearance of a ~250 nm-centered peak (Figure 5.1b- see SI section 7). This process is commonly known as 'photo-bleaching', where the signature blue color of MB^+ (λ_{max} = ~650 nm) disappears and the mixture turns colorless (Figure 5.1c).

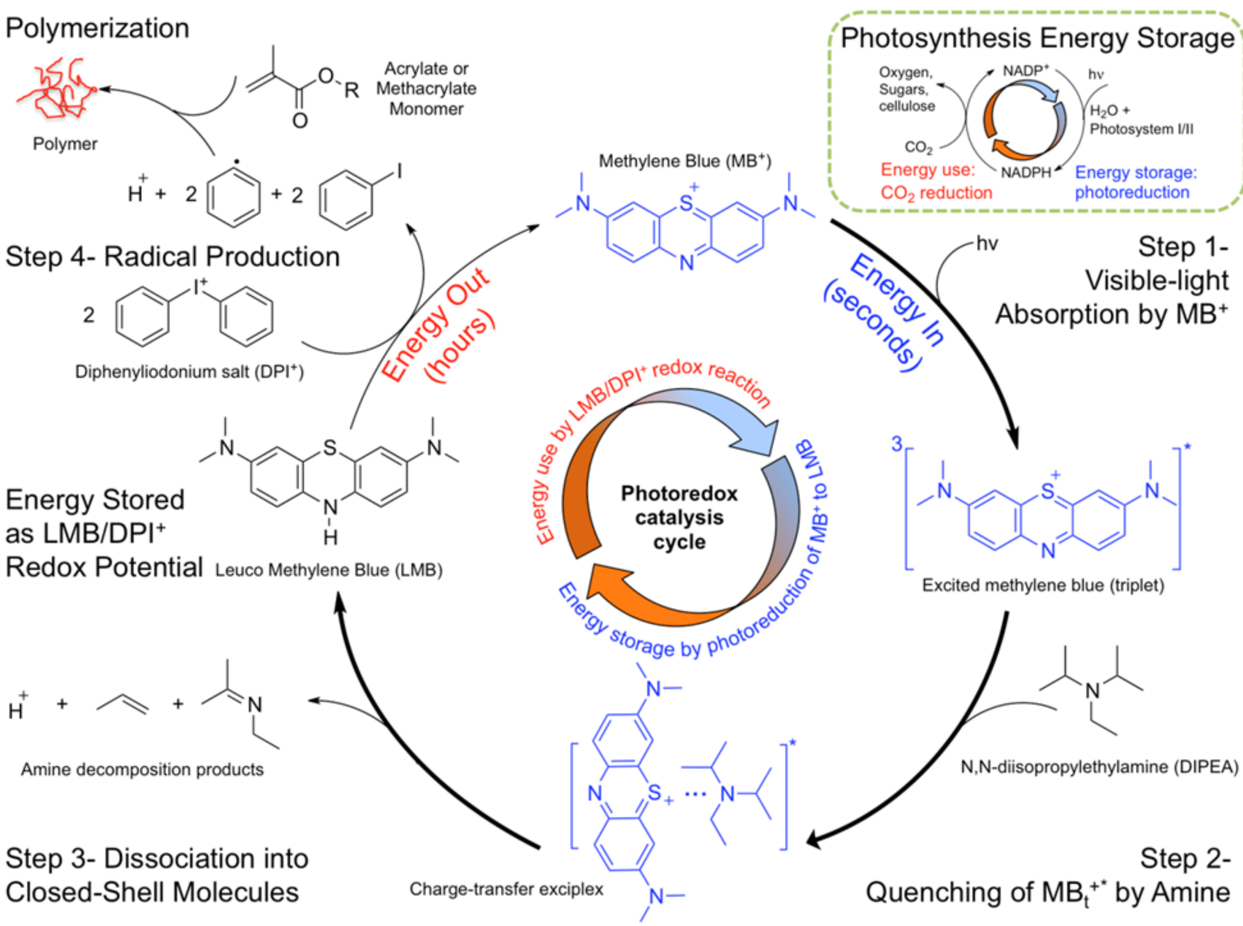

Figure 5.2: Free radical initiated polymer synthesis with light energy harvesting cycle.
Step 1: Visible-light (hv) excitation of MB^+ to the singlet state (not shown), which quickly decays to the longer-lived triplet state (MB_t^{+*}) via intersystem crossing. Step 2: excess DIPEA quenches MB_t^{+*} to colorless LMB via transfer of two electrons and one proton (reaction 1) through formation of a charge-transfer excited state complex (exciplex). Step 3: after a $2e^-/1H^+$ transfer, the exciplex separates into LMB and DIPEA-decomposition products. DIPEA decomposes to closed-shell molecules, and does not initiate polymerization. Step 4: LMB is oxidized back to MB^+ by DPI^+ to produce two phenyl radicals per LMB. Phenyl radicals are responsible for the fast initiation of chain-growth polymerization of HEMA. Faster (thicker arrows) MB^+ reduction and slower (thinner arrows) reoxidation steps allow LMB to accumulate, and also create a lag time between light absorption and radical generation. Thus, energy is stored as an electrochemical potential between LMB and DPI^+, which produces radicals beyond light absorption. This is analogous to the $NADP^+$/NADPH cycle (inset) known in photosynthesis in which the transfer of

$2e^-/1H^+$ in the photoredox cycle stores light-energy in the form of a chemical potential that is used to reduce carbon dioxide to higher molecular weight sugars and carbohydrates.

Next, we describe the PET process in greater detail, as illustrated in Figure 5.2. In step 1, absorption of photons excites MB^+, which undergoes intersystem crossing to ultimately produce the triplet excited-state MB_t^{+*}. Subsequently in step 2, an excited-state complex (exciplex) forms between DIPEA and MB_t^{+*} prior to the PET reaction.[291] It is important to note that in conventional PET reactions involving amines and chromophores, the amine reductant typically provides one electron (e^-) and one proton (H^+) to the photo-excited chromophore.[278, 280-281, 289-290, 292] For example, with the CQ chromophore and EDMAB reductant, transfer of $1e^-/1H^+$ results in the production of the alpha-aminoalkyl radical that is reactive towards vinyl monomers and thus initiates polymerization.[279, 293] If the analogous $1e^-/1H^+$ transfers occur in MB^+/DIPEA photoreduction, two DIPEA molecules would be required for each bleached MB^+ (reaction 1). As a result, each amine would result in an alpha-aminoalkyl radical that would be expected to cause fast polymerization of the methacrylate monomer. Quantum chemical simulations predict that creation of a monomer-based radical with the alpha-aminoalkyl radical, i.e. initiation of the polymerization, is barrierless and thus confirm that polymerization would be fast and diffusion-limited in solution if DIPEA-based radicals were produced. In Figure 5.3, we show the equilibrium structures of (a) reactant, (b) transition state (TS) and (c) product for the C-C bond formation reaction between the alpha-aminoalkyl radical and HEMA monomer.

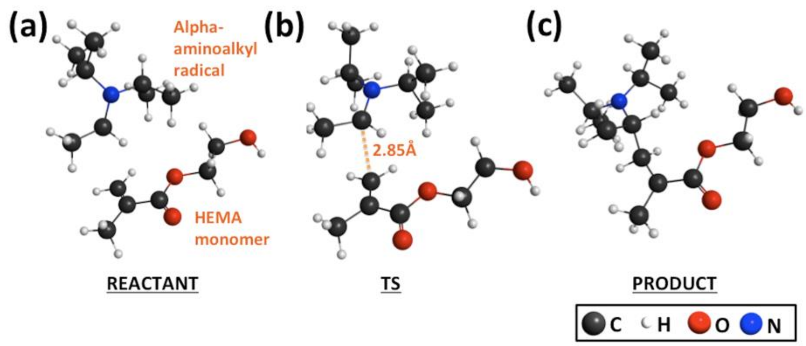

Figure 5.3: Reaction between alpha-aminoalkyl radical and HEMA monomer.
Equilibrium structures of (a) Reactant, (b) Transition state (TS) and (c) Product are determined using unrestricted M06/6-311G(d,p)/CPCM-methanol. The enthalpic barrier for this reaction is determined to be ΔH^0_{act} = -1.4 kcal/mol, after zero-point-energy (ZPE) and thermal corrections to 298K. Note that although ΔE^0_{act} is positive, thermal and zero-point corrections often produce a negative ΔH^0_{act} for reactions that are essentially barrierless.

Despite the formation of LMB, we observed no significant polymerization with MB^+/DIPEA (Figure 5.1a). This contrasts with other tertiary aliphatic amines that photoreduce MB^+ via $1e^-/1H^+$ transfers to produce alpha-aminoalkyl radicals that initiate polymerization efficiently, as previously reported,[277, 294-295] and confirmed by our FT-NIR spectroscopy measurements with other tertiary amines (SI, Section 2). This observation compelled us to propose that the strong and sterically-hindered DIPEA base plays a unique role in the MB^+ PET reaction examined here: it reacts rapidly with the photoexcited MB_t^{+*} in a 1-to-1 fashion, where DIPEA serves as a $2e^-/1H^+$ donor. Hence, closed-shell degradation products are produced from the PET reaction (Figure 5.2, Step 3), but not DIPEA-based (alpha-aminoalkyl) radicals. Using electrospray ionization-mass spectrometry (ESI^+), we identified both 2-ethyliminopropane and propene as the by-products of the entropy-driven DIPEA decomposition via carbon-nitrogen σ-bond cleavage (SI, section 3).

To our knowledge, this is the first time a $2e^-/1H^+$ transfer mechanism has been demonstrated for the photoreduction of a photocatalyst (MB^+) with an amine (DIPEA) in 1:1 ratio that produces no alpha-aminoalkyl radicals during the PET reaction.

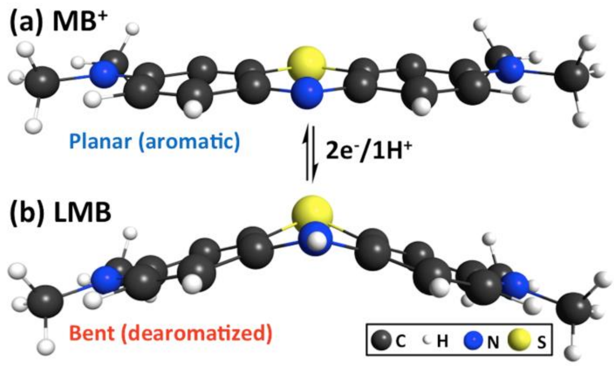

Figure 5.4: Dearomatization of MB^+ after a $2e^-/1H^+$ transfer.

(a) MB^+ is a planar aromatic molecule that absorbs strongly in the visible light spectrum (λ_{max} = ~650nm). (b) LMB is a photoproduct of a $2e^-/1H^+$ transfer in MB^+/DIPEA PET reaction. After a $2e^-/1H^+$ transfer, the thiazine ring in LMB is dearomatized and is significantly bent from the original planar structure. Time-dependent DFT (TD-DFT, Methods) using ωB97XD/LANL2dz/CPCM-methanol predicts that LMB absorbs at λ_{max} = ~300 nm, which corroborates the observed blue-shift of λ_{max} to ~250 nm and explains the bleaching of the solution to its colorless form.

Finally, the PET reaction in step 3 leads to the desired LMB product. Examination of the calculated LMB equilibrium structure (Figure 5.4) suggests that a dearomatization process occurs after $2e^-/1H^+$ transfer (1), where the thiazine ring distorts significantly from its original planar structure. Furthermore, excited state calculations using TD-DFT predict that the PET process significantly blue-shifts MB^+ absorption, which is typical of a dearomatization process. LMB is predicted to absorb only in the near-UV region at ~300 nm (compared to ~650 nm for MB^+), which agrees with the appearance of the ~250 nm peak during PET. Next, we examine how LMB, a meta-stable closed-shell product from PET, participates in a ground-state reaction with the DPI^+ oxidant to generate the radicals responsible for polymerization.

5.2.3 Radical production from LMB/DPI⁺ reaction. If photoreduction of MB^+ by DIPEA produces LMB by (1) but generates no radicals, then the radicals responsible for the fast polymerization of the monomer with MB^+/DIPEA/DPI^+ must arise from the ground-state oxidation of LMB back to MB^+ by DPI^+. This proposal is based on the fact that LMB has been observed to oxidize to MB^+ with O_2 as the oxidant, consistent with the observed gradual return of MB^+'s blue color (Figure 5.1c). Furthermore, LMB is an efficient reducing agent.[277, 296-298] Herein we propose that radical production in MB^+/DIPEA/DPI^+ (Figure 5.2, Step 4) occurs as follows:

$$\text{LMB} + 2\ \text{DPI}^+ = \text{MB}^+ + 2\ \text{Ph}^\bullet + 2\ \text{I-Ph} + \text{H}^+ \quad (2)$$

DFT calculations performed at the uM06/6-311G**//uωB97XD/LANL2dz level of theory in CPCM implicit methanol solvent (see Methods) support reaction (2) with a predicted ΔG^0_{rxn} of -5.2 kcal/mol. Furthermore, production of two highly reactive phenyl radicals per LMB accounts for the fast polymerization rate observed with MB^+/DIPEA/DPI^+ (Figure 5.1a) under irradiation. ESI^+ shows the production of iodobenzene-based products (SI, Section 3), which provides additional evidence for (2); the oxidation of LMB by DPI^+ via (2) also explains the observed return of MB^+'s blue color.

To further investigate the radical generation process described by reaction (2), we performed an Arrhenius analysis to determine that the activation barrier for the free radical production step in the polymerization of HEMA with MB^+/DIPEA/DPI^+ is $\Delta E_{act} = 6.6 \pm 1.0$ kcal/mol (Figure 5.5a and SI, Section 3). Next, we used real-time UV-Vis to quantify the regeneration rate of MB^+ at various temperatures after a 10 s irradiation (Figure 5.5b). We observed that light-activated MB^+ consumption is temperature independent (Figure 5.3b, Light), as expected for a PET reaction where diffusion restrictions are mitigated by excess reductant (DIPEA). In contrast, MB^+ regeneration is strongly temperature sensitive (Figure 5.5b, Shaded). From the UV-Vis results, we estimate that ΔE_{act} for MB^+ regeneration is 7.2 ± 1.3 kcal/mol (SI, Section 4).

Statistical agreement in ΔE_{act} values from independent Arrhenius analyses of both monomer consumption and MB^+ regeneration effectively confirms that the two observations are due to reoxidation of LMB by DPI^+. Notably, there is an alternative radical production pathway based on direct redox reaction between DIPEA and DPI^+; however, its ΔE_{act} is 13.1 ± 1.0 kcal/mol (SI, Section 4). From this we calculate that well over 90 % (depending on MB^+/DIPEA/DPI^+ concentrations) of the phenyl radicals originate from the LMB/DPI^+ reaction once LMB is generated via MB^+ photoreduction.

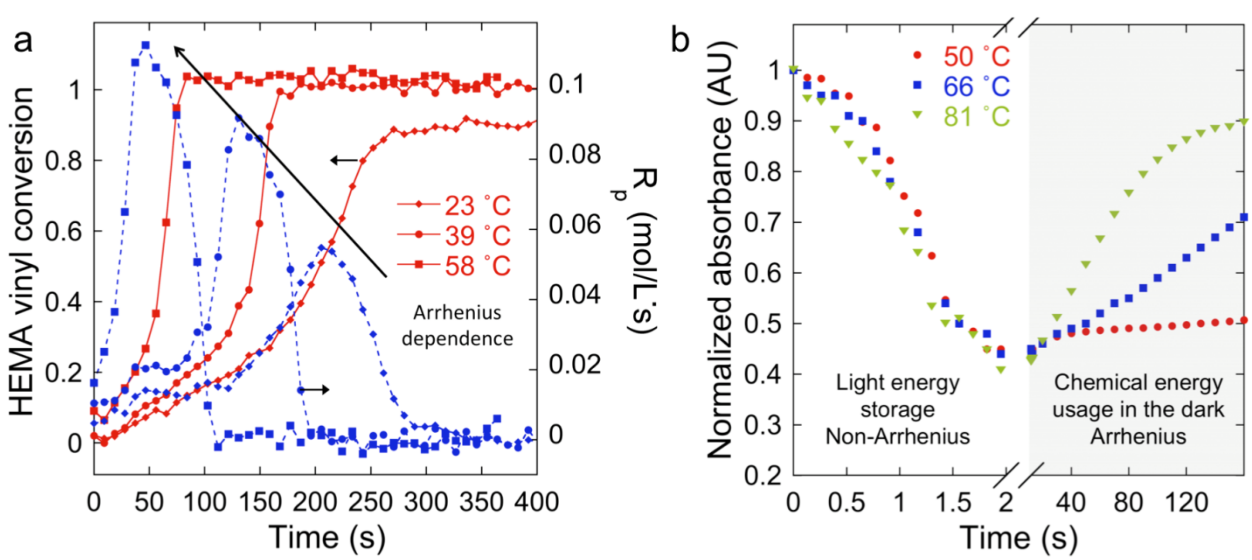

Figure 5.5: Activation energy for MB^+ regeneration matches initiation of polymerization.
a, Vinyl conversion (red continuous line) and R_p (blue dashed line-obtained from numerical differentiation of FT-IR data) under illumination show Arrhenius (temperature) dependence. Activation energy for initiation of

polymerization (ΔE_{act} = 6.6 ± 1 kcal/mol) is due to the redox reaction between LMB and DPI^+ (arrows indicate temperature increase). b, Absorbance monitoring (650 nm – MB^+ peak) proves temperature-insensitive (light-dependent) photoreduction of MB^+ by DIPEA, i.e. bleaching of the blue color. After 10 s of irradiation, MB^+ is regenerated in the absence of light. Activation energy for MB^+ regeneration (ΔE_{act} = 7.2 ± 1.2 kcal/mol) agrees with the estimated activation energy for the initiation of polymerization (from FT-NIR) because both are due to the LMB/DPI^+ reaction.

5.2.4 Stored energy in LMB extends radical production after irradiation. Having demonstrated that this photocatalysis mechanism most likely proceeds via a $2e^-/1H^+$ transfer, we now show that MB^+/DIPEA/DPI^+ can be tuned so that the polymerization reaction continues for hours after light cessation. In Figure 5.6a, we show that during a 1 min low-intensity light-exposure, the bulk polymerization of HEMA reached ~8% conversion for MB^+/DIPEA/DPI^+. Extinguishing the irradiation at this point led to the continued rise in conversion in the dark over the next 2 hours to reach 80%, with radical formation likely persisting over even longer timescales. This offers additional proof that the above-described radical production by LMB/DPI^+ occurs via a ground-state "dark" reaction. Similar studies with additional irradiation times are provided in SI section 5 to confirm this unique behavior. The initial PET reaction 'charges' the photocatalytic cycle by quickly converting MB^+ into LMB via steps 1-3 of Figure 5.2, also demonstrated in Figure 5.3b. The sample bleaches as LMB accumulates because step 4 (or equivalently reaction 2) is rate limiting. Light-energy is subsequently harvested as the chemical potential between MB^+ and LMB, and "dark" reaction with DPI^+ drives radical production and polymerization after the brief PET reaction. In contrast, polymerization did not continue in the dark for MB^+/DIPEA or CQ/EDMAB in HEMA. It is noteworthy that the final 'dark' conversion achieved with MB^+/DIPEA/DPI^+ is nearly the same as that obtained with continuous light exposure (86 %, Figure 5.1a), which indicates the final conversion is not significantly hampered by such a short initial light exposure period.

5.2.5 Photocatalysis cycle mimics photosynthesis. The photoredox catalysis here mimics nature's photosynthesis where energy from visible-light is stored as the chemical potential in the MB^+/LMB redox couple. This is analogous to photosynthesis, where visible-light absorbing proteins in Photosystem I and II undergo PET reactions to store energy in the $NADP^+$/NADPH redox couple. Both redox couples store energy using a $2e^-/1H^+$ transfer reaction and participate in ground state (light-independent analogous to the Calvin cycle) reactions to release the stored energy. While the closed-shell NADPH energy carrier drives the synthesis of sugars and natural polymers in the absence of light;[299-300] the system utilizes its stored energy, originally derived from light, in LMB to generate radicals (reaction 2) that initiate polymerization for the synthesis of macromolecules in the absence of light.

5.2.6 Spatial extension of radical production beyond the irradiation site. Next, we demonstrate that polymer synthesis with MB^+/DIPEA/DPI^+ not only extends temporally, but also spatially beyond the reach of photons (Figure 5.6b). HEMA was polymerized on a glass substrate by exposing the unmasked 2 mm fringe of an 8 mm long monomer sample to continuous irradiation for 10 min. The lateral extent of photo-activated polymerization into the shadow region was determined by washing away unreacted monomer with acetone after 30 min of storage in the absence of light. CQ/EDMAB yielded a patterned polymer that extended only 170 ± 190 µm into the masked region (Figure 5.6b, Islet). Notably, during this time, the MB^+/DIPEA/DPI^+ formulation shows 3.73 ± 0.73 mm of lateral polymerization into the dark area. This is due to relatively stable LMB produced in the irradiated region (reaction 2) diffusing into the masked region and reacting with DPI^+; thus, generating radicals and initiating polymerization 'far' (millimeters) from the LMB-formation site. Using embedded thermocouples, we verified that there is no thermal front involved in the extension of polymerization beyond the direct light activation.[301] While many photopolymer applications rely on the intrinsic spatial control associated with conventional photoinitiating systems, this approach uniquely decouples spatial restrictions from the photo-activation process. It is certainly advantageous in instances where radical generation around corners and into shadowed regions is desirable, such as in automotive and aerospace coatings of irregular surfaces and polymers for *in-situ* biomedical applications.

5.2.7 Photo-activated synthesis of thicker polymers. The aforementioned temporal and spatial extension of radical generation is utilized to achieve light-mediated synthesis of polymers at least an order of magnitude thicker than the millimeter-scale of conventional photoinitiated formulations under low-intensity and short exposure conditions. The full depth of ~1.2 cm thick HEMA polymer specimens (Figure 5.6c) was photocured with a 1 min exposure to 3.4 mW/cm^2 light. Under these very mild conditions, the photoreduction of MB^+ to LMB initially occurs near the top surface, close to the irradiation source, where photon flux is highest. As MB^+ is transformed into LMB, bleaching occurs in a gradient fashion allowing the light to penetrate deeper into the originally optically thick sample. Within one minute of illumination the sample is entirely colorless, but not yet polymerized. HEMA polymerization then continued in the dark using the radicals from the LMB/DPI^+ reaction. After 30 min, the sample was gelled throughout with polymerization continuing to completion in the dark over several hours.

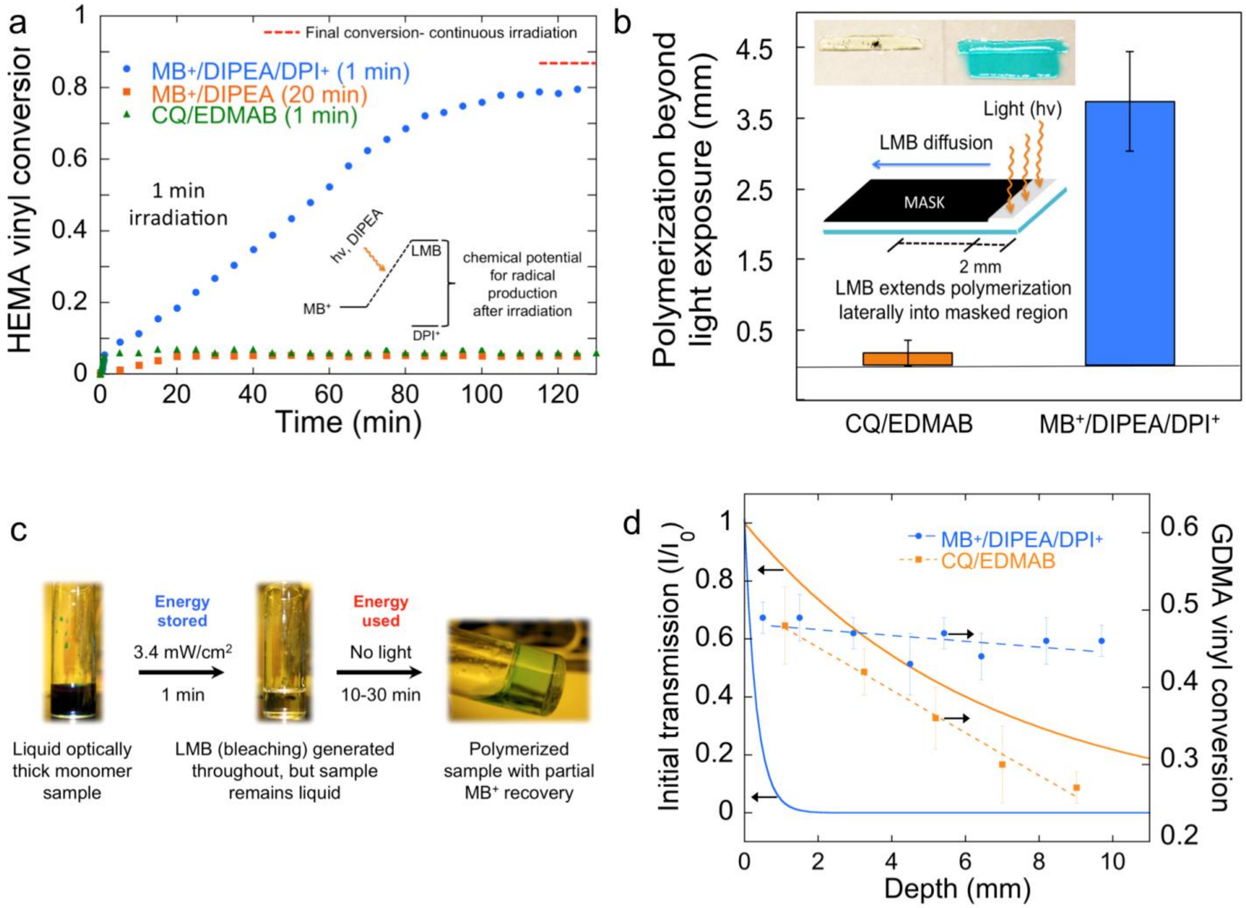

Figure 5.6: Radical generation in the dark from stored energy in LMB.

a, HEMA with MB^+/DIPEA/DPI^+ reaches 80 % conversion with 60 s of illumination after having achieved only 8 % conversion during active illumination. MB^+/DIPEA and CQ/EDMAB show no energy-harvesting capability. **b,** Stable LMB diffuses and extends radical production beyond the light absorption site. Polymerization is initiated into a masked region 3.7 ± 0.7 mm (standard deviation, n=3) away from the illuminated region (2 mm in width) with MB^+/DIPEA/DPI^+. Statistically negligible extension of polymerization was observed in the masked region with CQ/EDMAB at equivalent conditions. **c,** Polymerization of optically thick 1.2 cm (height) HEMA and GDMA. Poly-HEMA discs were made with 1 min irradiation (from the top). An analogous sample with CQ/EDMAB was irradiated with an equivalent number of absorbed photons showing negligible polymerization and remained liquid (SI section 5). **d,** Vinyl conversion by FT-NIR (with standard deviation, n= 3) is more uniform throughout the depth in a 10 times more optically opaque MB^+/DIPEA/DPI^+ sample than in a conventional CQ/EDMAB sample. Dashed lines indicate the linear regression of the final conversion profile, and solid lines indicate the local light transmission profile at the start of irradiation (based on the respective active wavelengths and molar absorptivities of CQ and MB^+ in GDMA).

Due to diffusion constraints in the polymer, the blue color in the polymer does not fully regenerate, as not all LMB is able to oxidize to MB^+. The multi-millimeter diffusion of the relatively stable high-energy close-shell LMB (Figure 5.4b) can aid in achieving centimeter plus-scale polymerization even if MB^+ photobleaching were not complete throughout the entire depth of the sample. For instance, CQ transmits more light through the 1.2 cm samples and can be bleached efficiently with EDMAB allowing for progressive light penetration in the same sample geometry; however, CQ/EDMAB specimens show noticeably less polymerization at equivalent photon absorption, i.e. essentially no polymerization of HEMA at these mild conditions (SI section 6).

These capabilities can also be exploited with other monomers, such as the crosslinking photopolymerization of glycerol dimethacrylate (GDMA) or triethylene glycol di(meth)acrylate. The higher modulus GDMA polymer was used to prepare similarly thick samples, which were then sectioned (~ 1 mm slices) to reveal a much more uniform conversion profile to a depth of at least 1 cm, than what is achieved with the analogous CQ/EDMAB sample, which has an initially 10-fold greater optical transparency (Figure 5.6d). The limiting GDMA conversion (~65 %) is achieved in the top layer with either initiator system with an equivalent amount of photons absorbed. However, it is remarkable that conversion in the MB^+/DIPEA/DPI^+ system reduces only marginally (~5%) at a depth of 1 cm under such mild irradiation conditions, while conversion in the CQ/EDMAB formulation drops precipitously to zero, as is typical for conventional radical-initiated photopolymerizations. In general, much higher intensities and/or longer exposures are needed to achieve this same outcome with conventional photoinitiators as demonstrated using CQ/EDMAB.

Such a small variation in monomer vinyl conversion with depth permits the design of photo-activated initiation systems for synthesis of optically thick polymers under milder, highly energy-efficient irradiation regimes and within a timescale comparable to conventional redox initiators,[302] but with unprecedented temporal activation control. We contend that this is the first photoredox catalysis employed to design a temporally-controlled redox initiation system where the active radicals are not generated directly by the light-dependent reaction, and in which the rates of photo-reduction and oxidation in the photoredox cycle can be tuned to achieve energy storage that extends polymerization well beyond the time and distance associated with the light absorption process.

5.3 Conclusion

The key to extend initiation beyond irradiation with photoredox catalysis concept is achieving a fast, efficient photochemical storage step (photobleaching), in which light-energy is converted into chemical energy and later released in a much longer time interval based on the chemical potential of the redox pair (e.g. LMB/DPI^+). The energy utilization on much longer timescales than that of light-absorption is tuned by the kinetics of the ground-state redox reaction. Thus, the primary reason for the use of DIPEA as the reductant in the presented system is its fast bleaching 'rate' with MB^+ and the lack of alpha-aminoalkyl radical formation. This approach unlocks new opportunities for the application of other chemistries that enable energy storage in bulk and solution polymer and possibly organic synthesis.[246]

The concentration of MB^+, and the associated LMB, will affect the rate (kinetics) and duration (thermodynamics) of the polymerization after the short light-pulse. The experimental parameters used herein were not optimized and we expect that this concept can be improved to synthesize even thicker polymers. This work serves only as proof of concept for the novel initiation scheme, and can be extended to a range of polymer applications and likely organic synthesis as well.

Ruthenium and iridium complexes produce photo-excited states that are a more powerful source of electrochemical potential,[257] which may allow for greater potential, however different sacrificial reductants or oxidants would be required to allow analogous storage of energy derived from light and to avoid initiation shortly after the light-absorption event. Ultimately we propose that additional organic and organometallic photocatalysis schemes can be engineered to delay light-energy utilization to hours after light-absorption by appropriate formulation design. Photoredox organocatalysis is an attractive alternative for any synthetic applications in which expensive photocatalysts (i.e. organometallic) cannot be recovered, as would be the case in bulk polymerizations. Additionally, organic photocatalysts are more versatile, lower-cost and usually less toxic alternatives.

This concept could provide significant advantages, including photopolymerization of optically thick UV-absorbing monomer formulations, in wide ranging industrial and biomedical applications, such as: cell encapsulation, orthopedic and dental cements, tumor phototherapy, adhesives and high-throughput polymer films. The final blue tone of the polymer films and discs varied with irradiation dose and initial concentrations. However, if desired, the reformed MB^+ and the blue color can be partially or completely removed from most polymers by swelling, as seen in SI section 7, depending on cross-linked density of the polymer network.

5.4 Experimental section

Materials. Methylene blue (MB^+), N,N-diisopropylethylamine (DIPEA), and diphenyliodonium chloride salt (DPI-Cl) were used as received. 2-Hydroxyethyl methacrylate (HEMA) and glycerol dimethacrylate (GDMA) were selected as monomer because it readily dissolves MB^+/DIPEA/DPI^+. Homogeneous samples were prepared by vortex mixing. Methanol (MeOH), acetonitrile (ACN) and DI-water were used as solvents (spectro grade). All materials were commercially obtained from Aldrich (Milwaukee, WI), and used as received.

Light source. A halogen dental curing light (Max, DENTSPLY/Caulk, Milford, DE) modified to deliver broadband 500-800 nm light was used in the MB^+/DIPEA/DPI^+ photopolymerization experiments. Incident irradiance was measured with a radiometer (6253, International Light Technologies, Peabody, MA) within the 400-700 nm range, i.e. not all of which is absorbed by MB^+. For all the CQ/EDMAB-initiated formulations, the 400-500 nm output of an unaltered halogen lamp was applied with the incident irradiance verified by radiometer.

Fourier transform-infrared spectroscopy (FT-IR). Bulk polymerizations of HEMA were monitored in real-time with a FT-near-IR spectrophotometer (Nicolet Magna-IR Series II, Thermo Scientific, West Palm Beach, FL) by following the peak area of the first overtone absorption band for the methacrylate $=CH_2$ group (6167 cm^{-1}). The spectrophotometer was equipped with a KBr beam splitter, a MCT/A detector, and an in-house fabricated horizontal stage adapted for *in-situ* photopolymerization experiments.[286] The distance between the light source and the sample was ~7 cm to ensure uniform irradiation across the entire sample with controlled irradiance values. An 800 nm cut-off filter was used to eliminate the 633 nm HeNe reference beam within the NIR output signal. The sample holder for the *in-situ* polymerization, both in the dark and in the light, consisted of a 1 mm height, 1.6 cm diameter disc fabricated by interjecting a perforated silicone rubber shim in between two 1 mm thick glass slides. Rate of polymerization was calculated by numerically differentiating the peak area as a function of time. Concentrations used were as follows: [MB^+] = 4 mM, [DIPEA] = 0.2 M, [DPI^+] = 0.04 M, [CQ] = 0.02 M and [EDMAB] = 0.04 M. All FT-NIR-monitored polymerizations with MB^+/DIPEA/DPI^+ were performed with 12-13 mW/cm^2. For the CQ/EDMAB system the intensity used was 22-23 mW/cm^2. These intensities gave an approximate 3*10^{-8} Einsteins/s*cm^2 of photons absorbed in both systems based on differences in molar absorptivities and concentrations of the MB^+ and CQ species.

Ultraviolet-visible (electronic) Spectroscopy (UV-Vis). A diode array spectrophotometer (Evolution 300, Thermo-Scientific, West Palm Beach, FL) was employed. Absorbance spectra were collected in quartz cuvettes with a 1 cm pathlength (l). FT-NIR samples were also employed to remotely monitor MB bleaching in real-time by UV-Vis in the same horizontal stage, but separately from the IR experiments. Concentrations used were as follows: [MB^+] = 4 mM, [DIPEA] = 0.2 M and [DPI^+] = 0.04 M. UV-Vis experiments were performed with an intensity of 60 mW/cm^2 to accelerate the bleaching rate of MB^+ and avoid significant polymer diffusion constraints to the reoxidation reaction between LMB and DPI^+.

Electrospray Ionization Mass Spectrometry (ESI-MS). Identification of the intermediates and final products of the reaction was performed in a LC/MS/MS mass spectrometer system (ABI 4000 Q TRAP®, Life Technologies, Carlsbad, CA) equipped with a triple quadruple/linear ion trap analyzer, and electrospray ionization (ESI) detection.

Quantum chemical calculations. Excited state calculations were performed using time-dependent density functional theory (TD-DFT) with the uωB97XD[303]/6-311G** level of theory where solvation in methanol was described using a polarizable continuum model (CPCM).[68] The reaction between an alpha amino-alkyl radical (derived from DIPEA) and HEMA monomer was determined to be barrierless, where the calculations were performed using uM06[121] /6-311G**/CPCM-methanol. In predicting the thermochemistry in reaction 2, we employed uM06/6-311G**//uωB97XD/LANL2dz in CPCM described methanol solvent. To estimate the entropy contribution to the free energy, a frequency calculation was performed using uωB97XD/LANL2dz. All calculations were performed using the GAUSSIAN09[61] and GAMESS[59] computational chemistry software packages.

Lateral polymerization experiments. Experiments were performed in a J500 Mask Aligner from Optical Associates. Exposed monomer borders a 500 µm thick opaque rubber spacer on all sides such that photo-generated molecules can diffuse only in one direction. The exposed fringes were 2 x 18 mm and the total monomer samples were 8 x 18 mm. Light intensity was chosen so R_p is equal in the MB^+/DIPEA/DPI^+ and CQ/EDMAB initiating systems, hence achieving ~80 % conversion during the 10 min irradiance in both cases, i.e., diffusion restrictions are roughly equivalent. The use of a collimated light-beam and a non-reflective surface prevented light from reflecting into the masked region from the exposed region of the sample. A black mask was used as a substrate at the bottom of the samples to eliminate any reflectance of photons into the masked region. A glass microscope slide was used as the top boundary to be able to obtain final polymer samples that adhered to the glass. Concentrations used were as follows: [MB^+] = 0.4 mM, [DIPEA] = 0.2 M, [DPI^+] = 0.04 M, [CQ] = 0.02 M and [EDMAB] = 0.04 M. Light intensity used was 12 mW/cm^2 for the MB^+/DIPEA/DPI^+ system and 23 mW/cm^2 for the CQ/EDMAB system to obtain approximately equivalent amounts of absorbed photons.

Thick disc polymerization experiments. MB^+/DIPEA/DPI^+ and CQ/EDMAB samples were prepared in HEMA. Monomer (1.5 ml) with each initiator in glass vials was irradiated for 1 min at 3.4 mW/cm^2 (>500 nm) for MB^+/DIPEA/DPI^+, and 6.6 mW/cm^2 (400-500 nm) for CQ/EDMAB to achieve equivalent photon absorption. Samples were then stored in a closed container with no light access for over 30 min. The progression of the viscosity of the samples was periodically monitored in both cases qualitatively and photographed. Concentrations used in these experiments were as follows: [MB^+] = 0.4 mM, [DIPEA] = 0.2 M, [DPI^+] = 0.04 M, [CQ] = 0.02 M, [EDMAB] = 0.04 M. At these conditions the HEMA with CQ/EDMAB remains liquid and cannot be sectioned for FT-NIR analysis. Thus, additional experiments with GDMA were performed using 9-10 mW/cm^2 for MB^+/DIPEA/DPI^+ and 17-18 mW/cm^2 for CQ/EDMAB. At these intensities, the ~ 1.2 cm thick samples were sectioned to ~ 1.5 mm slices, which were analyzed with FT-NIR after 60 s irradiation and 90-120 min in dark storage. To determine conversion means and standard deviations as a function of depth the experiments were repeated 3-4 times. All samples were purged with nitrogen for 5 minutes before irradiation at a pressure of 10-20 psi.

Methylene blue extraction from poly-HEMA gel. A 1.2 x 1.1 cm poly-HEMA disc was polymerized from bulk HEMA (97 %) with MB^+/DIPEA/DPI^+ using 5 min irradiation at 11 mW/cm^2 of a white LED lamp. The sample was left to react in the dark for 30 min. Then, the polymer gel was removed from the mold and introduced into 20 ml of water. UV-Vis absorbance of the water solution was monitored with time to track the change in the peak at ~ 660 nm, indicative of the MB^+ concentration in solution.

Bibliography

1. Beckman, E. J. Green Chemical Processing Using CO2. *Industrial & Engineering Chemistry Research* **2003,** *42* (8), 1598-1602.

2. Darensbourg, D. J. Chemistry of Carbon Dioxide Relevant to Its Utilization: A Personal Perspective. *Inorganic Chemistry* **2010,** *49* (23), 10765-10780.

3. Mikkelsen, M.; Jorgensen, M.; Krebs, F. C. The teraton challenge. A review of fixation and transformation of carbon dioxide. *Energy & Environmental Science* **2010,** *3* (1), 43-81.

4. Choi, S.; Drese, J. H.; Jones, C. W. Adsorbent Materials for Carbon Dioxide Capture from Large Anthropogenic Point Sources. *ChemSusChem* **2009,** *2* (9), 796-854.

5. Figueroa, J. D.; Fout, T.; Plasynski, S.; McIlvried, H.; Srivastava, R. D. Advancesn in CO(2) capture technology - The US Department of Energy's Carbon Sequestration Program. *International Journal of Greenhouse Gas Control* **2008,** *2* (1), 9-20.

6. Jacobson, M. Z. Review of solutions to global warming, air pollution, and energy security. *Energy & Environmental Science* **2009,** *2* (2), 148-173.

7. Ma, S. Q.; Zhou, H. C. Gas storage in porous metal-organic frameworks for clean energy applications. *Chemical Communications* **2010,** *46* (1), 44-53.

8. White, C. M.; Strazisar, B. R.; Granite, E. J.; Hoffman, J. S.; Pennline, H. W. Separation and capture of CO2 from large stationary sources and sequestration in geological formations - Coalbeds and deep saline aquifers. *Journal of the Air & Waste Management Association* **2003,** *53* (6), 645-715.

9. Arakawa, H.; Aresta, M.; Armor, J. N.; Barteau, M. A.; Beckman, E. J.; Bell, A. T.; Bercaw, J. E.; Creutz, C.; Dinjus, E.; Dixon, D. A.; Domen, K.; DuBois, D. L.; Eckert, J.; Fujita, E.; Gibson, D. H.; Goddard, W. A.; Goodman, D. W.; Keller, J.; Kubas, G. J.; Kung, H. H.; Lyons, J. E.; Manzer, L. E.; Marks, T. J.; Morokuma, K.; Nicholas, K. M.; Periana, R.; Que, L.; Rostrup-Nielson, J.; Sachtler, W. M. H.; Schmidt, L. D.; Sen, A.; Somorjai, G. A.; Stair, P. C.; Stults, B. R.; Tumas, W. Catalysis research of relevance to carbon management: Progress, challenges, and opportunities. *Chemical Reviews* **2001,** *101* (4), 953-996.

10. Olah, G. A.; Goeppert, A.; Prakash, G. K. S. Chemical Recycling off Carbon Dioxide to Methanol and Dimethyl Ether: From Greenhouse Gas to Renewable, Environmentally Carbon Neutral Fuels and Synthetic Hydrocarbons. *Journal of Organic Chemistry* **2009,** *74* (2), 487-498.

11. Olah, G. A.; Prakash, G. K. S.; Goeppert, A. Anthropogenic Chemical Carbon Cycle for a Sustainable Future. *J Am Chem Soc* **2011,** *133* (33), 12881-12898.

12. Jiang, Z.; Xiao, T.; Kuznetsov, V. L.; Edwards, P. P. Turning carbon dioxide into fuel. *Philosophical Transactions of the Royal Society A: Mathematical, Physical and Engineering Sciences* **2010,** *368* (1923), 3343-3364.

13. Ganesh, I. Conversion of carbon dioxide to methanol using solar energy. *Current Science* **2011,** *101* (6), 731-733.

14. Hoffmann, M. R.; Moss, J. A.; Baum, M. M. Artificial photosynthesis: semiconductor photocatalytic fixation of CO2 to afford higher organic compounds. *Dalton Trans.* **2011,** *40* (19), 5151-5158.

15. Ashley, A. E.; Thompson, A. L.; O'Hare, D. Non-Metal-Mediated Homogeneous Hydrogenation of CO2 to CH3OH. *Angew Chem Int Edit* **2009,** *48* (52), 9839-9843.

16. Chakraborty, S.; Zhang, J.; Krause, J. A.; Guan, H. An Efficient Nickel Catalyst for the Reduction of Carbon Dioxide with a Borane. *J Am Chem Soc* **2010,** *132* (26), 8872-8873.
17. Cokoja, M.; Bruckmeier, C.; Rieger, B.; Herrmann, W. A.; Kühn, F. E. Transformation of Carbon Dioxide with Homogeneous Transition-Metal Catalysts: A Molecular Solution to a Global Challenge? *Angewandte Chemie International Edition* **2011,** *50* (37), 8510-8537.
18. Huang, F.; Lu, G.; Zhao, L. L.; Li, H. X.; Wang, Z. X. The Catalytic Role of N-Heterocyclic Carbene in a Metal-Free Conversion of Carbon Dioxide into Methanol: A Computational Mechanism Study. *J Am Chem Soc* **2010,** *132* (35), 12388-12396.
19. Huang, F.; Zhang, C. G.; Jiang, J. L.; Wang, Z. X.; Guan, H. R. How Does the Nickel Pincer Complex Catalyze the Conversion of CO(2) to a Methanol Derivative? A Computational Mechanistic Study. *Inorganic Chemistry* **2011,** *50* (8), 3816-3825.
20. Menard, G.; Stephan, D. W. Room Temperature Reduction of CO2 to Methanol by Al-Based Frustrated Lewis Pairs and Ammonia Borane. *J Am Chem Soc* **2010,** *132* (6), 1796-+.
21. Zimmerman, P. M.; Zhang, Z. Y.; Musgrave, C. B. Simultaneous Two-Hydrogen Transfer as a Mechanism for Efficient CO2 Reduction. *Inorganic Chemistry* **2010,** *49* (19), 8724-8728.
22. Temkin, O. N.; Zeigarnik, A. V.; Kuz'min, A. E.; Bruk, L. G.; Slivinskii, E. V. Construction of the reaction networks for heterogeneous catalytic reactions: Fischer-Tropsch synthesis and related reactions. *Russian Chemical Bulletin* **2002,** *51* (1), 1-36.
23. Krylov, O. V.; Mamedov, A. K. HETEROGENEOUS CATALYTIC REACTIONS OF CARBON-DIOXIDE. *Uspekhi Khimii* **1995,** *64* (9), 935-959.
24. Dai, W. L.; Luo, S. L.; Yin, S. F.; Au, C. T. The direct transformation of carbon dioxide to organic carbonates over heterogeneous catalysts. *Applied Catalysis a-General* **2009,** *366* (1), 2-12.
25. Benson, E. E.; Kubiak, C. P.; Sathrum, A. J.; Smieja, J. M. Electrocatalytic and homogeneous approaches to conversion of CO(2) to liquid fuels. *Chemical Society Reviews* **2009,** *38* (1), 89-99.
26. Rakowski Dubois, M.; Dubois, D. L. Development of Molecular Electrocatalysts for CO2 Reduction and H2 Production/Oxidation. *Accounts of Chemical Research* **2009,** *42* (12), 1974-1982.
27. Savéant, J.-M. Molecular Catalysis of Electrochemical Reactions. Mechanistic Aspects. *Chemical Reviews* **2008,** *108* (7), 2348-2378.
28. Agarwal, J.; Johnson, R. P.; Li, G. Reduction of CO2 on a Tricarbonyl Rhenium(I) Complex: Modeling a Catalytic Cycle. *The Journal of Physical Chemistry A* **2011,** *115* (13), 2877-2881.
29. Alstrum-Acevedo, J. H.; Brennaman, M. K.; Meyer, T. J. Chemical Approaches to Artificial Photosynthesis. 2. *Inorganic Chemistry* **2005,** *44* (20), 6802-6827.
30. Huang, K.-W.; Han, J. H.; Musgrave, C. B.; Fujita, E. Carbon Dioxide Reduction by Pincer Rhodium η2-Dihydrogen Complexes: Hydrogen-Binding Modes and Mechanistic Studies by Density Functional Theory Calculations. *Organometallics* **2006,** *26* (3), 508-513.
31. Meyer, T. J. Chemical approaches to artificial photosynthesis. *Accounts of Chemical Research* **1989,** *22* (5), 163-170.
32. Aurian-Blajeni, B.; Halmann, M.; Manassen, J. Photoreduction of carbon dioxide and water into formaldehyde and methanol on semiconductor materials. *Solar Energy* **1980,** *25* (2), 165-170.

33. Halmann, M. Photoelectrochemical reduction of aqueous carbon dioxide on p-type gallium phosphide in liquid junction solar cells. *Nature* **1978,** *275* (5676), 115-116.

34. Kumar, B.; Llorente, M.; Froehlich, J.; Dang, T.; Sathrum, A.; Kubiak, C. P. Photochemical and Photoelectrochemical Reduction of CO2. In *Annual Review of Physical Chemistry, Vol 63*, Johnson, M. A. M. T. J., Ed. 2012; Vol. 63, pp 541-+.

35. Morris, A. J.; Meyer, G. J.; Fujita, E. Molecular Approaches to the Photocatalytic Reduction of Carbon Dioxide for Solar Fuels. *Accounts of Chemical Research* **2009,** *42* (12), 1983-1994.

36. Tran, P. D.; Wong, L. H.; Barber, J.; Loo, J. S. C. Recent advances in hybrid photocatalysts for solar fuel production. *Energy & Environmental Science* **2012,** *5* (3), 5902-5918.

37. Yotsuhashi, S.; Deguchi, M.; Zenitani, Y.; Hinogami, R.; Hashiba, H.; Yamada, Y.; Ohkawa, K. Photo-induced CO2 Reduction with GaN Electrode in Aqueous System. *Applied Physics Express* **2011,** *4* (11).

38. Yui, T.; Kan, A.; Saitoh, C.; Koike, K.; Ibusuki, T.; Ishitani, O. Photochemical Reduction of CO2 Using TiO2: Effects of Organic Adsorbates on TiO2 and Deposition of Pd onto TiO2. *Acs Applied Materials & Interfaces* **2011,** *3* (7), 2594-2600.

39. Barton, E. E.; Rampulla, D. M.; Bocarsly, A. B. Selective Solar-Driven Reduction of CO2 to Methanol Using a Catalyzed p-GaP Based Photoelectrochemical Cell. *J Am Chem Soc* **2008,** *130* (20), 6342-6344.

40. Cole, E. B.; Lakkaraju, P. S.; Rampulla, D. M.; Morris, A. J.; Abelev, E.; Bocarsly, A. B. Using a One-Electron Shuttle for the Multielectron Reduction of CO(2) to Methanol: Kinetic, Mechanistic, and Structural Insights. *J Am Chem Soc* **2010,** *132* (33), 11539-11551.

41. Morris, A. J.; McGibbon, R. T.; Bocarsly, A. B. Electrocatalytic Carbon Dioxide Activation: The Rate-Determining Step of Pyridinium-Catalyzed CO(2) Reduction. *ChemSusChem* **2011,** *4* (2), 191-196.

42. Seshadri, G.; Lin, C.; Bocarsly, A. B. A new homogeneous electrocatalyst for the reduction of carbon dioxide to methanol at low overpotential. *Journal of Electroanalytical Chemistry* **1994,** *372* (1–2), 145-150.

43. Keith, J. A.; Carter, E. A. Theoretical Insights into Pyridinium-Based Photoelectrocatalytic Reduction of CO2. *J Am Chem Soc* **2012,** *134* (18), 7580-7583.

44. Tossell, J. A. Calculation of the properties of molecules in the pyridine catalyst system for the photochemical conversion of CO(2) to methanol. *Computational and Theoretical Chemistry* **2011,** *977* (1-3), 123-127.

45. Yasukouchi, K.; Taniguchi, I.; Yamaguchi, H.; Shiraishi, M. Cathodic reduction of pyridinium ion in acetonitrile. *Journal of Electroanalytical Chemistry and Interfacial Electrochemistry* **1979,** *105* (2), 403-408.

46. Hickey, J. E.; Spritzer, M. S.; Elving, P. J. Polarographic reduction of pyridinium ion in pyridine tetraethylammonium perchlorate as background electrolyte. *Analytica Chimica Acta* **1966,** *35* (0), 277-285.

47. Tompkins, P. C.; Schmidt, C. L. A. A polarographic characterization of nicotinic acid and related compounds I. Pyridine and nicotinic acid. *Journal of Biological Chemistry* **1942,** *143* (3), 643-653.

48. Shikata, M.; Tachi, I. Study of the Electrolytic Reduction Potentials of Organic Compounds. Part II. The Reduction Potentials of Pyridine. *J. Agri. Chem. Soc. Japan* **1927,** *3* (746).
49. Jenkins, S. J. Aromatic adsorption on metals via first-principles density functional theory. *Proceedings of the Royal Society A: Mathematical, Physical and Engineering Science* **2009,** *465* (2110), 2949-2976.
50. Bard, A. J.; Faulkner, L. R. *Electrochemical Methods: Fundamentals and Applications*. Second ed.; Wiley: 2001.
51. Koppenol, W. H.; Rush, J. D. REDUCTION POTENTIAL OF THE CO2/CO2.- COUPLE - A COMPARISON WITH OTHER C1 RADICALS. *Journal of Physical Chemistry* **1987,** *91* (16), 4429-4430.
52. Leuschner, R.; Krohn, H.; Dohrmann, J. K. TERMINATION RATES BY TIME-RESOLVED ELECTRON-SPIN-RESONANCE - THE N-HYDROPYRIDINYL RADICAL IN SOLUTION AND THE INFLUENCE OF NON-UNIFORM RADICAL CONCENTRATION ON THE APPARENT RATE-CONSTANT. *Ber. Bunsen-Ges. Phys. Chem. Chem. Phys.* **1984,** *88* (5), 462-466.
53. Muñoz-García, A. B.; Carter, E. A. Non-innocent Dissociation of H2O on GaP(110): Implications for Electrochemical Reduction of CO2. *J Am Chem Soc* **2012,** *134* (33), 13600-13603.
54. Paldus, J. *Coupled-cluster theory*. Plenum, New York, 1992; Vol. 293, p 99-194.
55. Woon, D. E.; Dunning, T. H. GAUSSIAN-BASIS SETS FOR USE IN CORRELATED MOLECULAR CALCULATIONS .3. THE ATOMS ALUMINUM THROUGH ARGON. *J Chem Phys* **1993,** *98* (2), 1358-1371.
56. Dunning, T. H. GAUSSIAN-BASIS SETS FOR USE IN CORRELATED MOLECULAR CALCULATIONS .1. THE ATOMS BORON THROUGH NEON AND HYDROGEN. *J Chem Phys* **1989,** *90* (2), 1007-1023.
57. Harihara.Pc; Pople, J. A. INFLUENCE OF POLARIZATION FUNCTIONS ON MOLECULAR-ORBITAL HYDROGENATION ENERGIES. *Theoretica Chimica Acta* **1973,** *28* (3), 213-222.
58. Binkley, J. S.; Pople, J. A. MOLLER-PLESSET THEORY FOR ATOMIC GROUND-STATE ENERGIES. *Int. J. Quantum Chem.* **1975,** *9* (2), 229-236.
59. Schmidt, M. W.; Baldridge, K. K.; Boatz, J. A.; Elbert, S. T.; Gordon, M. S.; Jensen, J. H.; Koseki, S.; Matsunaga, N.; Nguyen, K. A.; Su, S. J.; Windus, T. L.; Dupuis, M.; Montgomery, J. A. GENERAL ATOMIC AND MOLECULAR ELECTRONIC-STRUCTURE SYSTEM. *J. Comput. Chem.* **1993,** *14* (11), 1347-1363.
60. Gordon, M. S.; Schmidt, M. W. Chapter 41 - Advances in electronic structure theory: GAMESS a decade later. In *Theory and Applications of Computational Chemistry*, Clifford, E. D.; Gernot, F.; Kwang, S. K.; Gustavo E. ScuseriaA2 - Clifford E. Dykstra, G. F. K. S. K.; Gustavo, E. S., Eds. Elsevier: Amsterdam, 2005; pp 1167-1189.
61. Gaussian 09 Revision A.1; Frisch, M. J. T., G. W.; Schlegel, H. B.; Scuseria, G. E.; Robb, M. A.; Cheeseman, J. R.; Scalmani, G.; Barone, V.; Mennucci, B.; Petersson, G. A.; Nakatsuji, H.; Caricato, M.; Li, X.; Hratchian, H. P.; Izmaylov, A. F.; Bloino, J.; Zheng, G.; Sonnenberg, J. L.; Hada, M.; Ehara, M.; Toyota, K.; Fukuda, R.; Hasegawa, J.; Ishida, M.; Nakajima, T.; Honda, Y.; Kitao, O.; Nakai, H.; Vreven, T.; Montgomery, Jr., J. A.; Peralta, J. E.; Ogliaro, F.; Bearpark, M.; Heyd, J. J.; Brothers, E.; Kudin, K. N.; Staroverov, V. N.; Kobayashi, R.; Normand, J.;

Raghavachari, K.; Rendell, A.; Burant, J. C.; Iyengar, S. S.; Tomasi, J.; Cossi, M.; Rega, N.; Millam, N. J.; Klene, M.; Knox, J. E.; Cross, J. B.; Bakken, V.; Adamo, C.; Jaramillo, J.; Gomperts, R.; Stratmann, R. E.; Yazyev, O.; Austin, A. J.; Cammi, R.; Pomelli, C.; Ochterski, J. W.; Martin, R. L.; Morokuma, K.; Zakrzewski, V. G.; Voth, G. A.; Salvador, P.; Dannenberg, J. J.; Dapprich, S.; Daniels, A. D.; Farkas, Ö.; Foresman, J. B.; Ortiz, J. V.; Cioslowski, J.; Fox, D. J. Gaussian, Inc., Wallingford CT, 2009.

62. B.O.Roos. The CASSCF Method and its Application in Electronic Structure Calculations. In *Advances in Chemical Physics*, K.P.Lawley, Ed. Wiley Interscience: New York, 1987; pp 339-445.

63. Johnson, E. R.; Mori-Sanchez, P.; Cohen, A. J.; Yang, W. Delocalization errors in density functionals and implications for main-group thermochemistry. *The Journal of Chemical Physics* **2008,** *129* (20), 204112-6.

64. Kang, J. K.; Musgrave, C. B. Prediction of transition state barriers and enthalpies of reaction by a new hybrid density-functional approximation. *The Journal of Chemical Physics* **2001,** *115* (24), 11040-11051.

65. Zhang, Y.; Yang, W. A challenge for density functionals: Self-interaction error increases for systems with a noninteger number of electrons. *The Journal of Chemical Physics* **1998,** *109* (7), 2604-2608.

66. Cohen, A. J.; Mori-Sánchez, P.; Yang, W. Insights into Current Limitations of Density Functional Theory. *Science* **2008,** *321* (5890), 792-794.

67. Li, H.; Pomelli, C. S.; Jensen, J. H. Continuum solvation of large molecules described by QM/MM: a semi-iterative implementation of the PCM/EFP interface. *Theoretical Chemistry Accounts* **2003,** *109* (2), 71-84.

68. Li, H.; Jensen, J. H. Improving the efficiency and convergence of geometry optimization with the polarizable continuum model: New energy gradients and molecular surface tessellation. *J. Comput. Chem.* **2004,** *25* (12), 1449-1462.

69. Marenich, A. V.; Cramer, C. J.; Truhlar, D. G. Universal Solvation Model Based on Solute Electron Density and on a Continuum Model of the Solvent Defined by the Bulk Dielectric Constant and Atomic Surface Tensions. *The Journal of Physical Chemistry B* **2009,** *113* (18), 6378-6396.

70. Camaioni, D. M.; Dupuis, M.; Bentley, J. Theoretical Characterization of Oxoanion, XOmn-, Solvation. *The Journal of Physical Chemistry A* **2003,** *107* (30), 5778-5788.

71. Chipman, D. M.; Chen, F. Cation electric field is related to hydration energy. *The Journal of Chemical Physics* **2006,** *124* (14), 144507-5.

72. Chipman, D. M. Anion electric field is related to hydration energy. *The Journal of Chemical Physics* **2003,** *118* (22), 9937-9942.

73. Kamerlin, S. C. L.; Haranczyk, M.; Warshel, A. Are Mixed Explicit/Implicit Solvation Models Reliable for Studying Phosphate Hydrolysis? A Comparative Study of Continuum, Explicit and Mixed Solvation Models. *ChemPhysChem* **2009,** *10* (7), 1125-1134.

74. Ho, J.; Coote, M. L. pKa Calculation of Some Biologically Important Carbon Acids - An Assessment of Contemporary Theoretical Procedures. *Journal of Chemical Theory and Computation* **2009,** *5* (2), 295-306.

75. Mulliken, R. S. Electronic Population Analysis on LCAO[Single Bond]MO Molecular Wave Functions. I. *The Journal of Chemical Physics* **1955,** *23* (10), 1833-1840.

76. Spackman, M. A. Potential derived charges using a geodesic point selection scheme. *J. Comput. Chem.* **1996,** *17* (1), 1-18.
77. Montgomery, J. A.; Frisch, M. J.; Ochterski, J. W.; Petersson, G. A. A complete basis set model chemistry. VI. Use of density functional geometries and frequencies. *J Chem Phys* **1999,** *110* (6), 2822-2827.
78. Winget, P.; Cramer, C. J.; Truhlar, D. G. Computation of equilibrium oxidation and reduction potentials for reversible and dissociative electron-transfer reactions in solution. *Theoretical Chemistry Accounts: Theory, Computation, and Modeling (Theoretica Chimica Acta)* **2004,** *112* (4), 217-227.
79. Liptak, M. D.; Shields, G. C. Accurate pKa Calculations for Carboxylic Acids Using Complete Basis Set and Gaussian-n Models Combined with CPCM Continuum Solvation Methods. *J Am Chem Soc* **2001,** *123* (30), 7314-7319.
80. Koch, D. M.; Toubin, C.; Peslherbe, G. H.; Hynes, J. T. A theoretical study of the formation of the aminoacetonitrile precursor of glycine on icy grain mantles in the interstellar medium. *Journal of Physical Chemistry C* **2008,** *112* (8), 2972-2980.
81. Somani, S.; Mukhopadhyay, A.; Musgrave, C. Atomic Layer Deposition of Tantalum Nitride Using A Novel Precursor. *The Journal of Physical Chemistry C* **2011,** *115* (23), 11507-11513.
82. Mukhopadhyay, A. B.; Musgrave, C. B. The role of ammonia in atomic layer deposition of tungsten nitride. *Applied Physics Letters* **2007,** *90* (17), 173120-3.
83. Kang, J. K.; Musgrave, C. B. The mechanism of HF/H2O chemical etching of SiO2. *J Chem Phys* **2002,** *116* (1), 275-280.
84. Bianco, R.; Hay, P. J.; Hynes, J. T. Theoretical Study of O–O Single Bond Formation in the Oxidation of Water by the Ruthenium Blue Dimer. *The Journal of Physical Chemistry A* **2011,** *115* (27), 8003-8016.
85. Mikulski, R. L.; Silverman, D. N. Proton transfer in catalysis and the role of proton shuttles in carbonic anhydrase. *Biochimica Et Biophysica Acta-Proteins and Proteomics* **2010,** *1804* (2), 422-426.
86. DuBois, D. L.; Bullock, R. M. Molecular Electrocatalysts for the Oxidation of Hydrogen and the Production of Hydrogen - The Role of Pendant Amines as Proton Relays. *European Journal of Inorganic Chemistry* **2011,** (7), 1017-1027.
87. Bonin, J.; Costentin, C.; Robert, M.; Saveant, J. M.; Tard, C. Hydrogen-Bond Relays in Concerted Proton-Electron Transfers. *Accounts of Chemical Research* **2012,** *45* (3), 372-381.
88. Haake, P.; Wallerberg, G.; Boger, J. Catalysis in dipolar aprotic solvents. Proton-relay mechanism resembling the mechanism of action of serine enzyme. *J Am Chem Soc* **1971,** *93* (19), 4938-4939.
89. Fetter, J. R.; Qian, J.; Shapleigh, J.; Thomas, J. W.; García-Horsman, A.; Schmidt, E.; Hosler, J.; Babcock, G. T.; Gennis, R. B.; Ferguson-Miller, S. Possible proton relay pathways in cytochrome c oxidase. *Proceedings of the National Academy of Sciences* **1995,** *92* (5), 1604-1608.
90. Nair, S. K.; Christianson, D. W. Unexpected pH-dependent conformation of His-64, the proton shuttle of carbonic anhydrase II. *J Am Chem Soc* **1991,** *113* (25), 9455-9458.

91. Han, S. Y.; Chu, I.; Kim, J. H.; Song, J. K.; Kim, S. K. Photoelectron spectroscopy and ab initio study of mixed cluster anions of (CO2)(1-3)(Pyridine)(1-6) (-): Formation of a covalently bonded anion core of (C5H5N-CO2)(-). *J Chem Phys* **2000,** *113* (2), 596-601.
92. Bryantsev, V. S.; Diallo, M. S.; Goddard Iii, W. A. Calculation of Solvation Free Energies of Charged Solutes Using Mixed Cluster/Continuum Models. *The Journal of Physical Chemistry B* **2008,** *112* (32), 9709-9719.
93. Borden, J.; Crans, D. C.; Florián, J. Transition State Analogues for Nucleotidyl Transfer Reactions: Structure and Stability of Pentavalent Vanadate and Phosphate Ester Dianions. *The Journal of Physical Chemistry B* **2006,** *110* (30), 14988-14999.
94. Kamrath, M. Z.; Relph, R. A.; Johnson, M. A. Vibrational Predissociation Spectrum of the Carbamate Radical Anion, C(5)H(5)N-CO(2)(-), Generated by Reaction of Pyridine with (CO(2))(m)(-). *J Am Chem Soc* **2010,** *132* (44), 15508-15511.
95. Schleyer, P. V.; Puhlhofer, F. Recommendations for the evaluation of aromatic stabilization energies. *Organic Letters* **2002,** *4* (17), 2873-2876.
96. Cyranski, M. K. Energetic aspects of cyclic Pi-electron delocalization: Evaluation of the methods of estimating aromatic stabilization energies. *Chemical Reviews* **2005,** *105* (10), 3773-3811.
97. Evans, M. G.; Polanyi, M. Some applications of the transition state method to the calculation of reaction velocities, especially in solution. *Transactions of the Faraday Society* **1935,** *31* (1), 0875-0893.
98. Hull, J. F.; Himeda, Y.; Wang, W.-H.; Hashiguchi, B.; Periana, R.; Szalda, D. J.; Muckerman, J. T.; Fujita, E. Reversible hydrogen storage using CO2 and a proton-switchable iridium catalyst in aqueous media under mild temperatures and pressures. *Nat Chem* **2012,** *4* (5), 383-388.
99. Doherty, M. D.; Grills, D. C.; Muckerman, J. T.; Polyansky, D. E.; Fujita, E. Toward more efficient photochemical CO2 reduction: Use of scCO2 or photogenerated hydrides. *Coordination Chemistry Reviews* **2010,** *254* (21–22), 2472-2482.
100. Kumar, B.; Llorente, M.; Froehlich, J.; Dang, T.; Sathrum, A.; Kubiak, C. P. Photochemical and Photoelectrochemical Reduction of CO2. *Annual Review of Physical Chemistry* **2012,** *63* (1), 541-569.
101. Chen, Z.; Glasson, C. R. K.; Holland, P. L.; Meyer, T. J. Electrogenerated polypyridyl ruthenium hydride and ligand activation for water reduction to hydrogen and acetone to iso-propanol. *Phys. Chem. Chem. Phys.* **2013,** *15* (24), 9503-9507.
102. Kang, P.; Meyer, T. J.; Brookhart, M. Selective electrocatalytic reduction of carbon dioxide to formate by a water-soluble iridium pincer catalyst. *Chemical Science* **2013,** *4* (9), 3497-3502.
103. Costentin, C.; Robert, M.; Saveant, J.-M. Catalysis of the electrochemical reduction of carbon dioxide. *Chemical Society Reviews* **2013,** *42* (6), 2423-2436.
104. Gennaro, A.; Isse, A. A.; Saveant, J. M.; Severin, M. G.; Vianello, E. Homogeneous electron transfer catalysis of the electrochemical reduction of carbon dioxide. Do aromatic anion radicals react in an outer-sphere manner? *J Am Chem Soc* **1996,** *118* (30), 7190-7196.
105. Balaraman, E.; Gunanathan, C.; Zhang, J.; Shimon, L. J. W.; Milstein, D. Efficient hydrogenation of organic carbonates, carbamates and formates indicates alternative routes to methanol based on CO2 and CO. *Nature Chemistry* **2011,** *3* (8), 609-614.

106. Jeletic, M. S.; Mock, M. T.; Appel, A. M.; Linehan, J. C. A Cobalt-Based Catalyst for the Hydrogenation of CO2 under Ambient Conditions. *J Am Chem Soc* **2013,** *135* (31), 11533-11536.
107. Ohtsu, H.; Tanaka, K. An Organic Hydride Transfer Reaction of a Ruthenium NAD Model Complex Leading to Carbon Dioxide Reduction. *Angewandte Chemie International Edition* **2012,** *51* (39), 9792-9795.
108. Riduan, S. N.; Zhang, Y. G.; Ying, J. Y. Conversion of Carbon Dioxide into Methanol with Silanes over N-Heterocyclic Carbene Catalysts. *Angew Chem Int Edit* **2009,** *48* (18), 3322-3325.
109. Canfield, D.; Frese, K. W. Reduction of Carbon Dioxide to Methanol on n - and p - GaAs and p - InP . Effect of Crystal Face, Electrolyte and Current Density. *Journal of The Electrochemical Society* **1983,** *130* (8), 1772-1773.
110. Frese, K. W.; Canfield, D. Reduction of CO 2 on n - GaAs Electrodes and Selective Methanol Synthesis. *Journal of The Electrochemical Society* **1984,** *131* (11), 2518-2522.
111. Zimmerman, P. M.; Paul, A.; Zhang, Z. Y.; Musgrave, C. B. The Role of Free N-Heterocyclic Carbene (NHC) in the Catalytic Dehydrogenation of Ammonia-Borane in the Nickel NHC System. *Angew Chem Int Edit* **2009,** *48* (12), 2201-2205.
112. Lim, C.-H.; Holder, A. M.; Hynes, J. T.; Musgrave, C. B. Roles of the Lewis Acid and Base in the Chemical Reduction of CO2 Catalyzed by Frustrated Lewis Pairs. *Inorganic Chemistry* **2013,** *52* (17), 10062-10066.
113. Eisner, U.; Kuthan, J. Chemistry of dihydropyridines. *Chemical Reviews* **1972,** *72* (1), 1-42.
114. McSkimming, A.; Colbran, S. B. The coordination chemistry of organo-hydride donors: new prospects for efficient multi-electron reduction. *Chemical Society Reviews* **2013,** *42* (12), 5439-5488.
115. Connon, S. J. Asymmetric organocatalytic reductions mediated by dihydropyridines. *Organic & Biomolecular Chemistry* **2007,** *5* (21), 3407-3417.
116. Chen, Q.-A.; Chen, M.-W.; Yu, C.-B.; Shi, L.; Wang, D.-S.; Yang, Y.; Zhou, Y.-G. Biomimetic Asymmetric Hydrogenation: In Situ Regenerable Hantzsch Esters for Asymmetric Hydrogenation of Benzoxazinones. *J Am Chem Soc* **2011,** *133* (41), 16432-16435.
117. Schmakel, C. O.; Santhanam, K. S. V.; Elving, P. J. Nicotinamide and N'-Methylnicotinamide: Electrochemical Redox Pattern: Behavior of Free Radical, Dimeric, and Dihydropyridine Species. *Journal of The Electrochemical Society* **1974,** *121* (3), 345-353.
118. Kaye, R. C.; Stonehill, H. I. 7. A polarographic study of the electroreduction of acridine. *Journal of the Chemical Society (Resumed)* **1951,** (0), 27-38.
119. Fujii, S.; Tatsumoto, N.; Yamaoka, K. Effect of poly(α-D-glutamic acid) on the polarographic reduction of 3,6-diaminoacridines. *Journal of Electroanalytical Chemistry and Interfacial Electrochemistry* **1988,** *244* (1–2), 235-248.
120. Lim, C.-H.; Holder, A. M.; Musgrave, C. B. Mechanism of Homogeneous Reduction of CO2 by Pyridine: Proton Relay in Aqueous Solvent and Aromatic Stabilization. *J Am Chem Soc* **2012,** *135* (1), 142-154.
121. Zhao, Y.; Truhlar, D. The M06 suite of density functionals for main group thermochemistry, thermochemical kinetics, noncovalent interactions, excited states, and transition elements: two new functionals and systematic testing of four M06-class functionals and 12 other functionals. *Theoretical Chemistry Accounts* **2008,** *120* (1-3), 215-241.

122. Bianco, R.; Hay, P. J.; Hynes, J. T. Proton relay and electron flow in the O-O single bond formation in water oxidation by the ruthenium blue dimer. *Energy & Environmental Science* **2012,** *5* (7), 7741-7746.
123. Stirling, A. s.; Pápai, I. H2CO3 Forms via HCO3− in Water. *The Journal of Physical Chemistry B* **2010,** *114* (50), 16854-16859.
124. Wang, B.; Cao, Z. How water molecules modulate the hydration of CO2 in water solution: Insight from the cluster-continuum model calculations. *J. Comput. Chem.* **2013,** *34* (5), 372-378.
125. Barton, B. E.; Olsen, M. T.; Rauchfuss, T. B. Aza- and Oxadithiolates Are Probable Proton Relays in Functional Models for the [FeFe]-Hydrogenases. *J Am Chem Soc* **2008,** *130* (50), 16834-16835.
126. Lutz, S.; Tubert-Brohman, I.; Yang, Y.; Meuwly, M. Water-assisted Proton Transfer in Ferredoxin I. *Journal of Biological Chemistry* **2011,** *286* (27), 23679-23687.
127. Bonin, J.; Costentin, C.; Robert, M.; Savéant, J.-M.; Tard, C. Hydrogen-Bond Relays in Concerted Proton–Electron Transfers. *Accounts of Chemical Research* **2011,** *45* (3), 372-381.
128. Bianco, R.; Hynes, J. T. A theoretical study of the reaction of ClONO2 with HCl on ice. *J. Phys. Chem. A* **1999,** *103* (20), 3797-3801.
129. Huynh, M. H. V.; Meyer, T. J. Proton-Coupled Electron Transfer. *Chemical Reviews* **2007,** *107* (11), 5004-5064.
130. Benson, S. W. *The foundations of chemical kinetics*. McGraw-Hill: New York, 1960.
131. Qu, S.; Dang, Y.; Song, C.; Wen, M.; Huang, K.-W.; Wang, Z.-X. Catalytic Mechanisms of Direct Pyrrole Synthesis via Dehydrogenative Coupling Mediated by PNP-Ir or PNN-Ru Pincer Complexes: Crucial Role of Proton-Transfer Shuttles in the PNP-Ir System. *J Am Chem Soc* **2014,** *136* (13), 4974-4991.
132. Liang, Y.; Liu, S.; Xia, Y.; Li, Y.; Yu, Z.-X. Mechanism, Regioselectivity, and the Kinetics of Phosphine-Catalyzed [3+2] Cycloaddition Reactions of Allenoates and Electron-Deficient Alkenes. *Chemistry – A European Journal* **2008,** *14* (14), 4361-4373.
133. Huang, D.; Makhlynets, O. V.; Tan, L. L.; Lee, S. C.; Rybak-Akimova, E. V.; Holm, R. H. Fast Carbon Dioxide Fixation by 2,6-Pyridinedicarboxamidato-nickel(II)-hydroxide Complexes: Influence of Changes in Reactive Site Environment on Reaction Rates. *Inorganic Chemistry* **2011,** *50* (20), 10070-10081.
134. Huang, D.; Makhlynets, O. V.; Tan, L. L.; Lee, S. C.; Rybak-Akimova, E. V.; Holm, R. H. Kinetics and mechanistic analysis of an extremely rapid carbon dioxide fixation reaction. *Proceedings of the National Academy of Sciences* **2011,** *108* (4), 1222-1227.
135. Martin, R. L.; Hay, P. J.; Pratt, L. R. Hydrolysis of Ferric Ion in Water and Conformational Equilibrium. *The Journal of Physical Chemistry A* **1998,** *102* (20), 3565-3573.
136. Wen, M.; Huang, F.; Lu, G.; Wang, Z.-X. Density Functional Theory Mechanistic Study of the Reduction of CO2 to CH4 Catalyzed by an Ammonium Hydridoborate Ion Pair: CO2 Activation via Formation of a Formic Acid Entity. *Inorganic Chemistry* **2013,** *52* (20), 12098-12107.
137. Strajbl, M.; Sham, Y. Y.; Villà, J.; Chu, Z. T.; Warshel, A. Calculations of Activation Entropies of Chemical Reactions in Solution. *The Journal of Physical Chemistry B* **2000,** *104* (18), 4578-4584.

138. Srinivasan, R.; Medary, R. T.; Fisher, H. F.; Norris, D. J.; Stewart, R. The pyridinium-dihydropyridine system. Reduction potentials and the mechanism of oxidation of 1,4-dihydropyridines by a Schiff base. *J Am Chem Soc* **1982,** *104* (3), 807-812.
139. Tanaka, R.; Yamashita, M.; Chung, L. W.; Morokuma, K.; Nozaki, K. Mechanistic Studies on the Reversible Hydrogenation of Carbon Dioxide Catalyzed by an Ir-PNP Complex. *Organometallics* **2011,** *30* (24), 6742-6750.
140. This contrasts with a recent theoretical estimate (ref. 152) of the conduction band minimum (E_{CBM}) of p-GaP of -0.9V vs. SCE, which is significantly below the observed E_{CBM} of -1.5 V vs. SCE. This estimate led the authors to conclude that homogeneous PyH^0 species cannot be formed in the p-GaP electrode system.
141. Gratzel, M. Photoelectrochemical cells. *Nature* **2001,** *414* (6861), 338-344.
142. Walter, M. G.; Warren, E. L.; McKone, J. R.; Boettcher, S. W.; Mi, Q.; Santori, E. A.; Lewis, N. S. Solar Water Splitting Cells. *Chemical Reviews* **2010,** *110* (11), 6446-6473.
143. Beranek, R. (Photo)electrochemical Methods for the Determination of the Band Edge Positions of TiO2-Based Nanomaterials. *Advances in Physical Chemistry* **2011,** *2011*.
144. The reported p-GaP conduction band minimum, E_{CBM}, is ~ -1.0V vs. NHE at pH= 1. Correcting for the SCE reference potential shifts the band edge by -0.24V from NHE. At the same time the band edge shifts to more cathodic potentials with increasing pH by -0.059V/pH at 298K (ref. 143)
145. Lebègue, E.; Agullo, J.; Morin, M.; Bélanger, D. The Role of Surface Hydrogen Atoms in the Electrochemical Reduction of Pyridine and CO2 in Aqueous Electrolyte. *ChemElectroChem* **2014**, 1, 1013.
146. An anonymous reviewer of an earlier version of this manuscript suggested the importance of examination of CO_2 reduction with pyridine under acidic conditions with a carbon electrode. In connection with an experiment very recently reported (ref. 145), it was suggested that PyH^0 was produced with a glassy carbon electrode, and a catalytic current was observed in the presence of CO_2. Further detailed results for this system will be of considerable interest in connection with the present work.
147. Xiang, D.; Magana, D.; Dyer, R. B. CO2 Reduction Catalyzed by Mercaptopteridine on Glassy Carbon. *J Am Chem Soc* **2014**.
148. Boston, D. J.; Xu, C.; Armstrong, D. W.; MacDonnell, F. M. Photochemical Reduction of Carbon Dioxide to Methanol and Formate in a Homogeneous System with Pyridinium Catalysts. *J Am Chem Soc* **2013,** *135* (44), 16252-16255.
149. In Ref. 148, after 6 hours of photochemical reduction of CO_2 catalyzed by pyridine, formate was produced at relatively high yield (18mM), but methanol was produced at low yield (66μM). The issue of formate formation is discussed in section 3.5.
150. Boston, D. J.; Pachón, Y. M. F.; Lezna, R. O.; de Tacconi, N. R.; MacDonnell, F. M. Electrocatalytic and Photocatalytic Conversion of CO2 to Methanol using Ruthenium Complexes with Internal Pyridyl Cocatalysts. *Inorganic Chemistry* **2014,** *53* (13), 6544-6553.
151. Keith, J. A.; Carter, E. A. Electrochemical reactivities of pyridinium in solution: consequences for CO2 reduction mechanisms. *Chemical Science* **2013,** *4* (4), 1490-1496.

152. Keith, J. A.; Carter, E. A. Theoretical Insights into Electrochemical CO2 Reduction Mechanisms Catalyzed by Surface-Bound Nitrogen Heterocycles. *The Journal of Physical Chemistry Letters* **2013,** *4* (23), 4058-4063.
153. Costentin, C.; Canales, J. C.; Haddou, B.; Savéant, J.-M. Electrochemistry of Acids on Platinum. Application to the Reduction of Carbon Dioxide in the Presence of Pyridinium Ion in Water. *J Am Chem Soc* **2013,** *135* (47), 17671-17674.
154. Ertem, M. Z.; Konezny, S. J.; Araujo, C. M.; Batista, V. S. Functional Role of Pyridinium during Aqueous Electrochemical Reduction of CO2 on Pt(111). *The Journal of Physical Chemistry Letters* **2013**, 745-748.
155. Yan, Y.; Zeitler, E. L.; Gu, J.; Hu, Y.; Bocarsly, A. B. Electrochemistry of Aqueous Pyridinium: Exploration of a Key Aspect of Electrocatalytic Reduction of CO2 to Methanol. *J Am Chem Soc* **2013,** *135* (38), 14020-14023.
156. Portenkirchner, E.; Enengl, C.; Enengl, S.; Hinterberger, G.; Schlager, S.; Apaydin, D.; Neugebauer, H.; Knör, G.; Sariciftci, N. S. A Comparison of Pyridazine and Pyridine as Electrocatalysts for the Reduction of Carbon Dioxide to Methanol. *ChemElectroChem* **2014,** *1* (9), 1543-1548.
157. The loss of PyH^0's aromaticity is unfortunately not conveyed in the molecular structure of Scheme 2.
158. This result contrasts the proposal that PyH^0 is not reactive due to its high pK_a of ~27 (ref. 43). We calculated a similarly high pK_a of ~31 (ref. 120). However, we argued that a pK_a analysis only applies to reactions occurring via the sequence of PT then ET, which is irrelevant for PyH^0's reaction with CO_2 that occurs via the sequence of first ET followed by PT (ref. 120).
159. Raghavan, R.; Iwamoto, R. T. Characterization of the dimeric one-electron electrolytic reduction products of 1-alkylpyridinium ions in acetonitrile. *Journal of Electroanalytical Chemistry and Interfacial Electrochemistry* **1978,** *92* (1), 101-114.
160. Kikuchi, K.; Koizumi, M. Photoreduction of Proflavine in the Aqueous Solution. I. A Flash Photolysis Study. *B Chem Soc Jpn* **1967,** *40* (4), 736-743.
161. A similar process has been observed (ref. 160) for the quenching of two 3,6-diaminoacridinium radicals to form the corresponding dihydropyridine species (3,6-diaminoacridane) and 3,6-diaminoacridine.
162. Rose, M. C.; Stuehr, J. Kinetics of proton transfer reactions in aqueous solution. III. Rates of internally hydrogen-bonded systems. *J Am Chem Soc* **1968,** *90* (26), 7205-7209.
163. The rate constant for PyH^0 quenching is ~10^9 $M^{-1}s^{-1}$. (ref. 52). On the other hand, the rate constant for protonation/deprotonation ranges from 10^4-10^9 $M^{-1}s^{-1}$ (ref. 162) depending on pK_a differences between the donor and acceptor and other factors. Given that [HA] >> [PyH^0], it is likely that PyH_2 production via PT-ET to PyH^0 dominates over radical self quenching.
164. PyH^0 is predominantly protonated at its C2 carbon (pK_a = 4.1) over its C3 (pK_a=0.2) and C4 (pK_a= 2.4) positions; see SI, section 1b for details.
165. Protonation of related pyridine neutral radical species has been observed, e.g. the pK_a to protonate the C-9 position of 3,6-Bis(dimethylamino) acridinium radical was determined to be 5.1 in aqueous solution (ref. 166)

166. Vogelmann, E.; Rauscher, W.; Kramer, H. E. A. REACTIVITY OF ACRIDINE DYE TRIPLET STATES IN ELECTRON TRANSFER REACTIONS. *Photochemistry and Photobiology* **1979,** *29* (4), 771-776.
167. Vlachy, V. IONIC EFFECTS BEYOND POISSON-BOLTZMANN THEORY. *Annual Review of Physical Chemistry* **1999,** *50* (1), 145-165.
168. Bu, W.; Vaknin, D.; Travesset, A. How Accurate Is Poisson−Boltzmann Theory for Monovalent Ions near Highly Charged Interfaces? *Langmuir* **2006,** *22* (13), 5673-5681.
169. Hunter, R. J. *Zeta potential in colloid science: principles and applications*. Academic press London: 1981; Vol. 8.
170. Angulo, M.; Montoya, M. R.; Galvin, R. M.; Mellado, J. M. R. Electroreduction of some pyridine carboxamides on carbon electrodes in aqueous solutions. *Electroanalysis* **1997,** *9* (4), 345-349.
171. Hapiot, P.; Moiroux, J.; Saveant, J. M. Electrochemistry of NADH/NAD+ analogs. A detailed mechanistic kinetic and thermodynamic analysis of the 10-methylacridan/10-methylacridinium couple in acetonitrile. *J Am Chem Soc* **1990,** *112* (4), 1337-1343.
172. Johnston, C. C.; Gardner, J. L.; Suelter, C. H.; Metzler, D. E. Acid-Catalyzed Addition of Water to 1,4-Dihydronicotinamide Derivatives*. *Biochemistry* **1963,** *2* (4), 689-696.
173. Shinkai, S.; Hamada, H.; Kusano, Y.; Manabe, O. Coenzyme models. Part 16. Studies of general-acid catalysis in the NADH model reduction. *Journal of the Chemical Society, Perkin Transactions 2* **1979,** (5), 699-702.
174. Calvin, M. PATH OF CARBON IN PHOTOSYNTHESIS. *Science* **1962,** *135* (3507), 879-&.
175. Raines, C. The Calvin cycle revisited. *Photosynthesis Research* **2003,** *75* (1), 1-10.
176. Koizumi, T.-a.; Tanaka, K. Reversible Hydride Generation and Release from the Ligand of [Ru(pbn)(bpy)2](PF6)2 Driven by a pbn-Localized Redox Reaction. *Angewandte Chemie International Edition* **2005,** *44* (36), 5891-5894.
177. The proposed sequential PT-ET-PT-ET steps for $Ru(bpy)_2(pbnH_2)^{2+}$ formation are consistent with the production of dihydropyridine species for the related nicotinamide and acridines (ref. 117-119). More importantly, this is analogous to PyH_2 formation, thus corroborating the viability of Scheme 2 and 4’s routes I, II, V and VI.
178. Chen, Q.-A.; Gao, K.; Duan, Y.; Ye, Z.-S.; Shi, L.; Yang, Y.; Zhou, Y.-G. Dihydrophenanthridine: A New and Easily Regenerable NAD(P)H Model for Biomimetic Asymmetric Hydrogenation. *J Am Chem Soc* **2012,** *134* (4), 2442-2448.
179. Horn, M.; Schappele, L. H.; Lang-Wittkowski, G.; Mayr, H.; Ofial, A. R. Towards a Comprehensive Hydride Donor Ability Scale. *Chemistry – A European Journal* **2013,** *19* (1), 249-263.
180. Richter, D.; Mayr, H. Hydride-Donor Abilities of 1,4-Dihydropyridines: A Comparison with π Nucleophiles and Borohydride Anions. *Angewandte Chemie International Edition* **2009,** *48* (11), 1958-1961.
181. DuBois, D. L.; Berning, D. E. Hydricity of transition-metal hydrides and its role in CO2 reduction. *Applied Organometallic Chemistry* **2000,** *14* (12), 860-862.
182. Ellis, W. W.; Raebiger, J. W.; Curtis, C. J.; Bruno, J. W.; DuBois, D. L. Hydricities of BzNADH, C5H5Mo(PMe3)(CO)2H, and C5Me5Mo(PMe3)(CO)2H in Acetonitrile. *J Am Chem Soc* **2004,** *126* (9), 2738-2743.

183. Muckerman, J. T.; Achord, P.; Creutz, C.; Polyansky, D. E.; Fujita, E. Calculation of thermodynamic hydricities and the design of hydride donors for CO2 reduction. *Proceedings of the National Academy of Sciences* **2012,** *109* (39), 15657-15662.
184. The N values of of 1,4-cyclohexadiene, 10-methyl-9,10-dihydroacridine, and the Hantzsch ester were tabulated for HT in dichloromethane solvent while DMSO being the solvent for $NaBH_4$. In contrast, our calculations on $PhenH_2$ and PyH_2 were performed with CPCM-modeled aqueous solvent. It has been experimentally observed (ref. 179) that the N value is slightly greater when a more polar solvent is used (e.g. water).
185. The linear dependence of $\Delta G^{\ddagger}_{HT}$ on N is implied from Mayr et al.'s log k(20^{o}C) = s(N+E) equation (defined in Figure 1), where the logarithm of the rate constant depends linearly on $\Delta G^{\ddagger}_{HT}$ that is linearly related to N.
186. Since aqueous solution is considered for the reduction reactions, the possibility that PyH_2 is destroyed via HT to the water solvent ($PyH_2 + H_2O= PyH^+ + OH^- + H_2$) requires consideration. In section 3.7, we discount the PyH_2 destruction route via HT to PyH^+ (the dominant cation acid in the solution) to form H_2 ($PyH_2 + PyH^+ = PyH^+ + Py + H_2$), with a calculated free energy barrier 24.0kcal/mol. Since water (pK_a = 15.7) is a very much weaker acid than PyH^+ (pK_a =5.3), PyH_2 HT to water will have a much higher barrier than does HT to PyH^+, and at the same time be even more thermodynamically unfavorable.
187. Although PyH^+ is depicted as the sole proton donor in Scheme 6, any H_3O^+ present can also certainly protonate $HCOO^-$ to form HCOOH
188. As was the case for HT from ammonia borane (ref. 112), no pre-bending of CO_2 is found to precede the TS.
189. Proust-De Martin, F.; Dumas, R.; Field, M. J. A Hybrid-Potential Free-Energy Study of the Isomerization Step of the Acetohydroxy Acid Isomeroreductase Reaction. *J Am Chem Soc* **2000,** *122* (32), 7688-7697.
190. Yoshioka, Y.; Schaefer, H. F.; Jordan, K. D. Theoretical investigation of the electron affinity of CO2. *The Journal of Chemical Physics* **1981,** *75* (2), 1040-1041.
191. Valadbeigi, Y.; Farrokhpour, H. DFT, CBS-Q, W1BD and G4MP2 calculation of the proton and electron affinities, gas phase basicities and ionization energies of saturated and unsaturated carboxylic acids (C1–C4). *Int. J. Quantum Chem.* **2013,** *113* (12), 1717-1721.
192. Winkelman, J. G. M.; Ottens, M.; Beenackers, A. A. C. M. The kinetics of the dehydration of methylene glycol. *Chemical Engineering Science* **2000,** *55* (11), 2065-2071.
193. Bell, R. P.; Evans, P. G. Kinetics of the Dehydration of Methylene Glycol in Aqueous Solution. *Proceedings of the Royal Society of London. Series A. Mathematical and Physical Sciences* **1966,** *291* (1426), 297-323.
194. Beno, B. R.; Houk, K. N.; Singleton, D. A. Synchronous or Asynchronous? An "Experimental" Transition State from a Direct Comparison of Experimental and Theoretical Kinetic Isotope Effects for a Diels−Alder Reaction. *J Am Chem Soc* **1996,** *118* (41), 9984-9985.
195. Labet, V.; Morell, C.; Toro-Labbe, A.; Grand, A. Is an elementary reaction step really elementary? Theoretical decomposition of asynchronous concerted mechanisms. *Phys. Chem. Chem. Phys.* **2010,** *12* (16), 4142-4151.

196. Bekele, T.; Christian, C. F.; Lipton, M. A.; Singleton, D. A. "Concerted" Transition State, Stepwise Mechanism. Dynamics Effects in C2-C6 Enyne Allene Cyclizations. *J Am Chem Soc* **2005,** *127* (25), 9216-9223.
197. Williams, A. *Concerted Organic and Bio-Organic Mechanisms*. CRC Press: 1999.
198. Black, K.; Liu, P.; Xu, L.; Doubleday, C.; Houk, K. N. Dynamics, transition states, and timing of bond formation in Diels–Alder reactions. *Proceedings of the National Academy of Sciences* **2012,** *109* (32), 12860-12865.
199. This sentence defines what we mean by "coupled". In other language sometimes used (ref. 194-198), the HTPT process could be termed "concerted asynchronous". However, the definitions of the terms "concerted" and "asynchronous" are sometimes defined/interpreted differently (ref. 194-198), so we do not insist on this usage.
200. Barnes, D.; Zuman, P. Polarographic reduction of aldehydes and ketones: XV. Hydration and acid-base equilibria accompanying reduction of aliphatic aldehydes. *Journal of Electroanalytical Chemistry and Interfacial Electrochemistry* **1973,** *46* (2), 323-342.
201. Norkus, E.; Pauliukaite, R.; Vaskelis, A.; Butkus, E.; Jusys, Z.; Kreneviciene, M. Influence of Ionic Strength and Cation Nature on the Deprotonation of Methanediol in Alkaline Solution[dagger]. *Journal of Chemical Research, Synopses* **1998,** (6), 320-321.
202. Russell, P. G.; Kovac, N.; Srinivasan, S.; Steinberg, M. The Electrochemical Reduction of Carbon Dioxide, Formic Acid, and Formaldehyde. *Journal of The Electrochemical Society* **1977,** *124* (9), 1329-1338.
203. The possible destruction of the methanediol via HT from PyH_2 to produce the diolate negative ion, H_2 and PyH^+ can be neglected due to the diol's high pK_a value of ~ 13 (ref. 200 and 201), along the lines of the argument for the unimportance of HT from PyH_2 to H_2O in ref. 186. We thank Prof. Matt Kanan (Stanford) for raising this issue.
204. Ballinger, P.; Long, F. A. Acid Ionization Constants of Alcohols. II. Acidities of Some Substituted Methanols and Related Compounds1,2. *J Am Chem Soc* **1960,** *82* (4), 795-798.
205. Fukuzumi, S.; Ishikawa, M.; Tanaka, T. Mechanism of acid-catalysed reduction of aromatic aldehydes and p-benzoquinone derivatives by an nadh model compound. *Tetrahedron* **1986,** *42* (4), 1021-1034.
206. Kellogg, R. M. 1.3 - Reduction of CX to CHXH by Hydride Delivery from Carbon. In *Comprehensive Organic Synthesis*, Trost, B. M.; Fleming, I., Eds. Pergamon: Oxford, 1991; pp 79-106.
207. Dumas, R.; Biou, V.; Halgand, F.; Douce, R.; Duggleby, R. G. Enzymology, Structure, and Dynamics of Acetohydroxy Acid Isomeroreductase. *Accounts of Chemical Research* **2001,** *34* (5), 399-408.
208. It was suggested that (ref. 152) a surface hydride can be formed on a GaP surface, which is then transferred to the N of an adsorbed Py to form a surface-adsorbed dihydropyridine (assuming PT occurs from the solution phase). However, this proposal does not explain the observed catalytic role of Py: if GaP is capable of producing a hydride, this hydride can directly transfer to CO_2, thus eliminating the role of Py as a HT mediator.
209. In SI section 7, we calculate a ΔG^0_{rxn} of ~60 kcal/mol for the HT proposed in ref. 152 from the N-H bond of 1,4-dihydropyridine to CO_2 to form $HCOO^-$. In addition, binding of 1,4-dihydropyridine to a surface Lewis acid site through the N lone pair, as proposed in ref. 152,

causes the N-H bond to be an even weaker hydride donor with a ΔG^0_{rxn} larger than the already high 60 kcal/mol for free 1,4-dihydropyridine. Thus HT from the N-H bond of either a solution phase or surface-adsorbed dihydropyridine is highly endergonic and is highly unlikely.
210. Gunanathan, C.; Milstein, D. Metal–Ligand Cooperation by Aromatization–Dearomatization: A New Paradigm in Bond Activation and "Green" Catalysis. *Accounts of Chemical Research* **2011,** *44* (8), 588-602.
211. Milstein, D. Discovery of Environmentally Benign Catalytic Reactions of Alcohols Catalyzed by Pyridine-Based Pincer Ru Complexes, Based on Metal–Ligand Cooperation. *Top Catal* **2010,** *53* (13-14), 915-923.
212. No surface reaction is invoked in our development, but we argue that the electrical double layer near the cathode plays the important role of assisting protonation in both the protonation of PyH^0 (section 3.2) en route to PyH_2 and of formate anion (section 3.4).
213. Shaffer, G. Long-term effectiveness and consequences of carbon dioxide sequestration. *Nat. Geosci.* **2010,** *3* (7), 464-467.
214. Chakraborty, S.; Zhang, J.; Krause, J. A.; Guan, H. R. An Efficient Nickel Catalyst for the Reduction of Carbon Dioxide with a Borane. *J Am Chem Soc* **2010,** *132* (26), 8872-+.
215. Momming, C. M.; Otten, E.; Kehr, G.; Frohlich, R.; Grimme, S.; Stephan, D. W.; Erker, G. Reversible Metal-Free Carbon Dioxide Binding by Frustrated Lewis Pairs. *Angew Chem Int Edit* **2009,** *48* (36), 6643-6646.
216. Stephan, D. W.; Erker, G. Frustrated Lewis Pairs: Metal-free Hydrogen Activation and More. *Angew Chem Int Edit* **2010,** *49* (1), 46-76.
217. Jiang, C. F.; Stephan, D. W. Phosphinimine-borane combinations in frustrated Lewis pair chemistry. *Dalton Trans.* **2013,** *42* (3), 630-637.
218. Reddy, J. S.; Xu, B. H.; Mahdi, T.; Frohlich, R.; Kehr, G.; Stephan, D. W.; Erker, G. Alkenylborane-Derived Frustrated Lewis Pairs: Metal-Free Catalytic Hydrogenation Reactions of Electron-Deficient Alkenes. *Organometallics* **2012,** *31* (15), 5638-5649.
219. Peuser, I.; Neu, R. C.; Zhao, X. X.; Ulrich, M.; Schirmer, B.; Tannert, J. A.; Kehr, G.; Frohlich, R.; Grimme, S.; Erker, G.; Stephan, D. W. CO2 and Formate Complexes of Phosphine/Borane Frustrated Lewis Pairs. *Chemistry-a European Journal* **2011,** *17* (35), 9640-9650.
220. Appelt, C.; Westenberg, H.; Bertini, F.; Ehlers, A. W.; Slootweg, J. C.; Lammertsma, K.; Uhl, W. Geminal Phosphorus/Aluminum-Based Frustrated Lewis Pairs: C-H versus C equivalent to C Activation and CO(2) Fixation. *Angew Chem Int Edit* **2011,** *50* (17), 3925-3928.
221. Roy, L.; Zimmerman, P. M.; Paul, A. Changing Lanes from Concerted to Stepwise Hydrogenation: The Reduction Mechanism of Frustrated Lewis Acid–Base Pair Trapped CO2 to Methanol by Ammonia–Borane. *Chemistry – A European Journal* **2011,** *17* (2), 435-439.
222. Kwon, H. J.; Kim, H. W.; Rhee, Y. M. On the Mechanism of Irreversible Carbon Dioxide Binding with a Frustrated Lewis Pair: Solvent-Assisted Frustration and Transition-State Entropic Encouragement. *Chemistry-a European Journal* **2011,** *17* (23), 6501-6507.
223. Although Rhee et al. [ref. 222] demonstrated that explicit solvent encourages FLP•CO_2 formation the role of the LA and LB in FLP-catalyzed CO_2 reduction examined here is the same whether an implicit or explicit solvent model is employed.

224. Grimme, S. Semiempirical GGA-type density functional constructed with a long-range dispersion correction. *J. Comput. Chem.* **2006,** *27* (15), 1787-1799.
225. Grimme, S.; Kruse, H.; Goerigk, L.; Erker, G. The Mechanism of Dihydrogen Activation by Frustrated Lewis Pairs Revisited. *Angew Chem Int Edit* **2010,** *49* (8), 1402-1405.
226. Olah, G. A.; Torok, A.; Joschek, J. P.; Bucsi, I.; Esteves, P. M.; Rasul, G.; Prakash, G. K. S. Efficient chemoselective carboxylation of aromatics to arylcarboxylic acids with a superelectrophilically activated carbon Dioxide-Al2Cl6/Al system. *J Am Chem Soc* **2002,** *124* (38), 11379-11391.
227. Ren, J.; Cramer, C. J.; Squires, R. R. Superacidity and Superelectrophilicity of BF3−Carbonyl Complexes. *J Am Chem Soc* **1999,** *121* (11), 2633-2634.
228. Menard, G.; Stephan, D. W. CO2 reduction via aluminum complexes of ammonia boranes. *Dalton Trans.* **2013,** *42* (15), 5447-5453.
229. Mains, G. J.; Nantsis, E. A.; Carper, W. R. Ab Initio Bonding, Molecular Structure, and Quadrupole Coupling Constants of Aluminum Chlorides. *The Journal of Physical Chemistry A* **2001,** *105* (17), 4371-4378.
230. Norris, J. F.; Rubinstein, D. The Formation of Intermediate Compounds in Hydrocarbon Syntheses by the Friedel and Crafts Reaction, and the Preparation of Certain Symmetrical Trialkylbenzenes. *J Am Chem Soc* **1939,** *61* (5), 1163-1170.
231. Aarset, K.; Shen, Q.; Thomassen, H.; Richardson, A. D.; Hedberg, K. Molecular Structure of the Aluminum Halides, Al2Cl6, AlCl3, Al2Br6, AlBr3, and AlI3, Obtained by Gas-Phase Electron-Diffraction and ab Initio Molecular Orbital Calculations. *The Journal of Physical Chemistry A* **1999,** *103* (11), 1644-1652.
232. Besides optimizing the concentration of 7, the stability of 10 should also be considered. For example, for LA = $B(C_6F_5)_3$ and AB = NMe_3BH_3, a side reaction occurs (ref. 228) where a ligand of $B(C_6F_5)_3$ displaces a hydrogen of NMe_3BH_3 to form $NMe_3B(C_6F_5)H_2$, where the reduction of CO_2 to formate was not observed.
233. Saito, S.; Yamamoto, H. Designer Lewis acid catalysts-bulky aluminium reagents for selective organic synthesis. *Chemical Communications* **1997,** (17).
234. Adachi, T.; Sugimoto, H.; Aida, T.; Inoue, S. Aluminum thiolate complexes of porphyrin as excellent initiators for Lewis acid-assisted high-speed living polymerization of methyl methacrylate. *Macromolecules* **1993,** *26* (6), 1238-1243.
235. Appel, A. M.; Bercaw, J. E.; Bocarsly, A. B.; Dobbek, H.; DuBois, D. L.; Dupuis, M.; Ferry, J. G.; Fujita, E.; Hille, R.; Kenis, P. J. A.; Kerfeld, C. A.; Morris, R. H.; Peden, C. H. F.; Portis, A. R.; Ragsdale, S. W.; Rauchfuss, T. B.; Reek, J. N. H.; Seefeldt, L. C.; Thauer, R. K.; Waldrop, G. L. Frontiers, Opportunities, and Challenges in Biochemical and Chemical Catalysis of CO2 Fixation. *Chemical Reviews* **2013,** *113* (8), 6621-6658.
236. Lewis, N. S.; Nocera, D. G. Powering the planet: Chemical challenges in solar energy utilization. *Proceedings of the National Academy of Sciences* **2006,** *103* (43), 15729-15735.
237. Deno, N. C.; Peterson, H. J.; Saines, G. S. The Hydride-Transfer Reaction. *Chemical Reviews* **1960,** *60* (1), 7-14.
238. Moret, S.; Dyson, P. J.; Laurenczy, G. Direct synthesis of formic acid from carbon dioxide by hydrogenation in acidic media. *Nat Commun* **2014,** *5*.

239. Lim, C.-H.; Holder, A. M.; Hynes, J. T.; Musgrave, C. B. Reduction of CO2 to Methanol Catalyzed by a Biomimetic Organo-Hydride Produced from Pyridine. *J Am Chem Soc* **2014,** *136* (45), 16081-16095.
240. Matsubara, Y.; Fujita, E.; Doherty, M. D.; Muckerman, J. T.; Creutz, C. Thermodynamic and Kinetic Hydricity of Ruthenium(II) Hydride Complexes. *J Am Chem Soc* **2012,** *134* (38), 15743-15757.
241. Ohtsu, H.; Tsuge, K.; Tanaka, K. Remarkable accelerating and decelerating effects of the bases on CO2 reduction using a ruthenium NADH model complex. *Journal of Photochemistry and Photobiology A: Chemistry* **2015**.
242. Zhu, X.-Q.; Tan, Y.; Cao, C.-T. Thermodynamic Diagnosis of the Properties and Mechanism of Dihydropyridine-Type Compounds as Hydride Source in Acetonitrile with "Molecule ID Card". *The Journal of Physical Chemistry B* **2010,** *114* (5), 2058-2075.
243. Zhu, X.-Q.; Zhang, M.-T.; Yu, A.; Wang, C.-H.; Cheng, J.-P. Hydride, Hydrogen Atom, Proton, and Electron Transfer Driving Forces of Various Five-Membered Heterocyclic Organic Hydrides and Their Reaction Intermediates in Acetonitrile. *J Am Chem Soc* **2008,** *130* (8), 2501-2516.
244. O'Leary, M. H.; Jaworski, R. J.; Hartman, F. C. 13C nuclear magnetic resonance study of the CO2 activation of ribulosebisphosphate carboxylase from Rhodospirillum rubrum. *Proceedings of the National Academy of Sciences* **1979,** *76* (2), 673-675.
245. Hecht, S. M.; Adams, B. L.; Kozarich, J. W. Chemical transformations of 7,9-disubstituted purines and related heterocycles. Selective reduction of imines and immonium salts. *The Journal of Organic Chemistry* **1976,** *41* (13), 2303-2311.
246. Shih, H.-W.; Vander Wal, M. N.; Grange, R. L.; MacMillan, D. W. C. Enantioselective α-Benzylation of Aldehydes via Photoredox Organocatalysis. *J Am Chem Soc* **2010,** *132* (39), 13600-13603.
247. Hawker, C. J.; Wooley, K. L. The Convergence of Synthetic Organic and Polymer Chemistries. *Science* **2005,** *309* (5738), 1200-1205.
248. Kilambi, H.; Reddy, S. K.; Schneidewind, L.; Stansbury, J. W.; Bowman, C. N. Copolymerization and dark polymerization studies for photopolymerization of novel acrylic monomers. *Polymer* **2007,** *48* (7), 2014-2021.
249. Hoyle, C. E.; Bowman, C. N. Thiol–Ene Click Chemistry. *Angewandte Chemie International Edition* **2010,** *49* (9), 1540-1573.
250. Adzima, B. J.; Tao, Y.; Kloxin, C. J.; DeForest, C. A.; Anseth, K. S.; Bowman, C. N. Spatial and temporal control of the alkyne–azide cycloaddition by photoinitiated Cu(II) reduction. *Nat Chem* **2011,** *3* (3), 256-259.
251. Narayanam, J. M. R.; Stephenson, C. R. J. Visible light photoredox catalysis: applications in organic synthesis. *Chemical Society Reviews* **2011,** *40* (1), 102-113.
252. Xuan, J.; Xiao, W.-J. Visible-Light Photoredox Catalysis. *Angewandte Chemie International Edition* **2012,** *51* (28), 6828-6838.
253. Dai, C.; Narayanam, J. M. R.; Stephenson, C. R. J. Visible-light-mediated conversion of alcohols to halides. *Nat Chem* **2011,** *3* (2), 140-145.

254. Lee, T. Y.; Roper, T. M.; Jönsson, E. S.; Guymon, C. A.; Hoyle, C. E. Influence of Hydrogen Bonding on Photopolymerization Rate of Hydroxyalkyl Acrylates. *Macromolecules* **2004,** *37* (10), 3659-3665.
255. Fors, B. P.; Hawker, C. J. Control of a Living Radical Polymerization of Methacrylates by Light. *Angewandte Chemie International Edition* **2012,** *51* (35), 8850-8853.
256. Wang, J.-S.; Matyjaszewski, K. Controlled/"living" radical polymerization. atom transfer radical polymerization in the presence of transition-metal complexes. *J Am Chem Soc* **1995,** *117* (20), 5614-5615.
257. Yoon, T. P.; Ischay, M. A.; Du, J. Visible light photocatalysis as a greener approach to photochemical synthesis. *Nat Chem* **2010,** *2* (7), 527-532.
258. Allonas, X.; Lalevée, J.; Fouassier, J.-P. Investigation of cleavage processes in photoinitiators: from experiments to molecular modeling. *Journal of Photochemistry and Photobiology A: Chemistry* **2003,** *159* (2), 127-133.
259. Fouassier, J. P. L., J. *Photoinitiators for Polymer Synthesis: Scope, Reactivity, and Efficiency*. 1st ed. ed.; Wiley-VCH: 2012.
260. Eaton, D. F. Nonlinear Optical Materials. *Science* **1991,** *253* (5017), 281-287.
261. Fouassier, J. P.; Morlet-Savary, F. Photopolymers for laser imaging and holographic recording: design and reactivity of photosensitizers. *OPTICE* **1996,** *35* (1), 304-312.
262. Liu, N.; Liu, H.; Zhu, S.; Giessen, H. Stereometamaterials. *Nat Photon* **2009,** *3* (3), 157-162.
263. Scott, T. F.; Kowalski, B. A.; Sullivan, A. C.; Bowman, C. N.; McLeod, R. R. Two-Color Single-Photon Photoinitiation and Photoinhibition for Subdiffraction Photolithography. *Science* **2009,** *324* (5929), 913-917.
264. Catilaz-Simonin, L.; Fouassier, J. P. Investigation of a system capable of photoinitiating radical polymerizations in thick pigmented media. *Journal of Applied Polymer Science* **2001,** *79* (10), 1911-1923.
265. Goodner, M. D.; Bowman, C. N. Development of a comprehensive free radical photopolymerization model incorporating heat and mass transfer effects in thick films. *Chemical Engineering Science* **2002,** *57* (5), 887-900.
266. DeForest, C. A.; Polizzotti, B. D.; Anseth, K. S. Sequential click reactions for synthesizing and patterning three-dimensional cell microenvironments. *Nat Mater* **2009,** *8* (8), 659-664.
267. Fisher, J. P.; Dean, D.; Mikos, A. G. Photocrosslinking characteristics and mechanical properties of diethyl fumarate/poly(propylene fumarate) biomaterials. *Biomaterials* **2002,** *23* (22), 4333-4343.
268. Stansbury, J. W. Curing Dental Resins and Composites by Photopolymerization. *Journal of Esthetic and Restorative Dentistry* **2000,** *12* (6), 300-308.
269. Hasenwinkel, J. M.; Lautenschlager, E. P.; Wixson, R. L.; Gilbert, J. L. A novel high-viscosity, two-solution acrylic bone cement: Effect of chemical composition on properties. *Journal of Biomedical Materials Research* **1999,** *47* (1), 36-45.
270. Nakos, e. a. Dual curing coating method for substrates with shadow areas. U.S. Patent 4,699,802, 1987.

271. Kwon, T.-Y.; Bagheri, R.; Kim, Y. K.; Kim, K.-H.; Burrow, M. F. Cure mechanisms in materials for use in esthetic dentistry. *Journal of Investigative and Clinical Dentistry* **2012,** *3* (1), 3-16.
272. Nason, C.; Roper, T.; Hoyle, C.; Pojman, J. A. UV-Induced Frontal Polymerization of Multifunctional (Meth)acrylates. *Macromolecules* **2005,** *38* (13), 5506-5512.
273. Crivello, J. V. Hybrid free radical/cationic frontal photopolymerizations. *Journal of Polymer Science Part A: Polymer Chemistry* **2007,** *45* (18), 4331-4340.
274. Gregory, S. Ultraviolet curable resin compositions having enhanced shadow cure properties. U.S. Patent 6,245,827, 2001.
275. Gugg, A.; Gorsche, C.; Moszner, N.; Liska, R. Frontal Polymerization: Polymerization Induced Destabilization of Peracrylates. *Macromolecular Rapid Communications* **2011,** *32* (14), 1096-1100.
276. Lalevée, J.; Tehfe, M.-A.; Morlet-Savary, F.; Graff, B.; Dumur, F.; Gigmes, D.; Blanchard, N.; Fouassier, J.-P. Photoredox Catalysis for Polymerization Reactions. *CHIMIA International Journal for Chemistry* **2012,** *66* (6), 439-441.
277. Kim, D.; Scranton, A. The role of diphenyl iodonium salt (DPI) in three-component photoinitiator systems containing methylene blue (MB) and an electron donor. *Journal of Polymer Science Part A: Polymer Chemistry* **2004,** *42* (23), 5863-5871.
278. Padon, K. S.; Scranton, A. B. A mechanistic investigation of a three-component radical photoinitiator system comprising methylene blue, N-methyldiethanolamine, and diphenyliodonium chloride. *Journal of Polymer Science Part A: Polymer Chemistry* **2000,** *38* (11), 2057-2066.
279. Pierre Fouassier, J.; Lalevee, J. Three-component photoinitiating systems: towards innovative tailor made high performance combinations. *RSC Advances* **2012,** *2* (7), 2621-2629.
280. Tehfe, M.-A.; Lalevée, J.; Morlet-Savary, F.; Graff, B.; Blanchard, N.; Fouassier, J.-P. Organic Photocatalyst for Polymerization Reactions: 9,10-Bis[(triisopropylsilyl)ethynyl]anthracene. *ACS Macro Letters* **2012,** *1* (1), 198-203.
281. Zhang, G.; Song, I. Y.; Ahn, K. H.; Park, T.; Choi, W. Free Radical Polymerization Initiated and Controlled by Visible Light Photocatalysis at Ambient Temperature. *Macromolecules* **2011,** *44* (19), 7594-7599.
282. Kim, D.; Stansbury, J. W. A photo-oxidizable kinetic pathway of three-component photoinitiator systems containing porphrin dye (Zn-tpp), an electron donor and diphenyl iodonium salt. *Journal of Polymer Science Part A: Polymer Chemistry* **2009,** *47* (12), 3131-3141.
283. Kim, D.; Stansbury, J. W. Kinetic pathway investigations of three-component photoinitiator systems for visible-light activated free radical polymerizations. *Journal of Polymer Science Part A: Polymer Chemistry* **2009,** *47* (3), 887-898.
284. Kavarnos, G. J. *In Photoinduced Electron Transfer I*. Springer: 1990.
285. Scholes, G. D.; Fleming, G. R.; Olaya-Castro, A.; van Grondelle, R. Lessons from nature about solar light harvesting. *Nat Chem* **2011,** *3* (10), 763-774.
286. Stansbury, J. W.; Dickens, S. H. Determination of double bond conversion in dental resins by near infrared spectroscopy. *Dental Materials* **2001,** *17* (1), 71-79.
287. Galagan, Y.; Hsu, S.-H.; Su, W.-F. Monitoring time and temperature by methylene blue containing polyacrylate film. *Sensors and Actuators B: Chemical* **2010,** *144* (1), 49-55.

288. Mills, A.; Lawrie, K.; McFarlane, M. Blue bottle light: lecture demonstrations of homogeneous and heterogeneous photo-induced electron transfer reactions. *Photochemical & Photobiological Sciences* **2009,** *8* (3), 421-425.
289. Goodspeed, F. C.; Scott, B. L.; Burr, J. G. Photooxidation of Tertiary Nitrogen Compounds by Methylene Blue. *The Journal of Physical Chemistry* **1965,** *69* (4), 1149-1153.
290. Kavarnos, G. J.; Turro, N. J. Photosensitization by reversible electron transfer: theories, experimental evidence, and examples. *Chemical Reviews* **1986,** *86* (2), 401-449.
291. Kim, D.; Scranton, A. B.; Stansbury, J. W. Analysis of association constant for ground-state dye-electron acceptor complex of photoinitiator systems and the association constant effect on the kinetics of visible-light-induced polymerizations. *Journal of Polymer Science Part A: Polymer Chemistry* **2009,** *47* (5), 1429-1439.
292. Sirovatka Padon, K.; Scranton, A. B. The effect of oxygen on the three-component radical photoinitiator system: Methylene blue, N-methyldiethanolamine, and diphenyliodonium chloride. *Journal of Polymer Science Part A: Polymer Chemistry* **2000,** *38* (18), 3336-3346.
293. Asmusen, S.; Arenas, G.; Cook, W. D.; Vallo, C. Photobleaching of camphorquinone during polymerization of dimethacrylate-based resins. *Dental Materials* **2009,** *25* (12), 1603-1611.
294. Eaton, D. F. Dye Sensitized Photopolymerization. In *Advances in Photochemistry*, John Wiley & Sons, Inc.: 2007; pp 427-487.
295. Kim, D.; Scranton, A. B.; Stansbury, J. W. Effect of the electron donor structure on the shelf-lifetime of visible-light activated three-component initiator systems. *Journal of Applied Polymer Science* **2009,** *114* (3), 1535-1542.
296. Dektar, J. L.; Hacker, N. P. Photochemistry of diaryliodonium salts. *The Journal of Organic Chemistry* **1990,** *55* (2), 639-647.
297. Galagan, Y.; Su, W.-F. Reversible photoreduction of methylene blue in acrylate media containing benzyl dimethyl ketal. *Journal of Photochemistry and Photobiology A: Chemistry* **2008,** *195* (2–3), 378-383.
298. Impert, O.; Katafias, A.; Kita, P.; Mills, A.; Pietkiewicz-Graczyk, A.; Wrzeszcz, G. Kinetics and mechanism of a fast leuco-Methylene Blue oxidation by copper(ii)-halide species in acidic aqueous media. *Dalton Trans.* **2003,** (3), 348-353.
299. Hertle, Alexander P.; Blunder, T.; Wunder, T.; Pesaresi, P.; Pribil, M.; Armbruster, U.; Leister, D. PGRL1 Is the Elusive Ferredoxin-Plastoquinone Reductase in Photosynthetic Cyclic Electron Flow. *Molecular Cell* **2013,** *49* (3), 511-523.
300. Munekage, Y.; Hashimoto, M.; Miyake, C.; Tomizawa, K.-I.; Endo, T.; Tasaka, M.; Shikanai, T. Cyclic electron flow around photosystem I is essential for photosynthesis. *Nature* **2004,** *429* (6991), 579-582.
301. Datta, P.; Efimenko, K.; Genzer, J. The effect of confinement on thermal frontal polymerization. *Polymer Chemistry* **2012,** *3* (12), 3243-3246.
302. Mathew, J.; Mahadevan, V. Redox polymerization of 2-hydroxyethyl methacrylate, 2. Kinetics, mechanism and solvent effect using manganese triacetate/cyanoacetic acid as the redox system. *Macromolecular Chemistry and Physics* **1996,** *197* (1), 367-374.
303. Chai, J.-D.; Head-Gordon, M. Long-range corrected hybrid density functionals with damped atom-atom dispersion corrections. *Phys. Chem. Chem. Phys.* **2008,** *10* (44), 6615-6620.

304. Kresse, G.; Furthmuller, J. Efficient iterative schemes for ab initio total-energy calculations using a plane-wave basis set. *Physical Review B* **1996,** *54* (16), 11169-11186.
305. Kresse, G.; Furthmuller, J. Efficiency of ab-initio total energy calculations for metals and semiconductors using a plane-wave basis set. *Computational Materials Science* **1996,** *6* (1), 15-50.
306. Perdew, J. P.; Burke, K.; Ernzerhof, M. Generalized gradient approximation made simple. *Physical Review Letters* **1996,** *77* (18), 3865-3868.
307. Kresse, G.; Joubert, D. From ultrasoft pseudopotentials to the projector augmented-wave method. *Physical Review B* **1999,** *59* (3), 1758-1775.
308. Henkelman, G.; Arnaldsson, A.; Jonsson, H. A fast and robust algorithm for Bader decomposition of charge density. *Computational Materials Science* **2006,** *36* (3), 354-360.
309. Sanville, E.; Kenny, S. D.; Smith, R.; Henkelman, G. Improved grid-based algorithm for Bader charge allocation. *J. Comput. Chem.* **2007,** *28* (5), 899-908.
310. Becke, A. D. DENSITY-FUNCTIONAL EXCHANGE-ENERGY APPROXIMATION WITH CORRECT ASYMPTOTIC-BEHAVIOR. *Physical Review A* **1988,** *38* (6), 3098-3100.
311. Lee, C. T.; Yang, W. T.; Parr, R. G. DEVELOPMENT OF THE COLLE-SALVETTI CORRELATION-ENERGY FORMULA INTO A FUNCTIONAL OF THE ELECTRON-DENSITY. *Physical Review B* **1988,** *37* (2), 785-789.
312. He, H.; Zapol, P.; Curtiss, L. A. A Theoretical Study of CO2 Anions on Anatase (101) Surface. *The Journal of Physical Chemistry C* **2010,** *114* (49), 21474-21481.
313. da Silva, G.; Kennedy, E. M.; Dlugogorski, B. Z. Ab Initio Procedure for Aqueous-Phase pKa Calculation: The Acidity of Nitrous Acid. *The Journal of Physical Chemistry A* **2006,** *110* (39), 11371-11376.
314. Hwang, S. G.; Jang, Y. H.; Chung, D. S. Gas phase proton affinity, basicity, and pK(a) values for nitrogen containing heterocyclic aromatic compounds. *Bulletin of the Korean Chemical Society* **2005,** *26* (4), 585-588.
315. Jang, Y. H.; Goddard, W. A.; Noyes, K. T.; Sowers, L. C.; Hwang, S.; Chung, D. S. pKa Values of Guanine in Water: Density Functional Theory Calculations Combined with Poisson−Boltzmann Continuum−Solvation Model. *The Journal of Physical Chemistry B* **2002,** *107* (1), 344-357.
316. Zhang, S. A reliable and efficient first principles-based method for predicting pKa values. III. Adding explicit water molecules: Can the theoretical slope be reproduced and pKa values predicted more accurately? *J. Comput. Chem.* **2012,** *33* (5), 517-526.
317. Shapley, W. A.; Bacskay, G. B.; Warr, G. G. Ab initio quantum chemical studies of the pK(a)'s of hydroxybenzoic acids in aqueous solution with special reference to the hydrophobicity of hydroxybenzoates and their binding to surfactants. *J. Phys. Chem. B* **1998,** *102* (11), 1938-1944.
318. Kallies, B.; Mitzner, R. pK(a) values of amines in water from quantum mechanical calculations using a polarized dielectric continuum representation of the solvent. *J. Phys. Chem. B* **1997,** *101* (15), 2959-2967.
319. Sastre, S.; Casasnovas, R.; Muñoz, F.; Frau, J. Isodesmic reaction for pK a calculations of common organic molecules. *Theoretical Chemistry Accounts* **2012,** *132* (2), 1-8.

320. Klots, C. E.; Compton, R. N. Electron attachment to carbon dioxide clusters in a supersonic beam. *The Journal of Chemical Physics* **1977,** *67* (4), 1779-1780.
321. ZIEMCZONEK, L.; WROBLEWSKI, T.; KARWASZ, G. P. Ab initio study of formic acid monomer, dimer and trimer. *Optica Applicata* **2006,** *36* (4), 587-591.
322. Roberts, G. M.; Pierce, P. J.; Woo, L. K. Palladium Complexes with N-Heterocyclic Carbene Ligands As Catalysts for the Alkoxycarbonylation of Olefins. *Organometallics* **2013,** *32* (6), 2033-2036.

Appendix

A. Supporting information – Mechanism of Homogeneous Reduction of CO_2 by Pyridine: Proton Relay in Aqueous Solvent and Aromatic Stabilization

A.1 Solvated PyH^+ Adsorption on the Pt (111) Surface

Simulations of PyH^+ (aq) adsorbed on the (111) face of Pt modeled using a 180-atom Pt surface model, 102 water molecules and a Cl^- counterion were performed using plane wave periodic boundary condition DFT as implemented in the Vienna Ab initio Simulation Program (VASP).[304-305] We employed the Perdew–Burke–Ernzerhof (PBE) generalized gradient approximation (GGA) exchange and correlation functional[306] along with projector augmented wave (PAW) pseudopotentials.[307] PAW's were used to describe the hydrogen 1s; nitrogen and carbon 2s and 2p; chlorine 3s and 3p; and platinum 6s and 5d electrons explicitly. Optimization of the Pt unit cell was performed with a 4 × 4 × 4 Monkhorst-Pack k-point mesh expansion. All calculations were spin polarized and utilized a 500 eV cut off energy, and all supercell calculations were conducted at the Γ-point; as extensive Brillouin zone folding for large supercells enables the Γ-point to span a larger fraction of k-space without the added computational expense of a k-point expansion. For the supercell calculations we used a 180-atom Pt (111) surface model of 5 layers thick with the bottom 3 layers of Pt atoms frozen. To model the solvation effects of PyH^+ adsorption 102 waters and 8 Å of vacuum space were placed in the 28 Å gap between the front and backsides of the Pt slab as illustrated in Figure S1a. Molecular dynamics simulations were performed to anneal the water structure to a bulk-like density for simulation of the aqueous layer. Bader charge analysis was conducted using software from the Henkelman group.[308-309]

The adsorption energy (no ZPE correction) of water solvated PyH^+ on the Pt (111) surface is found to be 1.0 eV per molecule. The strong interaction of PyH^+ with the Pt surface is indicated by the adsorbed PyH^+ projected density of states (PDOS) which show a significant broadening and population of the adsorbate states as a result of mixing with the surface states (see Figure S1b). The strong absorption energy of aromatic heterocyclic PyH^+ is consistent with the reported strong absorption energies on metal surfaces of other aromatics; such as benzene, which ranges from 1.21-2.88 eV on Pt, Pd, Rh, and Ir.[49] Bader charge analysis predicts 0.56 e^- transferred to PyH^+ from the Pt surface. On the Pt surface, N gains 0.19 e^- while the remaining heterocyclic ring gains 0.37 e^-, suggesting significant charge is donated into the PyH^+ π-space when adsorbed on the surface, which further suggests the reduction potential of PyH^+ on the Pt surface will be decreased (less negative) relative to its homogeneous phase value. The energy offset due to the decreased reduction potential on the surface must be accounted for by thermal activation or an applied overpotential to facilitate PyH^0 desorption into the homogenous phase.

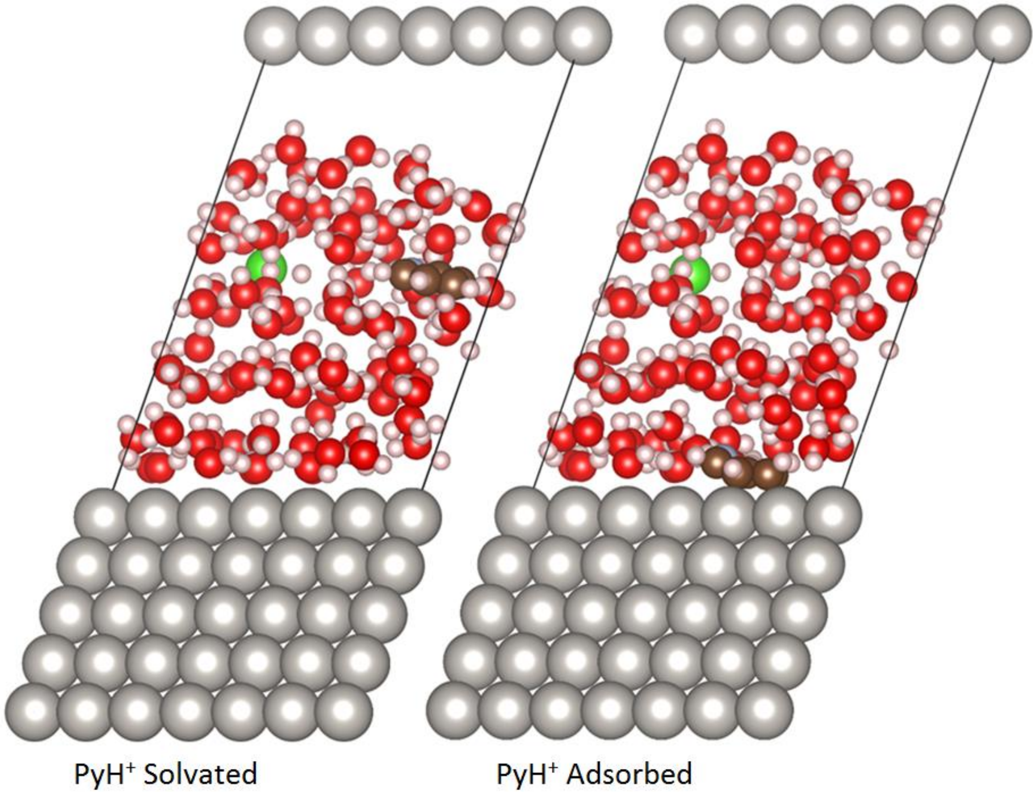

Figure S1a: Solvated PyH^+ adsorption on (111) Pt surface simulated using an 180 atom Pt surface with 102 solvating waters and a charge balancing Cl^- counterion (additional boundary atoms shown for clarity).

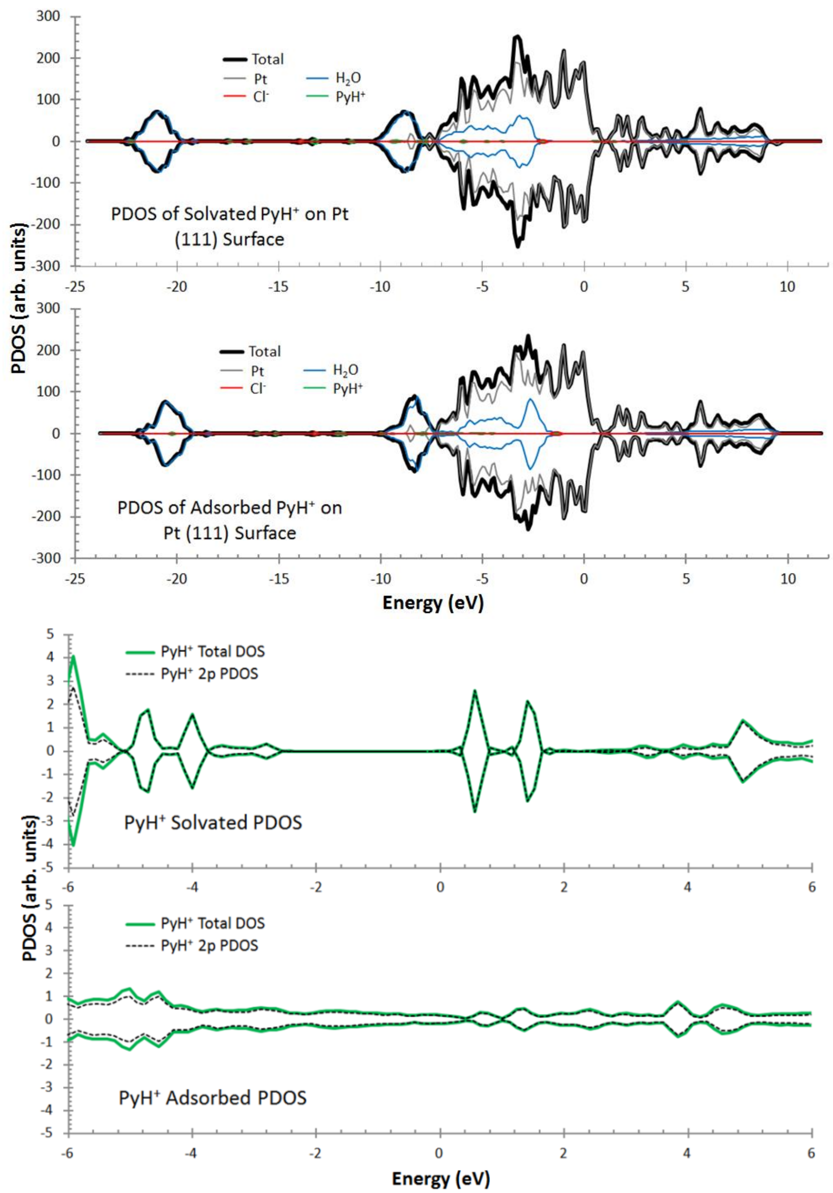

Figure S1b: Projected density of states (PDOS) of solvated PyH^+ adsorption on (111) Pt surface decomposed by molecular species (top) and an enlarged view of the PDOS of PyH^+ near the Fermi energy (bottom).

A.2 Calculation of K_{eq} for the Zwitterionic Py•CO_2 Complex

Tossell determined that at least one explicit water must be used in order to describe the formation of the zwitterionic Py•CO_2 complex by the reaction Py + CO_2 + H_2O = Py•CO_2 + H_2O (**eq. 1**), depicted in Figure S2 as the product.[44] We determined that $\Delta H^0 = -0.2$ kcal/mol for **eq. 1** at the CBS-QB3/CPCM-H_2O level of theory.[77] Meanwhile, $T\Delta S^0 = -8.4$ kcal/mol for **eq. 1**, but was calculated in the absence of the explicit water using B3LYP/6-31+G**/CPCM-H_2O.[310-311] Including $T\Delta S^0$ from this one water molecule is not physically accurate because in aqueous solvent many water molecules are available to participate in Py•CO_2 formation at only a minor entropic penalty. ΔG^0(Py•CO_2 formation) = $\Delta H^0 - T\Delta S^0$ = 8.2kcal/mol. K_{eq}= $\exp(-\Delta G^0/RT)$ = ~1E-06

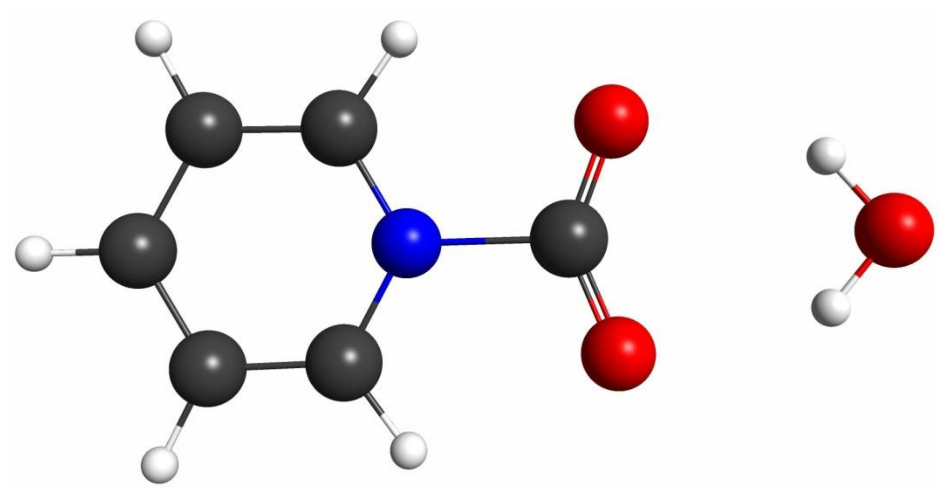

Figure S2: The Py•CO_2 zwitterionic complex in the presence of one explicit water.

A.3 Determination of Multi-reference Character in the Reduction of CO_2 by PyH^0

Single-point CASSCF (15,14) calculations[62] at roMP2[58]/6-31+G**/CPCM-H_2O geometries for the reactant, TS and product of the PyH^0+CO_2+1H_2O reaction were used to determine the extent of multi-reference character in these structures. Calculations were performed using the GAMESS computational chemistry software package.[59-60] All chemical bonds that form and break along the reaction coordinate are included in the active space of the CASSCF calculation; in particular we included 15 electrons and 14 orbitals chosen to be consistent along the reaction pathway in our calculations to fully describe the system. CI (configuration interaction) coefficients from the CASSCF output were analyzed to determine the weight of the ground state electronic configuration contribution to the CASSCF wave function. As a general rule, a ground state CI coefficient >0.9 indicates a system with insignificant multi-reference character such that a single Slater determinant wave function is sufficient to describe the system correctly and accurately. The reactant, TS and product structures of the PyH^0+CO_2+1H_2O reaction have CI coefficients of >0.9 for the ground state wave function. Thus, the high level couple-cluster CCSD(T) single reference method is a reliable benchmark for this system. Up to ten of the largest CI coefficients from the CASSCF calculations are included below for reference with the ground state electronic configuration coefficient indicated by bold red text.

PyH^0+CO_2+1H_2O (reactant)

ALPHA	BETA	COEFFICIENT
11111111000000	11111110000000	**0.9256435**
11111101100000	11111100100000	0.1227180
11111110100000	11111101000000	-0.1098035
11101111001000	11101110001000	0.1079563
11111110010000	11111011000000	-0.1057333
10111111000100	10111110000100	0.0898409
11111110010000	11111100100000	0.0691305
11111111000000	11111100100000	-0.0614998
11111111000000	11111001100000	-0.0574147
11111111000000	11111010010000	-0.0568963

$PyH^0+CO_2+1H_2O$ (TS)

ALPHA	BETA	COEFFICIENT
11111111000000	11111110000000	**0.9138129**
11111110100000	11111101000000	0.1493099
11111101100000	11111100100000	0.1297380
11111110010000	11111011000000	0.1116958
11111101100000	11111110000000	0.0766102
11111111000000	11111100100000	0.0726996
11111111000000	11111011000000	0.0634205
11111011100000	11111100010000	0.0616641
11111011010000	11111110000000	0.0594992
11111101010000	11111010100000	0.0585255

$PyH^0+CO_2+1H_2O$ (Product)

ALPHA	BETA	COEFFICIENT
11111111000000	11111110000000	**0.9170002**
11111110100000	11111101000000	0.1391589
11111101100000	11111100100000	0.1281615
11111110010000	11111011000000	-0.1060477
11111111000000	11111011000000	-0.0768217
11111101100000	11111110000000	0.0744552
11111111000000	11111100100000	0.0647038
11111011010000	11111110000000	-0.0603841
11111110010000	11111100100000	-0.0585207

01111111000100 | 01111110000100 | 0.0581762

A.4 Further Discussion on the use of CPCM to Treat Solvation

a. Derivation of enthalpic barrier in aqueous solutions

The free energy in solution is defined by[74]:

$$G_{soln} = E_{soln} + G_{nes} + G_{gas} - E_{gas} \quad (1)$$

where G_{soln} is the free energy of solute in solution, E_{soln} is the solvated electronic energy described by the implicit solvent model, such as CPCM, G_{nes} is the non-electrostatic contribute to solvation free energy, G_{gas} is the free energy of the solute calculated in vacuum, and E_{gas} is the electronic energy calculated in vacuum. Eq. (1) can be further simplified to eq. (2) using $G_{gas} = E_{gas} + PV_{gas} - TS_{gas}$.

$$G_{soln} = E_{soln} + G_{nes} + PV_{gas} - TS_{gas} \quad (2)$$

Next, the activation free energy for $PyCOOH^0$ product formation can be defined as:

$$\Delta G_{ac,soln} = (E_{soln}^{TS} - E_{soln}^{R}) + (G_{nes}^{TS} - G_{nes}^{R}) - (TS_{gas}^{TS} - TS_{gas}^{R}) \quad (3)$$

Where the PV_{gas} term cancels out, the superscript "TS" denotes the solute at Transition State and "R" denotes the reactants. We will show in part (b) below that, ignoring the non-electrostatic term results in an insignificant ~1.5kcal/mol of error in $\Delta G_{ac,soln}$. Thus, eq.3 is simplifies to eq. 4.

$$\Delta G_{ac,soln} = (E_{soln}^{TS} - E_{soln}^{R}) - (TS_{gas}^{TS} - TS_{gas}^{R}) \quad (4)$$

Note that $\Delta G_{ac,soln}$ can also be expressed by:

$$\Delta G_{ac,soln} = \Delta H_{ac,soln} - T\Delta S_{ac,soln} \quad (5)$$

Thus by comparing eq. 4 to eq. 5, $(E_{soln}^{TS} - E_{soln}^{R}) \approx \Delta H_{ac,soln}$ (the enthalpic barrier reported in Table 1) because strictly speaking, the second term on the right of eq. (4) is the entropic contribution calculated in gas phase rather than in solution phase as expressed in eq. (5). The E_{soln} and G_{nes} both contain parameters to account for this difference.

b. Cancellation of non-electrostatic term G_{nes} between the TS and reactant

We used the SMD[69] model at roMP2/6-31+G**level of theory on PyH^0+CO_2+3H_2O to estimate contributions of the non-electrostatic term to solvation. We find that $\Delta G_{nes} = G_{nes}^{TS} - G_{nes}^{R} = 9.72\,\frac{kcal}{mol} - 8.23\,\frac{kcal}{mol} = 1.5\,\frac{kcal}{mol}$

c. Comparing gas phase to implicit solvent CPCM

Table S1: Comparing gas phase to implicit CPCM calculations for PyH^0•CO_2+mH_2O + nH_2O(S) to form $PyCOOH^0$ where m is the number of active H_2Os in the proton relay and n is the number of solvating H_2Os.

System[(a)]	*Gas phase*		*CPCM*	
	ΔH^0_{act}	ΔH^0_{rxn}	ΔH^0_{act}	ΔH^0_{rxn}
PyH^0 + CO_2 + 3H_2O	*22.1*	*-3.7*	*18.5*	*-3.2*
PyH^0 + CO_2 + 3H_2O + 4H_2O(S)	*12.5*	*-8.2*	*14.6*	*-4.0*

[a]Enthalpies in unit kcal/mol and calculations were performed at roMP2/6-31+G**

In PyH^0 + CO_2 + 3H_2O, the gas phase ΔH^0_{act} is higher than the CPCM where CPCM stabilizes the more polar TS relative to the reactant. In contrast, in the case of PyH^0 + CO_2 + 3H_2O + 4H_2O(S), the gas phase calculation (reaction core plus explicit solvent, but not embedded in implicit solvent) predicts a lower barrier, which shows that without CPCM to interact with the first explicit solvation shell, the explicit solvent can over-stabilize the TS relative to the reactant resulting in a lower ΔH^0_{act}.

A.5 Effect of Explicit Solvent

a. ΔH^0_{act} of PyH^0+CO_2+$3H_2O$+$6H_2O(S)$ in two different explicit solvent configurations

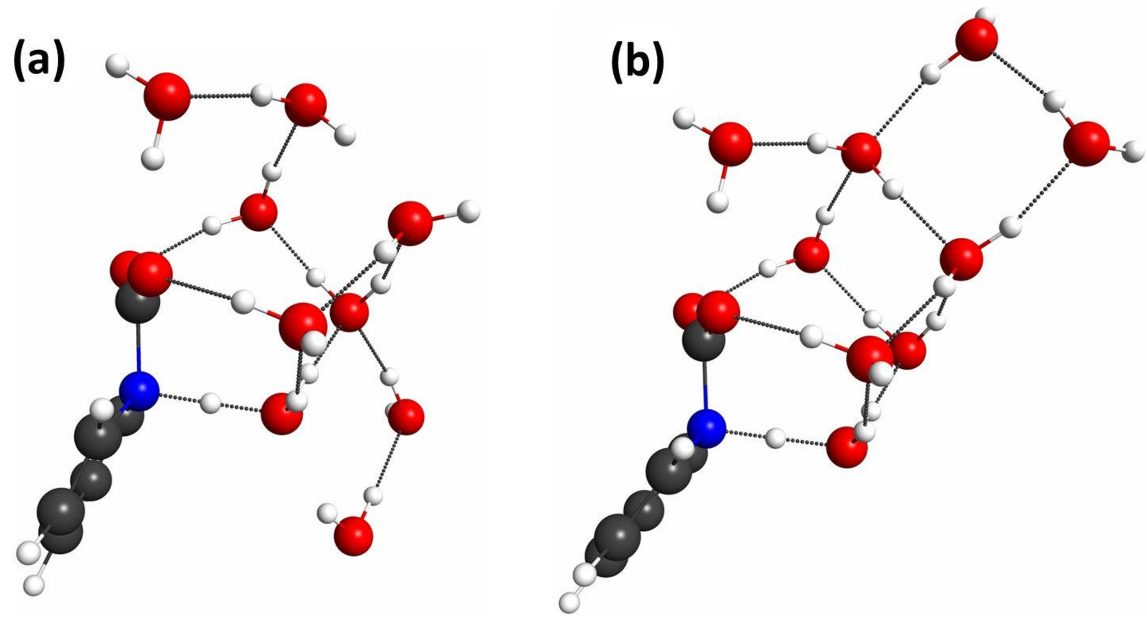

Figure S3: TS structures resulting from two different explicit solvent configurations for PyH^0+CO_2+$3H_2O$ + $6H_2O(S)$. (a) ΔH^0_{act}=15.3 kcal/mol. (b) ΔH^0_{act}=14.5 kcal/mol

b. Product for PyH^0+CO_2+$2H_2O$ + $5H_2O(S)$

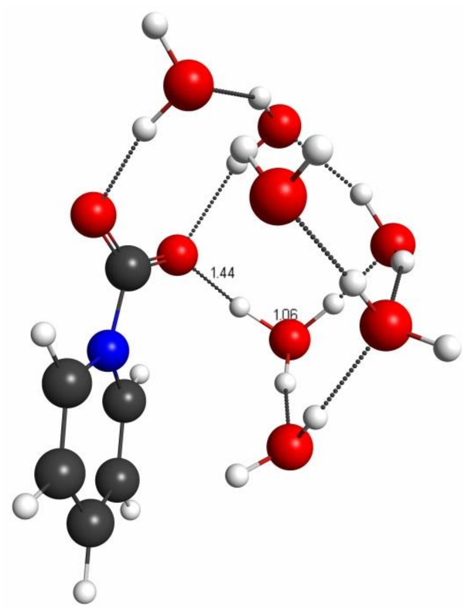

Figure S4: The cis $PyCOOH^0$ product with partial proton transfer with O-H bond of 1.44 Å. A different explicit solvent configuration will result in complete proton transfer to form the cis $PyCOOH^0$ product.

c. Estimation of enthalpic barrier for PyH^0+CO_2+1H_2O + 6H_2O(S)

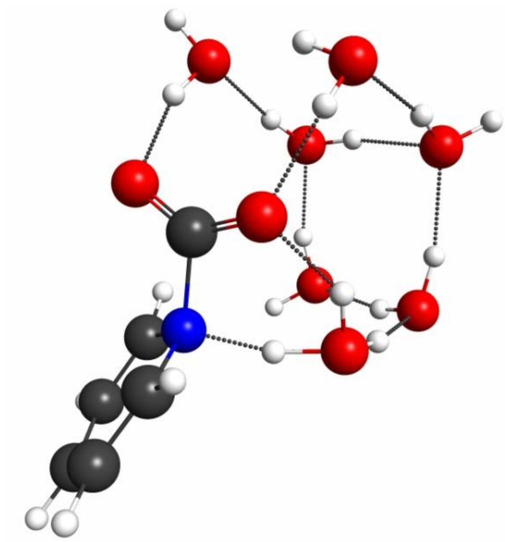

Figure S5: An estimated TS structure for PyH^0 + CO_2 + 1H_2O + 6H_2O(S). Six explicit solvating waters are allowed to relax around the frozen PyH^0+CO_2+1H_2O TS structure at the roMP2/6-31+G** level of theory. The energy of this guessed TS structure is then compared to the IRC reactant of PyH^0 + CO_2 + 3H_2O + 4H_2O(S), where the enthalpic barrier is obtained after adding the ZPE and thermal corrections from the PyH^0 + CO_2 + 3H_2O + 4H_2O(S) case. The estimated enthalpic barrier for PyH^0 + CO_2 + 1H_2O + 6H_2O(S) is 22.8 kcal/mol. We attempted to locate the TS for PyH^0 + CO_2 + 1H_2O + 6H_2O(S), but the calculations converged to the lower energy TS of PyH^0 + CO_2 + 3H_2O + 4H_2O(S), thus we resort to this estimation.

d. Convergence of barrier for $PyH^0 + CO_2 + 3H_2O + nH_2O(S)$

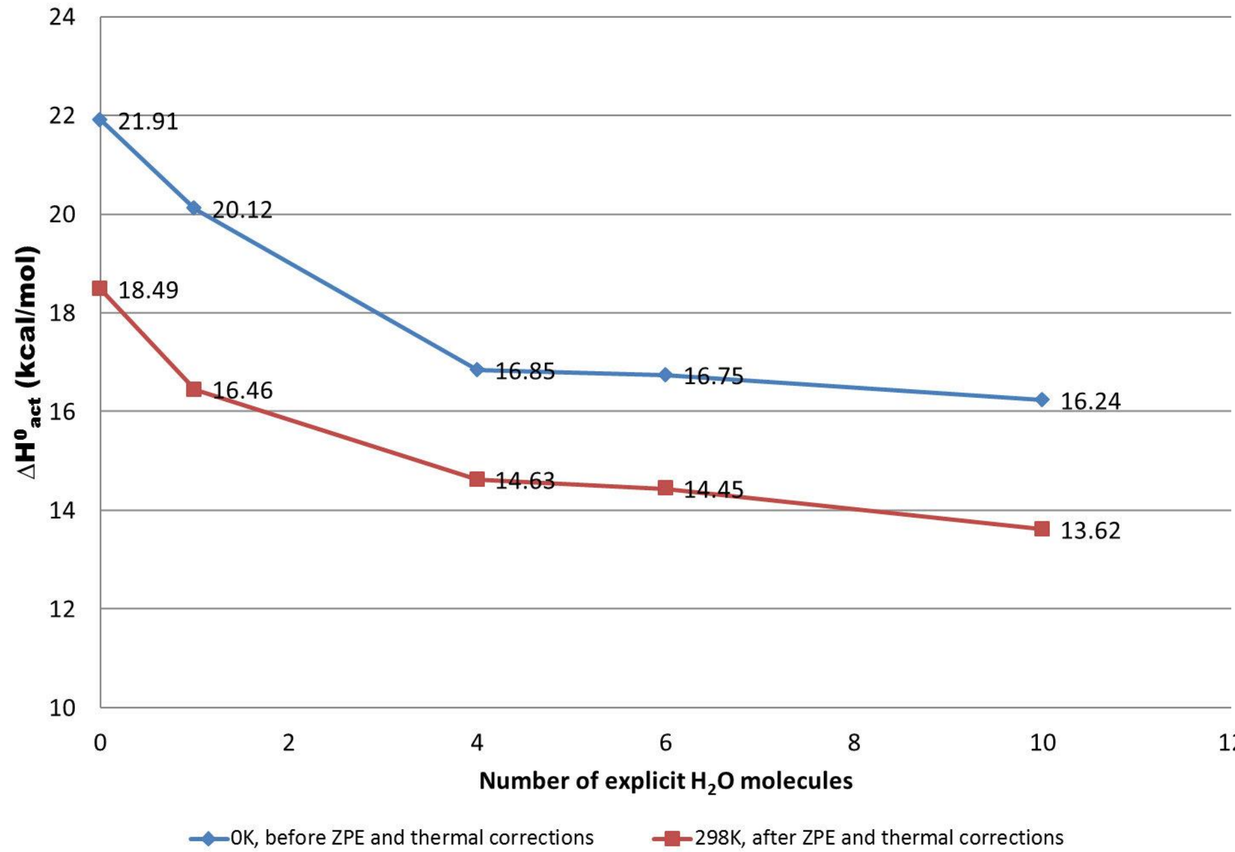

Figure S6: Convergence of barrier calculated at roMP2/6-31+G**/CPCM-H_2O for $PyH^0 + CO_2 + 3 H_2O + nH_2O$ (S) is examined, where n is number of explicit H2O molecules. Both the 0K (before ZPE and thermal corrections) and 298K (after ZPE and thermal corrections) are shown for comparison. In both cases at the limit of 4, 6 and 10H2O(s), the barriers converge to approximately 16.5±0.3 kcal/mol and 14.1±0.5 kcal/mol, which is well within the accuracy of roMP2 method.

A.6 Standard Reduction Potential and pKa Calculations

Standard reduction potentials, E^0 were calculated following the same procedure used by Winget *et al*. and Tossell.[44, 78] A value of -100.5 kcal/mol was assumed for the reduction free energy of the standard hydrogen electrode (SHE) as described in Ref. [312]. Thus, $E^0 = (-100.5 - \Delta G_{red})/23.05$ (vs. SHE), where ΔG_{red} is defined as the Gibbs free energy of reduction of A ($A + e^- = A^-$ **eq. 1**), which was calculated at the CBS-QB3 level of theory[77] in CPCM-H_2O solvent. To reference to the Saturated Calomel Electrode (SCE), E^0 (vs. SHE) is converted to E^0 (vs. SCE) using E^0 (vs. SCE) = E^0 (vs. SHE) - 0.24 V.

Various approaches have been used to calculate pKa's.[313-316] We employed the method described by Liptak *et al*. (with slight modification) where the detailed instructions can be found in SI ref. [[79]]. Here we summarize key equations and procedures to obtain pKa's in aqueous solution. pKa is defined as $pKa=\Delta G^0_{aq}/2.303RT$, where ΔG^0_{aq} is defined as the change in Gibbs free energy of the reaction $AH_{aq} = A^-_{aq} + H^+_{aq}$ (**eq. 2**) in aqueous solution at standard conditions and 1M AH. ΔG^0_{aq} can be calculated using a thermodynamic cycle with $\Delta G^0_{aq} = \Delta G^0_{gas} + \Delta G^0_s(A^-) - \Delta G^0_s(AH) + \Delta G^0_s(H^+)$. ΔG^0_{gas} is the change in Gibbs free energy for **eq. 2** in gas phase and was calculated at the CBS-QB3 level of theory. For ΔG^0_{gas} calculations, an experimental value of -6.28 kcal/mol was used for $G^0_{gas}(H^+)$ at a reference pressure of 1 atm. ΔG^0_s uses a reference state of 1M. Conversions can be calculated using ΔG^0_{gas} (1M) = ΔG^0_{gas} (1atm.) + RTln(24.46). ΔG^0_s (A^-) and ΔG^0_s (AH) are changes in Gibbs free energy for solvating A^- and AH from the gas phase, i.e. $\Delta G^0_s (A^-) = G^0_s (A^-) - G^0_{gas}(A^-)$. Instead of using Hartree-Fock (HF)/CPCM-H_2O to approximate solvation free energies as done by Liptak *et al*., we used B3LYP/6-31+G**/CPCM-H_2O. For example, $\Delta G^0_s (A^-)$ was approximated by $E(A^-, 0K)_{B3LYP/CPCM-H2O} - E(A^-, 0K)_{B3LYP/gas-phase}$. Finally, an experimental value of -259.5 kcal/mol was used for $\Delta G^0_s(H^+)$,[317-318] which reproduces the experimental pKa of PyH^+/Py of 5.3 ($pKa_{calc.}$=4.4), instead of -264.61 kcal/mol which was used by Liptak *et al*. to calculate the pKa for carboxylic acids.[79]

A.7 Contribution of Strain Energies to the Activation Barrier of $PyH^0 + CO_2$

To estimate the strain energy due to the C-O-H angular strain in $PyH^0 + CO_2$, we used $COOH^0$ as the model species. As shown in Figure 8 of the manuscript, -0.60 e charge was transferred to CO_2 while an O-H bond was partially formed at the TS (Figure 1b), thus $COOH^0$ should be an appropriate model to estimate C-O-H angular strain. As shown in Figure 6a, the strain energy was estimated to be ΔE(0K)=~15 kcal/mol (not including ZPE) to bend C-O-H from 109° (relaxed) to 79° calculated using roMP2/6-31+G**/CPCM-H_2O. On the other hand, $PyCOO^-$ species was used as a model to estimate the strain due to dihedral rotation between the Py and CO_2 planes. To rotate the dihedral of $PyCOO^-$ from its equilibrium structure to the angle of the TS (68°), an energy of ΔE(0K)=~10 kcal/mol (not including ZPE) is required.

A.8 Mulliken Population Analysis and CHELPG Charge Analysis

In Figure S7 below, net charges on PyH^0 and CO_2 determined using the CHELPG[76] and Mulliken[75] methods are plotted against the reaction coordinate $R_{N\text{-}C}$ for $PyH^0 + CO_2 + 3H_2O$. The plot shows that these two methods agree with each other qualitatively, and that the magnitude of charges along the reaction coordinate predicted using the more reliable potential derived CHELPG method are larger than those predicted by a Mulliken population analysis.

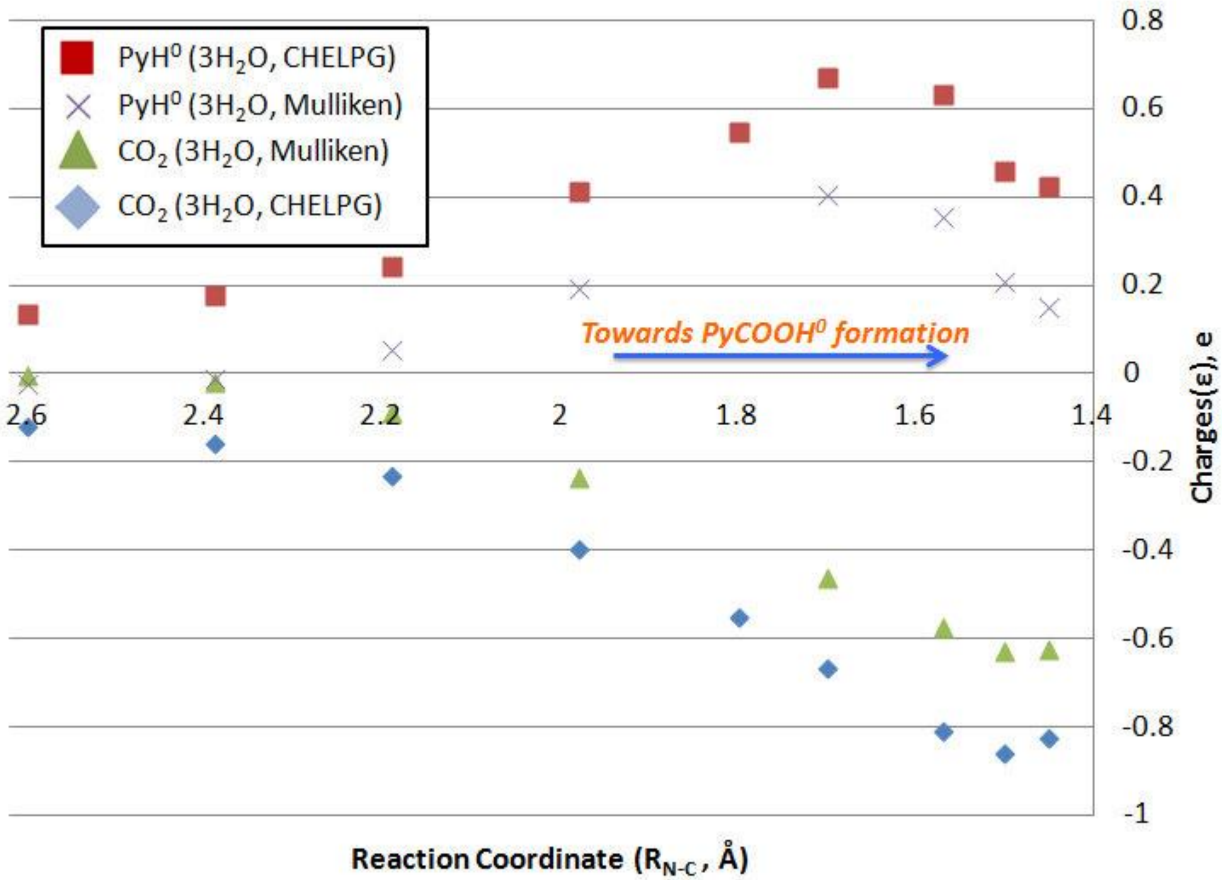

Figure S7: Net charges on PyH^0 and CO_2 using the CHELPG and Mulliken population charge analysis methods along the reaction coordinate $R_{N\text{-}C}$ for the reaction $PyH^0 + CO_2 + 3H_2O$.

A.9 Coordinates of Molecular Structures

All coordinates are reported as XYZ Cartesian coordinates. 0 K energies (not ZPE and thermally corrected) reported are calculated at roMP2/6-31+G**/CPCM-H_2O in unit Hartrees.

a) PyH^0+ CO_2

Reactant (-436.21021094)

C	2.03255	0.02140	0.89458
C	1.51679	1.18694	0.28969
C	0.69577	1.11731	-0.81711
N	0.27383	-0.13579	-1.28245
C	0.92178	-1.29042	-0.82734
C	1.74106	-1.21689	0.27767
H	2.68149	0.07841	1.75728
H	1.77825	2.16902	0.66470
H	0.27768	1.97902	-1.31552
H	-0.15762	-0.17223	-2.19663
H	0.67228	-2.21075	-1.33373
H	2.18286	-2.13609	0.64240
C	-2.08401	0.20194	0.52193
O	-1.52966	-0.40193	1.36996
O	-2.65903	0.80801	-0.31317

TS (-436.13149226)

C	2.52590	-0.00004	0.22235
C	1.82726	1.20204	0.05754
C	0.48235	1.21244	-0.25698
N	-0.23424	0.00031	-0.46296
C	0.48241	-1.21201	-0.25845
C	1.82733	-1.20193	0.05603
H	3.57785	-0.00016	0.47023
H	2.32318	2.15725	0.17441
H	-0.09216	2.11630	-0.40583
H	-1.18544	0.00081	-1.36623
H	-0.09207	-2.11570	-0.40837
H	2.32330	-2.15728	0.17162
C	-1.70846	-0.00017	0.19211
O	-1.93462	-0.00092	1.37923
O	-2.38495	0.00045	-0.91062

Product 1(cis $PyCOOH^0$) (-436.19668471)

C	2.57803	0.01018	-0.19735
C	1.89397	1.07063	0.43581
C	0.53045	1.05038	0.60238
N	-0.22263	-0.02505	0.09190
C	0.45409	-1.14909	-0.41810
C	1.83117	-1.10861	-0.57216
H	3.64999	0.03691	-0.33028

H	2.42966	1.92896	0.81985
H	-0.04303	1.83189	1.07311
H	-1.70427	-1.23583	-1.33177
H	-0.11878	-2.05123	-0.56657
H	2.31060	-1.99324	-0.97167
C	-1.60784	0.09935	0.07378
O	-2.21522	0.96224	0.70140
O	-2.27867	-0.81613	-0.66983

Product 2(trans $PyCOOH^0$)(-436.20606329)

C	2.57065	-0.04547	-0.08790
C	1.89677	1.05019	0.47405
C	0.52007	1.09896	0.53775
N	-0.24384	0.03182	0.02935
C	0.41341	-1.07788	-0.53586
C	1.79252	-1.10099	-0.58722
H	3.64984	-0.07418	-0.13544
H	2.44164	1.89368	0.87805
H	-0.04566	1.91456	0.95625
H	-3.18662	-0.81203	-0.34236
H	-0.21569	-1.86703	-0.90909
H	2.25560	-1.97275	-1.03151
C	-1.62067	0.13000	0.09652
O	-2.22037	1.09932	0.56659
O	-2.22904	-0.96801	-0.41572

b) PyH^0+ CO_2+ H_2O

Reactant (-512.46090998)

C	2.57129	0.61251	-0.43121
C	1.83770	-0.24358	-1.28121
C	0.74091	-0.94246	-0.81913
N	0.28019	-0.72196	0.48229
C	1.08671	-0.02932	1.38708
C	2.18101	0.67017	0.92900
H	3.43995	1.14791	-0.78824
H	2.14137	-0.39819	-2.30968
H	0.14838	-1.60714	-1.43097
H	-0.46301	-1.31932	0.83773
H	0.75136	-0.01675	2.41401
H	2.75918	1.23731	1.64837
C	-1.66576	1.19920	-0.63902
O	-0.90760	2.09566	-0.52877
O	-2.44255	0.31687	-0.75767
O	-2.09062	-2.22258	1.30859
H	-2.83799	-1.97696	0.74558
H	-2.14198	-3.18555	1.38117

TS (-512.40875407)

C	2.72923	-0.20147	-0.10781
C	1.89972	-0.69947	-1.11048
C	0.51998	-0.56912	-1.03736
N	-0.10111	-0.01643	0.13120
C	0.76753	0.66099	1.03662
C	2.13016	0.51469	0.95196
H	3.80372	-0.30188	-0.17045
H	2.30988	-1.18056	-1.98959
H	-0.16318	-0.93276	-1.79113
H	-0.72004	-1.17809	0.71663
H	0.27365	1.23057	1.80864
H	2.73654	0.99246	1.71113
C	-1.39556	0.76710	-0.23378
O	-1.31634	1.99601	-0.15353
O	-2.34214	-0.01034	-0.55885
O	-1.53740	-1.90972	0.89528
H	-2.17402	-1.43493	0.26519
H	-1.32668	-2.79380	0.54737

Product (-512.45169649)

C	2.72468	-0.39337	0.05446
C	1.78965	-1.07989	-0.73313
C	0.47361	-0.66819	-0.82091
N	0.03627	0.44552	-0.07932
C	0.98995	1.21874	0.60946
C	2.29396	0.78023	0.69761
H	3.74902	-0.72961	0.12790
H	2.07883	-1.94148	-1.32181
H	-0.24437	-1.12097	-1.48484
H	-0.87173	-2.88961	0.42741
H	0.61060	2.10941	1.08171
H	2.98411	1.38758	1.26941
C	-1.28891	0.88194	-0.09391
O	-1.61156	2.02506	0.22965
O	-2.19523	-0.02125	-0.52087
O	-1.70408	-2.41788	0.57433
H	-1.96108	-0.94080	-0.22947
H	-2.38955	-3.10109	0.52999

c) PyH^0+ CO_2+ $2H_2O$

Reactant (-588.71285063)

C	2.93560	-0.08644	-0.73215
C	2.73667	-0.51223	0.60166
C	1.58852	-0.18667	1.29153
N	0.54633	0.47200	0.63140
C	0.81019	1.08637	-0.59873

C	1.95575	0.76004	-1.29524
H	3.83716	-0.33823	-1.27296
H	3.50082	-1.07587	1.12314
H	1.39542	-0.49348	2.30914
H	-0.20412	0.87210	1.19451
H	0.03400	1.72921	-0.98790
H	2.10063	1.20322	-2.27314
C	-0.85946	-1.70915	-0.87821
O	-0.05758	-2.47274	-0.47688
O	-1.67766	-0.96726	-1.30057
O	-3.44208	1.30285	-0.24018
H	-3.09708	0.52119	-0.69576
H	-4.39174	1.13948	-0.15389
O	-1.71410	1.81791	1.90950
H	-2.07250	1.55274	2.76693
H	-2.43200	1.66161	1.26401

TS (-588.67401253)

C	2.92741	0.77227	-0.14546
C	2.59372	-0.18576	0.81706
C	1.33164	-0.74988	0.87077
N	0.27646	-0.24283	0.04520
C	0.69348	0.56076	-1.07076
C	1.96204	1.09479	-1.11467
H	3.91946	1.20003	-0.18446
H	3.33136	-0.54562	1.52331
H	1.03563	-1.51275	1.57220
H	-0.41244	0.61369	0.78707
H	-0.08290	0.76929	-1.78927
H	2.20247	1.74396	-1.94711
C	-0.85885	-1.26479	-0.30990
O	-0.76027	-2.36213	0.25446
O	-1.71203	-0.75714	-1.07590
O	-3.21114	1.31272	-0.03392
H	-2.92878	0.51980	-0.53729
H	-4.05703	1.08685	0.37968
O	-1.04318	1.44468	1.33921
H	-1.13577	1.28776	2.29366
H	-1.97286	1.47411	0.92302

Product (-588.70737271)

C	2.33463	1.01470	0.16794
C	2.23253	-0.18944	0.88863
C	1.21935	-1.09399	0.64727
N	0.20325	-0.77001	-0.27058
C	0.37773	0.34638	-1.10933
C	1.41312	1.22593	-0.87476

H	3.14241	1.70911	0.35120
H	2.96490	-0.44997	1.64211
H	1.09248	-2.02607	1.17306
H	0.37174	1.80097	1.48421
H	-0.32261	0.45633	-1.92087
H	1.50268	2.07774	-1.53693
C	-0.86403	-1.66299	-0.42905
O	-0.80476	-2.82577	-0.03252
O	-1.94102	-1.16520	-1.05865
O	-2.41440	1.30541	-0.29036
H	-2.08576	-0.19868	-0.82747
H	-3.29491	1.37136	0.10662
O	-0.54751	2.06991	1.63874
H	-0.72174	1.86997	2.56923
H	-1.78492	1.59155	0.40723

d) PyH^0+ CO_2+ $3H_2O$

Reactant (-664.96489049)

C	-3.53086	-0.55935	0.32508
C	-3.03189	-0.40449	-0.99008
C	-1.84326	0.25015	-1.22799
N	-1.05053	0.67021	-0.15627
C	-1.60006	0.68329	1.13074
C	-2.78894	0.02452	1.37425
H	-4.46722	-1.06565	0.51424
H	-3.59607	-0.76153	-1.84319
H	-1.42556	0.39445	-2.21409
H	-0.28039	1.30813	-0.35991
H	-1.00320	1.14981	1.90104
H	-3.15956	0.00665	2.39232
C	0.29124	-1.82844	0.81106
O	-0.54639	-2.47677	0.29642
O	1.14210	-1.19757	1.33731
O	4.00894	-0.66750	0.51043
H	3.24578	-0.91927	1.04982
H	4.78224	-0.86025	1.05782
O	1.04985	2.56996	-0.81206
H	0.91464	3.08943	-1.61556
H	1.99816	2.31803	-0.81881
O	3.73257	1.81930	-0.74293
H	3.87344	0.97787	-0.26287
H	4.29390	2.46861	-0.29897

TS (-664.92998217)

C	-3.44847	0.52283	0.34278
C	-3.02485	0.01571	-0.88855
C	-1.71979	-0.39448	-1.09263

N	-0.72028	-0.18956	-0.08454
C	-1.21290	0.15887	1.21904
C	-2.51999	0.55319	1.39717
H	-4.47318	0.83144	0.49576
H	-3.71942	-0.10722	-1.71019
H	-1.35331	-0.82324	-2.01035
H	-0.04228	0.85163	-0.46432
H	-0.46412	0.15566	1.99395
H	-2.81852	0.85573	2.39296
C	0.43616	-1.25606	-0.07446
O	0.49935	-1.94066	-1.10438
O	1.13492	-1.17199	0.96067
O	3.79635	-0.57816	0.65288
H	2.90784	-0.94256	0.85762
H	4.30873	-0.64717	1.46964
O	0.54600	1.85389	-0.76659
H	0.38293	2.10862	-1.68985
H	1.55878	1.82272	-0.61547
O	3.06650	1.81212	-0.38882
H	3.42109	0.99557	0.04276
H	3.39100	2.55945	0.13292

Product (-664.97046392)

C	-3.61310	0.38779	0.29031
C	-3.16352	-0.27516	-0.86518
C	-1.86635	-0.72778	-0.98157
N	-0.96362	-0.55581	0.08058
C	-1.38302	0.13474	1.23115
C	-2.68858	0.57668	1.32870
H	-4.63156	0.73943	0.37480
H	-3.82462	-0.44038	-1.70636
H	-1.47322	-1.23822	-1.84475
H	0.12946	2.37063	-0.02494
H	-0.64914	0.25345	2.00924
H	-2.96912	1.09214	2.23864
C	0.35264	-0.96996	-0.09815
O	0.75416	-1.48346	-1.14645
O	1.09240	-0.77185	1.00089
O	3.67836	-0.85107	0.46787
H	2.05736	-0.92123	0.77597
H	4.25218	-0.96008	1.23868
O	0.74775	2.06171	-0.70214
H	0.45469	2.48936	-1.51888
H	2.56045	1.92897	-0.48062
O	3.51902	1.72986	-0.46320
H	3.77943	0.08447	0.18040
H	3.93274	2.46402	0.00951

e) PyH^0+ CO_2+ $3H_2O$+ $1H_2O(S)$

Reactant (-741.21714641)

C	-3.75935	-1.00132	0.42845
C	-3.14202	-1.17459	-0.83094
C	-2.13928	-0.32785	-1.25656
N	-1.63869	0.64168	-0.38240
C	-2.38034	0.97461	0.75356
C	-3.38182	0.13184	1.18605
H	-4.55153	-1.65862	0.75931
H	-3.47050	-1.95490	-1.50693
H	-1.63007	-0.42787	-2.20389
H	-0.99197	1.33965	-0.75192
H	-2.05073	1.84510	1.30189
H	-3.89828	0.38196	2.10485
C	0.62041	-0.99783	0.62246
O	0.33108	-0.75636	1.73997
O	0.91231	-1.26129	-0.49142
O	3.79775	-2.06941	-1.14568
H	3.00074	-2.03193	-1.69233
H	4.53469	-2.01832	-1.76974
O	0.27953	2.63132	-1.28155
H	0.43482	2.71854	-2.23126
H	1.16769	2.51773	-0.88011
O	2.72756	2.36367	0.01591
H	3.49727	2.75725	-0.41563
H	3.01457	1.46819	0.29850
O	3.41520	-0.17603	0.87522
H	4.11030	-0.22984	1.54466
H	3.65504	-0.83209	0.18885

TS (-741.18508841)

C	-3.86947	-0.21267	-0.13248
C	-3.06355	-0.59309	-1.20660
C	-1.68231	-0.54854	-1.12992
N	-1.02583	-0.01098	0.02719
C	-1.86970	0.26304	1.15987
C	-3.23969	0.19564	1.05682
H	-4.94717	-0.26388	-0.20001
H	-3.49938	-0.95809	-2.12810
H	-1.02104	-0.84756	-1.92669
H	-0.54331	1.14388	-0.29311
H	-1.33559	0.57185	2.04397
H	-3.81897	0.44986	1.93526
C	0.31294	-0.71728	0.41304
O	0.80328	-0.25813	1.46544
O	0.69948	-1.55966	-0.41864

O	3.43561	-2.13120	-0.50236
H	2.45930	-2.04302	-0.52661
H	3.70894	-2.25188	-1.42140
O	-0.09373	2.24309	-0.50344
H	-0.53153	2.69883	-1.23989
H	0.91878	2.26982	-0.64467
O	2.45036	2.30775	-0.72806
H	2.83242	2.31170	-1.61702
H	2.91107	1.59156	-0.21980
O	3.47172	0.34932	0.83327
H	2.62786	0.10828	1.26589
H	3.70348	-0.46148	0.33722

Product (-741.22080142)

C	-3.91786	-0.01768	-0.12627
C	-3.23658	-0.88226	-1.00517
C	-1.90053	-1.17013	-0.84223
N	-1.17886	-0.58859	0.21435
C	-1.84701	0.25469	1.12271
C	-3.19417	0.52188	0.94287
H	-4.96640	0.20553	-0.26288
H	-3.74914	-1.34979	-1.83584
H	-1.33421	-1.82620	-1.48193
H	-0.62778	2.13857	-0.13814
H	-1.26990	0.60890	1.95969
H	-3.66880	1.17174	1.66723
C	0.19693	-0.77235	0.25873
O	0.75791	-0.13717	1.28791
O	0.79492	-1.46182	-0.58295
O	3.55635	-2.09155	-0.62117
H	2.59227	-2.01690	-0.75691
H	3.94519	-2.15930	-1.50336
O	-0.06285	2.34172	-0.89810
H	-0.48401	3.10646	-1.31584
H	1.77327	2.49764	-0.63569
O	2.73151	2.52715	-0.44160
H	3.16221	2.75618	-1.27574
H	3.25968	1.01075	0.39157
O	3.29001	0.19116	0.93195
H	1.76765	-0.10465	1.16504
H	3.61780	-0.52116	0.34517

f) PyH^0+ CO_2+ $3H_2O$+ $4H_2O$(S)

Reactant (-969.98251341)

C	-3.70937	1.15677	-0.70562
C	-3.60865	0.71624	0.63331
C	-2.76716	-0.31907	0.98510

N	-1.93158	-0.88616	0.01949
C	-2.16048	-0.61071	-1.33042
C	-3.00083	0.42524	-1.68527
H	-4.37287	1.96470	-0.98129
H	-4.21281	1.16636	1.41200
H	-2.66472	-0.69668	1.99221
H	-1.36818	-1.70414	0.25711
H	-1.63702	-1.23124	-2.04407
H	-3.12943	0.63726	-2.74022
C	-0.05171	1.23182	1.04463
O	-0.44196	1.92799	0.17733
O	0.33803	0.53168	1.91262
O	2.13943	3.08887	1.58806
H	2.64852	2.95711	2.40005
H	2.17217	4.04318	1.43117
O	-0.01362	-3.03708	0.39650
H	0.55070	-2.81933	1.15883
H	0.53237	-2.79489	-0.38174
O	1.61008	-2.10294	-1.69422
H	2.39335	-1.86112	-1.16582
H	1.25551	-1.24531	-2.00731
O	2.73235	1.39961	-0.60757
H	3.09770	0.57760	-0.22886
H	2.60590	2.01346	0.14064
O	0.76581	0.51328	-2.33843
H	-0.12445	0.71984	-2.01691
H	1.38275	0.97046	-1.72574
O	3.50580	-1.19566	0.25206
H	4.43753	-1.44889	0.31581
H	3.08248	-1.51383	1.07560
O	1.86142	-2.01528	2.39164
H	1.47612	-1.23533	2.81830
H	2.20227	-2.55749	3.11828

TS1 (formation of $PyCOO^{-}$• H_3O^{+}•2 H_2O •4 $H_2O(S)$ (-969.95566275)

C	-4.53352	-0.15130	-0.04205
C	-3.85735	-0.11331	1.15939
C	-2.46253	-0.01996	1.21458
N	-1.67531	-0.00040	0.00717
C	-2.41756	0.03106	-1.22763
C	-3.77750	-0.07354	-1.24416
H	-5.61181	-0.21909	-0.07437
H	-4.38566	-0.13891	2.10401
H	-1.89157	0.03000	2.12690
H	-1.02617	-1.04452	0.00180
H	-1.80647	0.10263	-2.11313
H	-4.26883	-0.08194	-2.20876

C	-0.49651	1.04449	0.06682
O	-0.30352	1.65989	-0.98930
O	0.08443	1.02930	1.17779
O	2.41276	2.57426	1.34739
H	1.53479	2.14518	1.27162
H	2.26199	3.51096	1.16298
O	-0.33929	-2.11775	0.03556
H	0.12228	-2.11724	0.90651
H	0.40062	-2.08472	-0.65076
O	1.70421	-1.93599	-1.59141
H	2.45939	-1.98583	-0.97370
H	1.77335	-1.04103	-1.99858
O	3.92283	1.04389	-0.45424
H	3.91525	0.16454	-0.03297
H	3.48425	1.63733	0.18990
O	1.99593	0.68451	-2.43125
H	1.22917	1.16379	-2.07088
H	2.73398	0.90919	-1.82220
O	3.47741	-1.59156	0.61215
H	4.19540	-2.12893	0.97614
H	2.79628	-1.54865	1.31249
O	1.14482	-1.35816	2.20538
H	0.80653	-0.44235	2.15666
H	1.10298	-1.62106	3.13614

Product 1 (-969.98612686)

C	-4.23311	-0.72827	0.31084
C	-3.52011	-0.25513	1.42535
C	-2.33071	0.43254	1.28546
N	-1.78938	0.64661	0.00692
C	-2.53193	0.26085	-1.12233
C	-3.71806	-0.43093	-0.96237
H	-5.15836	-1.27478	0.42674
H	-3.89363	-0.40370	2.43083
H	-1.76286	0.83575	2.10735
H	-1.39957	-1.96411	-0.68012
H	-2.09719	0.51560	-2.07413
H	-4.24531	-0.72824	-1.86034
C	-0.47977	1.14741	-0.13692
O	-0.11585	1.43148	-1.33241
O	0.22058	1.25224	0.91819
O	2.45079	2.75517	1.36522
H	1.58089	2.33975	1.16666
H	2.38047	3.67543	1.07853
O	-0.58493	-2.41469	-0.41206
H	-0.34811	-2.05332	0.46532
H	0.93935	-2.15497	-1.38419

O	1.83930	-1.93320	-1.70995
H	2.42622	-2.09216	-0.94424
H	1.98575	-0.38581	-1.96754
O	3.86896	0.97419	-0.15749
H	3.83394	0.11980	0.31851
H	3.51392	1.65428	0.46000
O	2.10999	0.62331	-1.97935
H	1.18051	1.04680	-1.66813
H	2.83467	0.82509	-1.28374
O	3.24298	-1.63324	0.73637
H	3.86140	-2.22823	1.18373
H	2.44310	-1.59146	1.30341
O	0.70313	-1.27466	1.83403
H	0.52515	-0.31410	1.71353
H	0.48605	-1.48125	2.75462

TS2 (proton transfer from H_3O^+ to $PyCOO^-$ to form $PyCOOH^0$) (-969.98585859)

C	-4.39052	0.28978	-0.37079
C	-3.63943	-0.50249	-1.25683
C	-2.37160	-0.94224	-0.93621
N	-1.79434	-0.58872	0.29516
C	-2.54948	0.15802	1.21651
C	-3.81628	0.59422	0.87320
H	-5.37972	0.63821	-0.63198
H	-4.04257	-0.80115	-2.21623
H	-1.76791	-1.57225	-1.56757
H	-1.36044	2.14895	0.03337
H	-2.07289	0.35143	2.16294
H	-4.35547	1.17782	1.60896
C	-0.45555	-0.91491	0.56396
O	-0.05723	-0.67989	1.76581
O	0.24062	-1.38601	-0.38502
O	2.42587	-3.02461	-0.48775
H	1.57436	-2.55281	-0.35743
H	2.39715	-3.79801	0.09138
O	-0.56360	2.47757	-0.40842
H	-0.36282	1.84049	-1.12234
H	1.02530	2.58890	0.51655
O	1.94395	2.49792	0.84939
H	2.48495	2.35772	0.04751
H	2.10606	1.10224	1.63760
O	3.89251	-0.83372	0.29099
H	3.82240	-0.18659	-0.43886
H	3.51884	-1.67812	-0.04713
O	2.19880	0.15722	1.98134
H	1.19327	-0.31024	1.86433
H	2.87471	-0.29149	1.37180

O	3.20798	1.33018	-1.40907
H	3.79864	1.73513	-2.05943
H	2.38125	1.10780	-1.88781
O	0.62281	0.63009	-2.19462
H	0.47526	-0.22512	-1.73265
H	0.36295	0.49238	-3.11693

Product 2 (-969.98896203)

C	-4.51199	0.13036	-0.35012
C	-3.70559	-0.60427	-1.23186
C	-2.40169	-0.93305	-0.91857
N	-1.85155	-0.52321	0.30993
C	-2.65341	0.19299	1.21894
C	-3.95456	0.50957	0.88050
H	-5.53029	0.38704	-0.60525
H	-4.08689	-0.94353	-2.18637
H	-1.75250	-1.51974	-1.54611
H	-1.34353	2.35990	-0.12816
H	-2.18659	0.46327	2.15053
H	-4.53134	1.06814	1.60664
C	-0.52086	-0.79215	0.57232
O	-0.16349	-0.51078	1.81528
O	0.23276	-1.25844	-0.31228
O	2.37635	-3.03468	-0.55487
H	1.54829	-2.55486	-0.36179
H	2.36412	-3.82099	0.00717
O	-0.44455	2.53914	-0.43516
H	-0.27320	1.92227	-1.17233
H	1.15996	2.61792	0.56325
O	2.08124	2.53628	0.87734
H	2.58887	2.31317	0.07426
H	2.24961	1.00378	1.80305
O	4.02868	-0.89967	0.20202
H	3.88370	-0.20934	-0.47222
H	3.58062	-1.70204	-0.13364
O	2.28764	0.06856	2.11093
H	0.85715	-0.40162	1.88796
H	2.94378	-0.35426	1.50839
O	3.25904	1.32473	-1.43277
H	3.84961	1.73613	-2.07896
H	2.42890	1.12241	-1.91221
O	0.65889	0.67449	-2.25422
H	0.49741	-0.17325	-1.79303
H	0.41319	0.53393	-3.17999

g) PyH^0+ CO_2+ $3H_2O$+ $6H_2O(S)$

Reactant (-1122.48934424)

C	-4.63901	1.44869	-0.15021
C	-4.53796	0.99238	1.18294
C	-3.72560	-0.07211	1.51555
N	-2.91806	-0.65482	0.53476
C	-3.15316	-0.35986	-0.81018
C	-3.96703	0.70302	-1.14529
H	-5.28356	2.27619	-0.41215
H	-5.11874	1.45404	1.97261
H	-3.62378	-0.46317	2.51749
H	-2.39016	-1.49807	0.75774
H	-2.65837	-0.98984	-1.53601
H	-4.10190	0.92881	-2.19662
C	-0.89391	1.29966	1.53381
O	-1.31302	2.07467	0.75026
O	-0.47380	0.51894	2.31438
O	1.33451	3.11218	2.11873
H	1.87871	2.97570	2.90699
H	1.34847	4.06923	1.97565
O	-1.02965	-2.85653	0.79884
H	-0.45547	-2.71490	1.57422
H	-0.50485	-2.50324	0.04745
O	0.49475	-1.85923	-1.31074
H	1.33266	-1.68795	-0.83592
H	0.18519	-0.97302	-1.60495
O	1.81480	1.50035	-0.15835
H	2.15827	0.64943	0.17279
H	1.73230	2.08269	0.62096
O	-0.21896	0.76175	-1.87220
H	-1.09438	1.00072	-1.53262
H	0.42863	1.18327	-1.26458
O	2.51120	-1.17468	0.53491
H	3.43870	-1.45068	0.52630
H	2.13156	-1.52601	1.36632
O	0.98229	-2.09987	2.72517
H	0.70766	-1.36614	3.29545
H	1.34995	-2.76221	3.32834
O	-1.30006	-5.46138	-0.38351
H	-1.27338	-4.65922	0.16911
H	-0.86498	-5.17851	-1.20882
O	0.08612	-4.29992	-2.62856
H	0.26530	-3.39599	-2.30053
H	-0.37663	-4.18261	-3.46838

TS (config1, enthalpic barrier of 15.3 kcal/mol)(-1122.45969726)

C	-4.37259	0.92077	-0.13599
C	-3.66749	1.44847	0.92978
C	-2.27377	1.51992	0.92263

N	-1.52157	0.92220	-0.15269
C	-2.28074	0.56746	-1.32515
C	-3.64557	0.51105	-1.28407
H	-5.45231	0.87341	-0.12198
H	-4.17707	1.85677	1.79375
H	-1.67905	1.92977	1.72216
H	-1.08327	-0.15358	0.31560
H	-1.68556	0.29735	-2.18194
H	-4.16077	0.17360	-2.17417
C	-0.17147	1.64605	-0.44230
O	0.13803	1.70959	-1.64053
O	0.41290	1.99031	0.61430
O	2.97375	3.08774	0.44870
H	2.03280	2.81307	0.43057
H	3.01941	3.89611	-0.07952
O	-0.62118	-1.19660	0.83004
H	-0.20542	-0.89602	1.67636
H	0.15921	-1.53003	0.27429
O	1.45865	-2.01910	-0.50362
H	2.18569	-1.94835	0.15178
H	1.71559	-1.39476	-1.23160
O	4.18756	0.73192	-0.46381
H	4.01925	0.11207	0.26909
H	3.87043	1.60138	-0.14225
O	2.26313	-0.12110	-2.26622
H	1.59065	0.58326	-2.23834
H	3.01646	0.23327	-1.74124
O	3.22130	-1.17192	1.48207
H	3.81420	-1.67484	2.05832
H	2.57386	-0.73823	2.07225
O	0.94722	0.10529	2.62036
H	0.82255	0.96534	2.17204
H	0.85578	0.27141	3.57007
O	-2.10040	-3.84675	0.63342
H	-1.85866	-2.94621	0.89334
H	-1.35746	-4.13679	0.07056
O	0.20149	-4.51152	-0.92379
H	0.74943	-3.70346	-0.92399
H	0.11272	-4.76452	-1.85224

<u>TS (config2, enthalpic barrier of 14.5 kcal/mol)(</u> -1122.46412085)

C	-5.33235	0.21378	-0.06207
C	-4.58118	0.56932	-1.16289
C	-3.18535	0.48144	-1.15713
N	-2.47473	0.03116	0.01285
C	-3.29302	-0.36911	1.12942

C	-4.65239	-0.25668	1.09441
H	-6.41118	0.27973	-0.07490
H	-5.04865	0.92025	-2.07416
H	-2.56070	0.73335	-1.99791
H	-1.79166	0.98864	0.38846
H	-2.73964	-0.73282	1.98067
H	-5.20316	-0.54610	1.98000
C	-1.32519	-0.99142	-0.32888
O	-1.20784	-1.92010	0.48134
O	-0.68299	-0.65049	-1.35055
O	1.55730	-2.19254	-1.99200
H	0.69211	-1.77618	-1.79422
H	1.37980	-3.13513	-2.11189
O	-1.07087	1.97992	0.72058
H	-0.58180	2.24257	-0.09424
H	-0.35948	1.69974	1.38097
O	0.90208	1.20124	2.25773
H	1.66828	1.40187	1.68227
H	0.92308	0.22269	2.35970
O	3.05438	-1.29607	0.16932
H	2.88528	-0.33139	0.09108
H	2.61174	-1.69465	-0.61223
O	1.08566	-1.58318	2.17773
H	0.31578	-1.87700	1.65851
H	1.83784	-1.64357	1.55328
O	2.68279	1.46433	0.11246
H	3.58993	1.79217	-0.07809
H	2.09589	1.76903	-0.60441
O	0.42844	1.93243	-1.56471
H	0.09211	1.04308	-1.78930
H	0.40361	2.45356	-2.38008
O	5.77779	-0.85160	-0.25011
H	4.87699	-1.18188	-0.04730
H	6.37219	-1.29205	0.37100
O	5.36451	1.90391	-0.35928
H	5.88064	2.41301	0.27935
H	5.65939	0.97306	-0.26506

Product1 (config1, enthalpic barrier of 15.3 kcal/mol)(-1122.49485115)

C	-5.68991	1.50943	1.33019
C	-4.66124	1.42289	2.27993
C	-3.33862	1.29689	1.90555
N	-2.99708	1.25435	0.54168
C	-4.01467	1.34743	-0.42576
C	-5.32999	1.47061	-0.02527
H	-6.72309	1.60796	1.63149

H	-4.87416	1.45605	3.34063
H	-2.51098	1.24196	2.59231
H	-1.95123	-3.09973	-0.34007
H	-3.69622	1.30258	-1.45261
H	-6.07986	1.53422	-0.80331
C	-1.66925	1.12507	0.19077
O	-1.45600	1.19929	-1.11444
O	-0.77641	0.96440	1.05742
O	1.40255	2.60055	1.73989
H	0.56077	2.16182	1.51104
H	1.26693	3.53747	1.54297
O	-1.00869	-3.15044	-0.12946
H	-0.88487	-2.66038	0.70982
H	0.31116	-2.48781	-1.22530
O	1.16066	-2.19275	-1.61467
H	1.75691	-2.12595	-0.84035
H	0.95851	-0.39248	-1.94017
O	2.90050	1.03299	-0.04359
H	2.90166	0.15019	0.37187
H	2.51125	1.63569	0.62151
O	0.89470	0.58507	-1.88174
H	-0.47981	0.97399	-1.34053
H	1.62829	0.83780	-1.27248
O	2.46510	-1.65332	0.82840
H	3.14031	-2.19905	1.25518
H	1.67807	-1.68595	1.41064
O	-0.09870	-1.55901	1.97700
H	-0.38150	-0.63633	1.80749
H	-0.28879	-1.73566	2.90971
O	0.26760	-5.72642	-0.66425
H	-0.21365	-4.92223	-0.40673
H	0.76882	-5.46652	-1.45850
O	1.77485	-4.62904	-2.86462
H	1.63672	-3.69995	-2.59074
H	1.47094	-4.68111	-3.78026

Product2 (config2, enthalpic barrier of 14.5 kcal/mol)(-1122.49698904)

C	-5.66592	1.49401	1.32139
C	-4.64422	1.41899	2.27971
C	-3.31830	1.29454	1.91667
N	-2.96605	1.23979	0.55600
C	-3.97616	1.32410	-0.42009
C	-5.29503	1.44577	-0.03090
H	-6.70180	1.59100	1.61380
H	-4.86549	1.46077	3.33839
H	-2.49592	1.24811	2.61042

H	-2.01611	-3.03344	-0.45509
H	-3.64967	1.27196	-1.44408
H	-6.03886	1.50158	-0.81530
C	-1.63467	1.10739	0.21714
O	-1.41220	1.16886	-1.08735
O	-0.74941	0.95455	1.09221
O	1.44077	2.58903	1.72665
H	0.58777	2.16332	1.51406
H	1.33324	3.52082	1.49211
O	-1.08657	-3.13382	-0.21224
H	-0.96934	-2.64209	0.62429
H	0.32941	-2.57544	-1.28020
O	1.17621	-2.20225	-1.59729
H	1.73537	-2.19016	-0.79622
H	0.99161	-0.45099	-1.86881
O	2.92856	0.89200	0.10030
H	2.69032	0.01390	0.47566
H	2.52928	1.55627	0.70205
O	0.93665	0.53398	-1.84727
H	-0.43599	0.93816	-1.30627
H	1.67024	0.80102	-1.25235
O	2.39515	-1.68849	0.90080
H	3.21401	-1.97847	1.35629
H	1.64044	-1.79053	1.51133
O	-0.20707	-1.62580	2.00920
H	-0.43034	-0.68488	1.86024
H	-0.46685	-1.82609	2.91965
O	5.63063	0.38636	0.57040
H	4.73612	0.69305	0.30980
H	6.15534	0.39121	-0.24105
O	4.96932	-2.01412	1.86678
H	5.52011	-2.76563	1.61029
H	5.34366	-1.23771	1.39946

h) PyH^0+ CO_2+ $3H_2O$+ $10H_2O(S)$

Reactant (-1427.50181327)

C	-5.31792	1.30409	1.08443
C	-4.69545	0.49871	2.06430
C	-3.69683	-0.39046	1.72520
N	-3.20673	-0.41401	0.41543
C	-3.94923	0.20035	-0.59709
C	-4.94879	1.08972	-0.26398
H	-6.11023	1.99153	1.34596
H	-5.01548	0.53598	3.09865
H	-3.19194	-1.02716	2.43696
H	-2.58009	-1.18071	0.17163

H	-3.62867	0.00860	-1.61066
H	-5.46834	1.59624	-1.06822
C	-0.77822	1.17505	0.73237
O	-0.97710	1.72884	-0.29161
O	-0.54359	0.63406	1.75550
O	1.68287	3.61507	1.04678
H	1.05909	3.95025	1.70368
H	1.46096	4.06179	0.20041
O	-1.18699	-2.50272	0.19746
H	-0.82463	-2.47171	1.10316
H	-0.43433	-2.25606	-0.38011
O	1.14916	-1.95700	-1.26913
H	1.69964	-1.82144	-0.46755
H	1.21444	-1.12591	-1.77873
O	2.41058	1.14039	0.19338
H	2.25641	0.35799	0.76493
H	2.14448	1.95273	0.67910
O	1.28143	0.74881	-2.24284
H	0.35306	1.02485	-2.24264
H	1.62695	0.97407	-1.34567
O	2.26742	-1.40482	1.20213
H	3.18927	-1.64651	1.44222
H	1.66755	-1.75213	1.88915
O	0.06194	-2.23018	2.77645
H	-0.24496	-1.51133	3.34837
H	0.09369	-3.00933	3.35120
O	-1.41499	-5.15276	-0.92193
H	-1.46683	-4.30120	-0.45147
H	-0.62212	-5.05220	-1.48036
O	0.96329	-4.50845	-2.41656
H	1.11803	-3.59232	-2.10938
H	0.87779	-4.44453	-3.37705
O	2.34584	3.06941	-3.46363
H	2.11072	2.16304	-3.18449
H	3.30213	3.06881	-3.60150
O	1.29781	4.73340	-1.46018
H	1.67457	4.18723	-2.18166
H	0.41414	4.98408	-1.75920
O	5.19163	0.73216	0.09367
H	4.24851	0.98901	0.03147
H	5.52374	0.73623	-0.81394
O	4.98471	-1.63412	1.55726
H	5.47806	-2.38106	1.19300
H	5.20763	-0.86299	0.99332

TS (formation of $PyCOO^{-}$•H_3O^{+}•$2H_2O$•$10H_2O$(S)(-1427.47593239)

C	5.29156	0.42843	-0.33121

C	4.61485	0.44395	-1.53297
C	3.21959	0.52685	-1.59066
N	2.43759	0.48232	-0.37777
C	3.17648	0.63587	0.85314
C	4.53768	0.55463	0.86857
H	6.37034	0.37032	-0.29859
H	5.14406	0.42380	-2.47715
H	2.64580	0.56141	-2.50156
H	1.94287	-0.65426	-0.33841
H	2.56233	0.74809	1.73152
H	5.03242	0.62117	1.82893
C	1.13199	1.31737	-0.45705
O	0.81721	1.87847	0.61211
O	0.56216	1.23157	-1.56605
O	-1.86282	2.78559	-1.41331
H	-1.02176	2.31568	-1.57739
H	-1.65289	3.39087	-0.67279
O	1.40357	-1.79766	-0.34539
H	1.00977	-1.88878	-1.25000
H	0.61495	-1.80608	0.28332
O	-0.75033	-1.83993	1.15808
H	-1.44755	-1.96873	0.47527
H	-0.97413	-0.98076	1.58353
O	-3.27536	0.72814	-0.24444
H	-2.91266	-0.08691	-0.65508
H	-2.89931	1.48200	-0.75634
O	-1.46423	0.77053	1.85376
H	-0.70250	1.21127	1.42749
H	-2.18587	0.81313	1.18434
O	-2.35128	-1.75098	-1.07388
H	-3.18695	-2.19241	-1.35023
H	-1.72448	-1.77525	-1.81985
O	0.01581	-1.36267	-2.62296
H	0.14966	-0.39580	-2.62160
H	0.14911	-1.65829	-3.53591
O	2.71207	-4.12898	1.10873
H	2.52162	-3.43013	0.46635
H	1.91176	-4.16099	1.66675
O	0.25649	-4.06547	2.57418
H	-0.22182	-3.29652	2.20994
H	0.26227	-3.93394	3.53168
O	-1.94206	3.17499	3.27659
H	-1.92155	2.24398	2.98106
H	-2.83780	3.32621	3.60649
O	-0.89406	4.23213	0.83812
H	-1.33242	4.01683	1.68512
H	-0.11163	3.65501	0.82447

O	-5.89480	-0.12104	-0.71136
H	-5.05978	0.32774	-0.46312
H	-6.48205	-0.03529	0.05088
O	-4.89949	-2.56523	-1.63844
H	-5.26545	-3.35163	-1.21248
H	-5.39193	-1.80164	-1.26885

Product (-1427.51101847)

C	-5.63153	1.41995	1.35200
C	-4.61774	1.33790	2.31752
C	-3.28754	1.23188	1.96361
N	-2.92412	1.20422	0.60494
C	-3.92634	1.29876	-0.37850
C	-5.24939	1.40061	0.00225
H	-6.67071	1.50181	1.63717
H	-4.84786	1.36055	3.37488
H	-2.47009	1.18521	2.66329
H	-2.05165	-3.03704	-0.39336
H	-3.59133	1.26894	-1.40064
H	-5.98741	1.46509	-0.78689
C	-1.59083	1.08778	0.27880
O	-1.35757	1.18554	-1.02727
O	-0.70666	0.92096	1.15059
O	1.38608	2.85564	1.29982
H	0.60521	2.27599	1.36093
H	1.18506	3.47622	0.56684
O	-1.10646	-3.07525	-0.19289
H	-0.98959	-2.64622	0.68037
H	0.24242	-2.38307	-1.27176
O	1.12527	-2.11341	-1.59900
H	1.66539	-2.07461	-0.77912
H	1.07882	-0.32620	-1.94779
O	2.96397	0.91619	0.16076
H	2.67794	0.06329	0.55783
H	2.51883	1.63097	0.67309
O	1.06897	0.65071	-1.82719
H	-0.38616	0.99307	-1.22644
H	1.79869	0.81997	-1.18454
O	2.31099	-1.66514	0.87324
H	3.13562	-2.02904	1.26506
H	1.57683	-1.79993	1.50288
O	-0.24418	-1.67429	2.06012
H	-0.45189	-0.72540	1.94159
H	-0.47320	-1.89384	2.97465
O	0.16934	-5.64469	-0.73906
H	-0.30872	-4.83543	-0.49020
H	0.71669	-5.38009	-1.50058

O	1.79605	-4.53116	-2.84392
H	1.64183	-3.60794	-2.55782
H	1.53857	-4.56392	-3.77459
O	0.92173	3.04725	-3.25528
H	1.05359	2.11793	-2.98652
H	1.60998	3.23562	-3.90722
O	0.88200	4.52099	-0.87857
H	0.87439	4.06038	-1.74415
H	0.08465	5.06637	-0.86381
O	5.60772	0.35228	0.85506
H	4.75546	0.69515	0.51330
H	6.25921	0.51129	0.15973
O	4.86966	-2.20417	1.72887
H	5.38223	-2.92536	1.34079
H	5.27612	-1.37637	1.39598

B. Supporting information – Reduction of CO_2 to Methanol Catalyzed by a Biomimetic Organo-Hydride Produced from Pyridine

B.1: Computational Methods

a) Benchmarking of Electronic Structure Calculations

In Table S1, we demonstrate that the MP2 method we employ reproduces CCSD(T) activation energies for hydride transfer, $\Delta E^{\ddagger}_{HT}$, within ~3 kcal/mol and thus is accurate for describing hydride transfer reactions. $\Delta E^{\ddagger}_{HT}$ is defined by E(transition state) – E(separated reactants), where E is computed energy at 0 K and does not include zero-point corrections. Details of the computational methods are described in the manuscript.

In Figure S1, we show that the MP2/aug-cc-PVTZ/CPCM-H_2O and M06/6-31+G**/CPCM-H_2O predicted geometries for the **PyH_2** + CO_2's TS are similar (mean absolute error = 0.057 angströms), demonstrating that the use of M06 geometries is reliable.

Table S1: Benchmarking Computational Methods.

System[a]	rM06/ 6-31+G**	rMP2/ aug-ccPVDZ[b]	rMP2/ aug-ccPVTZ[c]	rCCSD(T)/ aug-ccPVDZ[d]	rCCSD(T)/ aug-ccPVTZ[e]
PyH_2 + CO_2	20.1	20.5	22.2	23.1	25.0
$NABH_4$ + CO_2	7.5	10.6	10.7	10.5	10.7

(a) Reported hydride transfer activation energies ($\Delta E^{\ddagger}_{HT}$) at 0 K are in kcal/mol (referenced to separated reactants), and do not include zero-point energy (ZPE) corrections. For (b)-(e), single point energy calculations were performed at the stationary geometries obtained from rM06/6-31+G** calculations. In all calculations, electrostatic solute-solvent interactions were treated using a CPCM description of aqueous solvent.

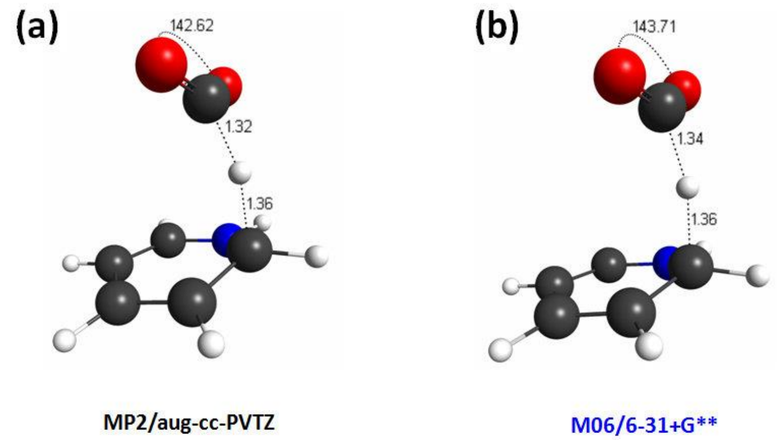

Figure S1: Comparison of TS geometries (PyH_2 + CO_2) between MP2/aug-cc-PVTZ and M06/6-31+G, both solvated with CPCM-H_2O. Lengths reported in Å and angles in degrees.**

b) pK_a and E^0

We computed pK_a values using an approach similar to the method described by Liptak *et al.*; the details of this method are described in the SI of ref. [79]. Here we summarize the key equations and procedures used to obtain pK_a's in aqueous solution. pK_a is defined as $pK_a=\Delta G^0_{aq}/2.303RT$, where ΔG^0_{aq} is defined as the change in Gibbs free energy of the reaction $AH_{aq} = A^-_{aq} + H^+_{aq}$ (**eq. 1**) in aqueous solution at standard conditions and 1 M AH. ΔG^0_{aq} can be calculated using a thermodynamic cycle with $\Delta G^0_{aq} = \Delta G^0_{gas} + \Delta G^0_s(A^-) - \Delta G^0_s(AH) + \Delta G^0_s(H^+)$. ΔG^0_{gas} is the change in Gibbs free energy for **eq. 1** in the gas phase. For the calculation of ΔG^0_{gas}, an experimental value of -6.28 kcal/mol was used for $G^0_{gas}(H^+)$ at a reference pressure of 1 atm. ΔG^0_s uses a reference state of 1M. Conversions can be calculated using ΔG^0_{gas} (1 M) = ΔG^0_{gas} (1 atm.) + RTln(24.46). ΔG^0_s (A^-) and ΔG^0_s (AH) are changes in Gibbs free energy for solvating A^- and AH from the gas phase, i.e. $\Delta G^0_s (A^-) = G^0_s (A^-) - G^0_{gas}(A^-)$. Rather than using the Hartree-Fock (HF)/CPCM-H_2O level of theory to approximate solvation free energies as done by Liptak *et al.*, we used the more accurate rM06/6-31+G** method in CPCM-H_2O solvent to evaluate these energies, e.g. $G(AH_{aq})$ and $G(A^-_{aq})$ are calculated at this level of theory. CPCM here refers to conductor-like polarized continuum model, which is an implicit solvent model used to approximate solvation free energies. Finally, an experimental value of -259.5 kcal/mol was used for $\Delta G^0_s(H^+)$,[317-318] which reproduces the experimental pK_a of PyH^+/Py of 5.3 ($pK_{a,calc.}$=4.3), instead of -264.61 kcal/mol which was used by Liptak *et al.* to calculate the pK_a for carboxylic acids.[79]

Using the approach described here, we obtained the following pK_a's: pK_a (PyH^+/Py) = 4.3; pK_a ($PyH_{2,C2}^{+\cdot}/PyH^0$) = 3.1, pK_a ($PyH_{2,C3}^{+\cdot}/PyH^0$) = -0.8; pK_a ($PyH_{2,C4}^{+\cdot}/PyH^0$) = 1.4. The experimental value pK_a (PyH^+/Py) value is 5.3, whereas our calculation underestimates this value by 1 pK_a unit.

We consequently correct all calculated pK_a's by 1 pK_a unit to give: pK_a ($PyH_{2,C2}^{+\cdot}/PyH^0$) = 4.1; pK_a ($PyH_{2,C3}^{+\cdot}/PyH^0$) = 0.2; and pK_a ($PyH_{2,C4}^{+\cdot}/PyH^0$) = 2.4. Using the isodesmic approach[319], which references to the experimental pK_a of PyH^+ =5.3, the pK_a of ($PyH_{2,C2}^{+\cdot}/PyH^0$) was calculated to be 3.4.

Standard reduction potentials (E^0) were calculated following the same procedure used by Winget *et al*. and Tossell.[44, 78] A value of -100.5 kcal/mol was assumed for the reduction free energy of the standard hydrogen electrode (SHE) as described in Ref. [312]. Thus, $E^0 = (-100.5 - \Delta G_{red})/23.05$ (vs. SHE), where ΔG_{red} is defined as the Gibbs free energy of reduction of A ($A + e^- = A^-$, **eq. 2**), which was calculated at the rM06/6-31+G** level of theory[121] in CPCM-H_2O solvent. To reference to the Saturated Calomel Electrode (SCE), E^0 (vs. SHE) is converted to E^0 (vs. SCE) using E^0 (vs. SCE) = E^0 (vs. SHE) - 0.24 V.

c) Electron Affinities

We calculate the gas phase adiabatic electron affinities of CO_2 and formic acid using the compound CBS-QB3 method,[77] which was designed to give accurate thermochemical predictions. Electron affinity is defined as the negative of energy change associated with transferring an electron from vacuum to a species, e.g. a species with a negative electron affinity corresponds to requirement of energy input during energy transfer process.

CO_2 is known to have a negative electron affinity, and the experimental (gas phase) value is -0.6 ± 0.2 eV;[190, 320] our calculations predict a similar value of -0.60 eV. To the best of our knowledge, there is no published experimental electron affinity for formic acid. Our calculation predicts that formic acid has an electron affinity of -1.22 eV; this value coincides with other theoretical results. [191, 321]

d) Note on Explicit Water Treatment

The absolute free energy of an explicit water is $G^*(H_2O_{(liq)}) = G^o(H_2O_{(g)}) + \Delta G^o{\rightarrow}* + \Delta G^*_{self}(H_2O)$. When comparing the free energies of the TS relative to R (similarly for comparing free energies of P to R), the correction from ideal gas to solution phase standard state, $\Delta G^o{\rightarrow}*$, cancels. Specifically, the constant value of $\Delta G^o{\rightarrow}*$ of 1.894 kcal/mol is added to correct for the free energy of explicit water in R, TS and P; thus for relative free energies, e.g. G(TS) - G(R), the $\Delta G^o{\rightarrow}*$ correction cancels. We note that the sum of the gas phase free energy of a water molecule G^o (H2O(g)) and the water self-interaction $\Delta G^*_{self}(H_2O)$ represents the absolute free energy of an explicit water whose nearest neighbors are only other water molecules. However, in the reacting system the explicit water that mediates proton transfer also interacts with the solvated reacting complex where the interactions change as the reaction proceeds from R, to the TS and finally to P; the figure below shows the varying polarization of the explicit water along the reaction path as indicated by changes in H-bond and O-H bond lengths of the water molecule). Thus, the averaged self-interaction energy of -6.325 kcal/mol does not describe the polarization of the explicit water. Instead, the polarization of the explicit water throughout the reaction is captured quantum mechanically in the computed free energies of R, TS and P. The figure below shows charges and structures of **PyH_2**, OCH_2 and H_2O species in the reactant complex (R), transition state (TS) and product complex (P) determined from IRC calculations.

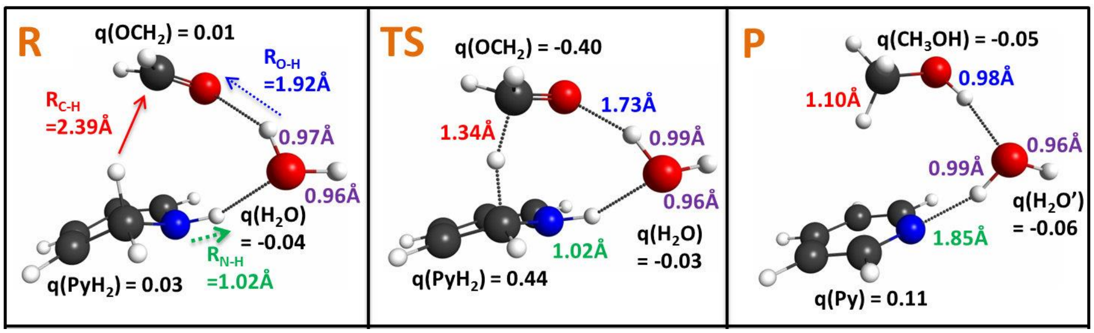

B.2 Overestimation of Activation Entropies Using Ideal Gas Partition Functions

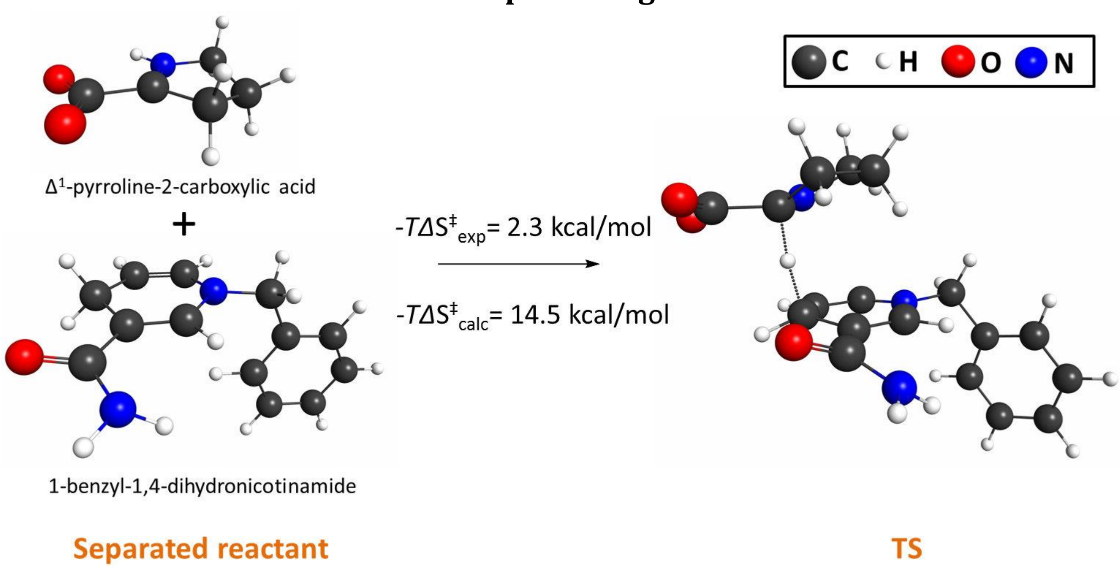

Figure S2: Activation entropy for the hydride transfer reaction between Δ^1-pyrroline-2-carboxylic acid and 1-benzyl-1,4-dihydronicotinamide.

When referenced to the separated reactants, the HT between Δ^1-pyrroline-2-carboxylic acid and 1-benzyl-1,4-dihydronicotinamide is predicted to have an activation entropy ($-T\Delta S^{\ddagger}_{calc}$) of 14.5 kcal/mol (Figure S2) using the ideal gas partition function which treats the hindered translation, rotation and vibration of the species in solution as unhindered gas phase motions. As a result, the ideal gas partition function overestimates $-T\Delta S^{\ddagger}$ by ~12 kcal/mol for this reaction relative to the experimental value of $-T\Delta S^{\ddagger}_{exp}$= 2.3 kcal/mol.[138] Thus, ideal gas-based calculated $-T\Delta S^{\ddagger}_{calc}$ values can have significant errors for solution phase reactions, including the HT reactions in aqueous solvent we investigate here.

Table S2 summarizes the computed gas-phase activation entropies (DHT-1H_2O model) of CO_2, formic acid and formaldehyde. The reported $-T\Delta S^{\ddagger}$ values omit the translational and rotational components that make up the total entropy, in accordance with Morokuma's approach.[139] Note that the VR approach ($-T\Delta S^{\ddagger}$ (vib. + rot.)), which estimates $-T\Delta S^{\ddagger}$ from the only the vibrational and rotational contributions produces values in close agreement with the $T\Delta S^{\ddagger}_{exp}$= 2.3 kcal/mol for the analogous HT between Δ^1-pyrroline-2-carboxylic acid and 1-benzyl-1,4-dihydronicotinamide

Table S2: Gas Phase Entropy for DHT-1H_2O Model

	CO_2	HCOOH	OCH_2
$-T\Delta S^{\ddagger}$ (trans.+ vib. + rot.)	13.9	13.1	13.5
$-T\Delta S^{\ddagger}$ (vib. + rot.)	3.0	2.2	2.7
$-T\Delta S^{\ddagger}$ (vib.)	-3.1	-4.0	-3.2

B.3 Thermodynamic Quantities Referenced to Reactant Complex

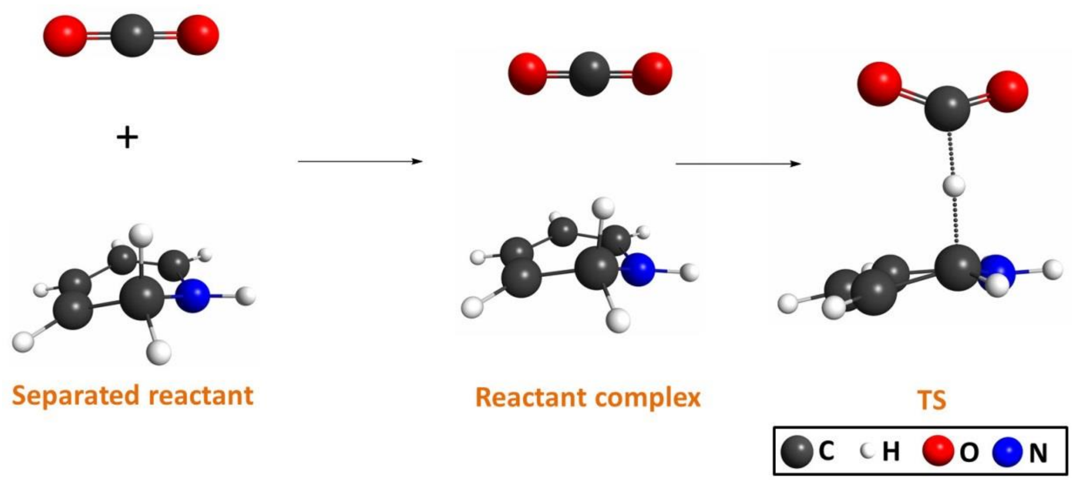

Figure S3: Separated Reactant vs Reactant Complex for CO_2 Reduction via the DHT Model.

Figure S3 shows that approach of the separated reactants (**PyH_2** + CO_2) to each other to form the reactant complex prior to forming the transition state complex. In the manuscript, we report the activation enthalpies ($\Delta H^{\ddagger}_{HT}$) referenced to the separated reactants, as is appropriate for bimolecular reactions.[130] For example, for the reaction between **PyH_2** and CO_2 described using the direct hydride transfer (DHT) model, $\Delta H^{\ddagger}_{HT}$ (separated reactant) = 20.9 kcal/mol. For comparison purposes, here we also report activation enthalpies referenced to the reactant complex, which for this case $\Delta H^{\ddagger}_{HT}$ (reactant complex) = 22.1 kcal/mol. Thus, a weak complexation enthalpy (-1.2 kcal/mol) is involved in forming the reactant complex from the separated reactants. Below, we report similar enthalpy quantities for formic acid (HCOOH) and formaldehyde (OCH_2) reduction.

PyH_2 + HCOOH (DHT model)

$\Delta H^{\ddagger}_{HT}$ (separated reactant) = 23.3 kcal/mol

$\Delta H^{\ddagger}_{HT}$ (reactant complex) = 24.9 kcal/mol

PyH_2 + OCH_2 (DHT model)

$\Delta H^{\ddagger}_{HT}$ (separated reactant) = 12.2 kcal/mol

$\Delta H^{\ddagger}_{HT}$ (reactant complex) = 13.2 kcal/mol

B.4 Recovery of the Pyridine Catalyst from the 4,4' Coupled Dimer

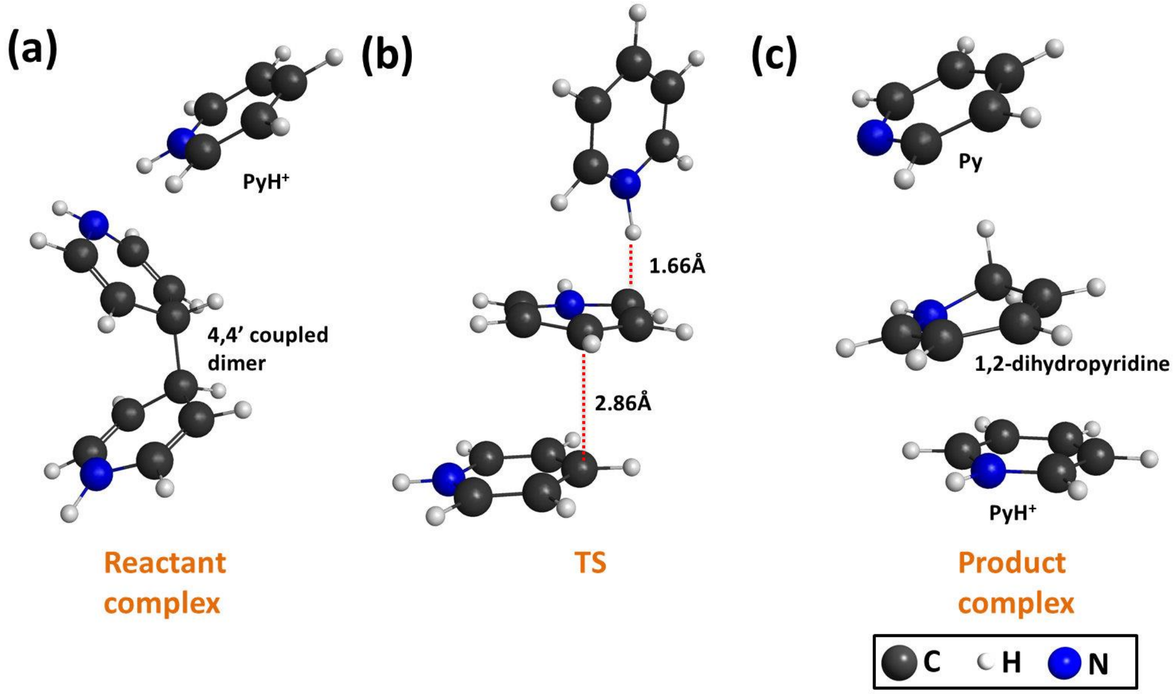

Figure S4: Reactant complex (a), transition state (b), and product complex (c) of the 4,4' coupled dimer reacting with PyH^+ to produce 1,2-dihydropyridine, Py and PyH^+.

Figure S4 shows the reactant complex, TS and product complex of the reaction between PyH^+ and the 4,4' coupled dimer (formed by the carbon-carbon coupling of two PyH^0s). In this reaction, 1,2-dihydropyridine is produced along with Py and PyH^+. The enthalpic barrier ($\Delta H^{\ddagger}_{HT}$) of this reaction is 31.0 kcal/mol and the enthalpy of reaction (ΔH^0_{rxn}) is -4.6 kcal/mol (referenced to separated reactants). PyH^+, with a pK_a= 5.3, acts as a proton donor in this reaction. The high barrier indicates that the recovery of the pyridine catalyst by decoupling the 4,4' dimer is not an active pathway at 298K. It should be noted that if H_3O^+, a much stronger proton donor with a pK_a= -1.7, is used as a proton donor to the 4,4' coupled dimer, the decoupling barrier is expected to decrease. All structures and energies were calculated using the rM06/6-31+G**/CPCM-H_2O level of theory.

B.5 Linearized Poisson-Boltzmann Model of Cation Concentration Near a Negatively Biased Cathode

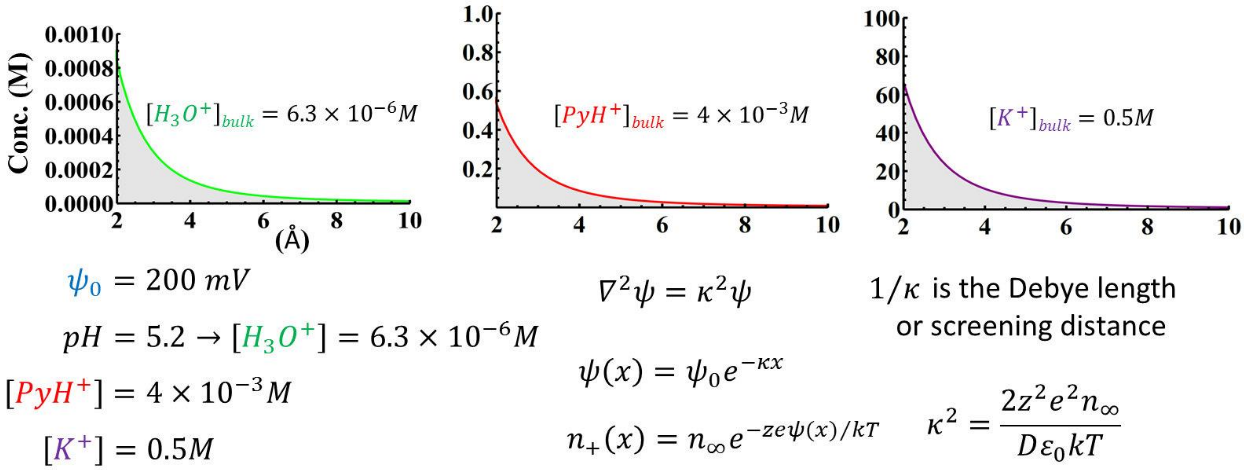

Figure S5: The distribution of cation (e.g. H_3O^+, PyH^+ and K^+ (without anion Cl^-) used as an electrolyte) concentration near a negatively biased cathode ($\psi_0 = 200\ mV$) according to a linearized Poisson-Boltzmann model. ψ_0 is the negative potential applied at the cathode, ψ(x) is electrostatic potential as a function of x (distance from the electrode), z is the charge on the cation, e is the elementary charge, n_∞ is bulk concentration of the cation, D is dielectric constant of the medium (78.5 for aqueous solution), ε_0 is the vacuum permittivity, k is the Boltzmann constant and T is temperature (298 K). Note that the Debye length 1/κ is proportional to (ionic strength)$^{-1/2}$; which in this case for monovalent cation and anion, ionic strength = n_∞.

Figure S5 shows the distribution of cations near a negatively biased cathode. The linearized Poisson-Boltzmann model[167] is used to describe the electrostatic attraction between the negatively biased cathode and cations in dielectric media. In an aqueous solution (D = 78.5) with a negatively biased cathode at 200 mV, cation concentration increases exponentially towards the cathode. For example, at 2 Å away from the cathode, the concentration of the cations increases by ~2 order of magnitude. Thus, the pH in the vicinity of the cathode is expected to be much lower than in the bulk. We note that this model likely does not accurately describe cation concentrations at a distance < 2 Å away from the cathode where the continuum model begins to break down.

B.6 Reactivity of 1,2-dihydropyridine and 1,4-dihydropyridine Towards CO_2

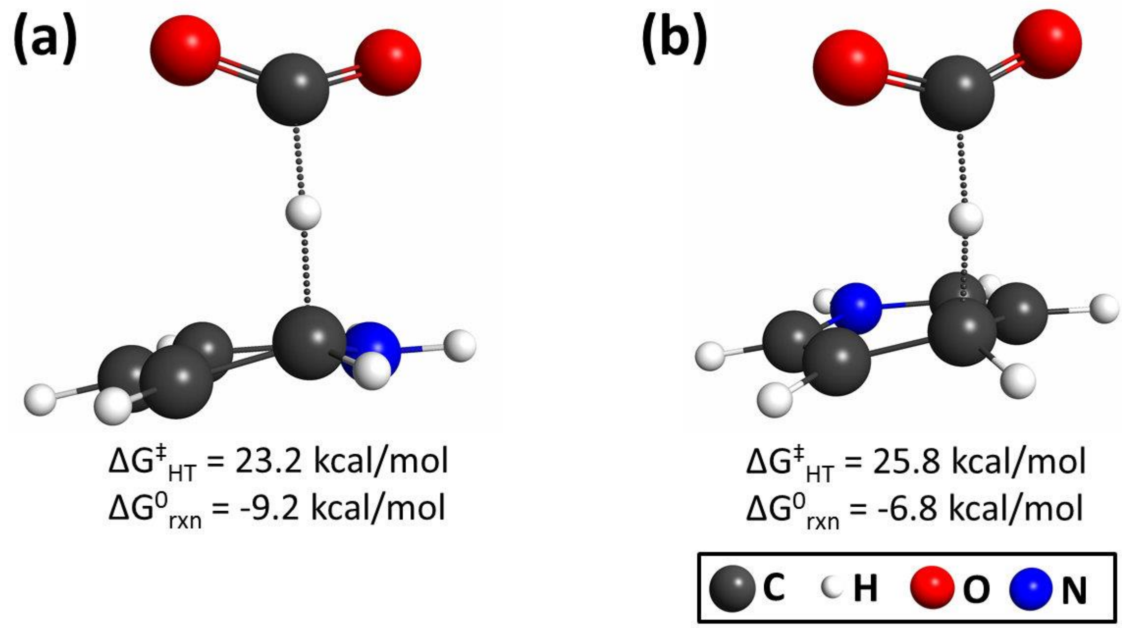

Figure S6: Transition state structures for (a) 1,2-dihydropyridine + CO_2 and (b) 1,4-dihydropyridine + CO_2. Calculations performed at rMP2/aug-ccPVTZ//rM06/6-31+G with solvent described using CPCM for aqueous solvent.**

Figure S6 shows the transition state structures, standard activation free energies ($\Delta G^{\ddagger}_{HT}$) and reaction free energies (ΔG^{0}_{rxn}) for (a) 1,2-dihydropyridine + CO_2 and (b) 1,4-dihydropyridine + CO_2. The comparison between these two species shows that 1,2-dihydropyridine is more reactive than 1,4-dihydropyridine, exhibiting both a lower $\Delta G^{\ddagger}_{HT}$ and a more negative ΔG^{0}_{rxn}.

B.7 Hydride Transfer from N-H Bond of 1,4-dihydropyridine

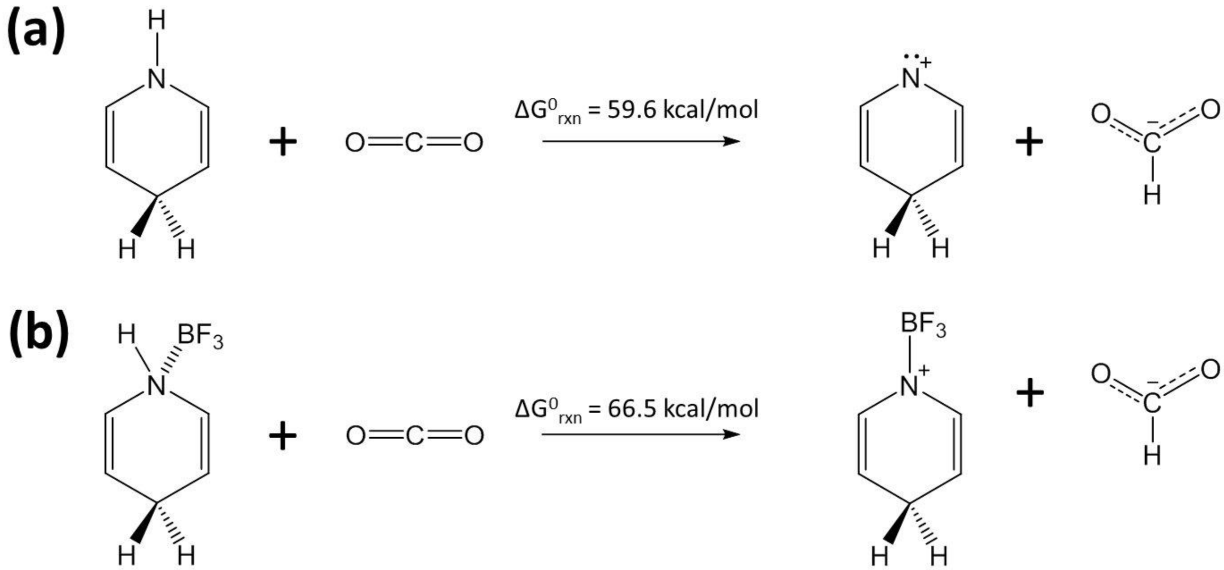

Figure S7: (a) Hydride transfer from the N-H bond of 1,4-dihydropyridine to the C atom of CO_2 to form formate and pyridinum protonated in the C-4 position, (b) analogous to reaction in (a) except that a BF_3 Lewis acid, which is used to model a Lewis acidic surface site, is bound to the N of 1,4-dihydropyridine during the reaction. All calculations were performed using rM06/6-31+G/CPCM-H_2O.**

From Figure S7a, we show that hydride transfer from the N-H bond of 1,4-dihydropyridine to CO_2, as proposed in ref. [152] , is highly endergonic with ΔG^0_{rxn}= 59.6 kcal/mol. This result clearly demonstrates that hydridic character of the N-H hydrogen is highly unfavorable under standard conditions.

In Figure S7b, we use BF_3 Lewis acid to model a Lewis acidic surface site. It was also proposed in ref. [152] that 1,4-dihydropyridine performs a hydride transfer while adsorbed to the Lewis acidic site on a surface (e.g. Pt or p-GaP). Our result predicts that the surface actually hinders hydride transfer in that it makes the N-H bond an even weaker hydride donor (ΔG^0_{rxn} =66.5 kcal/mol) than free DHP.

B.8 Coordinates of Molecular Structures

All coordinates are reported as XYZ Cartesian coordinates. In “red” are rM06/6-31+G**/CPCM-H_2O energies. In “black”, we report rMP2/aug-ccPVTZ/CPCM-H_2O single point energies computed at rM06/6-31+G**/CPCM-H_2O geometries. Energies reported here are computed at 0 K (not ZPE and thermally corrected) and are stated in Hartrees units. In “blue”, the imaginary frequencies (in unit cm^{-1}) of transition state structures are also reported. Unless otherwise noted, all energies reported were calculated using the GAUSSIAN 09 computational chemistry package.[61]

CO_2 (-188.51263107, -188.32329603)

C	2.18926	0.01112	0.30294
O	1.79513	0.03673	1.39377
O	2.58406	-0.01448	-0.78759

1,4-Cyclohexadiene (-233.24433548, -232.90378431)

H	0.74904	1.87385	-1.96853
C	-0.18776	1.13475	1.30625
C	0.76573	0.24524	1.59579
H	2.46751	0.27133	-1.44663
H	-1.29457	1.64109	-0.45593
H	-0.93345	1.38521	2.06078
H	0.78500	-0.21732	2.58267
C	-0.30028	1.82638	-0.01767
C	1.72191	0.52192	-0.69207
H	-0.27215	2.91890	0.12599
C	0.76841	1.41142	-0.98159
C	1.83451	-0.16958	0.63192
H	2.82878	0.01567	1.07020
H	1.80645	-1.26214	0.48827

Reactant complex (-421.76051246, -421.23289602)

H	0.72190	1.84063	-1.98314
C	-0.19775	1.12303	1.29995
C	0.75374	0.23009	1.58836
H	2.43697	0.23298	-1.46306
H	-1.28964	1.70560	-0.44435
H	-0.96003	1.35228	2.04469
H	0.75385	-0.25615	2.56406
C	-0.28617	1.84434	-0.00981
C	1.70937	0.50630	-0.69893
C	-1.46984	-1.65892	-0.27016
O	-0.73301	-2.47623	0.10987
O	-2.21544	-0.85266	-0.65741
H	-0.20994	2.93199	0.15303
C	0.75777	1.39885	-0.98727
C	1.84693	-0.15348	0.63905

H	2.82839	0.08891	1.07899
H	1.87373	-1.24866	0.51787

TS (-421.69168248, -421.1442666, 378.43i)

H	1.89776	0.88243	-2.16549
C	1.62343	0.15940	1.20167
C	2.84842	-0.37564	1.41805
H	4.13907	-0.06652	-1.79498
H	0.27242	-0.75148	-0.50706
H	0.91078	0.27462	2.01276
H	3.13968	-0.68864	2.41784
C	1.24052	0.54975	-0.11784
C	3.41764	-0.02185	-0.98281
C	-0.01359	-1.89742	-0.68496
O	-1.10451	-2.02961	-1.24471
O	0.86420	-2.65321	-0.26470
H	0.34243	1.15159	-0.24440
C	2.18874	0.50512	-1.18978
C	3.83771	-0.53171	0.33617
H	4.79241	-0.06438	0.63263
H	4.12086	-1.59629	0.24795

10-methyl-9,10-dihydroacridine + CO_2

10-methyl-9,10-dihydroacridine (-595.66353648, -594.85216855)

C	0.22032	0.62179	1.45229
C	1.35343	-0.20008	1.59671
H	-1.16435	-0.25225	0.08909
C	-0.48207	0.61555	0.12643
C	1.63524	-0.31925	-0.79074
H	-1.11082	1.50652	0.00833
N	1.81303	-0.90944	0.47298
C	0.50931	0.50052	-0.99389
C	2.54262	-0.51330	-1.83948
C	0.32927	1.12341	-2.22346
C	2.32963	0.10093	-3.07219
H	3.04558	-0.06141	-3.87477
C	1.99184	-0.27892	2.84077
C	1.50488	0.44961	3.92451
H	2.01225	0.37476	4.88377
C	0.39531	1.27683	3.78203
H	0.02161	1.85111	4.62596
C	-0.23370	1.35914	2.53976
H	-1.10906	1.99486	2.41052
C	1.22822	0.92726	-3.27191
H	2.87889	-0.89298	2.96883

H	3.42673	-1.12886	-1.69863
H	1.06755	1.41206	-4.23157
H	-0.54406	1.75967	-2.36341
C	2.85713	-1.89714	0.64680
H	3.86003	-1.45306	0.74878
H	2.64662	-2.49380	1.53793
H	2.86111	-2.57608	-0.20948

Reactant complex (-784.18144416, -783.1838096), MP2 calculation performed with GAMESS

C	0.21543	0.61607	1.45333
C	1.34533	-0.20926	1.59814
H	-1.18614	-0.22892	0.08230
C	-0.48382	0.62331	0.12585
C	1.62970	-0.32472	-0.79047
C	-0.17807	-3.23458	0.28979
O	-0.42959	-3.15292	1.42387
O	0.06084	-3.33513	-0.84564
H	-1.09756	1.52495	0.00968
N	1.79624	-0.92873	0.47248
C	0.50713	0.49830	-0.99377
C	2.53795	-0.52027	-1.83733
C	0.33047	1.12342	-2.22298
C	2.32896	0.09648	-3.06959
H	3.04534	-0.06765	-3.87132
C	1.98474	-0.28793	2.84101
C	1.50154	0.44414	3.92420
H	2.01062	0.36988	4.88249
C	0.39401	1.27369	3.78191
H	0.02364	1.85117	4.62506
C	-0.23550	1.35643	2.54033
H	-1.10733	1.99662	2.41001
C	1.22999	0.92551	-3.27013
H	2.87093	-0.90248	2.97093
H	3.41907	-1.14021	-1.69853
H	1.07212	1.41169	-4.22951
H	-0.53997	1.76355	-2.36266
C	2.86824	-1.88948	0.64418
H	3.86146	-1.41985	0.71896
H	2.69226	-2.47343	1.55138
H	2.87167	-2.58486	-0.20000

TS (-784.12248563, -783.11289645, 648.01i)

C	1.53413	0.32881	1.14540
C	2.79274	-0.25663	1.42896
H	0.48378	-0.84512	-0.46662
C	1.14838	0.48285	-0.22182
C	3.42976	-0.09211	-0.89230

C	0.31100	-2.06717	-0.50950
O	0.26439	-2.53220	0.62376
O	0.26432	-2.46157	-1.67037
H	0.23233	1.03707	-0.43634
N	3.63549	-0.59718	0.38347
C	2.17792	0.48502	-1.21721
C	3.14719	-0.47417	2.77354
C	2.26965	-0.12846	3.78472
H	2.56881	-0.29417	4.81652
C	1.01582	0.43918	3.50757
H	0.34181	0.70114	4.31760
C	0.65816	0.65953	2.19582
H	-0.30817	1.09224	1.94446
C	4.43378	-0.12650	-1.87726
C	1.94906	0.98578	-2.51161
H	4.11667	-0.88260	3.03630
H	5.41799	-0.52465	-1.65516
H	0.97272	1.41115	-2.73535
C	4.18456	0.38716	-3.13718
C	2.94023	0.94476	-3.46872
H	4.97884	0.36303	-3.87882
H	2.76572	1.34202	-4.46418
C	4.83412	-1.38508	0.65533
H	5.68533	-0.75151	0.93069
H	4.62939	-2.08913	1.46205
H	5.08847	-1.97235	-0.22723

Dihydrophenanthridine + CO_2

Dihydrophenanthridine (-556.38699729, -555.63233510)

H	0.94556	2.14250	-1.69762
C	0.14324	1.60034	1.48421
C	0.98416	0.49540	1.70815
H	-1.00502	1.40049	-0.31375
C	-0.15038	1.99408	0.06582
C	1.59150	-0.17172	0.54560
N	1.03610	1.78625	-0.75344
C	1.61575	0.52532	-0.68435
H	-0.43922	3.04880	0.01262
C	-0.43522	2.27024	2.55855
C	-0.19481	1.85542	3.86631
H	-0.65273	2.38325	4.69930
C	0.64543	0.76759	4.09777
H	0.85281	0.44405	5.11512
C	1.23556	0.10157	3.02911
H	1.91140	-0.72720	3.22948

C	2.19037	-1.43442	0.61102
C	2.82718	-1.99606	-0.48992
H	3.28080	-2.98090	-0.41462
C	2.87312	-1.28339	-1.68931
H	3.36934	-1.70817	-2.55912
C	2.26948	-0.03628	-1.78826
H	-1.08301	3.12456	2.36569
H	2.29325	0.51510	-2.72719
H	2.15254	-1.99348	1.54407

Reactant complex (-744.90418834, -743.96286463)

H	0.94714	2.14066	-1.70085
C	0.14748	1.60202	1.48414
C	0.99522	0.50282	1.70993
H	-1.00495	1.42035	-0.31429
C	-0.14274	2.00209	0.06657
C	1.60678	-0.16359	0.54883
N	1.04013	1.78676	-0.75600
C	1.62076	0.52713	-0.68487
C	-0.98969	-2.23534	0.21717
O	-0.94113	-2.69328	1.28690
O	-1.04688	-1.78186	-0.85337
H	-0.42114	3.05992	0.01757
C	-0.44174	2.26414	2.55786
C	-0.20572	1.84707	3.86541
H	-0.67200	2.36914	4.69737
C	0.64091	0.76437	4.09847
H	0.84462	0.43893	5.11592
C	1.24088	0.10551	3.03117
H	1.92033	-0.72005	3.23267
C	2.20522	-1.42676	0.61582
C	2.82599	-1.99784	-0.48964
H	3.27730	-2.98365	-0.41376
C	2.86232	-1.29082	-1.69280
H	3.34750	-1.72197	-2.56565
C	2.26430	-0.04086	-1.79129
H	-1.09473	3.11428	2.36412
H	2.28124	0.50588	-2.73306
H	2.17206	-1.98221	1.55160

TS (-744.85472427, -743.90595079, 798.70i)

H	2.03008	0.79363	-1.98881
C	1.58541	0.28441	1.26225
C	2.83582	-0.29016	1.57185
H	0.48952	-0.68606	-0.42115
C	1.23608	0.50694	-0.13150
C	3.75547	-0.59979	0.47966

N	2.24544	0.51724	-1.03766
C	3.43850	-0.16162	-0.82240
C	0.31740	-1.86013	-0.87440
O	-0.26457	-2.54379	-0.04716
O	0.81268	-1.93237	-1.98723
H	0.40484	1.17588	-0.35475
C	3.13704	-0.51857	2.92341
C	2.22141	-0.20721	3.91608
H	2.47720	-0.39384	4.95591
C	0.97637	0.34573	3.59482
H	0.26476	0.58538	4.37979
C	0.66137	0.58862	2.26963
H	-0.30034	1.01897	1.99651
C	4.96499	-1.29127	0.65634
C	5.82363	-1.52276	-0.40452
H	6.75163	-2.06337	-0.24051
C	4.30719	-0.38612	-1.89555
H	4.03315	-0.03283	-2.88755
H	5.23354	-1.65934	1.64286
H	4.09862	-0.93716	3.20719
C	5.49533	-1.06309	-1.68524
H	6.16740	-1.24367	-2.51969

Hantzsch's ester + CO_2

Hantzsch's ester (-862.01667438, -860.93400653)

C	0.06173	1.60753	1.59883
C	1.04869	0.69388	1.80927
H	2.43371	-0.51633	0.89842
H	-1.41152	1.68621	0.03071
C	-0.36749	1.99749	0.20561
C	1.50060	0.53387	-0.59739
H	-0.40174	3.09367	0.12486
C	0.52560	1.44117	-0.87650
N	1.69754	0.15196	0.71620
C	0.21988	1.94191	-2.21237
C	-0.68607	2.27289	2.66052
O	-0.71333	2.70341	-2.44046
O	-1.60229	3.05715	2.44101
O	1.04197	1.51442	-3.18451
O	-0.29395	1.96823	3.90813
C	0.76864	1.96734	-4.52014
H	0.81457	3.06270	-4.54014
H	-0.25101	1.67162	-4.79437
C	1.80177	1.33841	-5.41668

H	1.63674	1.64603	-6.45392
H	2.81213	1.64433	-5.12393
H	1.74473	0.24528	-5.36923
C	-0.99722	2.59346	4.99284
H	-0.89245	3.68152	4.90455
H	-2.06388	2.35251	4.91300
C	-0.39068	2.06736	6.26678
H	0.67662	2.30909	6.31911
H	-0.88709	2.51523	7.13323
H	-0.50142	0.97923	6.33103
C	1.55345	0.17089	3.11813
H	2.00313	0.96954	3.71533
H	0.74259	-0.25091	3.71728
H	2.30647	-0.60658	2.95951
C	2.43681	-0.13383	-1.55602
H	1.89718	-0.60603	-2.38023
H	3.12273	0.59178	-2.00425
H	3.03121	-0.89775	-1.04621

Reactant complex (-1050.53405796, -1049.26523689)

C	0.18348	1.74113	1.61417
C	1.15835	0.81422	1.81941
H	2.56313	-0.37314	0.90671
H	-1.24796	2.00115	0.03374
C	-0.18225	2.21194	0.22801
C	1.63089	0.68118	-0.58520
C	-1.26224	-0.94000	-1.39905
O	-1.18666	-1.25010	-0.27944
O	-1.34179	-0.63587	-2.52057
H	-0.11766	3.30959	0.17574
C	0.66328	1.59916	-0.86200
N	1.83976	0.30971	0.72718
C	0.32822	2.06896	-2.20306
C	-0.61285	2.35153	2.67391
O	-0.55710	2.88892	-2.41801
O	-1.48940	3.17952	2.45392
O	1.04583	1.51819	-3.19346
O	-0.32083	1.93656	3.91672
C	0.67739	1.86067	-4.53831
H	0.79743	2.94160	-4.67828
H	-0.38325	1.61895	-4.68244
C	1.57209	1.06423	-5.45027
H	1.34119	1.28827	-6.49627
H	2.62545	1.30623	-5.27062
H	1.43293	-0.01076	-5.28901
C	-1.09393	2.48867	4.99427
H	-0.96237	3.57716	5.00494

H	-2.15517	2.28199	4.81116
C	-0.59878	1.84273	6.26096
H	0.46426	2.05621	6.41826
H	-1.15685	2.22349	7.12188
H	-0.72955	0.75570	6.21963
C	1.61966	0.23861	3.12211
H	2.01148	1.01642	3.78355
H	0.79585	-0.24240	3.65621
H	2.40636	-0.50389	2.95981
C	2.53838	-0.01371	-1.55251
H	1.96986	-0.59361	-2.28614
H	3.13345	0.70529	-2.12206
H	3.21895	-0.69012	-1.02764

TS (-1050.48619705, -1049.21109993, 917.62i)

C	1.38636	0.23480	1.18046
C	2.61804	-0.29951	1.47751
H	4.39836	-0.87776	0.67077
H	0.25594	-0.61880	-0.60357
C	1.04555	0.48635	-0.19864
C	3.31498	-0.06662	-0.85157
C	-0.05253	-1.72637	-1.18186
O	-1.07027	-2.18587	-0.69050
O	0.78631	-1.97349	-2.03134
H	0.21677	1.17203	-0.37517
C	2.09624	0.48390	-1.18062
N	3.49685	-0.47247	0.44104
C	0.31096	0.48478	2.15898
C	1.70580	0.95656	-2.52178
C	3.13302	-0.71686	2.81259
H	3.31236	0.15797	3.44584
H	2.40699	-1.34286	3.33579
H	4.07105	-1.26899	2.71202
C	4.48476	-0.28095	-1.74870
H	4.21436	-0.94308	-2.57721
H	4.81238	0.66145	-2.19593
H	5.32270	-0.72244	-1.20348
O	0.59714	1.40460	-2.76220
O	-0.83867	0.71436	1.82336
O	0.71644	0.44527	3.42576
O	2.66437	0.83587	-3.43670
C	-0.28422	0.64652	4.44653
H	-0.73159	1.63669	4.30331
H	-1.07112	-0.10411	4.31234
C	0.41204	0.51589	5.77348
H	-0.30798	0.65429	6.58564
H	0.86476	-0.47594	5.88094

H	1.19842	1.27061	5.87946
C	2.34820	1.23774	-4.78554
H	2.07828	2.29986	-4.77911
H	1.47413	0.66757	-5.11999
C	3.56966	0.95940	-5.61845
H	3.82471	-0.10559	-5.59219
H	3.38496	1.24273	-6.65901
H	4.42983	1.53109	-5.25368

$NaBH_4$ + CO_2

BH_4^- (-27.33111504, -27.25783179)

H	-0.46475	1.61335	1.09007
H	0.42003	2.98568	-0.09947
H	1.43921	1.33805	0.47165
H	1.01374	2.78017	1.82157
B	0.60217	2.17970	0.82142

Reactant complex (-215.84674858, -215.58422919)

H	-0.46490	1.61381	1.08950
C	-0.22660	-0.71103	-0.33439
O	0.01568	-1.30008	0.64098
O	-0.48636	-0.17713	-1.33621
H	0.41954	2.98452	-0.10016
H	1.43914	1.33875	0.47150
H	1.01427	2.77963	1.82243
B	0.60235	2.18024	0.82197

TS (-215.83186656, -215.56399968, 402.19i)

H	0.14591	-0.51509	-0.30999
C	0.33296	-1.85368	-0.93092
O	0.62375	-2.59736	-0.03562
O	0.05300	-1.72280	-2.09015
H	0.59386	1.32806	-0.78708
H	2.10730	-0.02304	-0.64931
H	1.11271	0.52080	1.03918
B	1.06503	0.38729	-0.17158

4-CN-PyH_2 + CO_2

4-CN-PyH_2 (-341.48489265, -341.04129720)

H	0.61393	1.08308	-1.75451
C	0.30576	0.72033	1.53350
C	1.34630	-0.12808	1.70120
H	2.77226	-1.50335	0.69781
H	2.29642	-0.50566	-1.54613

H	-1.04653	0.11617	-0.01892
H	-0.15206	1.23373	2.37409
C	-0.26678	0.88489	0.15818
C	2.00403	-0.75172	0.56168
N	0.81340	0.77144	-0.81485
C	1.73829	-0.22029	-0.65830
H	-0.74714	1.86072	0.04305
C	1.86246	-0.36323	3.01516
N	2.28864	-0.57460	4.07802

Reactant complex (-530.00020482, -529.36941183)

H	0.60495	1.06670	-1.76114
C	0.30376	0.71456	1.53304
C	1.34841	-0.12814	1.70150
H	2.79188	-1.48781	0.69925
H	2.29821	-0.50858	-1.54675
H	-1.06209	0.13713	-0.01619
H	-0.15937	1.22059	2.37528
C	-0.26822	0.89043	0.15892
C	2.01202	-0.74780	0.56262
N	0.80561	0.75790	-0.82080
C	1.73929	-0.22248	-0.65921
C	-0.02415	-3.14375	-0.37868
O	-0.88407	-2.62519	0.21115
O	0.82324	-3.67562	-0.97432
H	-0.72981	1.87586	0.04690
C	1.86055	-0.36568	3.01649
N	2.28379	-0.57925	4.08006

TS (-529.95532787, -529.32198295, 1007.13i)

H	1.96661	0.61608	-2.01559
C	1.58826	0.29017	1.25139
C	2.81892	-0.24059	1.52347
H	4.68295	-1.03817	0.67563
H	4.04832	-0.35256	-1.64834
H	0.44030	-0.76658	-0.36046
H	0.88978	0.55238	2.03823
C	1.17823	0.41629	-0.12155
C	3.72401	-0.57905	0.46837
N	2.19292	0.38014	-1.05655
C	3.38557	-0.22047	-0.80109
C	0.14454	-1.87757	-0.98231
O	-0.58653	-2.55268	-0.28256
O	0.71150	-1.86762	-2.05910
H	0.35893	1.09038	-0.36398
C	3.22161	-0.43685	2.88499
N	3.55709	-0.60185	3.98550

$4\text{-}CONH_2\text{-}PyH_2 + CO_2$

$4\text{-}CONH_2\text{-}PyH_2$ (-417.93073099, -417.40240767)

H	0.63122	1.10844	-1.84384
C	0.34383	0.82949	1.45895
C	1.37298	-0.02221	1.65871
H	2.78633	-1.40899	0.67204
H	2.31553	-0.46977	-1.59265
H	-1.00771	0.20142	-0.09084
H	-0.10110	1.40246	2.26923
C	-0.22981	0.97505	0.07891
C	2.01895	-0.65839	0.52242
N	0.85001	0.84869	-0.89264
C	1.76204	-0.15676	-0.71065
H	-0.71207	1.94828	-0.05238
C	1.96741	-0.24788	3.00897
O	3.15567	-0.54673	3.15038
H	1.50985	-0.26549	4.99561
H	0.13739	-0.03293	3.96480
N	1.13802	-0.10366	4.07008

Reactant complex (-606.4462619, -605.73045608)

H	0.61822	1.08214	-1.85240
C	0.34240	0.82391	1.45779
C	1.37644	-0.02140	1.65864
H	2.81082	-1.39085	0.67574
H	2.31467	-0.47857	-1.59325
H	-1.03341	0.23677	-0.08733
H	-0.10871	1.38812	2.27090
C	-0.23143	0.98467	0.07932
C	2.03097	-0.65334	0.52444
N	0.83943	0.82904	-0.90005
C	1.76225	-0.16331	-0.71118
C	-0.15181	-3.13193	-0.00094
O	-1.07676	-2.44987	0.18820
O	0.75964	-3.83012	-0.19332
H	-0.68423	1.97297	-0.04786
C	1.96814	-0.24494	3.01057
O	3.15862	-0.53348	3.15437
H	1.50567	-0.27166	4.99573
H	0.13382	-0.04915	3.96190
N	1.13485	-0.10990	4.06978

TS (-606.40687771, -605.68748231, 1049.25i)

H	2.01715	0.87536	-1.98029

C	1.43160	0.22524	1.20886
C	2.64819	-0.30815	1.52227
H	4.54555	-1.04549	0.72504
H	4.08131	-0.12741	-1.56590
H	0.46585	-0.74466	-0.53145
H	0.65865	0.39207	1.95292
C	1.09982	0.43783	-0.17843
C	3.60351	-0.56230	0.49252
N	2.17745	0.53231	-1.04103
C	3.35756	-0.08509	-0.75972
C	0.33309	-1.98682	-0.94127
O	-0.02451	-2.66850	-0.00036
O	0.63494	-2.03847	-2.11794
H	0.26654	1.09350	-0.42591
C	3.02027	-0.68490	2.92465
O	3.74715	-1.65349	3.13531
N	2.50223	0.07799	3.90846
H	2.74285	-0.14209	4.86551
H	2.03053	0.95221	3.72800

4-OH-PyH$_2$ + CO$_2$

4-OH-PyH$_2$ (-324.49298059, -324.08061095)

H	0.55146	0.99795	-1.77585
C	0.30172	0.75072	1.54580
C	1.32465	-0.11080	1.71797
H	2.74261	-1.48964	0.73795
H	2.25579	-0.54669	-1.52926
H	-1.07039	0.15680	-0.02871
H	-0.16617	1.26163	2.38476
C	-0.27569	0.90788	0.16579
C	1.97611	-0.73761	0.58562
N	0.79414	0.77044	-0.82172
C	1.70887	-0.23154	-0.64399
H	-0.73660	1.89349	0.04203
O	1.88115	-0.42103	2.92599
H	1.38188	0.00853	3.63345

Reactant complex (-513.00832451, -512.4085234)

H	0.53909	0.97475	-1.78291
C	0.29843	0.74203	1.54488
C	1.32700	-0.11218	1.71772
H	2.77083	-1.46810	0.74116
H	2.25917	-0.54929	-1.52953
H	-1.09472	0.18970	-0.02621

H	-0.17499	1.24387	2.38637
C	-0.27864	0.91575	0.16629
C	1.98860	-0.73242	0.58723
N	0.78211	0.74969	-0.82840
C	1.71007	-0.23610	-0.64442
C	0.00080	-3.13481	-0.43513
O	-0.92055	-2.56213	-0.01204
O	0.90770	-3.72488	-0.86573
H	-0.71035	1.91540	0.04611
O	1.87860	-0.42413	2.92751
H	1.37434	0.00115	3.63404

TS (-512.97546746, -512.3698872, 1149.50i)

H	2.05813	0.76580	-2.04602
C	1.52931	0.29471	1.19400
C	2.72705	-0.29630	1.49069
H	4.58966	-1.11260	0.68862
H	4.09859	-0.28146	-1.62503
H	0.48197	-0.64023	-0.51921
H	0.80040	0.53346	1.96274
C	1.16998	0.46028	-0.19150
C	3.65750	-0.61193	0.45315
N	2.23821	0.48420	-1.09100
C	3.39407	-0.17247	-0.80763
C	0.20872	-1.92041	-0.87324
O	-0.06988	-2.52589	0.13909
O	0.36125	-2.02207	-2.07200
H	0.38479	1.17810	-0.42936
O	3.13401	-0.58923	2.73975
H	2.44714	-0.36918	3.38506

4-NH_2-PyH_2 + CO_2

4-NH_2-PyH_2 (-304.62449870, -304.21946693)

H	0.58384	1.00853	-1.73245
C	0.32635	0.71161	1.58331
C	1.33413	-0.17569	1.76477
H	2.71289	-1.56801	0.72872
H	2.26903	-0.55900	-1.50303
H	-1.03824	0.13986	-0.01113
H	-0.14086	1.21935	2.42523
C	-0.24737	0.89068	0.20573
C	1.96740	-0.78766	0.60468
N	0.82687	0.77376	-0.77997
C	1.72189	-0.25022	-0.61527
H	-0.71174	1.87659	0.09564

H	2.81643	-0.73317	3.04919
H	1.52503	0.03398	3.78321
N	1.81892	-0.55933	3.01661

Reactant complex (-493.13986095, -492.54740023)

H	0.57017	0.98484	-1.74028
C	0.32345	0.70299	1.58210
C	1.33646	-0.17780	1.76380
H	2.74163	-1.54780	0.73147
H	2.27196	-0.56207	-1.50428
H	-1.06210	0.17313	-0.00674
H	-0.14930	1.20149	2.42659
C	-0.25000	0.89891	0.20637
C	1.98040	-0.78274	0.60554
N	0.81512	0.75414	-0.78741
C	1.72318	-0.25475	-0.61652
C	-0.03509	-3.13481	-0.47858
O	-0.96360	-2.56105	-0.07286
O	0.87758	-3.72761	-0.89311
H	-0.68549	1.89880	0.10041
H	2.81565	-0.73069	3.05356
H	1.51634	0.02611	3.78384
N	1.81712	-0.56325	3.01680

TS (-493.11116931, -492.51207271, 1120.79i)

H	2.06065	0.77856	-2.01350
C	1.55098	0.27800	1.22863
C	2.73889	-0.35205	1.52789
H	4.57281	-1.19610	0.65500
H	4.09112	-0.29643	-1.61150
H	0.51015	-0.61568	-0.49886
H	0.82868	0.51748	2.00396
C	1.17705	0.45157	-0.15235
C	3.64743	-0.66460	0.45637
N	2.24879	0.50128	-1.05936
C	3.38957	-0.18863	-0.79071
C	0.23472	-1.92776	-0.87787
O	-0.00204	-2.53728	0.13899
O	0.35384	-1.99725	-2.07984
H	0.40233	1.18859	-0.36923
H	4.06397	-0.86574	3.00743
H	2.54433	-0.33816	3.56768
N	3.08789	-0.70823	2.80058

$PyH_2 + PyH^+ = Py + PyH^+ + H_2$

PyH$^+$ (-248.55901788, -248.22434238)

C	-2.20210	0.03517	0.61558
C	-1.83122	-1.22300	0.14644
C	-0.83616	-1.31593	-0.80411
N	-0.24833	-0.19142	-1.25413
C	-0.58240	1.03973	-0.82384
C	-1.57276	1.17753	0.12617
H	-2.98242	0.12645	1.36491
H	-2.30516	-2.12649	0.51233
H	-0.48427	-2.25113	-1.22283
H	0.48463	-0.27555	-1.95435
H	-0.04095	1.87093	-1.25922
H	-1.84298	2.16767	0.47472

Reactant complex (-497.85381785, -497.18013887)

H	0.04163	1.64011	-3.43578
C	-0.30768	2.49257	-0.23114
C	0.95784	2.21865	0.15169
H	2.84034	1.17191	-0.39213
H	2.16338	0.96938	-2.78373
H	-1.31468	0.94150	-1.36767
H	-0.97266	3.09302	0.38454
H	1.33556	2.59637	1.10073
C	-0.82920	1.92830	-1.52649
C	1.85154	1.47532	-0.71863
N	0.27975	1.80798	-2.46872
C	1.48698	1.35517	-2.02466
H	0.10724	0.28689	0.66968
H	-1.59327	2.57921	-1.96270
C	-1.70609	-2.13930	1.92727
C	-0.93068	-3.21447	1.49783
H	0.84772	-3.81026	0.41349
H	1.47136	-1.41571	-0.10787
H	-2.61338	-2.28881	2.50088
H	-1.23145	-4.22968	1.73843
C	-1.30297	-0.85827	1.61021
C	0.22934	-2.99025	0.75960
N	-0.17766	-0.67707	0.89631
C	0.59191	-1.69162	0.46449
H	-1.84336	0.03660	1.89912

TS (-497.80172698, -497.12593704, 1170.29i)

H	1.44192	0.00520	-2.26738
C	1.75342	0.49128	0.97646
C	3.03127	0.03455	1.11521
H	4.70186	-0.98407	0.12445
H	3.57949	-0.89375	-2.11653

H	0.22755	-1.00408	-0.03685
H	1.21166	0.94258	1.80095
H	3.54700	0.14440	2.06541
C	1.06770	0.28238	-0.26384
C	3.70385	-0.57429	0.01948
N	1.86172	-0.00721	-1.34544
C	3.10440	-0.54654	-1.20599
H	0.31790	-1.76164	0.51247
H	0.16937	0.84807	-0.49354
C	-0.08464	-4.27081	3.10345
C	1.13746	-4.93119	3.00877
H	3.04443	-4.98986	1.98178
H	2.46378	-3.01958	0.53273
H	-0.84229	-4.58297	3.81471
H	1.35285	-5.77882	3.65313
C	-0.32328	-3.19420	2.26259
C	2.08193	-4.49869	2.08162
N	0.59400	-2.79020	1.37893
C	1.76870	-3.41442	1.27622
H	-1.25577	-2.63520	2.28457

Product complex (-497.85157828, -497.18407379)

H	-0.63176	1.61952	-2.70772
C	0.07695	2.22334	0.42378
C	1.29677	1.55208	0.48651
H	2.73386	0.36218	-0.61555
H	1.36767	0.44882	-2.72809
H	-2.96199	0.32110	-2.58985
H	-0.33587	2.73130	1.28781
H	1.85798	1.53210	1.41592
C	-0.61608	2.24152	-0.76869
C	1.79311	0.90030	-0.63996
N	-0.10387	1.60494	-1.83835
C	1.06179	0.93534	-1.80958
H	-2.51859	-0.10971	-2.16986
H	-1.56949	2.73772	-0.90750
C	-1.33917	-1.23856	1.88971
C	-0.20919	-2.01603	2.12134
H	1.42741	-3.05942	1.16042
H	0.69634	-2.39310	-1.11865
H	-1.95760	-0.88155	2.70828
H	0.08114	-2.28357	3.13418
C	-1.66755	-0.92252	0.57393
C	0.53932	-2.44755	1.03070
N	-0.95381	-1.32200	-0.48472
C	0.12567	-2.07636	-0.24503
H	-2.55046	-0.31710	0.36190

$PyH_2 + CO_2$ (DHT model)

PyH_2 (-249.28675217, -248.94361711)

C	2.68767	-0.96049	0.73390
C	0.78167	1.00960	1.18288
C	1.99987	1.10478	1.74824
H	3.88705	0.01891	2.18724
H	3.40802	-1.73569	0.48309
H	1.34966	-1.75761	-0.57971
H	0.07242	1.83347	1.20433
H	2.30795	2.02638	2.23982
N	1.53003	-0.94679	-0.00474
C	2.94457	0.00717	1.65014
C	0.35748	-0.30203	0.58008
H	-0.10296	-0.95345	1.35341
H	-0.39336	-0.16230	-0.20438

Reactant complex (-437.80217478, -437.27141471)

H	0.55278	1.00727	-1.77259
C	0.31858	0.72522	1.54133
C	1.35649	-0.11465	1.71352
H	2.76652	-1.49735	0.69453
H	2.24950	-0.55329	-1.55280
H	-1.07333	0.15445	-0.00811
H	-0.14630	1.23953	2.37913
H	1.76150	-0.29019	2.70903
C	-0.27149	0.90082	0.16810
C	1.99353	-0.74585	0.57139
N	0.79302	0.75977	-0.82312
C	1.71125	-0.24590	-0.65864
C	-0.01442	-3.14082	-0.45552
O	-0.93544	-2.58615	-0.00821
O	0.89062	-3.71536	-0.91046
H	-0.72686	1.89002	0.05086

TS (-437.76732668, -437.23152599, 1134.86i)

H	2.06111	0.79939	-2.04196
C	1.55359	0.28150	1.18758
C	2.75295	-0.29501	1.47568
H	4.60701	-1.11977	0.63700
H	4.09456	-0.27104	-1.65871
H	0.48231	-0.66041	-0.49663
H	0.83305	0.53177	1.95917
H	3.02831	-0.49398	2.50804
C	1.17916	0.46335	-0.19669

C	3.66967	-0.61603	0.43097
N	2.23807	0.48385	-1.09649
C	3.39974	-0.17508	-0.83150
C	0.20325	-1.92141	-0.86115
O	-0.10884	-2.53960	0.13542
O	0.37943	-2.01932	-2.05836
H	0.38482	1.17001	-0.43552

Product complex (-437.8142724, -437.28747857)

H	-0.10348	-0.05701	-1.12843
C	0.30075	1.88859	1.56881
C	1.49928	1.36228	2.04397
H	3.05039	-0.11074	1.70933
H	1.93519	-0.98576	-0.37077
H	-2.14245	-1.24316	-0.97442
H	-0.20345	2.70099	2.08004
H	1.95005	1.76570	2.94597
C	-0.24885	1.35435	0.41850
C	2.11734	0.31793	1.36115
N	0.36468	0.34909	-0.22387
C	1.51846	-0.17454	0.21656
C	-1.86973	-1.21845	-2.06115
O	-2.62835	-1.78459	-2.85940
O	-0.79306	-0.59710	-2.33463
H	-1.17884	1.70711	-0.01674

Py (-248.11500199, -247.78284294)

C	-2.21814	0.03699	0.62584
C	-1.83236	-1.21190	0.15021
C	-0.81984	-1.27459	-0.80285
N	-0.19287	-0.19752	-1.28987
C	-0.57513	0.99641	-0.82231
C	-1.57619	1.16694	0.12985
H	-3.00453	0.12869	1.37081
H	-2.30346	-2.12318	0.50807
H	-0.49542	-2.23879	-1.19350
H	-0.05436	1.86272	-1.22955
H	-1.84196	2.16369	0.47084

HCOOH (-189.69049521, -189.49342926)

C	-0.78308	0.27980	-0.00659
O	-1.31889	0.21685	-1.08689
O	-1.42188	0.35599	1.15902
H	-2.38084	0.35076	0.99244
H	0.30383	0.28234	0.15582

PyH_2 + HCOOH (DHT model)

Reactant complex (-438.98062054, -438.44189429)

H	0.33165	0.12471	-1.17980
C	0.52733	1.36167	1.90587
C	1.84760	1.16993	2.08859
H	3.65396	0.12707	1.32549
H	2.58825	-0.34870	-0.87677
H	-0.52150	-0.36918	1.14461
H	-0.06056	1.98556	2.57492
H	2.36325	1.65099	2.91860
C	-0.17136	0.62707	0.79449
C	2.61429	0.37827	1.14407
N	0.74928	0.48406	-0.32924
C	2.03861	0.10550	-0.05515
O	-1.37568	-0.70016	-2.13295
O	-3.30968	-1.26627	-1.13078
H	-3.32536	-0.32178	-0.89335
C	-2.21480	-1.52000	-1.83912
H	-2.17900	-2.58062	-2.12280
H	-1.05959	1.17010	0.45276

TS (-438.93744912, -438.39748315, 1087.83i)

H	2.03988	0.06725	-1.77544
C	1.89109	0.40041	1.49973
C	3.20140	0.14472	1.78274
H	5.16217	-0.36818	0.94562
H	4.32274	-0.26219	-1.40881
H	0.74377	-0.95328	-0.02430
H	1.17083	0.61676	2.28204
H	3.54966	0.17595	2.81176
C	1.42247	0.31724	0.14662
C	4.12209	-0.14491	0.73684
N	2.39315	0.25516	-0.83481
C	3.68137	-0.08789	-0.55171
O	0.88506	-1.61492	-1.98652
O	-1.11970	-1.15278	-0.96134
H	-1.14998	-0.59779	-1.75488
C	0.18687	-1.68935	-0.92493
H	0.13429	-2.63849	-0.35267
H	0.51833	0.85846	-0.14397

Product complex (-439.00226827, -438.47127528)

H	-0.56092	-0.18481	-1.56328
C	0.55976	1.71973	1.91865
C	1.81660	1.17406	2.16008

H	3.30986	-0.20150	1.40653
H	1.94015	-0.80497	-0.58624
H	-0.86786	-2.25330	-0.84027
H	0.11720	2.44089	2.59929
H	2.38440	1.46198	3.04110
C	-0.12802	1.32069	0.77782
C	2.33437	0.25161	1.25654
N	0.36348	0.43783	-0.09852
C	1.57093	-0.08500	0.14411
O	-1.04723	-0.73219	-2.22636
O	-2.68577	-1.42918	-0.72140
H	-3.39046	-1.10417	-1.29666
C	-1.59475	-1.80404	-1.53256
H	-1.90130	-2.54966	-2.27778
H	-1.11561	1.72324	0.55583

$CH_2(OH)_2$ (-190.87620389, -190.67546094)

H	-0.60316	-0.14931	-1.58058
H	-0.87851	-2.28796	-0.83671
O	-1.01106	-0.74914	-2.21888
O	-2.67060	-1.41315	-0.72050
H	-3.38523	-1.10825	-1.29484
C	-1.59370	-1.81514	-1.52024
H	-1.90605	-2.53441	-2.28656

PyH_2 + OCH_2 (DHT model)

OCH_2 (-114.45023845, -114.32131256)

O	-1.18653	-1.24954	-2.25865
C	-1.59014	-1.81014	-1.26671
H	-0.91264	-2.37168	-0.59420
H	-2.65917	-1.79293	-0.97767

Reactant complex (-363.73997022, -363.26853873)

H	-0.05970	0.89952	-1.59668
C	-0.23470	1.15247	1.71756
C	0.92019	0.51962	1.99788
H	2.50930	-0.79588	1.17691
H	1.86405	-0.30160	-1.18058
H	-1.46995	0.07013	0.32204
H	-0.77901	1.71887	2.46891
H	1.35068	0.57206	2.99655
C	-0.83347	0.99015	0.34936
C	1.63940	-0.18721	0.95389
N	0.23984	0.90215	-0.63018

C	1.29194	0.06823	-0.33253
O	-1.18590	-1.24889	-2.26047
C	-1.59028	-1.80924	-1.26612
H	-1.48759	1.82652	0.08394
H	-0.91224	-2.37271	-0.59337
H	-2.66007	-1.79344	-0.97726

TS (-363.71586281, -363.24358942, 1069.54i)

H	2.08464	0.00776	-1.82839
C	1.70665	0.38378	1.42713
C	2.97175	0.05720	1.81011
H	4.95543	-0.58343	1.11908
H	4.31669	-0.41291	-1.28767
H	0.68495	-0.91882	-0.16796
H	0.93910	0.63958	2.15054
H	3.24488	0.07433	2.86197
C	1.33811	0.30826	0.03596
C	3.95021	-0.29472	0.83300
N	2.38350	0.23391	-0.87308
C	3.61790	-0.20399	-0.48424
O	1.00525	-1.59006	-2.15686
C	0.34613	-1.81664	-1.07714
H	0.48934	0.89854	-0.31432
H	0.59483	-2.71804	-0.47565
H	-0.74203	-1.59166	-1.05454

Product complex (-363.79261962, -363.32829116)

H	-0.77069	-0.52025	-1.75334
C	-0.14487	1.32863	1.80627
C	1.18975	1.12486	2.14227
H	3.04786	0.22537	1.48970
H	2.04677	-0.63772	-0.61898
H	-1.34683	-2.72474	-1.29008
H	-0.81438	1.88150	2.45848
H	1.59117	1.51736	3.07309
C	-0.61186	0.80571	0.60533
C	2.00088	0.40945	1.26739
N	0.16004	0.11706	-0.24364
C	1.44174	-0.07326	0.08881
O	-1.41596	-0.93414	-2.36659
C	-2.05686	-1.96404	-1.64741
H	-1.65173	0.94282	0.30730
H	-2.77222	-2.45415	-2.31484
H	-2.61155	-1.57992	-0.77738

CH_3OH (-115.66785816, -115.53401711)

H	-0.77198	-0.50805	-1.77342

H	-1.35130	-2.73420	-1.28767
O	-1.40982	-0.93583	-2.35529
C	-2.05818	-1.97053	-1.63734
H	-2.76655	-2.44387	-2.32178
H	-2.61627	-1.58477	-0.77414

$PyH_2 + CO_2 + 1H_2O$ (DHT-$1H_2O$ model)

$CO_2 + 1H_2O$ (-264.92026264, -264.66137293)

C	-1.01819	-1.91362	-0.27921
O	-1.62922	-2.56329	0.46585
O	-0.40152	-1.26286	-1.02340
O	-0.30388	0.29842	-3.69163
H	-0.87338	1.07401	-3.65063
H	-0.41254	-0.13756	-2.83717

Reactant complex (-514.21403428, -513.61295031)

H	0.78202	1.09495	-1.45257
C	-0.09448	1.51631	1.73525
C	0.83651	0.71053	2.28009
H	2.35146	-0.85959	1.86172
H	2.36274	-0.36057	-0.58028
H	-1.15428	0.68014	0.04487
H	-0.70259	2.18180	2.34329
H	1.00828	0.71857	3.35544
C	-0.36263	1.43542	0.25814
C	1.66542	-0.13350	1.43854
N	0.87266	1.09778	-0.44020
C	1.67355	0.12768	0.10594
C	-0.94155	-1.99840	-0.26958
O	-1.35021	-2.25651	0.78849
O	-0.54213	-1.75286	-1.33665
O	-0.43234	0.78483	-3.06355
H	-0.28085	0.95251	-4.00024
H	-0.65570	-0.15227	-3.00233
H	-0.74101	2.38436	-0.13804

TS (-514.18526226, -513.57929739, 1083.86i)

H	2.51421	0.35472	-1.94044
C	1.48604	0.49785	1.20876
C	2.57972	-0.05804	1.79746
H	4.48891	-1.08936	1.45492
H	4.42629	-0.65092	-1.00547
H	0.66966	-0.65721	-0.45621
H	0.66791	0.91398	1.78763
H	2.66766	-0.07169	2.88087

C	1.35844	0.43054	-0.23513
C	3.63508	-0.59842	1.00219
N	2.56316	0.26804	-0.92303
C	3.60867	-0.37978	-0.34545
C	0.33926	-1.99048	-0.69515
O	-0.03057	-2.45938	0.35132
O	0.56226	-2.21527	-1.86716
O	1.31368	0.04676	-3.45160
H	1.58798	-0.06704	-4.36769
H	0.99481	-0.82308	-3.15206
H	0.67936	1.13037	-0.72556

Product complex (-514.2266485, -513.62741842)

H	0.03200	0.88329	-1.00742
C	0.56613	2.25586	1.96509
C	1.43800	1.29784	2.47624
H	2.46454	-0.56749	2.07754
H	1.47704	-0.75211	-0.23374
H	-1.45645	-1.64852	-0.69683
H	0.27777	3.12509	2.54507
H	1.84522	1.41225	3.47637
C	0.06242	2.08639	0.69029
C	1.78814	0.19269	1.70400
N	0.41745	1.01228	-0.03322
C	1.25656	0.07358	0.43503
C	-1.56103	-2.41128	-1.51571
O	-1.95893	-3.54230	-1.18528
O	-1.25664	-2.00487	-2.67445
O	-0.54515	0.52466	-2.50960
H	0.03366	0.75670	-3.24342
H	-0.80354	-0.43784	-2.63504
H	-0.62143	2.78380	0.22045

HCOOH + 1H_2O (-266.10831756, -265.83982978)

O	-0.72149	-2.14189	-1.25745
O	-0.57979	0.33960	-2.74239
H	-0.69635	0.53354	-3.67988
H	-0.09264	-0.49723	-2.69397
O	-2.46504	-0.72223	-1.12918
H	-1.90819	-0.18818	-1.75913
C	-1.81764	-1.83473	-0.83318
H	-2.40156	-2.46254	-0.14415

PyH_2 + HCOOH + 1H_2O (DHT-1H_2O model)

Reactant complex (-515.40011118, -514.7899501)

H	0.05751	1.06801	-0.88996
C	0.51113	1.19935	2.41391
C	1.77914	0.74454	2.42708
H	3.34307	-0.30221	1.24721
H	2.16502	0.13571	-0.90962
H	-0.80606	-0.05719	1.25747
H	0.06240	1.68228	3.27862
H	2.39656	0.85818	3.31698
C	-0.33076	0.94855	1.19290
C	2.36348	0.16371	1.23227
N	0.52004	1.03945	0.01290
C	1.72442	0.38708	0.05402
O	-0.73259	-2.13666	-1.27946
O	-0.57590	0.30629	-2.72937
H	-0.57350	0.66663	-3.62416
H	-0.14961	-0.56423	-2.77135
O	-2.50540	-0.75260	-1.14380
H	-1.99334	-0.23954	-1.82131
C	-1.81194	-1.83021	-0.81524
H	-2.34042	-2.42334	-0.05466
H	-1.14328	1.67625	1.09834

TS (-515.35878397, -514.74791559, 1058.74i)

H	2.13351	0.48104	-1.76855
C	1.89323	0.35338	1.53443
C	3.19163	0.04429	1.81260
H	5.15149	-0.46586	0.96614
H	4.36298	-0.10622	-1.38270
H	0.75724	-0.87795	-0.01717
H	1.17165	0.54855	2.32120
H	3.52955	0.00748	2.84504
C	1.43440	0.35361	0.16986
C	4.12152	-0.19803	0.76045
N	2.42332	0.34892	-0.79621
C	3.70601	-0.01451	-0.52447
O	1.08121	-2.10392	-1.66238
O	0.91349	0.03445	-3.21990
H	1.03170	0.08157	-4.17418
H	1.08874	-0.89496	-2.93190
O	-0.94983	-1.10226	-1.20870
H	-0.72405	-0.60538	-2.01521
C	0.21561	-1.76576	-0.78746
H	-0.08579	-2.48645	-0.00188
H	0.54885	0.93466	-0.09967

Product complex (-515.4187148, -514.8160729)

H	0.01765	0.56420	-1.54065
C	0.59420	1.16340	2.35352
C	1.94399	0.93620	2.60313
H	3.83705	0.41879	1.68926
H	2.84603	0.25187	-0.58907
H	-1.27882	-1.45536	-0.22243
H	-0.09287	1.42456	3.15273
H	2.34119	1.01690	3.61158
C	0.13538	1.04881	1.04657
C	2.77758	0.60438	1.53990
N	0.92933	0.72887	0.01746
C	2.22578	0.51164	0.26707
O	-1.61478	-2.28470	-2.07614
O	-0.66385	0.37560	-2.23439
H	-0.52015	1.00342	-2.94986
H	-1.05861	-1.58108	-2.45559
O	-3.00060	-0.70111	-1.06614
H	-2.46763	0.02088	-1.44558
C	-2.11394	-1.76887	-0.87292
H	-2.67256	-2.57057	-0.38175
H	-0.91502	1.22093	0.80982

$CH_2(OH)_2 + 1H_2O$ (-267.29190769, -267.01911584)

H	0.12583	0.72681	-1.65441
H	-1.33187	-1.52060	-0.18837
O	-1.61332	-2.28516	-2.07842
O	-0.61539	0.40943	-2.18437
H	-0.59650	0.93781	-2.99134
H	-1.00229	-1.60448	-2.40619
O	-3.00500	-0.70392	-1.06730
H	-2.44773	0.03751	-1.35808
C	-2.14611	-1.79490	-0.87834
H	-2.74091	-2.60009	-0.43864

$PyH_2 + OCH_2 + 1H_2O$ (DHT-$1H_2O$ model)

$OCH_2 + 1H_2O$ (-190.86169752, -190.66300134)

O	-0.67178	-1.60790	-1.33899
O	-1.18052	0.77498	-2.88151
H	-1.41827	0.50387	-3.77388
H	-1.01961	-0.05303	-2.39547
C	-1.46778	-2.04570	-0.53756
H	-1.23830	-2.93625	0.07541
H	-2.45770	-1.57745	-0.38166

Reactant complex (-440.15498866, -439.6128502)

H	0.20954	0.88799	-1.26028
C	-0.05690	1.16300	2.04685
C	1.08906	0.53450	2.37372
H	2.71647	-0.77687	1.62562
H	2.14943	-0.31364	-0.75780
H	-1.25198	0.04799	0.63904
H	-0.61964	1.75072	2.76774
H	1.49041	0.60932	3.38334
C	-0.61357	0.96854	0.66511
C	1.84403	-0.18629	1.36665
N	0.48260	0.85314	-0.28145
C	1.53769	0.05292	0.06389
O	-0.75536	-1.85585	-1.54112
O	-1.24456	0.65162	-2.69172
H	-1.21821	0.83199	-3.63706
H	-1.18409	-0.31549	-2.59726
C	-1.45776	-2.02652	-0.56618
H	-1.10973	-2.61212	0.30558
H	-1.26171	1.79606	0.35813
H	-2.48426	-1.61512	-0.50591

TS (-440.13735004, -439.59418928, 1083.76i)

H	2.18181	0.50662	-1.83051
C	1.82630	0.44973	1.46927
C	3.06929	0.00397	1.79414
H	4.97865	-0.75859	1.01413
H	4.32798	-0.31633	-1.35834
H	0.71530	-0.70660	-0.09876
H	1.10804	0.74799	2.22643
H	3.37567	-0.04088	2.83625
C	1.40642	0.44639	0.08197
C	3.99592	-0.37007	0.77208
N	2.43587	0.37407	-0.84840
C	3.65345	-0.14193	-0.52643
O	1.15961	-1.97866	-1.75334
O	0.84705	0.22765	-3.22660
H	1.02401	0.17502	-4.17087
H	0.87506	-0.69824	-2.87476
C	0.42930	-1.86319	-0.70762
H	0.64884	-2.50265	0.17340
H	0.59628	1.11481	-0.21552
H	-0.65602	-1.65554	-0.82137

Product complex (-440.20757707, -439.67281457)

H	-0.34382	0.48397	-1.77200
C	0.03843	1.12111	2.16395

C	1.35882	0.83095	2.49343
H	3.26881	0.19463	1.69772
H	2.39749	0.03067	-0.62916
H	-1.04807	-1.91279	-0.31139
H	-0.67673	1.43690	2.91762
H	1.70327	0.91438	3.52089
C	-0.35403	0.99838	0.83597
C	2.23042	0.43146	1.48555
N	0.47739	0.61588	-0.14058
C	1.74470	0.33928	0.18571
O	-2.02098	-2.16708	-2.14502
O	-0.96128	0.36919	-2.53492
H	-0.47929	0.64997	-3.31945
H	-1.65082	-1.32597	-2.47878
C	-2.05254	-2.05816	-0.73896
H	-2.46462	-2.98700	-0.33296
H	-1.38053	1.21288	0.53746
H	-2.68906	-1.22499	-0.40328

CH_3OH + 1H2O (-192.08149121, -191.87651528)

H	0.25827	0.41892	-2.63271
H	-1.32632	-1.82881	-0.05715
O	-1.76807	-2.24015	-2.05769
O	-0.66707	0.32739	-2.37780
H	-1.14007	0.99026	-2.89404
H	-1.36657	-1.39603	-2.33350
C	-2.17000	-2.08770	-0.71320
H	-2.58569	-3.04091	-0.37300
H	-2.94496	-1.31583	-0.59768

PyH_2 + CO_2 + $2H_2O$ (DHT-$2H_2O$ model)

CO_2 + $2H_2O$ (-341.33366124, -341.00398495)

C	-0.98689	-2.35520	0.32045
O	-1.06805	-2.75754	1.40731
O	-0.90261	-1.95605	-0.77124
O	0.41722	2.33767	-2.78744
H	0.70655	2.33858	-3.70509
H	-0.28372	1.65988	-2.73710
O	-1.61453	0.37705	-2.61647
H	-2.48662	0.69432	-2.35619
H	-1.42934	-0.37335	-2.03591

Reactant complex (-590.62903929, -589.95820447)

H	1.19694	1.30825	-1.12003
C	-0.00955	1.31470	1.98794

C	0.79716	0.36314	2.49648
H	2.21949	-1.27084	2.00576
H	2.53541	-0.44393	-0.32659
H	-0.96456	0.74460	0.13382
H	-0.60228	1.96725	2.62454
H	0.87619	0.22854	3.57449
C	-0.15429	1.41913	0.49409
C	1.62972	-0.44411	1.62374
N	1.11543	1.07317	-0.13233
C	1.80047	-0.00669	0.34659
C	-0.93173	-2.22380	0.32816
O	-1.05462	-2.62225	1.41255
O	-0.82158	-1.83799	-0.76699
O	0.64191	1.84998	-2.94027
H	0.45723	2.77325	-3.14029
H	-0.22375	1.39467	-2.94072
O	-1.69186	0.31400	-2.72053
H	-2.49382	0.74096	-2.39770
H	-1.52976	-0.42347	-2.11591
H	-0.43491	2.43062	0.17890

TS (-590.60143999, -589.92683545, 1032.33i)

H	2.47116	0.71915	-1.96571
C	1.45784	0.45654	1.18335
C	2.55774	-0.16100	1.69340
H	4.43939	-1.18770	1.21222
H	4.34596	-0.48949	-1.18738
H	0.61033	-0.56775	-0.53632
H	0.66334	0.83849	1.81627
H	2.67628	-0.26346	2.76929
C	1.29183	0.49949	-0.25986
C	3.58205	-0.64778	0.82669
N	2.48101	0.40291	-0.98708
C	3.53504	-0.29323	-0.49299
C	0.27698	-1.93039	-0.68298
O	0.00324	-2.34568	0.41178
O	0.40569	-2.20881	-1.85771
O	2.05045	1.36570	-3.63409
H	1.81528	2.29798	-3.68639
H	1.23420	0.86179	-3.84310
O	-0.08334	-0.34483	-3.93320
H	-0.97973	-0.01151	-3.81651
H	0.04588	-1.01275	-3.23358
H	0.60327	1.23975	-0.67361

Product complex (-590.64281914, -589.97369813)

H	0.88891	1.02464	-1.03931

C	0.03776	1.20640	2.13210
C	1.06088	0.43543	2.67918
H	2.82148	-0.75036	2.24796
H	2.64472	-0.33340	-0.22800
H	-1.88432	-0.72792	0.02114
H	-0.72514	1.65996	2.75425
H	1.10926	0.28059	3.75277
C	0.00685	1.39314	0.76421
C	2.01936	-0.14042	1.84867
N	0.95225	0.83640	-0.01089
C	1.93983	0.07571	0.48657
C	-1.17523	-1.56796	-0.22083
O	-0.77628	-2.25765	0.73435
O	-0.87498	-1.68670	-1.44304
O	0.48649	1.49017	-2.61985
H	0.52781	2.42570	-2.84477
H	-0.42950	1.18211	-2.82329
O	-1.90166	0.26359	-2.92566
H	-2.67636	0.62978	-2.48668
H	-1.60322	-0.51571	-2.37727
H	-0.74864	1.97957	0.25075

HCOOH + 2H_2O (-342.52003611, -342.18089250)

O	-0.15475	-2.08148	-1.57167
O	-0.52214	1.73570	-2.59811
H	-0.93105	2.09949	-1.80619
H	-1.09413	0.99462	-2.86362
O	-2.00015	-0.66042	-3.11632
H	-2.63699	-0.83251	-3.82017
H	-1.30434	-1.33623	-3.18079
O	-1.88632	-1.19368	-0.43535
H	-2.18953	-0.94082	-1.34316
C	-0.73538	-1.83723	-0.53286
H	-0.36089	-2.13113	0.45780

PyH_2 + HCOOH + 2H_2O (DHT-2H_2O model)

Reactant complex (-591.81488784, -591.13379675)

H	0.62661	0.96034	-0.63259
C	0.65522	1.42166	2.66898
C	1.69996	0.62168	2.95750
H	3.03349	-0.98099	2.19282
H	2.36439	-0.56545	-0.17016
H	-0.85777	0.48324	1.44617
H	0.27398	2.14913	3.38181
H	2.19302	0.69114	3.92636
C	-0.05400	1.24570	1.35350
C	2.24129	-0.27859	1.95635

N	0.91497	0.84779	0.33760
C	1.87164	-0.06861	0.66396
O	-0.13848	-2.05640	-1.59744
O	-0.45865	1.47523	-2.21302
H	-0.95600	2.29141	-2.09426
H	-1.07615	0.84654	-2.62900
O	-2.04053	-0.68910	-3.14299
H	-2.67737	-0.73474	-3.86610
H	-1.37538	-1.37952	-3.29420
O	-1.89252	-1.20097	-0.46991
H	-2.22730	-1.01644	-1.38205
C	-0.70097	-1.76908	-0.56005
H	-0.27234	-1.95062	0.43857
H	-0.54097	2.17090	1.02467

TS (-591.77646278, -591.0962208, 1074.11i)

H	2.10045	0.65995	-1.81376
C	1.87623	0.38044	1.48613
C	3.15756	-0.00855	1.73945
H	5.07590	-0.60420	0.85275
H	4.29305	-0.10259	-1.47058
H	0.70937	-0.76415	-0.07008
H	1.17498	0.59569	2.28606
H	3.50655	-0.09047	2.76577
C	1.40486	0.43124	0.12418
C	4.06028	-0.27303	0.66824
N	2.38260	0.42259	-0.85290
C	3.64484	-0.01538	-0.60482
O	1.03061	-1.99188	-1.70897
O	1.37641	1.22569	-3.39305
H	0.86900	2.04390	-3.37874
H	0.77091	0.52849	-3.72321
O	-0.14410	-0.99877	-3.85738
H	-0.32198	-1.51794	-4.64837
H	0.40541	-1.54576	-3.23874
O	-1.06248	-1.24063	-1.08633
H	-1.03953	-0.93955	-2.01288
C	0.21092	-1.73362	-0.76574
H	0.09034	-2.45132	0.07152
H	0.53898	1.05163	-0.12204

Product complex (-591.83309921, -591.16040984)

H	-0.32004	1.53218	-0.98899
C	1.36001	2.23583	2.61935
C	1.84396	1.00371	3.04749
H	2.03445	-1.08703	2.52340
H	0.85703	-0.78520	0.33558

H	-0.40254	-3.24004	-0.09305
H	1.47140	3.12977	3.22570
H	2.34756	0.91045	4.00633
C	0.72178	2.30281	1.38615
C	1.67153	-0.10692	2.22780
N	0.54936	1.23924	0.59184
C	1.01874	0.05622	1.01028
O	0.25238	-2.03051	-1.56596
O	-0.77345	1.73735	-1.84558
H	-1.42389	2.41808	-1.64237
H	-1.44240	0.32888	-2.65572
O	-1.71538	-0.57561	-2.93622
H	-2.14554	-0.49131	-3.79326
H	-0.12361	-1.56776	-2.33640
O	-1.74446	-1.76335	-0.37782
H	-2.16917	-1.31627	-1.13041
C	-0.82151	-2.66517	-0.92472
H	-1.32834	-3.34906	-1.62476
H	0.33017	3.25017	1.01627

$CH_2(OH)_2 + 2H_2O$ (-343.70587519, -343.36237928)

H	-0.35691	1.55188	-1.01918
H	-0.43138	-3.31239	-0.13196
O	0.26914	-2.03926	-1.52888
O	-0.77952	1.78596	-1.85444
H	-1.38216	2.50827	-1.64234
H	-1.47481	0.33363	-2.69033
O	-1.71177	-0.58897	-2.92057
H	-2.15152	-0.56249	-3.77680
H	-0.08334	-1.55733	-2.29774
O	-1.73587	-1.79132	-0.35259
H	-2.15600	-1.31224	-1.08731
C	-0.82478	-2.68344	-0.93537
H	-1.33904	-3.31487	-1.67774

$PyH_2 + OCH_2 + 2H_2O$ (DHT-$2H_2O$ model)

$OCH_2 + 2H_2O$ (-267.27571965, -267.00628975)

O	-0.32911	-2.20762	-0.93571
O	-0.37532	1.99234	-3.12045
H	-0.65753	2.76348	-2.61914
H	-0.90729	1.24840	-2.77434
O	-1.89915	-0.15038	-2.12351
H	-2.50383	-0.55807	-2.75251
H	-1.39323	-0.88453	-1.72643

C	-0.40049	-2.54042	0.22723
H	0.27912	-3.30217	0.65006
H	-1.14374	-2.10017	0.91728

Reactant complex (-516.57383851, -515.96093412)

H	0.74233	1.25807	-0.98994
C	-0.27771	1.01427	2.18629
C	0.62130	0.09891	2.59454
H	2.17385	-1.34992	1.94296
H	2.27316	-0.39431	-0.35224
H	-1.31317	0.60935	0.32840
H	-0.90014	1.55732	2.89346
H	0.74585	-0.11073	3.65581
C	-0.49073	1.24895	0.71567
C	1.48372	-0.57023	1.63813
N	0.74983	0.98088	-0.00983
C	1.54670	-0.04942	0.38112
O	-0.44739	-2.23386	-1.04903
O	-0.19770	1.79634	-2.67320
H	-0.61626	2.66319	-2.68299
H	-0.92484	1.14462	-2.58079
O	-2.04411	-0.21399	-2.17340
H	-2.55812	-0.56831	-2.90699
H	-1.54253	-0.97090	-1.80763
C	-0.35328	-2.38937	0.15508
H	-0.79335	2.28328	0.51290
H	0.36618	-3.10503	0.59118
H	-1.01252	-1.86181	0.87021

TS (-516.55546645, -515.94247406, 962.01i)

H	2.21061	0.62180	-1.90276
C	1.65198	0.36195	1.36175
C	2.87135	-0.10856	1.73665
H	4.81567	-0.85757	1.03378
H	4.31165	-0.29348	-1.34771
H	0.64597	-0.72667	-0.29206
H	0.89521	0.64019	2.08851
H	3.12127	-0.19361	2.79141
C	1.31062	0.40558	-0.04819
C	3.84999	-0.45266	0.75279
N	2.39086	0.37245	-0.92258
C	3.58492	-0.16166	-0.55233
O	1.14208	-1.96947	-1.96130
O	1.48771	1.24703	-3.49157
H	1.09831	2.12721	-3.46432
H	0.75995	0.62756	-3.72484
O	-0.34349	-0.75648	-3.78731

H	-0.43950	-1.23649	-4.61582
H	0.21070	-1.32416	-3.18246
C	0.44938	-1.91829	-0.88636
H	0.51923	1.08718	-0.36871
H	0.77120	-2.51619	-0.00815
H	-0.65462	-1.81786	-0.95681

Product complex (-516.62378003, -516.01829799)

H	-1.11555	1.32433	-0.78347
C	1.01434	1.89369	2.67389
C	1.82739	0.76507	2.69994
H	2.30385	-1.08028	1.67370
H	0.60359	-0.69435	-0.10542
H	-1.75509	-1.24187	-0.55840
H	1.08723	2.66034	3.43954
H	2.55742	0.62758	3.49344
C	0.09749	2.02624	1.63722
C	1.69065	-0.18412	1.69221
N	-0.04108	1.11856	0.66397
C	0.74432	0.03404	0.69636
O	-0.30908	-2.56717	-1.27615
O	-1.60555	1.36030	-1.64354
H	-2.54120	1.29595	-1.42466
H	-0.98641	0.10940	-2.73005
O	-0.63197	-0.64860	-3.24793
H	0.10173	-0.30025	-3.76477
H	-0.27101	-2.00611	-2.07588
C	-1.56149	-2.32061	-0.67334
H	-0.55393	2.89715	1.58368
H	-1.55780	-2.77327	0.32322
H	-2.39127	-2.75793	-1.24765

$CH_3OH + 2H_2O$ (-268.49573111, -268.21998055)

H	-1.11143	1.60033	-0.83420
H	-1.78709	-1.37292	-0.40766
O	-0.25672	-2.56270	-1.18867
O	-1.57119	1.47685	-1.67279
H	-2.50925	1.45958	-1.45031
H	-0.96547	0.11873	-2.72736
O	-0.67205	-0.68177	-3.20814
H	-0.03145	-0.38201	-3.86118
H	-0.20355	-1.97263	-1.96424
C	-1.55970	-2.41836	-0.66618
H	-1.62861	-3.01732	0.24678
H	-2.32818	-2.77363	-1.36864

C. Supporting information – Roles of the Lewis Acid and Base in the Chemical Reduction of CO_2 Catalyzed by Frustrated Lewis Pairs

C.1 Computational Details

All ab initio calculations were conducted using GAMESS[59] and GAUSSIAN 09[61] computational chemistry software. All geometries and the relevant transition state (TS) structures, unless otherwise noted, were obtained using the B97-D density functional.[224] The B97-D functional was developed to correctly describe dispersion effects. Grimme *et al.* previously used the B97-D functional to describe the heterolytic cleavage of dihydrogen by a bulky Frustrated Lewis Pair (FLP) catalyst and demonstrated the erroneous results of the B3LYP functional in describing this system due to the incorrect description of dispersion effects.[225] The bulky ligands in the trichloroaluminum ($AlCl_3$) and trimesitylenephosphine ($PMes_3$, Mes = 2,4,6-$C_6H_2Me_3$) FLP system[20] of the present study also suggest significant dispersion effects and the B97-D functional was thus selected for describing this system. For accurate energies, we performed single point MP2[58] energy calculations at the optimized geometries of B97-D. A benchmarking study (Section 2) validated the MP2//B97-D method for describing the FLP system. The energy difference between MP2//B97-D and the high level CCSD(T)//MP2 was within 1 kcal mol^{-1} for both hydride transfer (HT) and complexation energy calculations. A moderate size 6-311G (d,p) Pople basis set was used for geometry optimizations with B97-D while the more extensive 6-311++G(d,p) Pople basis set was used for single point energy calculations with MP2, denoted as MP2/6-311++G(d,p)// B97-D/6-311G(d,p).

Solvation effects were described using the Polarizable Continuum Model (PCM).[67-68] Also, the use of C_6H_5Cl as the solvent instead of the experimentally used C_6H_5Br solvent[20] should give quantitatively similar TS structures and reaction energies because the main parameters in the PCM model of cavity size and dielectric constant are similar between C_6H_5Cl and C_6H_5Br. Hessian calculations on all TS structures verified that only one imaginary frequency was obtained and corresponded to the normal mode of the reaction pathway. The TS structures were further verified by Intrinsic Reaction Coordinate (IRC) calculations to confirm the correct corresponding reactants and products were connected by the TS identified. The reaction activation barrier was referenced to reactants determined from converged IRC calculations. Hessian calculations were also performed on the reactants to verify that those reactants correspond to stationary points along the reaction pathway.

Thermochemistry properties for a number of LA or/and LB catalyzed complexes were computed referencing to dimeric LA $(AlCl_3)_2$, free CO_2 and free LB ($PMes_3$) at T=298K and P= 1atm. $AlCl_3$ has been known to form dimers[226] at moderate temperatures in both non-coordinating solvent[229-230] and in gas phase.[231] The $AlCl_3$ dimer was thus chosen as the thermodynamic reference. The reported enthalpies, H, are zero point energy (ZPE) and thermally corrected (T=298.15K) at each stationary point. Solvation energy is implicitly included in the energy of converged geometries. The reported entropies, S, are determined using the ideal gas approximation (P = 1 atm, T=298.15K) for the associated partition functions. The calculated gas phase values for S provide an upper estimate due to the reduction in translational degrees of freedom from the gas phase system as compared to the experimental condensed phase system. The approximations imposed on entropy calculations do not affect the conclusions drawn on the role of LB, which is justified by the dominating enthalpic driving force leading to the formation of a high concentration of the activated FLP•CO_2 complex.

C.2 Benchmarking Studies

A HT benchmarking study was performed using a model system of 2$AlCl_3$•PH_3•CO_2 + AB, where the TS structure is shown in Figure S1a. In this structure, we replace the bulky trimesitylenephosphine base ($PMes_3$), with a phosphine base (PH_3). The HT barrier at MP2/6-311++G(d,p)//B97-D/6-311G(d,p) was compared to CCSD(T)/6-311++G(d,p)// MP2/6-311G(d,p). Both calculations were done in gas phase at T=0K and not ZPE corrected. Table S1 (system **a**) shows that MP2//B97-D differs by -0.1 kcal mol^{-1} as compared to the high level CCSD(T)//MP2 calculation. Thus, the chosen MP2//B97-D method should describe HT reactions correctly. The $AlCl_3$•PH_3 model system was chosen to benchmark the complexation energy (Figure S1b). The complexation energy was calculated based on the difference in energy of the $AlCl_3$•PH_3 complex and the infinitely separated reactants of $AlCl_3$ and PH_3. Results from Table S1 (system **b**) shows that MP2//B97-D differs by -0.8 kcal mol^{-1} as compared to the CCSD(T)//MP2 calculation. Table S1 (system **c**) shows strong evidence that B3LYP functional significantly underestimates the complexation energy due to an insufficient description of the dispersion interaction in the bulky $AlCl_3$•$PMes_3$ complex. B3LYP predicts a complexation energy of -15.8 kcal mol^{-1} while MP2//B97-D yields -40.0 kcal mol^{-1}. Not shown in Table S1, B97-D results in a complexation energy of -32.5 kcal mol^{-1} and is in agreement with the MP2//B97-D results. Based on the results of this benchmarking study, the MP2//B97-D level of theory was selected to describe the FLP systems of this investigation.

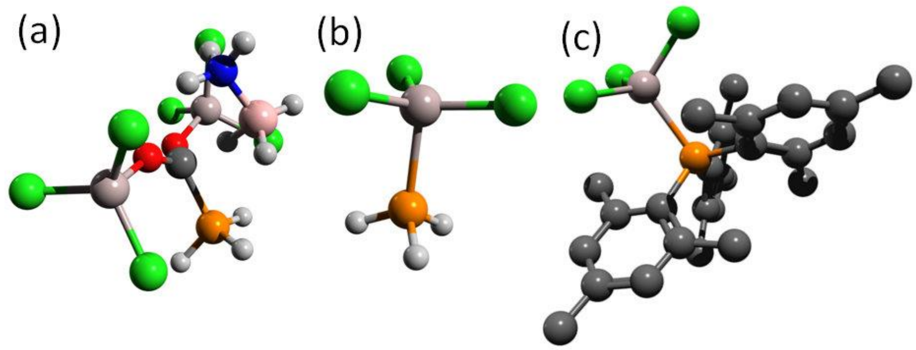

Figure S1. a) TS structure for hydride transfer for $2AlCl_3$•PH_3•CO_2 + AB b) $AlCl_3$•PH_3 complex c) $AlCl_3$•$PMes_3$ complex. H atoms in (c) omitted for clarity. Al, light gray; B, pink; C, gray; Cl, green; H, white; N, blue; O, red; P, orange.

Table S1. Benchmarking studies comparing different quantum chemical methods

System[a]	CCSD(T)//MP2[b]	MP2//B97-D[b]	B3LYP [c]
a) $2AlCl_3$•PH_3•CO_2 + AB, $\Delta E_{hydride}$	9.0	8.9	8.9
b) $AlCl_3$•PH_3, $\Delta E_{complex}$	-21.2	-22.0	-16.5
c) $AlCl_3$•$PMes_3$, $\Delta E_{complex}$	N/A	-40.0	-15.8

[a] Calculations performed in gas phase at T=0K, not ZPE and thermally corrected. [b] Basis sets: Single point energy at 6-311++G(d,p) and geometry optimizations at 6-311G(d,p), unit in kcal mol^{-1}. [c] Energy and geometry optimizations 6-311G(d,p), unit in kcal mol^{-1}.

C.3 Results

a. Hydride transfer reactants and TS energies

Table S2 below supplements the information reported in Table 1 of the paper with additional structural information of the C-H bond distance and imaginary frequency corresponding to the TS structures. In Table S3, we report energies of TS structures and reactants determined from IRC calculations, which were used to calculate the HT activation barriers.

Table S2. Hydride transfer TS properties and activation barriers at T=298K, P=1atm.

System[a]	$\Delta H_{hydride}$ [b]	C-H bond [c]	Freq. [d]
a) CO_2 + AB	25.3	1.21	947.4*i*
b) FLP•CO_2 + AB	7.9	1.48	227.6*i*
c) LA-O=C=O-LA + AB	–0.2	1.89	182.3*i*
d) CO_2•$(LA)_2$ + AB	4.1	1.83	210.2*i*
e) CO_2•(LA) + AB	3.8	1.84	314.5*i*

[a] All but case **c** were calculated at MP2/6-311++G(d,p)//B97-D/6-311G(d,p). Case **c** was calculated using CCSD(T)/6-311++G(d,p)// MP2/6-311G(d,p) because B97-D does not identify a HT TS. Solvation in C_6H_5Cl was treated with the CPCM model. LA=$AlCl_3$, AB=NH_3BH_3. [b] HT activation barriers referenced to reactants from IRC calculations, unit in kcal mol^{-1}. All calculations were zero-point energy (ZPE) and thermally corrected (298K). [c] Carbon-hydride bond distance at TS in Å. [d] Imaginary frequency at TS in cm^{-1}.

Table S3. Hydride transfer reactants and TS energies

System[a]	E(0K) [b]	H(298K) [c]
a) CO_2 + AB (TS)	-271.15296	-271.06874
CO_2 + AB (reactants)	-271.19964	-271.10910
b) FLP•CO_2 + AB (TS)	-4900.32847	-4899.67039
FLP•CO_2 + AB (reactants)	-4900.34234	-4899.68293
c) LA-O=C=O-LA + AB (TS)	-3513.65340	-3513.53432
LA-O=C=O-LA + AB (reactants)	-3513.65502	-3513.53400
d) CO_2•$(LA)_2$ + AB (TS)	-3513.53745	-3513.42267
CO_2•$(LA)_2$ + AB (reactants)	-3513.54550	-3513.42923
e) CO_2•(LA) + AB (TS)	-1892.36069	-1892.25694
CO_2•(LA) + AB (reactants)	-1892.36727	-1892.26298

[a] All but case **c** were calculated at MP2/6-311++G(d,p)//B97-D/6-311G(d,p). Case **c** was calculated using CCSD(T)/6-311++G(d,p)//MP2/6-311G(d,p) because B97-D does not identify a

HT TS. Solvation in C_6H_5Cl was treated with the CPCM model. LA=$AlCl_3$, LB=$PMes_3$, AB=NH_3BH_3. [b] Energy at T=0K, in Hartrees. [c] ZPE and thermally (T=298K) corrected energy, in Hartrees.

b. Formation of CO_2•$(LA)_2$ from free CO_2 and LA dimer

CO_2•$(LA)_2$ is an active complex for catalyzing HT to CO_2 (Table S2, case **d**). The activation barrier for the formation of CO_2•$(LA)_2$ from free CO_2 and LA dimer is 10.6 kcal mol^{-1}. The change of enthalpy for the formation of CO_2•$(LA)_2$ is +0.7 kcal mol^{-1}. Figure S2 shows the reactants, TS and product for the formation of CO_2•$(LA)_2$ complex. Table S4 below reports the energies used in determination of the activation barrier and complex formation energy.

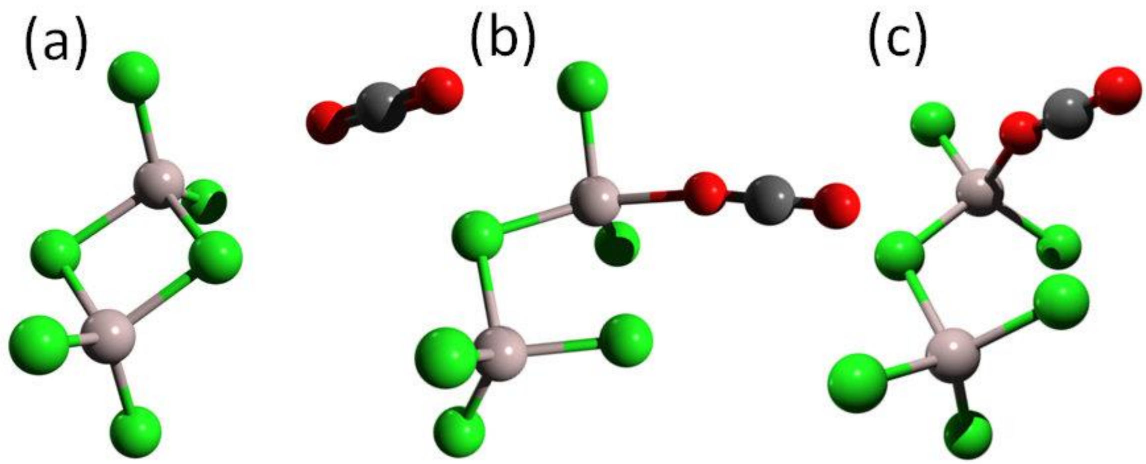

Figure S2. a) CO_2•$(LA)_2$ reactants b) CO_2•$(LA)_2$ TS structure c) CO_2•$(LA)_2$ product. Al, light gray; C, gray; Cl, green; and O, red.

Table S4. Energies for the formation of CO_2•$(LA)_2$ from free CO_2 and LA dimer

System[a]	E(0K) [b]	H(298K) [c]
CO_2 + $(LA)_2$ (TS)	-3430.54107	-3430.50192
CO_2 + $(LA)_2$ (reactants)	-3430.55871	-3430.51878
CO_2 + $(LA)_2$ (product)	-3430.55404	-3430.51765

[a] Calculations performed at MP2/6-311++G(d,p)//B97-D/6-311G(d,p). Solvation in C_6H_5Cl was treated with the CPCM model. LA=$AlCl_3$ [b] Energy at T=0K, in Hartrees. [c] ZPE and thermally (T=298K) corrected energy, in Hartrees.

c. Thermochemistry energies

Table S5 reports the energies used to calculate the thermochemical properties of LA or/and LB catalyzed complexes.

Table S5. Energies used to calculate thermochemical properties of LA or/and LB catalyzed complexes

Species[a]	E(0K) [b]	H(298K) [c]	G(298K) [d]
$(LA)_2$ dimer	-3,242.33636	-3,242.31275	-3,242.36891
CO_2	-188.21739	-188.20248	-188.22745
LB	-1,386.70731	-1,386.16815	-1,386.26220
LA	-1,621.14507	-1,621.13418	-1,621.17185
LA-O=C=O-LA	-3,430.53481	-3,430.49471	-3,430.56779
CO_2•(LA)	-1,809.38226	-1,809.35494	-1,809.40355
CO_2•$(LA)_2$	-3,430.55404	-3,430.51394	-3,430.58056
FLP•CO_2	-4,817.34610	-4,816.76139	-4,816.89432
$AlCl_3H^-$	-1621.88331	-1621.86553	-1621.90398
$NH_3BH_2^+$•CO_2	-270.42207	-270.34031	-270.37956
LA•AB	-1704.16852	-1704.08114	-1704.12923
AB	-82.97829	-82.90524	-82.93357
LA•LB	-3007.91636	-3007.36170	-3007.46822

[a] Calculations performed at MP2/6-311++G(d,p)//B97-D/6-311G(d,p). Solvation in C_6H_5Cl was treated with the CPCM model. LA=$AlCl_3$, LB=$PMes_3$. [b] Enthalpic energy at T=0K, in hartrees. [c] ZPE and thermally (T=298K) corrected energy, in hartrees. [d] Gibbs free energy, ZPE and thermally (298K) corrected, in hartrees.

C.4 FLP•CO_2 + AB Hydride Transfer (B3LYP)

Employing the B3LYP functional with a 6-311G(d,p) basis set, we located a TS corresponding to HT for the FLP•CO_2 + AB system at a C-H distance of 1.50 Å and with an imaginary frequency of 371*i* cm^{-1} (Figure S3a), consistent with our MP2//B97-D TS structure of 1.48 Å and 228*i* cm^{-1}. Also using the B3LYP functional, but with a 6-31+G(d,p) basis set (as used by Roy *et al.*[221]), we located a similar HT TS with a 1.50 Å C-H bond distance and a 428*i* cm^{-1} imaginary frequency, showing minimal difference between the 6-311G(d,p) and 6-31+G(d,p) basis sets in describing this reaction. A second TS (TS-B2) was identified, occurring after the initial HT along the reaction path, and corresponds to the dissociation of oxidized $NH_3BH_2^+$ from the reduced FLP•HCO_2^- complex with a 1.12 Å C-H distance and a 39*i* cm^{-1} imaginary frequency(Figure S3b), consistent with Roy *et al.*'s reported result of 1.12 Å and 41*i* cm^{-1}.[221] We believe the TS reported by Roy *et al.* was actually TS-B2, instead of the HT TS.

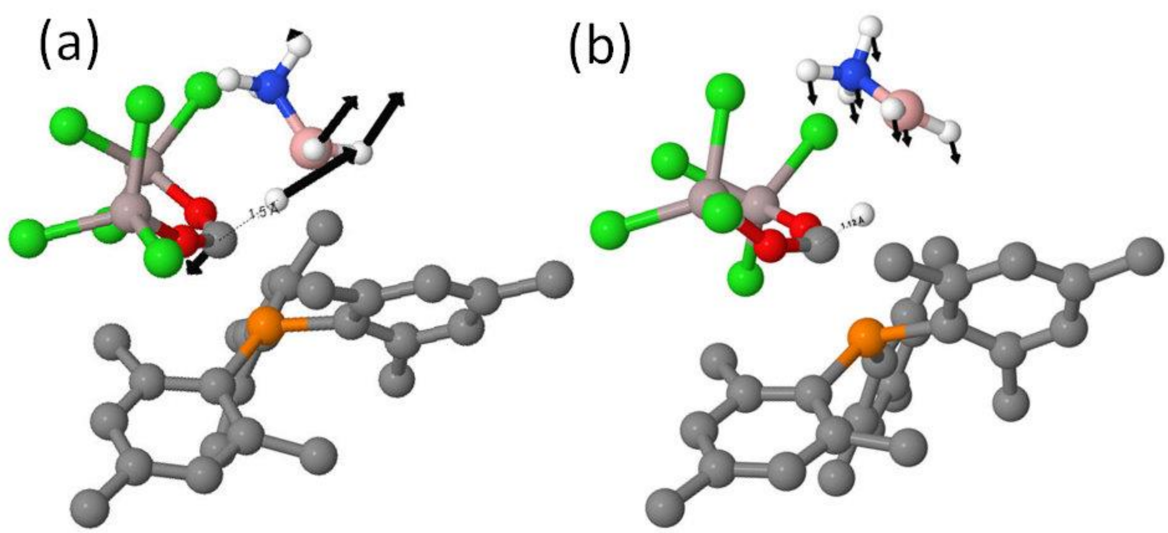

Figure S3. a) Hydride transfer TS structure for FLP•CO_2 + AB system with 1.50 Å C-H distance and 371*i* cm^{-1} imaginary frequency. Arrows indicate normal mode for HT reaction. b) TS-B2 structure with 1.12 Å C-H distance and 39*i* cm^{-1} imaginary frequency. Arrows indicate normal mode for dissociation of oxidized $NH_3BH_2^+$ from the reduced FLP•HCO_2^- complex after the initial HT. Calculations were performed using B3LYP/6-311G(d,p)/CPCM-C_6H_5Cl. Al, gray; B, pink; C, gray; Cl, green; H, white; O, red; N, blue; P, orange.

Figure S4 demonstrates the effect of dispersion on HT barriers for the FLP•CO_2 + AB system. Our B3LYP results show that the HT TS enthalpy is 14.9 kcal mol^{-1} higher than the separated reactants **R**; Meanwhile MP2//B97-D predicts the HT TS enthalpy to be -2.3 kcal mol^{-1}. This demonstrates that B3LYP, which neglects the effect of dispersion, produces qualitatively different results than the more accurate MP2//B97-D method.

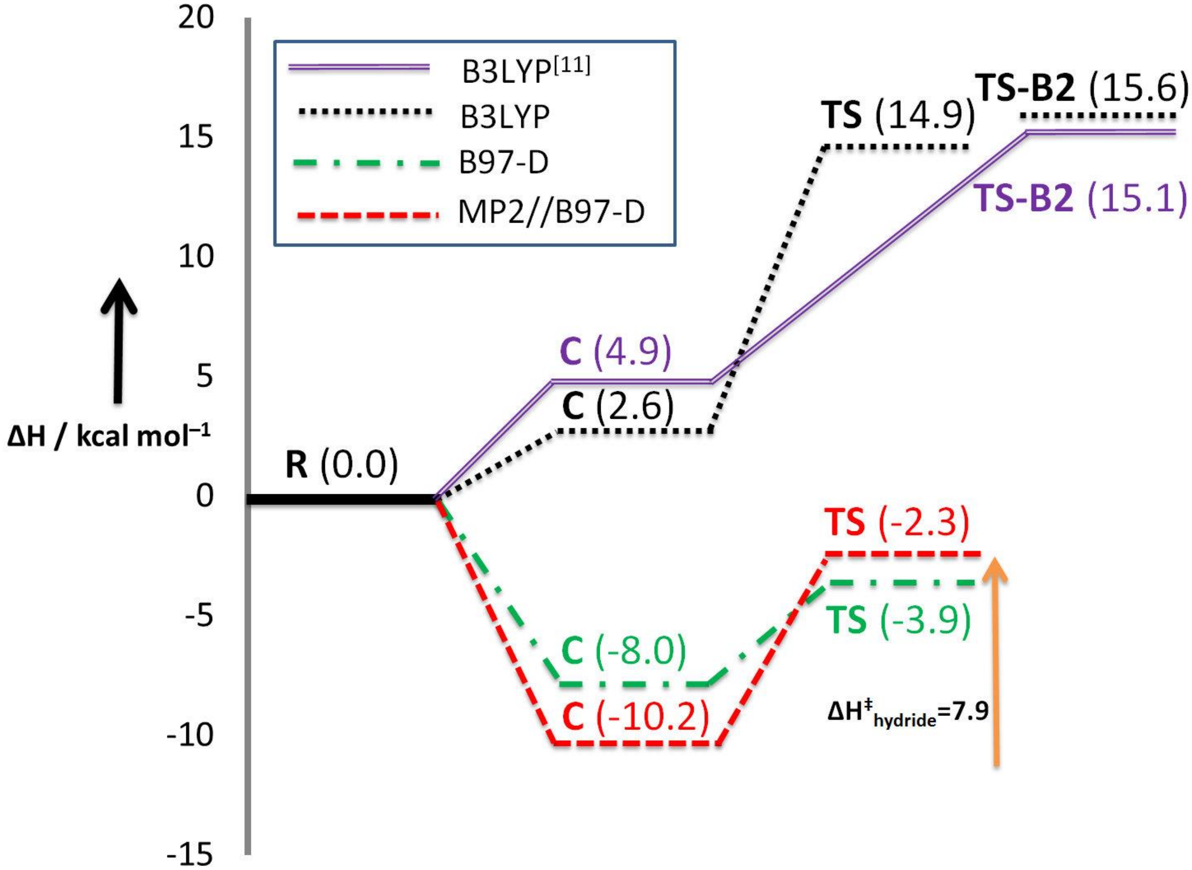

Figure S4. Comparison of various methods in determining hydride transfer barriers for FLP•CO_2 + AB system . **R** is infinitely separated reactants (FLP•CO_2 + AB); **C** is the reactant complex; **TS** is hydride transfer TS. **TS-B2** is the transition state corresponding to the dissociation of oxidized $NH_3BH_2^+$ from the reduced FLP•HCO_2^- complex after the initial HT.

C.5 Thermodynamics of Complex Formation Reported in Table 2

Table 2 of the manuscript reports the changes in enthalpy and entropy for reactions that form several complexes. The reference energy is that of the starting reactants, which are shown as case 1 and consist of two free CO_2 molecules, a free LA dimer (LA_2), two free Lewis bases and two free ammonia borane molecules. Equation 1 of the manuscript describes these reactions as $2CO_2 + (LA)_2 + 2LB + 2AB \xleftrightarrow{\Delta H;\ T\Delta S;\ Keq}$ Complexes 1 to 11 and conserves the number of molecular species, namely, we have two CO_2, two LA, two LB and two AB on both sides of the equation. The following examples explain how the thermodynamics of complexes 4 and 11 are determined:

Example 1

In complex 4 of Table 2, we have $2CO_2 + (LA)_2 + 2LB + 2AB$ = $\mathbf{CO_2{\bullet}(LA)_2}$ + CO_2 + 2LB + 2AB. This equation is equivalent to $CO_2 + (LA)_2$ = $\mathbf{CO_2{\bullet}(LA)_2}$ when the spectator species are omitted. Thus, for complex 4 as written in Table 2, we are evaluating the thermodynamics (ΔH, TΔS and K_{eq}) of forming $CO_2{\bullet}(LA)_2$ from $CO_2 + (LA)_2$.

Example 2

In complex 11 of Table 2, we have $2CO_2 + (LA)_2 + 2LB + 2AB$ = $2CO_2$ + **LA•LB** + **LA•AB** + LB + AB. This equation is equivalent to $(LA)_2$ + LB + AB = **LA•LB** + **LA•AB** when the spectator species are omitted. Thus, for complex 11 as written in Table 2, we are evaluating the thermodynamics (ΔH, TΔS and K_{eq}) of forming **LA•LB** + **LA•AB** from $(LA)_2$ + LB + AB.

C.6 Coordinates

All coordinates are reported in XYZ format. Al, gray; B, pink; C, gray; Cl, green; H, white; O, red; N, blue; P, orange. LA=$AlCl_3$, LB=$PMes_3$, AB=NH_3BH_3. . 0 K energies (not ZPE corrected) reported are calculated using MP2/6-311++G(d,p)//B97-D/6-311G(d,p). Except in the case of LA-O=C=O-LA + AB, energies were calculated at CCSD(T)/6-311++G(d,p)//MP2/6-311G(d,p). Solvation in C_6H_5Cl is modeled using CPCM. Reported energies in hartrees.

CO_2 + AB (TS) (-271.15296)

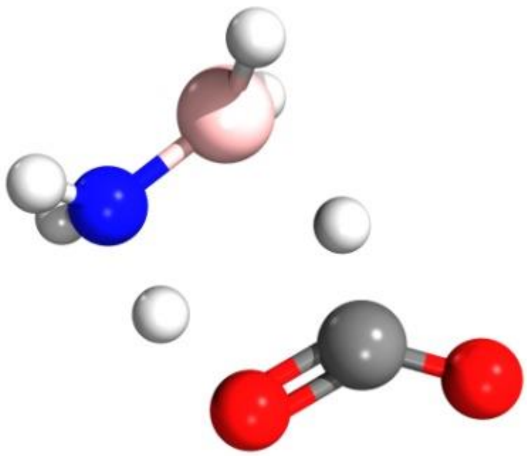

C	0.95836	-0.03588	-0.00590
O	2.09690	-0.45502	-0.00457
O	0.44519	1.12648	-0.01594
N	-1.91750	0.31998	0.00657
H	-2.42817	0.61533	-0.82506
H	-0.82811	0.88606	-0.00836
H	-2.41214	0.64229	0.83896
H	-1.53213	-1.72115	-1.02585
H	0.10804	-0.89932	0.00510
H	-1.51507	-1.70263	1.07755
B	-1.51341	-1.14179	0.02104

CO_2 + AB (reactants) (-271.19964)

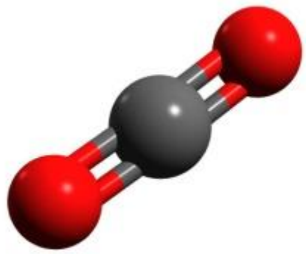

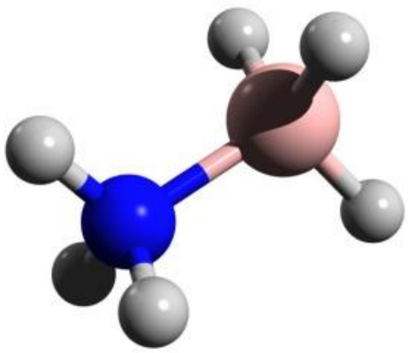

C	1.37846	0.28556	0.01737
O	2.07501	-0.64991	-0.00376
O	0.71234	1.24778	0.04092
N	-2.34404	0.22501	-0.03844
H	-2.78584	0.39856	-0.94281
H	-1.70776	1.00419	0.14052
H	-3.07874	0.26830	0.66947
H	-2.38294	-2.09616	-0.16314
H	-0.72128	-1.19184	-0.89876
H	-1.01471	-1.28398	1.10644
B	-1.54027	-1.22798	0.00392

FLP•CO_2 + AB (TS) (-4900.32847)

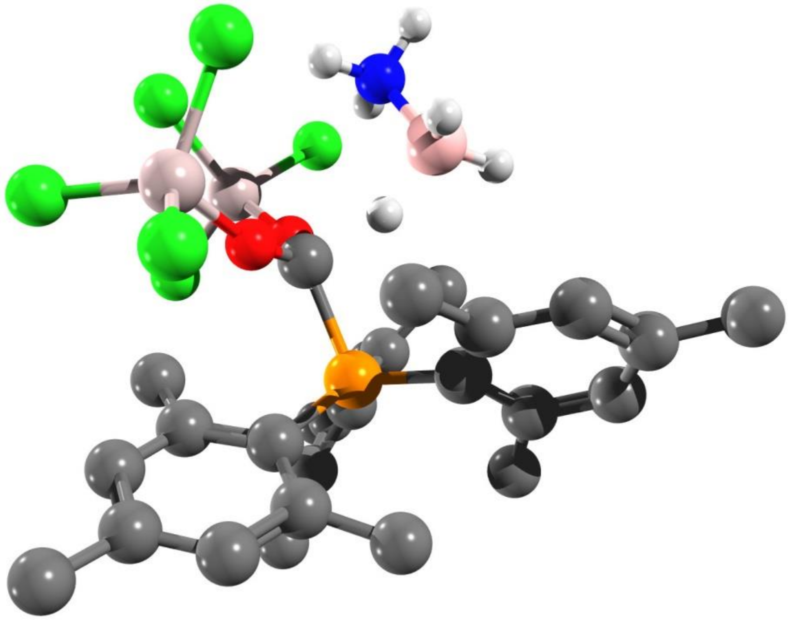

P	-0.00697	0.00478	0.00129
C	-0.01574	0.00735	2.02978
O	1.17254	0.00409	2.52390
Al	2.55353	0.11531	3.68747
Cl	1.86058	1.38058	5.30819
O	-0.96385	-0.72920	2.51486
Al	-1.62894	-1.92000	3.70737
Cl	-3.63994	-1.18412	4.08865
Cl	4.22418	1.02110	2.66395
Cl	3.11746	-1.85614	4.34217
Cl	-1.66898	-3.87987	2.83863
Cl	-0.46713	-1.76489	5.51004
H	-0.49915	1.39154	2.21320
B	-1.03677	2.38935	2.93642
N	-1.50400	1.68666	4.29634
H	-0.12622	3.13997	3.15231
H	-1.98055	2.76269	2.29395
H	-1.95266	2.38193	4.89959
H	-2.19414	0.93920	4.16120
H	-0.71720	1.30511	4.83472
C	-1.36160	-1.13059	-0.45746
C	-2.64720	-0.90820	0.11342
C	-1.14188	-2.26187	-1.29886
C	-3.62723	-1.89727	-0.02890
C	-2.16962	-3.20799	-1.40954

C	-3.39823	-3.07434	-0.74955
H	-4.60196	-1.72912	0.42816
H	-2.00413	-4.07510	-2.04841
C	-0.29318	1.71912	-0.54610
C	-1.27644	2.02175	-1.53424
C	0.44625	2.76873	0.06976
C	-1.61290	3.36642	-1.73535
C	0.06237	4.09233	-0.17998
C	-0.99444	4.41416	-1.03841
H	-2.36234	3.60279	-2.49035
H	0.62982	4.89225	0.29493
C	1.65370	-0.64365	-0.38789
C	2.50732	0.00227	-1.33012
C	2.11190	-1.79005	0.32323
C	3.83460	-0.43581	-1.42435
C	3.45066	-2.17426	0.18323
C	4.34064	-1.48940	-0.65111
H	4.48949	0.05528	-2.14365
H	3.79722	-3.04820	0.73415
C	1.69072	2.55986	0.90443
H	1.47071	2.59425	1.97538
H	2.19447	1.61428	0.70061
H	2.40205	3.36768	0.69332
C	-1.91346	1.01041	-2.47019
H	-1.21804	0.21048	-2.74595
H	-2.80166	0.53412	-2.03883
H	-2.22160	1.52433	-3.38869
C	0.08960	-2.49846	-2.15254
H	0.50754	-1.56815	-2.55028
H	0.88963	-3.00395	-1.59811
H	-0.18506	-3.13852	-2.99957
C	-3.09061	0.38736	0.75453
H	-3.68386	0.95778	0.02404
H	-3.73052	0.18492	1.61956
H	-2.27994	1.03891	1.07448
C	1.23719	-2.68860	1.17292
H	1.45153	-2.55496	2.23897
H	0.16749	-2.54338	1.01670
H	1.45863	-3.73535	0.92927
C	2.07644	1.09052	-2.29488
H	1.06921	0.92074	-2.69108
H	2.07878	2.08321	-1.82818
H	2.77447	1.11601	-3.14008

C	5.79513	-1.88293	-0.72765
H	6.36541	-1.35752	0.05412
H	5.92418	-2.96034	-0.56244
H	6.23061	-1.61214	-1.69793
C	-1.42858	5.84569	-1.23926
H	-1.83989	5.99928	-2.24518
H	-2.21608	6.10589	-0.51483
H	-0.59266	6.53946	-1.08279
C	-4.44513	-4.15789	-0.82508
H	-4.34839	-4.74134	-1.74952
H	-4.32628	-4.85102	0.02226
H	-5.45738	-3.73722	-0.76884

FLP•CO_2 + AB (reactants) (-4900.34234)

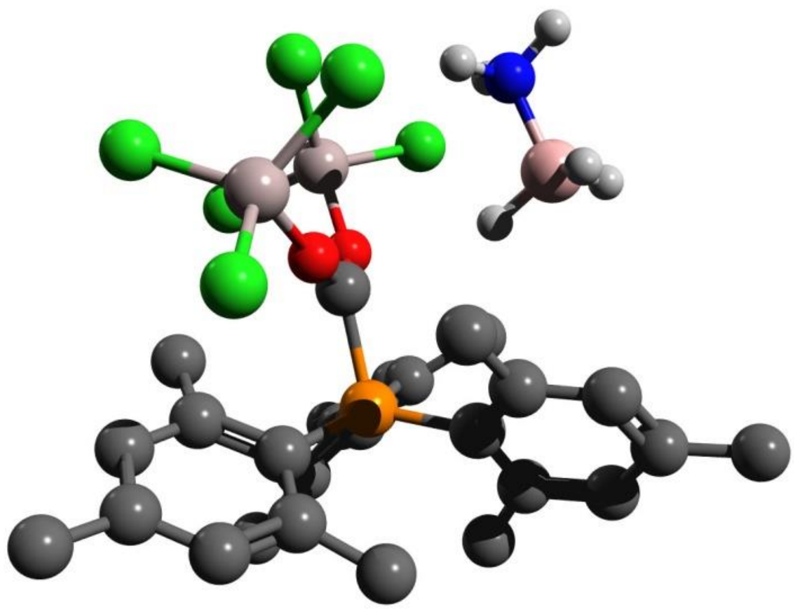

P	-0.05518	0.07217	-0.01144
C	-0.16923	0.08188	1.95094
O	0.90763	0.06039	2.58450
Al	2.31696	-0.10162	3.78125
Cl	2.20248	1.64452	5.03028
O	-1.32043	-0.03254	2.43460
Al	-2.34059	-0.43424	3.94621
Cl	-3.96042	0.97970	3.88791
Cl	4.11522	-0.12576	2.60537
Cl	2.03705	-1.97556	4.78580
Cl	-2.92480	-2.46715	3.61004

Cl	-1.13810	-0.12176	5.69257
H	-0.66018	2.62554	2.42375
B	-0.75799	3.68426	3.01751
N	-1.06392	3.29573	4.59323
H	0.29327	4.30455	3.01059
H	-1.70880	4.34445	2.62590
H	-1.10038	4.12333	5.19022
H	-1.95816	2.81166	4.70294
H	-0.34159	2.68030	4.97690
C	-1.67038	-0.62374	-0.48822
C	-2.83854	0.08502	-0.07321
C	-1.78617	-1.84368	-1.21504
C	-4.08236	-0.53302	-0.25256
C	-3.06496	-2.39520	-1.37261
C	-4.21846	-1.78516	-0.86419
H	-4.97319	-0.00257	0.08220
H	-3.15898	-3.32859	-1.92673
C	0.11648	1.77004	-0.65794
C	-0.61826	2.15128	-1.82256
C	0.94415	2.71667	0.00652
C	-0.63063	3.50710	-2.17138
C	0.88114	4.05692	-0.39363
C	0.06628	4.48431	-1.44672
H	-1.18358	3.80343	-3.06241
H	1.51129	4.77802	0.12511
C	1.38860	-1.01538	-0.23560
C	2.46205	-0.66425	-1.10540
C	1.44950	-2.21164	0.54070
C	3.60345	-1.47746	-1.09831
C	2.61891	-2.97685	0.49545
C	3.71890	-2.61517	-0.29062
H	4.42642	-1.21359	-1.76158
H	2.66256	-3.88962	1.08891
C	1.95414	2.35827	1.06698
H	1.52058	2.47924	2.06684
H	2.32904	1.33735	0.95303
H	2.81113	3.03846	0.99452
C	-1.31177	1.20142	-2.78355
H	-0.79002	0.24250	-2.87685
H	-2.34491	0.98336	-2.48576
H	-1.33879	1.66497	-3.77698
C	-0.64533	-2.56614	-1.90632
H	0.08593	-1.87748	-2.34264

H	-0.09855	-3.23086	-1.22668
H	-1.05534	-3.18286	-2.71471
C	-2.86777	1.51625	0.42576
H	-2.98199	2.18818	-0.43783
H	-3.73086	1.65894	1.08376
H	-1.98133	1.84732	0.96919
C	0.32080	-2.76001	1.39627
H	0.49829	-2.55479	2.45956
H	-0.67175	-2.38418	1.13020
H	0.28754	-3.85074	1.28781
C	2.45694	0.49823	-2.07946
H	1.50613	0.59086	-2.61457
H	2.64210	1.45559	-1.57717
H	3.25045	0.34933	-2.82073
C	4.98976	-3.42710	-0.26760
H	5.64910	-3.06296	0.53557
H	4.78065	-4.48617	-0.06976
H	5.53662	-3.33780	-1.21475
C	-0.03145	5.94413	-1.81450
H	-0.26224	6.07198	-2.87981
H	-0.83847	6.42226	-1.23776
H	0.90031	6.47519	-1.58151
C	-5.56943	-2.44602	-0.98701
H	-5.58630	-3.16655	-1.81431
H	-5.80507	-2.99201	-0.06033
H	-6.36201	-1.70226	-1.14112

LA-O=C=O-LA + AB (TS) (-3513.65340)

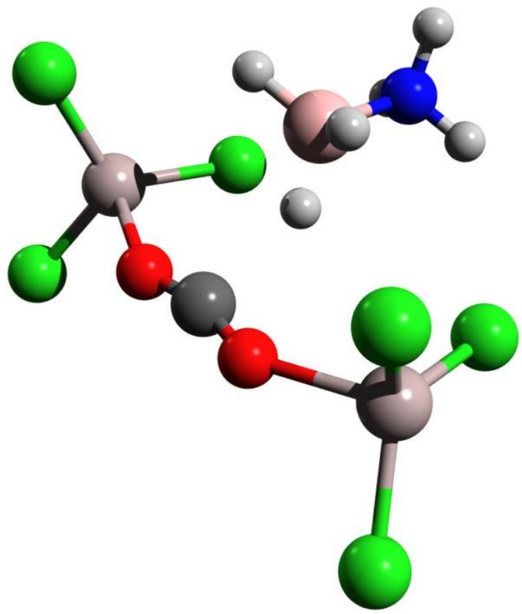

Al	3.09732	-0.17899	0.05690
Cl	2.68262	1.13950	-1.52129
Cl	3.63807	0.61511	1.91076
Cl	3.94861	-2.01579	-0.47308
Al	-3.10611	-0.21610	0.09243
Cl	-2.72058	1.10458	-1.49068
Cl	-3.88003	-2.08710	-0.43853
Cl	-3.70421	0.56793	1.93253
C	0.00296	-0.70038	0.48999
O	1.16231	-0.87474	0.50577
O	-1.15549	-0.86740	0.55643
N	0.00487	3.28891	-0.55018
H	-0.78464	3.19731	-1.18908
H	0.85854	3.21329	-1.10287
H	-0.03023	4.22967	-0.16020
H	-1.07891	2.26675	1.19003
H	0.00208	1.11914	-0.03224
H	0.94255	2.29163	1.28466
B	-0.03666	2.16914	0.59664

LA-O=C=O-LA + AB (reactants) (-3513.65502)

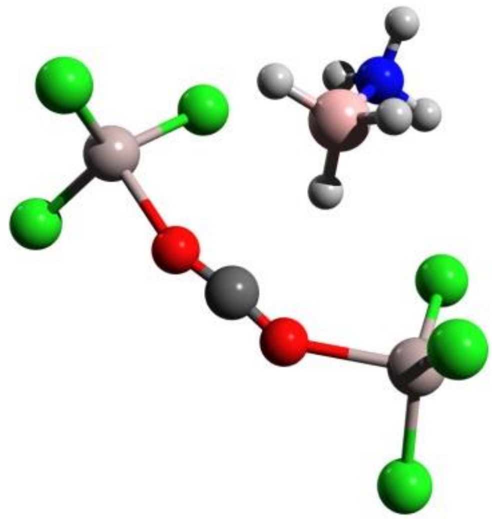

Al	3.11583	-0.21149	-0.02715
Cl	2.54272	1.00055	-1.63561
Cl	3.59433	0.66770	1.79816
Cl	4.01052	-2.03633	-0.50877
Al	-3.14497	-0.19679	0.05449
Cl	-2.63595	1.12947	-1.48636
Cl	-3.80955	-2.08958	-0.52791
Cl	-3.83108	0.56650	1.86549
C	0.00753	-0.85484	0.55593
O	1.15917	-1.03080	0.50344
O	-1.15333	-0.80246	0.63073
N	-0.06967	3.30975	-0.51362
H	-0.81228	2.95947	-1.11705
H	0.80100	3.23095	-1.03699
H	-0.25027	4.29990	-0.35988
H	-1.10768	2.44848	1.33672
H	0.38530	1.37125	0.54052
H	0.81777	3.02300	1.57321
B	0.00507	2.47284	0.86867

CO_2•$(LA)_2$ + AB (TS) (-3513.53745)

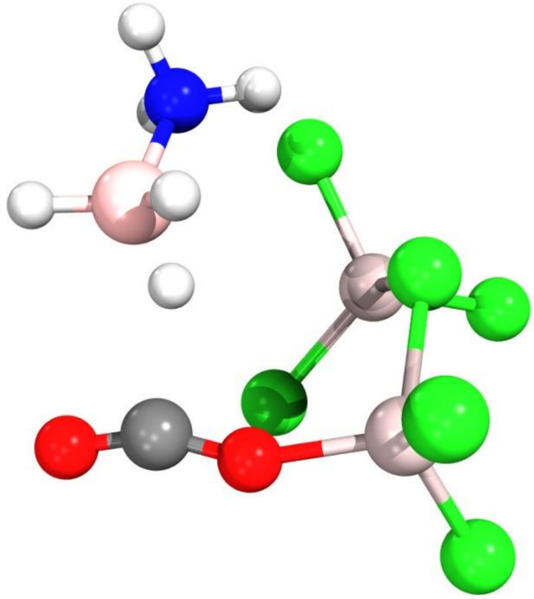

Al	-1.73413	0.97877	-0.26580
Cl	-1.36074	2.74242	0.82333
Cl	0.12258	0.29016	-1.34683
Cl	-3.35783	0.86212	-1.60414
Al	2.02551	0.12773	0.09931
Cl	2.95273	-1.63310	-0.70181
Cl	1.17630	-0.14453	2.04170
Cl	3.09048	1.94158	-0.20436
C	-1.87309	-1.47593	1.52500
O	-1.98195	-0.37831	1.03524
O	-1.98619	-2.30494	2.32543
N	0.12036	-3.49587	-1.46723
H	0.04877	-4.32591	-2.06200
H	0.91448	-3.64526	-0.83963
H	0.37848	-2.72090	-2.08234
H	-2.11327	-2.85163	-1.46105
H	-1.55554	-4.23088	-0.04171
H	-1.01073	-2.30873	0.14850
B	-1.27886	-3.23346	-0.66985

CO_2•$(LA)_2$ + AB (reactants) (-3513.54550)

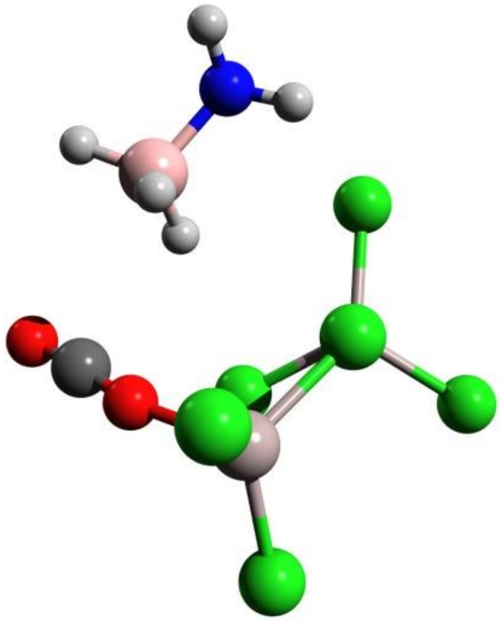

Al	-1.75134	1.00035	-0.31622
Cl	-1.47345	2.73134	0.84749
Cl	0.12842	0.38833	-1.35895
Cl	-3.37328	0.83127	-1.64451
Al	1.99840	0.07579	0.10708
Cl	2.87984	-1.70147	-0.69720
Cl	1.13701	-0.11802	2.05717
Cl	3.14842	1.84759	-0.17283
C	-1.88749	-1.33615	1.72385
O	-2.01492	-0.41190	0.99436
O	-1.84182	-2.19544	2.48418
N	0.18452	-3.64843	-1.70033
H	-0.20410	-4.37504	-2.30554
H	0.98587	-4.05905	-1.21717
H	0.55861	-2.91880	-2.31000
H	-1.78949	-2.50129	-1.28197
H	-1.36086	-4.04876	-0.03084
H	-0.31700	-2.32397	0.10667
B	-0.93184	-3.08041	-0.63382

CO_2•(LA) + AB (TS) (-1892.36069)

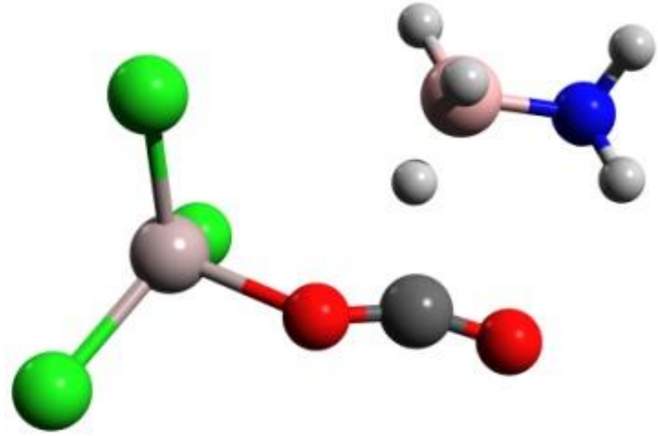

C	1.56482	1.35372	0.23468
O	0.44716	1.18255	-0.17686
O	2.51898	1.95621	0.52323
Al	-1.08258	-0.07014	-0.18758
Cl	-2.67647	1.27613	-0.64968
Cl	-0.59607	-1.45128	-1.73545
Cl	-1.10638	-0.84585	1.80131
N	4.18977	-0.65676	0.92191
H	4.17951	-0.86475	1.92313
H	4.39035	0.34048	0.81815
H	4.97841	-1.16319	0.51484
H	2.54013	-2.22929	0.42730
H	1.92377	-0.37179	0.76990
H	2.88746	-0.78829	-0.98695
B	2.78957	-1.06944	0.18743

CO_2•(LA) + AB (reactants) (-1892.36727)

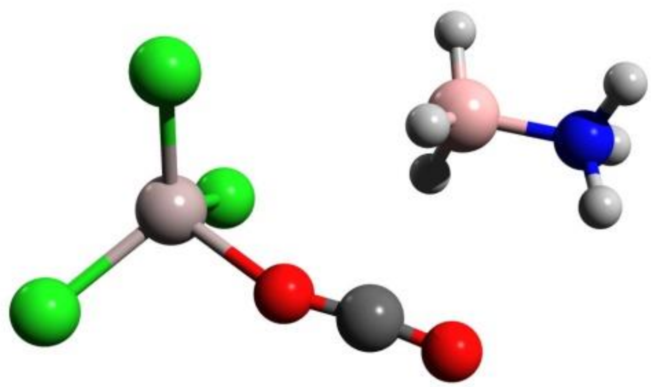

C	1.51086	1.55184	0.22557
O	0.43201	1.18549	-0.08299
O	2.52058	2.03446	0.50823
Al	-1.13520	-0.11220	-0.25631
Cl	-2.66226	1.28097	-0.77862
Cl	-0.49690	-1.40046	-1.81895
Cl	-1.25697	-0.92143	1.70509
N	4.35384	-0.75549	0.84276
H	4.54420	-1.00102	1.81592
H	4.53429	0.24520	0.74103
H	5.05200	-1.24019	0.27686
H	2.76711	-2.37482	0.32556
H	2.07342	-0.71418	1.24756
H	2.64720	-0.63263	-0.70674
B	2.81313	-1.15859	0.38148

$NH_3BH_2^+ \bullet CO_2 + AlCl_3H^-$ (TS) (-1892.33428)

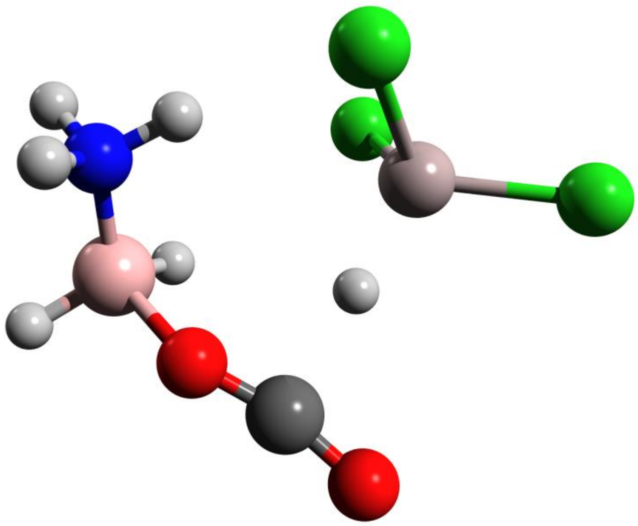

Al	3.72681	-0.59973	-0.17319
Cl	3.16352	-0.66469	-2.27366
Cl	2.04175	-1.04875	1.12012
Cl	5.32888	-2.09211	0.17302
N	7.67900	-0.03723	-0.92580
H	8.52449	-0.07026	-0.34999
H	7.95405	-0.32971	-1.86895
H	7.02189	-0.75736	-0.57451
H	4.36099	0.82898	0.18149
H	7.82624	2.25747	-1.23710
H	5.96440	1.38394	-1.55532
B	7.02403	1.40153	-1.01065
C	5.68013	1.94898	1.29066
O	6.66383	1.67926	0.66407
O	4.93942	2.35791	2.07923

$NH_3BH_2^+ \bullet CO_2 + AlCl_3H^-$ (reactant) (-1892.33969)

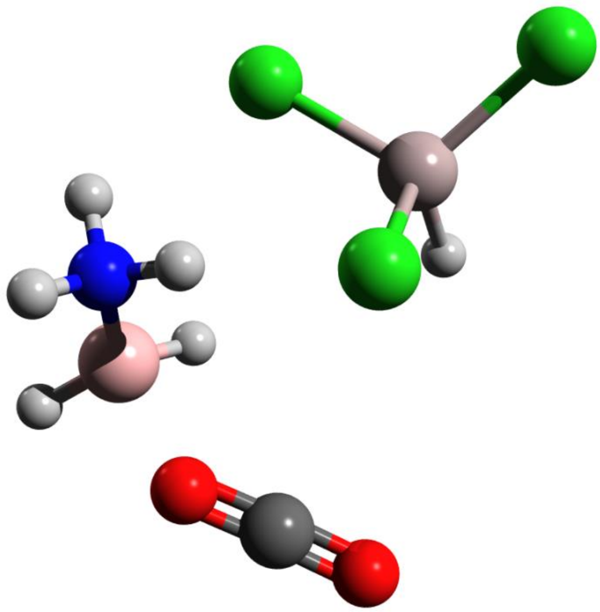

Al	-1.16271	-0.37288	-0.26992
Cl	-0.26704	-0.69965	-2.26681
Cl	-2.66532	-1.91033	0.09000
Cl	0.51788	-0.72953	1.17206
N	2.75007	0.15569	-1.03524
H	3.72281	-0.13397	-0.90759
H	2.42291	-0.21922	-1.93595
H	2.16101	-0.31549	-0.32074
H	-1.69211	1.11002	-0.10621
H	3.44623	2.35766	-1.38942
H	1.38847	2.02821	-1.10236
B	2.52774	1.70069	-1.02041
C	2.00267	2.29962	1.75077
O	2.77316	1.96811	0.91758
O	1.28432	2.63957	2.58826

CO_2 + $(LA)_2$ (TS) (-3430.54107)

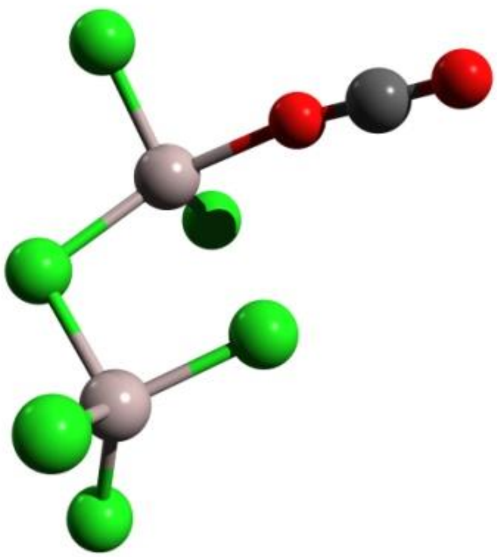

Al	-1.37226	-0.51542	0.20597
Cl	-1.79353	-1.39419	-1.66360
Cl	0.58137	-1.43637	1.04722
Cl	-2.63401	-0.86639	1.88256
Al	2.15175	-0.02886	0.09367
Cl	3.19405	0.92906	1.67657
Cl	0.64356	1.25151	-0.86070
Cl	3.30486	-1.14722	-1.29219
C	-2.61716	2.46008	-0.36802
O	-2.27540	1.36653	-0.09592
O	-2.96696	3.52795	-0.62669

CO_2 + $(LA)_2$ (reactants) (-3430.55871)

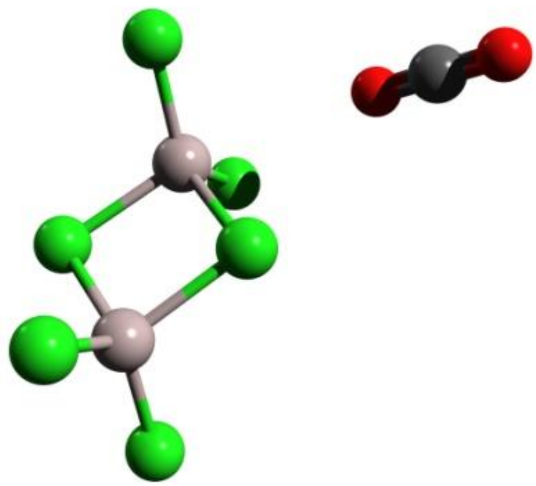

Al	-1.02849	-0.76847	0.22995
Cl	-1.80944	-1.65495	-1.51034
Cl	0.86900	-1.94825	0.88006
Cl	-2.19829	-0.39283	1.93741
Al	2.18870	-0.18601	0.22748
Cl	3.19625	0.64310	1.88050
Cl	0.30442	1.03761	-0.29685
Cl	3.23402	-0.69212	-1.53006
C	-3.04747	2.92852	-0.86770
O	-2.87406	1.77138	-0.86171
O	-3.22143	4.08180	-0.87506

CO_2 + $(LA)_2$ (product) (-3430.55404)

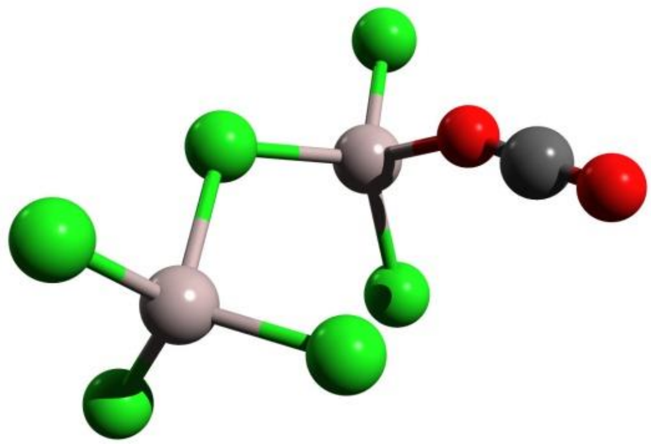

Al	-1.62802	-0.80121	0.36278
Cl	-1.54070	-1.33688	-1.66373
Cl	0.35128	-0.70799	1.37586
Cl	-3.05934	-1.58813	1.68411
Al	2.07011	0.22569	-0.04265
Cl	3.39785	1.04812	1.40463
Cl	0.97167	1.67292	-1.18730
Cl	2.78465	-1.44124	-1.15279
C	-2.08375	2.23429	-0.11903
O	-2.01614	1.15129	0.35560
O	-2.17421	3.29686	-0.54476

$(LA)_2$ dimer (-3,242.33636)

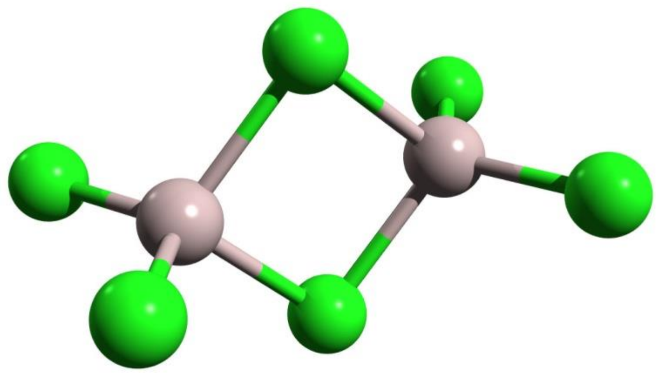

Al	0.09687	0.45942	0.24789
Cl	-0.10913	1.88272	1.78332
Cl	2.32144	-0.11537	0.02153
Cl	-0.78036	0.74273	-1.64347
Al	1.84678	-2.23623	0.80304
Cl	-0.37782	-1.66147	1.02932
Cl	2.72380	-2.51956	2.69450
Cl	2.05259	-3.65972	-0.73222

CO_2 (-188.21739)

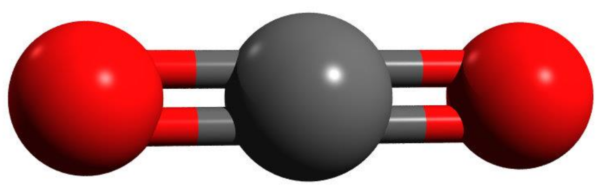

C	-0.78763	0.11991	-1.91756
O	-1.90224	0.13162	-2.26827
O	0.32696	0.10820	-1.56681

LB (-1,386.70731)

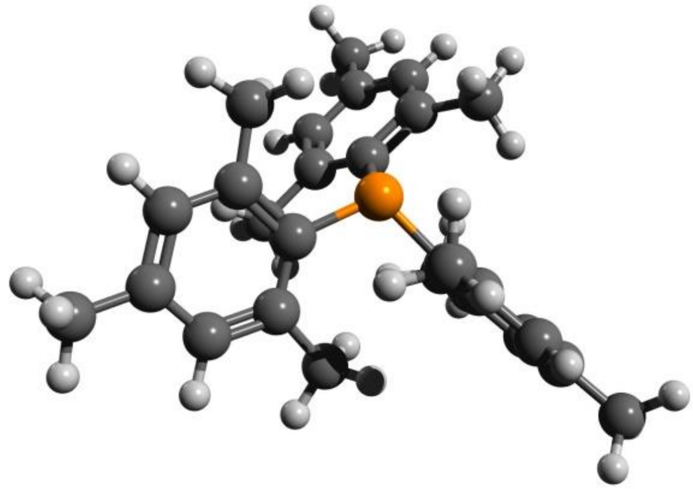

P	0.01596	0.00442	0.86400
C	1.58823	-0.74875	0.24239
C	1.99254	-1.92505	0.94329
C	3.21971	-2.52900	0.64140
C	4.08346	-2.00653	-0.33187
C	3.67167	-0.85857	-1.01678
C	2.44064	-0.22379	-0.76569
C	1.11069	-2.58758	1.98430
H	3.50268	-3.43392	1.18138
C	5.40901	-2.67209	-0.63304
H	4.31669	-0.45107	-1.79684
C	2.08245	0.95668	-1.64541
H	1.60748	-3.47576	2.39469
H	0.14902	-2.89906	1.55087
H	0.87454	-1.89896	2.80919
H	5.93942	-2.14997	-1.43964
H	5.26434	-3.71967	-0.93652
H	6.05625	-2.67840	0.25664
H	1.05664	0.87545	-2.02378
H	2.76823	1.00418	-2.50077
H	2.13926	1.91062	-1.10465
C	-0.12618	1.74417	0.24837
C	0.64705	2.69610	0.97496
C	0.51075	4.06285	0.69319
C	-0.37666	4.53365	-0.28354
C	-1.10702	3.58605	-1.01117
C	-0.99572	2.20495	-0.77905
C	1.66577	2.27737	2.01758

H	1.11808	4.77692	1.25115
C	-0.54567	6.01537	-0.53729
H	-1.77271	3.92808	-1.80532
C	-1.77020	1.28321	-1.69782
H	2.45467	1.65534	1.56922
H	1.20114	1.67274	2.81044
H	2.13717	3.15755	2.47229
H	-0.72147	6.21945	-1.60253
H	0.34141	6.57645	-0.21417
H	-1.41021	6.41034	0.01947
H	-2.09157	1.83188	-2.59264
H	-2.66189	0.86391	-1.21223
H	-1.15797	0.43032	-2.01106
C	-1.42418	-0.97725	0.24329
C	-2.64979	-0.72937	0.93227
C	-3.77967	-1.50486	0.64090
C	-3.74726	-2.53841	-0.30578
C	-2.54760	-2.75179	-0.99252
C	-1.39013	-1.98882	-0.75392
C	-2.79457	0.39100	1.94384
H	-4.71002	-1.29144	1.16968
C	-4.97009	-3.38940	-0.56978
H	-2.51050	-3.52247	-1.76432
C	-0.19267	-2.26330	-1.64022
H	-2.59411	1.36995	1.48469
H	-2.07850	0.28174	2.77187
H	-3.81093	0.40424	2.35718
H	-5.87033	-2.76750	-0.67644
H	-5.15103	-4.08192	0.26698
H	-4.84785	-3.98804	-1.48180
H	-0.50249	-2.86185	-2.50661
H	0.60056	-2.80953	-1.11287
H	0.25965	-1.33263	-2.00280

LA (-1,621.14507)

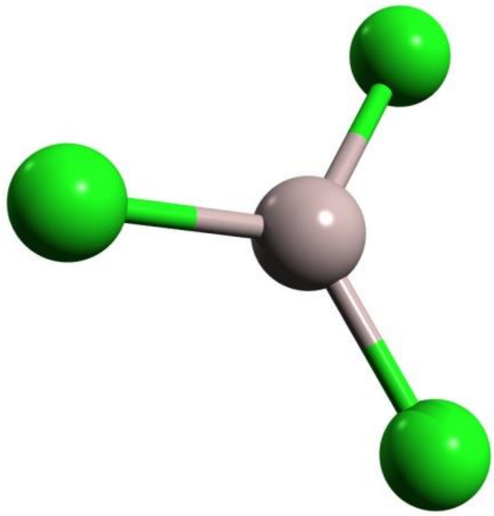

Al	0.43945	0.70786	0.01032
Cl	-0.57872	1.12612	1.79840
Cl	2.37702	-0.09896	0.06637
Cl	-0.45416	1.15186	-1.83687

LA-O=C=O-LA (-1,621.14507)

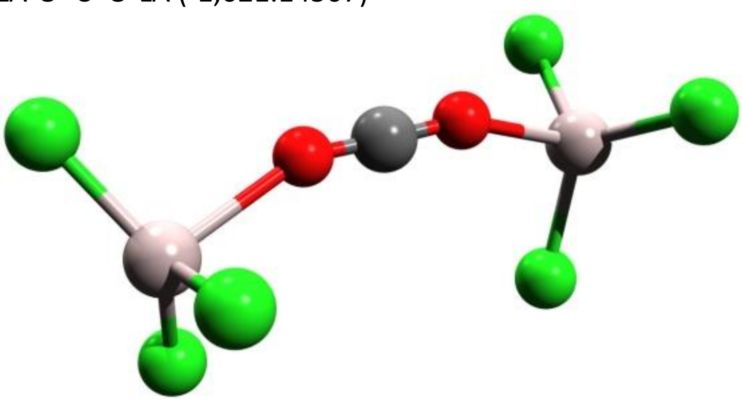

Al	3.27110	-0.46334	-0.04245
Cl	2.74885	0.56620	-1.81373
Cl	3.90493	0.66973	1.62479
Cl	3.87147	-2.48367	-0.17148
Al	-3.30171	-0.28698	-0.00091
Cl	-2.92888	1.33150	-1.30274
Cl	-3.42893	-2.23231	-0.81183
Cl	-4.17860	0.09435	1.87912

C	0.02003	-0.66243	0.70095
O	1.17059	-0.84081	0.66798
O	-1.12906	-0.49734	0.76285

CO_2•(LA) (-1,809.38226)

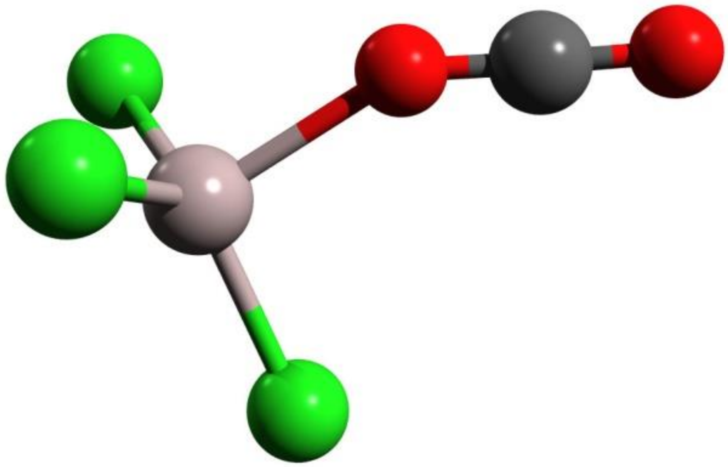

C	-0.56765	-2.61180	-0.13716
O	-0.63917	-1.43333	-0.10964
O	-0.52626	-3.76262	-0.16630
Al	0.28444	0.42269	-0.03144
Cl	-0.51849	1.16343	1.78777
Cl	2.31597	-0.20533	-0.01109
Cl	-0.43934	1.27491	-1.83488

CO_2•$(LA)_2$ (-3,430.55404)

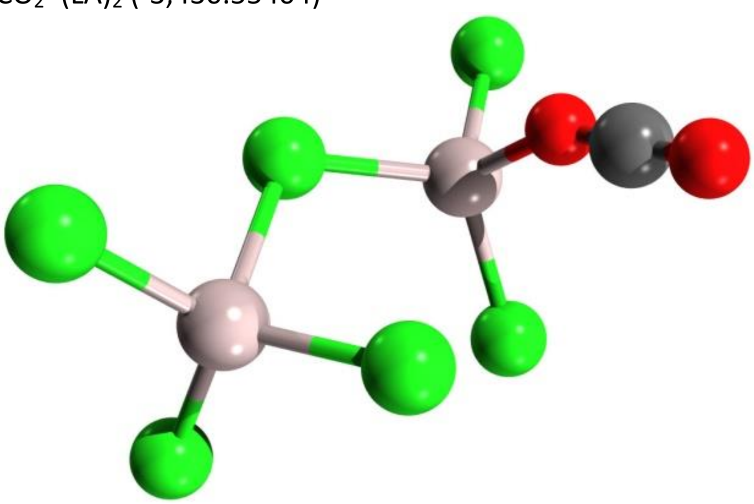

Al	-1.62802	-0.80121	0.36278

Cl	-1.54070	-1.33688	-1.66373
Cl	0.35128	-0.70799	1.37586
Cl	-3.05934	-1.58813	1.68411
Al	2.07011	0.22569	-0.04265
Cl	3.39785	1.04812	1.40463
Cl	0.97167	1.67292	-1.18730
Cl	2.78465	-1.44124	-1.15279
C	-2.08375	2.23429	-0.11903
O	-2.01614	1.15129	0.35560
O	-2.17421	3.29686	-0.54476

FLP•CO_2 (-4,817.34610)

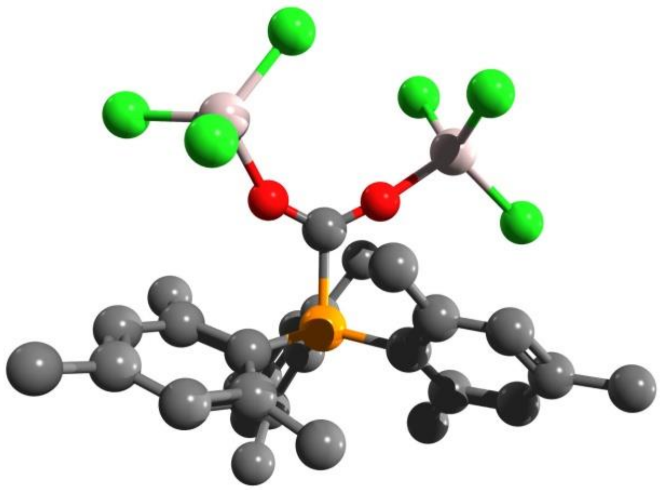

P	-0.00499	0.18287	-1.37669
C	-0.09451	0.21102	0.57242
O	0.97123	0.03291	1.19918
Al	2.45960	0.00951	2.31201
Cl	2.29388	1.76253	3.53675
O	-1.24283	0.28918	1.06898
Al	-2.30959	-0.22705	2.53218
Cl	-3.91625	1.19909	2.52715
Cl	4.15305	0.10428	0.98141
Cl	2.35693	-1.87618	3.33186
Cl	-2.90820	-2.21374	1.96732
Cl	-1.09968	-0.15116	4.29594
C	-1.64608	-0.48527	-1.81374
C	-2.78752	0.27136	-1.40073
C	-1.81445	-1.74367	-2.46037
C	-4.04353	-0.34156	-1.47529
C	-3.10510	-2.28675	-2.51718

C	-4.22234	-1.63422	-1.98236
H	-4.91094	0.22054	-1.13143
H	-3.23571	-3.25170	-3.00652
C	0.12730	1.87630	-2.05108
C	-0.48719	2.13908	-3.31067
C	0.74030	2.92844	-1.31839
C	-0.56264	3.46939	-3.74227
C	0.62216	4.23652	-1.80272
C	-0.05397	4.53699	-2.99190
H	-1.02716	3.67201	-4.70670
H	1.09140	5.04033	-1.23661
C	1.42455	-0.91152	-1.63733
C	2.50472	-0.55750	-2.50212
C	1.45549	-2.13684	-0.90627
C	3.58787	-1.44127	-2.58930
C	2.57779	-2.96175	-1.03339
C	3.65631	-2.63508	-1.86098
H	4.41116	-1.18029	-3.25302
H	2.59704	-3.89627	-0.47344
C	1.55940	2.71755	-0.06693
H	0.93161	2.61324	0.82771
H	2.20533	1.83636	-0.14720
H	2.20466	3.58618	0.10286
C	-1.02307	1.08444	-4.26074
H	-0.44674	0.15254	-4.23088
H	-2.06685	0.82905	-4.03803
H	-0.97728	1.46943	-5.28628
C	-0.72516	-2.52061	-3.17634
H	0.05425	-1.87803	-3.59536
H	-0.23015	-3.24645	-2.52019
H	-1.18245	-3.08247	-3.99968
C	-2.78788	1.73875	-1.00538
H	-2.86118	2.34953	-1.91723
H	-3.65970	1.95145	-0.37787
H	-1.90124	2.08100	-0.47062
C	0.35823	-2.66367	0.00338
H	0.66838	-2.59026	1.05380
H	-0.61561	-2.17674	-0.10353
H	0.19690	-3.72780	-0.20898
C	2.58574	0.70013	-3.34587
H	1.70867	0.83307	-3.98767
H	2.67622	1.60112	-2.72703
H	3.46899	0.64535	-3.99186

C	4.86602	-3.53114	-1.95442
H	5.62317	-3.21755	-1.21936
H	4.60442	-4.57476	-1.73920
H	5.32565	-3.47471	-2.94967
C	-0.21696	5.96418	-3.45369
H	-0.35278	6.01678	-4.54088
H	-1.10572	6.41092	-2.98173
H	0.64976	6.57368	-3.16764
C	-5.57819	-2.29459	-1.96500
H	-5.70781	-2.96372	-2.82532
H	-5.68418	-2.90141	-1.05238
H	-6.38303	-1.54874	-1.96394

D. Supporting information – A Benzimidazole-Based Organo-Hydride for the Reduction of CO_2

D.1 Experimental details

a) Materials

Reagents were purchased from Sigma-Aldrich: Benzimidazole (98%), 5,6-Dimethylbenzimidazole (≥99%), 2-Methylbenzimidazole (98%), Iodomethane (99%), 1,3,5-trimethoxybenzene (≥99%), Sodium borohydride (99%), $^{13}CO_2$ (99 atom % ^{13}C, <3 atom % ^{18}O), Potassium Iodide (≥99%), Potassium Bromide (≥99%), Sodium Iodide (≥99%), and Lithium Bromide (≥99%). $^{12}CO_2$ gas cylinder was purchased from Air Products (Bone Dry, 99.9%). Deuterated solvents were purchased from Cambridge Isotope Laboratories, Inc.: DMSO-D^6 (D, 99.9%), MeCN-D^3 (D, 99.8%), Methanol-D^4 (D, 99.8%). All reagents were used as received. Glass tube reactors were purchased from Ace Glass Incorporated: Tube, 9ml, 150psig, 19mm O.D., 10.2cm long (part # 8648-62).

b) Analytical Techniques

^1H and ^{13}C NMR spectroscopy were performed in a Bruker Ascend 400 MHz spectrometer. Chemical shifts are referenced to the internal solvent resonance and reported as parts-per-million relative to tetramethylsilane. ESI-MS analysis was performed at the University of Colorado Boulder mass spectrometry facility.

c) General Experimental Procedure

A 9ml glass tube reactor (purchased from Ace Glass Incorporated), shown in Fig. S1, was charged with a small stir bar and 29.8mg (0.50M) of KBr. 0.50ml of DMSO-D^6 solvent containing 8.1mg (0.10M) of species 2c and 4.2mg (0.05M) of 1,3,5-trimethoxybenzene was transferred to the tube via a pipette. The tube was then sealed and degassed under vacuum while vigorous stirring (3min) and sonication (2min) for a total of 5min. After degassing, the valve connecting to the vacuum was closed and $^{12}CO_2$ at 30psig (or $^{13}CO_2$ at ~20psig) was then introduced to the tube reactor. The tube reactor was kept at 50^oC in an oil bath. After 11hr, the reaction was completed, 0.20ml of methanol-D^4 was introduced to the tube; the reaction solution was then analyzed by ^1H NMR (and in some cases ^{13}C NMR).

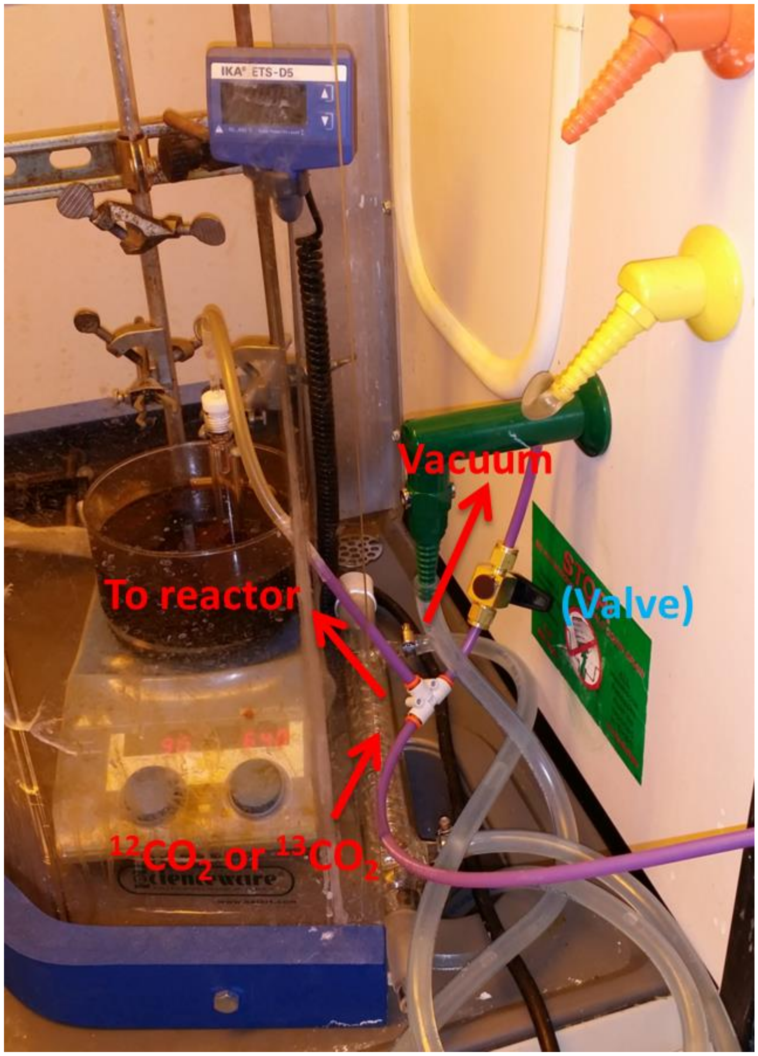

Fig. S1. Photograph of the general reaction setup for chemical reduction of CO_2 by species 2c.

d) Synthesis

Synthetic procedure highlighted in Fig. S2 applies to transforming benzimidazole derivatives to their corresponding cations (species **1**) and neutral organo-hydrides (species **2**); this procedure was modified from those reported in the literature.[243, 322] We illustrate the procedure using 2-methylbenzimidazole as an example. A 250 mL round bottom flask was charged with 60ml of MeOH and a stir bar. The following reagents were then added to the flask: 2-methylbenzimidazole (6.61g, 0.05mol, 1 eq.), Iodomethane (12.5ml, 0.20mol, 4 eq.) and K_2CO_3 (6.91g, 0.05mol, 1 eq.). This mixture was subsequently heated at reflux for 18h, and was allowed to cool to RT. The solution was reduced in volume to ~30ml via rotary evaporation, which was subsequently filtered. The solids contained residual K_2CO_3 and the desired product 1,2,3-trimethyl-1H-benzimidazol-3-ium (species **1c**). Crystallization was employed to isolate species **1c** from K_2CO_3. The solids were added to a 250 mL round bottom flask containing 150ml of MeOH. The solution was heated to near boiling to dissolve all species **1c** but K_2CO_3. The hot solution was then filtered and the filtrate was collected. The filtrate was allowed to cool to RT and then was allowed to further cool in the freezer for 4 hours, at which point crystals were formed. The crystals were isolated via filtration, and was subsequently washed with acetone and dried under vacuum. The desired product 1,2,3-trimethyl-1H-benzimidazol-3-ium (species **1c**) was isolated with 76% yield.

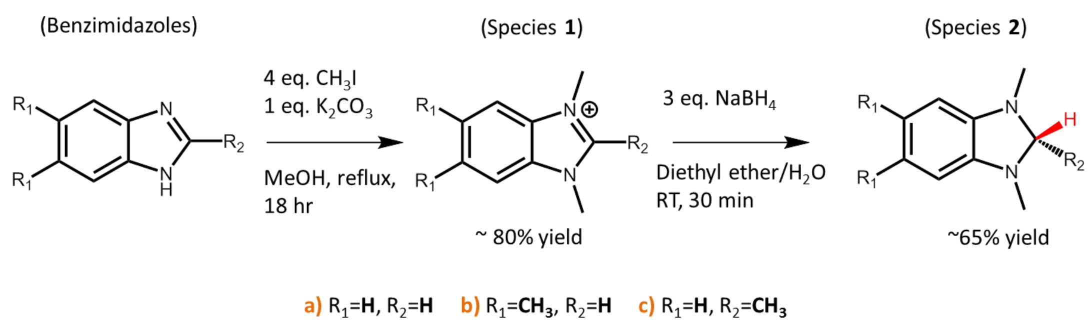

Fig. S2. Synthesis of benzimidazolium cations (species 1) and their corresponding benzimidazole-based organo-hydrides (species 2) from benzimidazoles.

In the second step of the synthesis, 1,2,3-trimethyl-1H-benzimidazol-3-ium (species **1c**) was reacted with $NaBH_4$ to form the organo-hydride 1,2,3-trimethyl-2,3-dihydro-1H-benzimidazole (species **2c**). A 250 mL round bottom flask was charged with 40ml of H_2O, 60ml of diethyl ether and a stir bar. The following reagents were added to the flask: species **1c** (2.88g, 0.01mol, 1 eq.) and $NaBH_4$ (1.13g, 0.03mol, 3 eq.). This mixture was allowed to react under vigorous stirring for 1hr in RT. The diethyl ether organic phase was then isolated via a separatory funnel, washed twice with DI water to remove any trace of $NaBH_4$, and washed for the third time with saturated brine water. The organic layer was dried with $MgSO_4$, filtered, and the volatiles were removed under reduced pressure to reveal a white solid. Species **2c** was isolated with 65% yield. The product was stored under Ar in the freezer until further use.

^{1}H-NMR, ^{13}C-NMR, and ESI-MS results were reported in the following figures: Species **1a-c** (Fig. S3-F5) and Species **2a-c** (Fig. S6-S8).

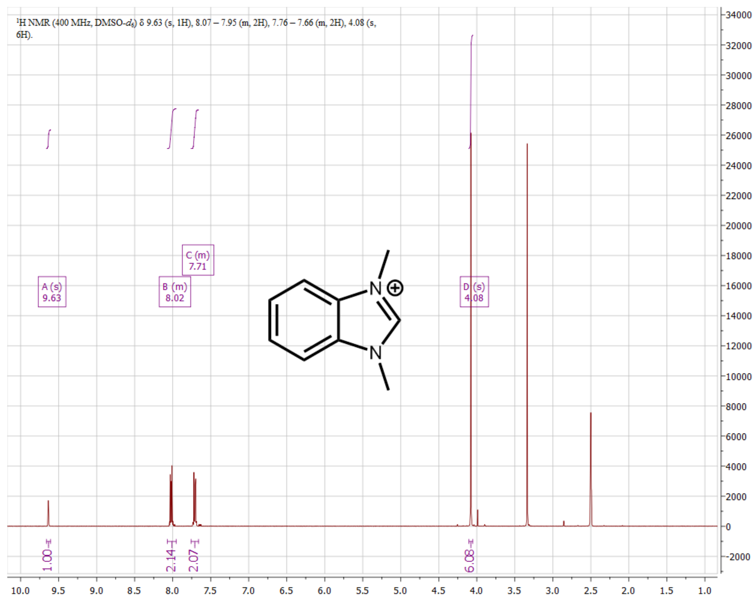

Fig. S3. ^{1}H NMR spectrum of species **1a**. ^{1}H NMR (400 MHz, DMSO-d_6) δ 9.63 (s, 1H), 8.07 – 7.95 (m, 2H), 7.76 – 7.66 (m, 2H), 4.08 (s, 6H). ^{13}C NMR (101 MHz, DMSO-d_6) δ 143.10 , 131.64 , 126.40 , 113.41 , 33.23 . HRMS (ESI): calc'd for $C_9H_{11}N_2^+$, 147.0922; found 147.0925.

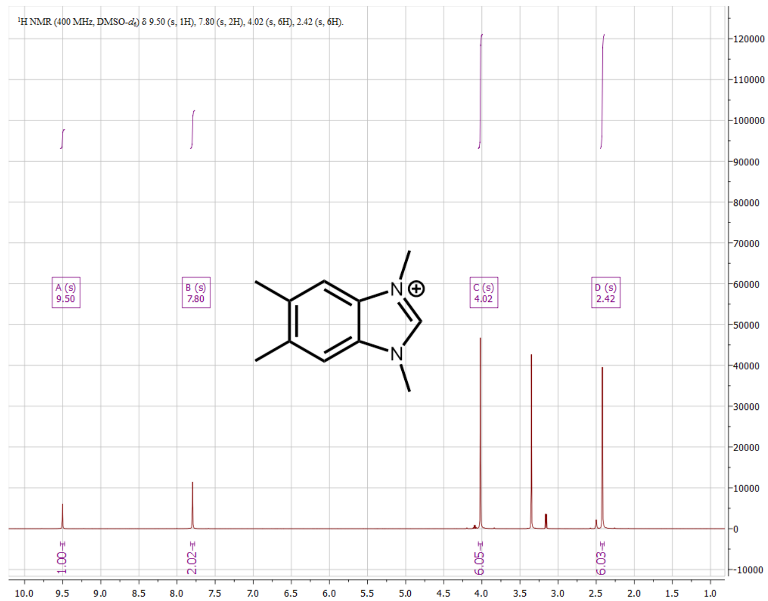

Fig. S4. ^{1}H NMR spectrum of species **1b**. 1H NMR (400 MHz, DMSO-d_6) δ 9.50 (s, 1H), 7.80 (s, 2H), 4.02 (s, 6H), 2.42 (s, 6H). ^{13}C NMR (101 MHz, DMSO-d_6) δ 141.81 , 136.04 , 130.12 , 112.91 , 33.06 , 19.96 . HRMS (ESI): calc'd for $C_{11}H_{15}N_2^+$, 175.1235; found 175.1233.

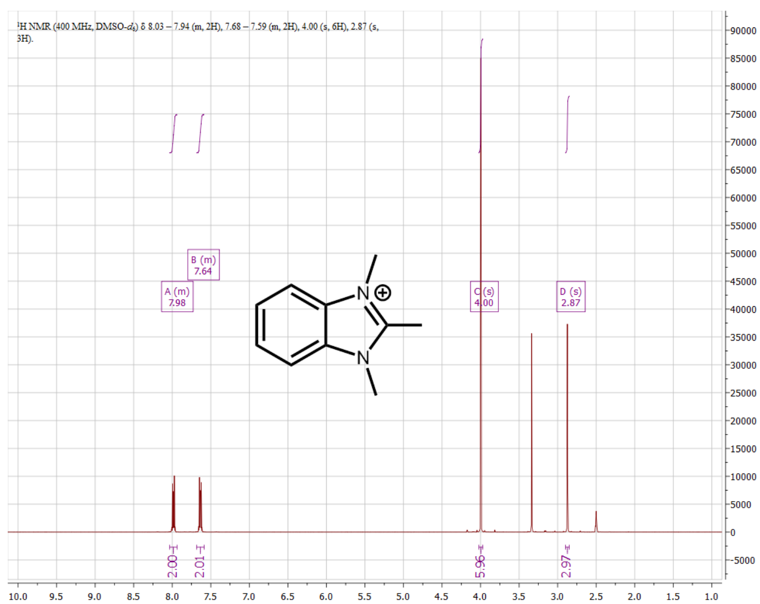

Fig. S5. ^{1}H NMR spectrum of species **1c**. ^{1}H NMR (400 MHz, DMSO-d_6) δ 8.03 – 7.94 (m, 2H), 7.68 – 7.59 (m, 2H), 4.00 (s, 6H), 2.87 (s, 3H). ^{13}C NMR (101 MHz, DMSO-d_6) δ 152.25 , 131.29 , 125.81 , 112.69 , 31.72 , 10.62 . HRMS (ESI): calc'd for $C_{10}H_{13}N_2^+$, 161.1079; found 161.1078.

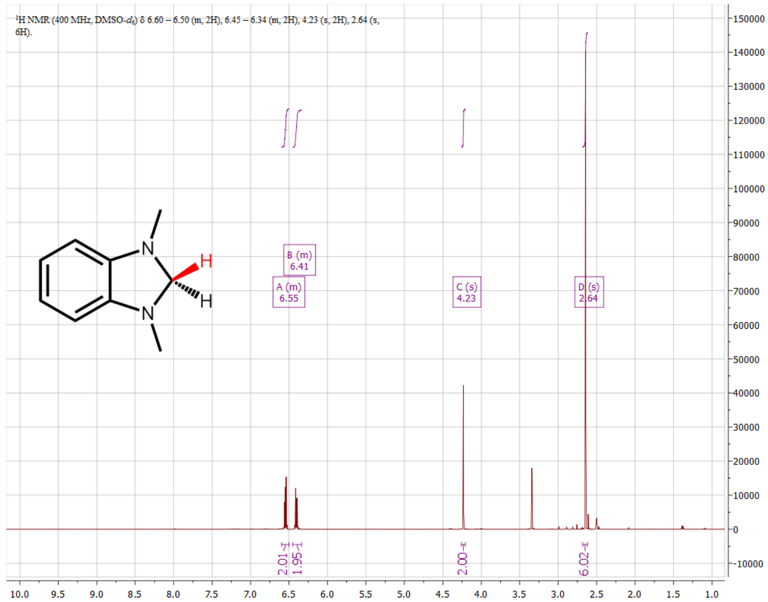

Fig. S6. ^{1}H NMR spectrum of species **2a**. 1H NMR (400 MHz, DMSO-d_6) δ 6.60 – 6.50 (m, 2H), 6.45 – 6.34 (m, 2H), 4.23 (s, 2H), 2.64 (s, 6H). ^{13}C NMR (101 MHz, DMSO-d_6) δ 143.21 , 118.63 , 105.90 , 79.68 , 34.13 . HRMS (ESI): calc'd for $(C_9H_{12}N_2)Li^+$, 155.1161; found 155.1163.

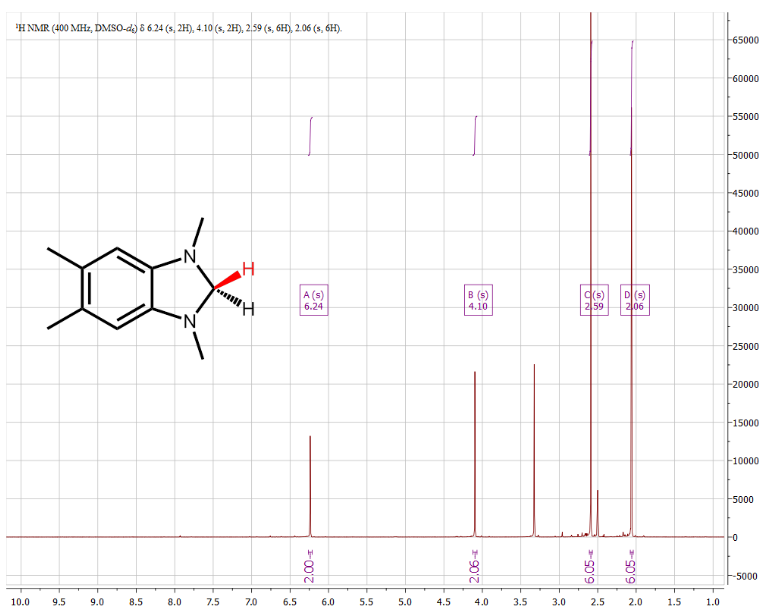

Fig. S7. ^{1}H NMR spectrum of species **2b**. 1H NMR (400 MHz, DMSO-d_6) δ 6.24 (s, 2H), 4.10 (s, 2H), 2.59 (s, 6H), 2.06 (s, 6H). ^{13}C NMR (101 MHz, DMSO-d_6) δ 141.39 , 125.25 , 108.37 , 80.28 , 34.68 , 19.23 . HRMS (ESI): calc'd for $(C_{11}H_{16}N_2)Li^+$, 183.1474; found 183.1478.

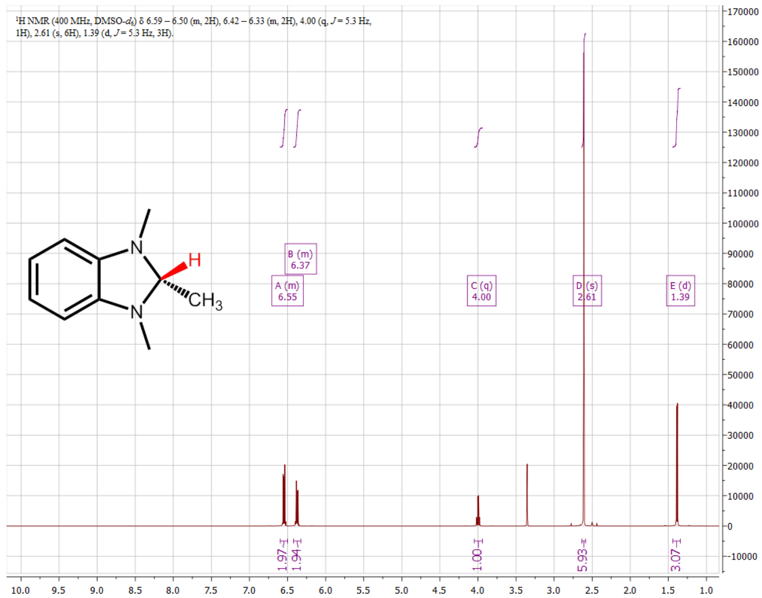

Fig. S8. ^{1}H NMR spectrum of species **2c**. ^{1}H NMR (400 MHz, DMSO-d_6) δ 6.59 – 6.50 (m, 2H), 6.42 – 6.33 (m, 2H), 4.00 (q, J = 5.3 Hz, 1H), 2.61 (s, 6H), 1.39 (d, J = 5.3 Hz, 3H). ^{13}C NMR (101 MHz, DMSO-d_6) δ 142.59 , 118.68 , 105.65 , 86.13 , 33.52 , 18.13. HRMS (ESI): calc'd for $(C_{10}H_{14}N_2)Li^+$, 169.1317; found 169.1319.

D.2 Computational methods

We compute stationary geometries (reactants, transition states and products) for the systems studied using density functional theory based on the M06 density functional[121] and 6-31+G** basis set.[57] An adequate treatment of solvent is crucial to correctly describe reactions involving a polar TS, such as those involving hydride transfers which are of particular interest here. Therefore, we employed the implicit polarized continuum solvation model (CPCM) in all calculations to treat the solute-solvent electrostatic interactions in dimethyl sulfoxide (DMSO) solvent.[67-68] We calculate vibrational force constants at the M06/6-31+G** level of theory to: 1) verify that the reactant and product structures have only positive vibrational modes, 2) confirm that each TS has only one imaginary mode and that it connects the desired reactant and product structures via Intrinsic Reaction Coordinate (IRC) calculations, and 3) compute entropies, zero-point energies (ZPE) and thermal corrections included in the reported free energies at 298K.

For the activation and reaction enthalpies, entropies and free energies for each of the various reactions examined within, we define the reference state as the separated reactants in solution, as is appropriate for solution phase bimolecular reactions.[130] It is important to recognize that commonly employed entropy evaluations within the rigid rotor, harmonic oscillator and ideal gas approximations normally overestimate the entropic cost for reactions occurring in solution phase, because ideal gas partition functions do not explicitly take into account hindered translation, rotation and vibration of the solute surrounded by solvent molecules.[18, 131-136] While various empirical correction factors for $-T\Delta S^{\ddagger}_{calc}$ values have been proposed,[18, 131, 136-137] all of which significantly lower $-T\Delta S^{\ddagger}_{calc}$, our approach to better estimate $-T\Delta S^{\ddagger}$ is to employ the experimentally obtained $-T\Delta S^{\ddagger}_{exp}$ = 2.3 kcal/mol value for an analogous HT reaction.[138] This $-T\Delta S^{\ddagger}_{exp}$ value is then added to our calculated $\Delta H^{\ddagger}_{HT}$ in order to obtain more accurate estimates to the activation free energy $\Delta G^{\ddagger}_{HT}$. Details of this approach is discussed in ref. [239]. Finally, reaction free energies (ΔG^{0}_{rxn}) are reported by adding ΔH^{0}_{rxn} to $-T\Delta S^{0}_{rxn}$ in Table 1 of the manuscript. Because the number of species remains constant on going from reactants to products in the reactions described here, the overestimation issue for the calculated $-T\Delta S^{0}_{rxn}$ is less severe. All reported energies were referenced to separated reactants in solution (as noted above) and calculations were performed using the GAUSSIAN 09[61] computational software packages.

D.3 ¹H NMR for formate detection

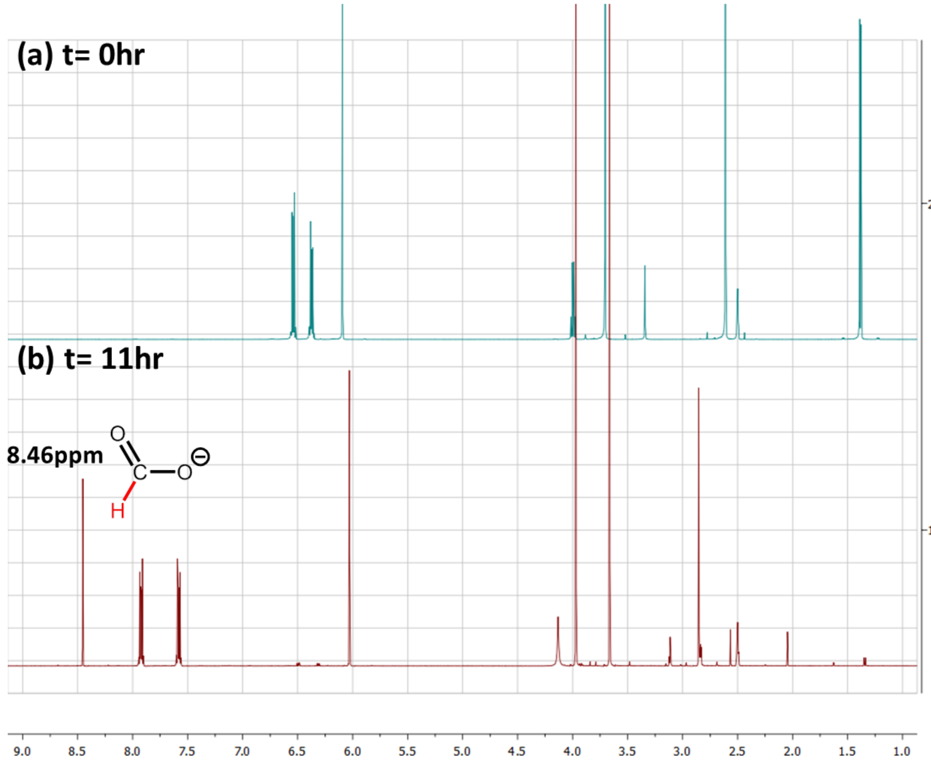

Fig. S9. (a) At t=0hr, the reaction solution contained: 0.10M species 2c, 30psig CO_2, 0.50M KBr, 0.05M 1,3,5-trimethoxybenzene; T = 50^{o}C. (b) At t=11hr, species 2c was close to be fully consumed while species 1c and formate ion (δ = 8.46 ppm) were formed.

D.4 ESI-MS for formate detection

Electrospray ionization mass spectroscopy (ESI-MS, negative mode) was used to detect the presence of $HCOO^-$ anion in the reaction solution. In Fig. S10, in the presence of low 0.05M KI salt concentration, $HCOO^-$ was detected at +4.4ppm error. In Fig. S11, in the presence of high 0.20M KBr salt concentration, (a) $HCOO^-$●KBr cluster was detected at +1.8ppm error while (b) $HCOO^-$●2KBr cluster was detected at +2.8ppm error.

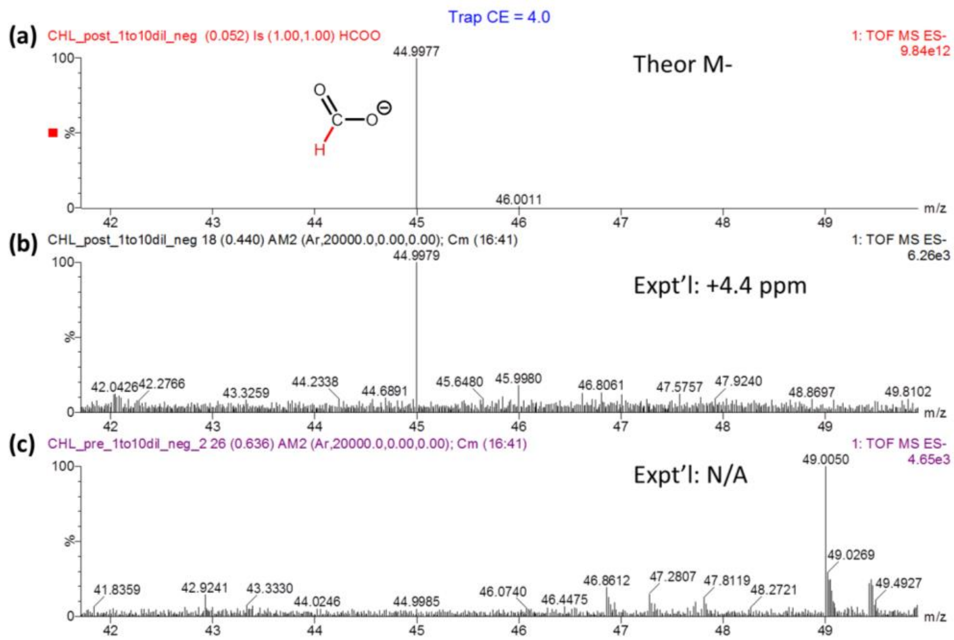

Fig. S10. (a) Theoretical mass of $HCOO^-$ anion at 44.9977 Da. (b) Observed mass of $HCOO^-$ anion at 44.9979 Da; error = +4.4ppm. (c) Blank sample. Reaction condition: 0.10M species 2c, 30psig CO_2, 0.05M KI, 0.05M 1,3,5-trimethoxybenzene, T = 50^{o}C, t = 11hr.

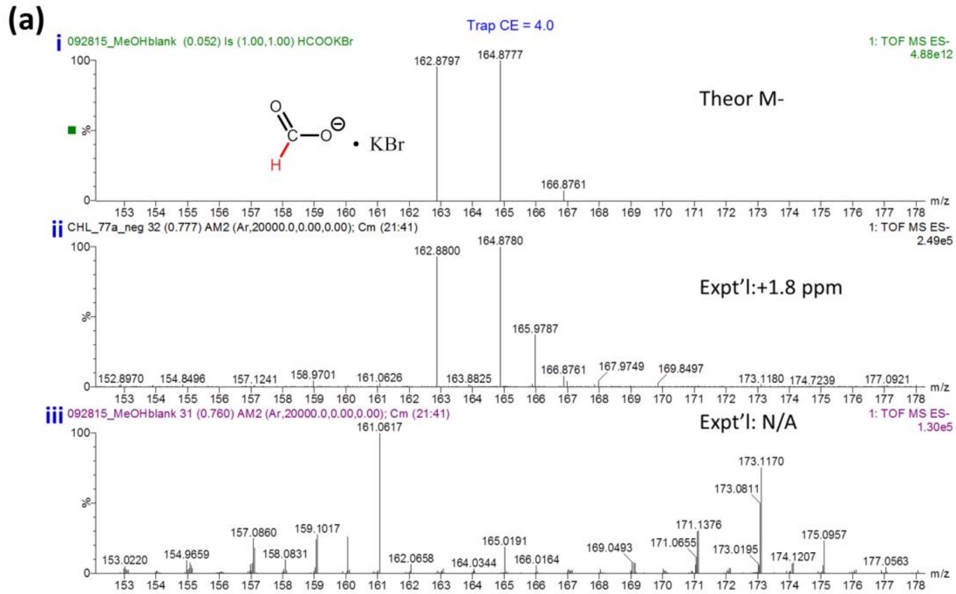

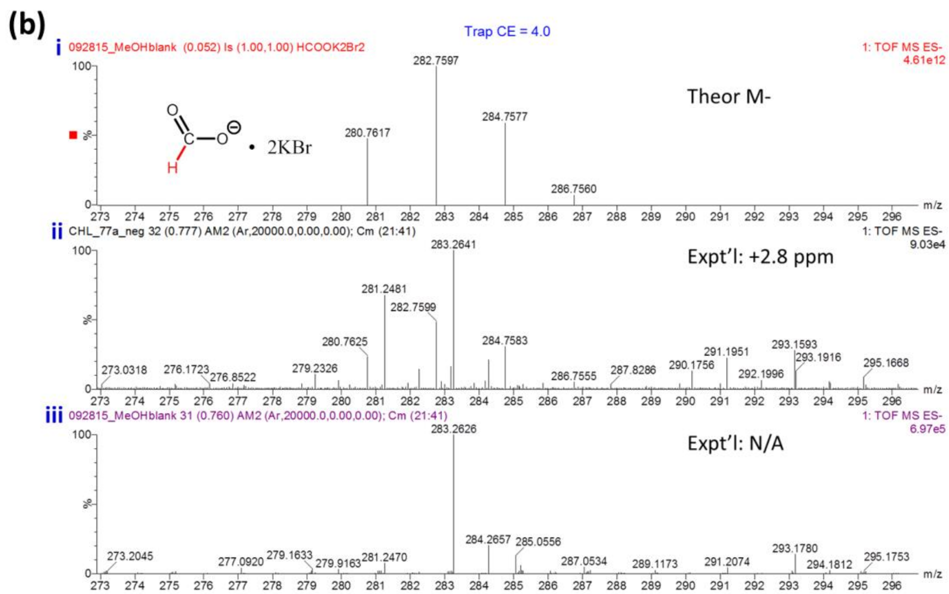

Fig. S11. (a) $HCOO^-$●KBr cluster. i) Theoretical masses of $HCOO^-$●KBr cluster at 162.8797 Da, 164.8777 Da and 166.8761 Da. ii) Observed masses of $HCOO^-$●KBr cluster at 162.8800 Da, 164.8780 Da and 166.8761 Da; error = +1.8ppm. iii) Blank sample. (b) $HCOO^-$●2KBr cluster. i) Theoretical masses of $HCOO^-$●2KBr cluster at 280.7617 Da, 282.7597 Da, 284.7577 Da and 286.7560 Da. ii) Observed masses of $HCOO^-$●2KBr cluster at 280.7625 Da, 282.7599 Da, 284.7583 Da and 286.7555 Da; error = +2.8ppm. iii) Blank sample. Reaction conditions: 0.10M species 2c, 30psig CO_2, 0.20M KBr, 0.05M 1,3,5-trimethoxybenzene, T = 50^{o}C, t = 11hr.

D.5 ^1H NMR for $^{13}CO_2$ experiment

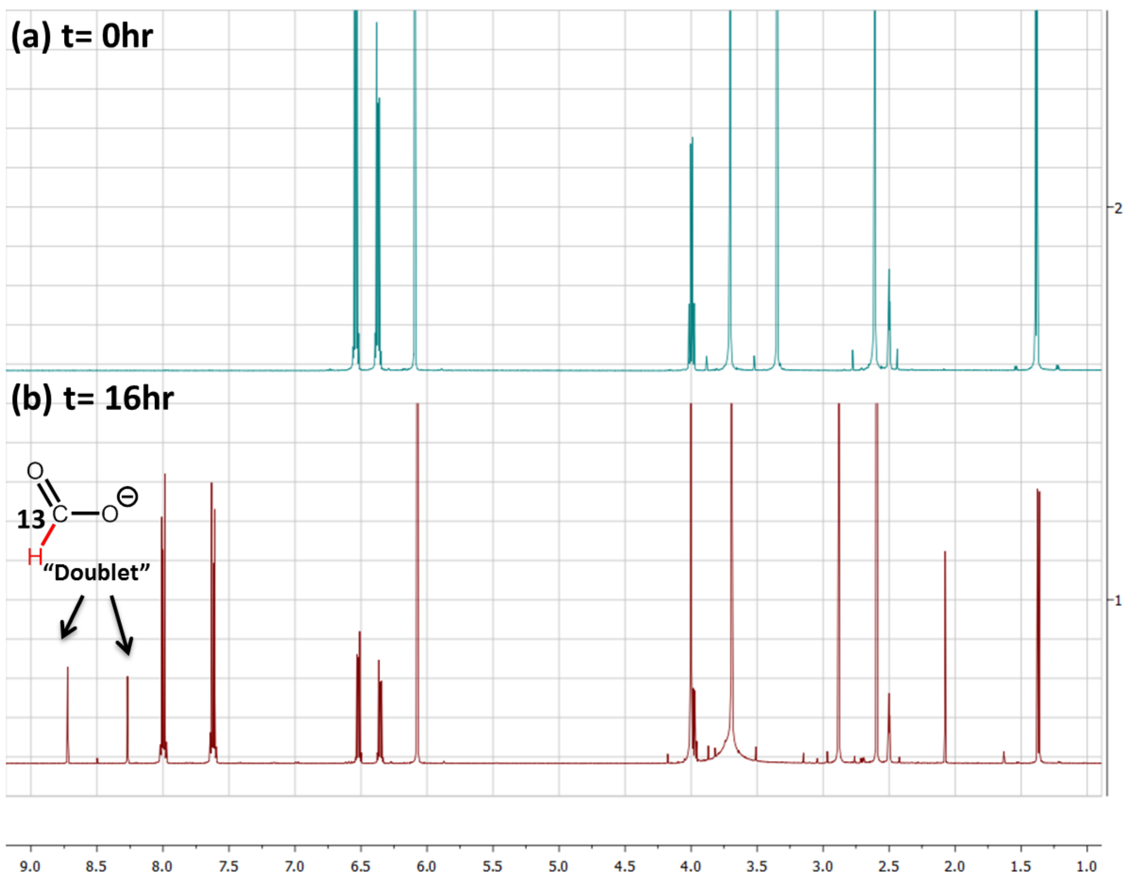

Fig. S12. $^{13}CO_2$ experiment was performed in the following conditions: 0.10M species 2c, ~20psig $^{13}CO_2$, 0.20M KBr, 0.05M 1,3,5-trimethoxybenzene, T = 50°C. (a) t = 0hr. (b) t = 16hr. After the reaction, ^1H NMR showed the appearance of doublet peaks at δ= 8.27 and 8.72ppm; this indicated the dominant presence of ^{13}C nucleus in the produced formate due to the introduced $^{13}CO_2$ (99 atom % ^{13}C). A small singlet formate peak at 8.50ppm was also observed, which was due to the remaining 1 atom % $^{12}CO_2$.

D.6 Coordinates of Molecular Structures

All coordinates are reported as XYZ Cartesian coordinates. In parenthesis's are rM06/6-31+G**/CPCM-DMSO energies. Energies reported here are computed at 0 K (not ZPE and thermally corrected) and are stated in Hartrees units. All energies reported were calculated using the GAUSSIAN 09 computational chemistry package

CO_2 (-188.51260258)

C	2.18926	0.01112	0.30294
O	1.79513	0.03673	1.39377
O	2.58406	-0.01448	-0.78759

$HCOO^-$ (-189.23196244)

H	0.38144	-0.51638	-0.38765
C	0.06843	-1.54184	-0.72830
O	-0.39175	-2.29598	0.16197
O	0.22460	-1.78265	-1.94930

Species 1a (-458.62929816)

C	-2.99120	-0.26682	-0.02841
C	-1.59297	-0.26689	-0.02851
C	-0.85695	0.91383	0.00601
C	-1.58843	2.09239	0.04010
C	-2.99548	2.09246	0.04022
C	-3.72710	0.91398	0.00624
H	0.22902	0.91166	0.00595
H	-1.06113	3.04171	0.06797
H	-3.52268	3.04184	0.06816
H	-4.81306	0.91193	0.00630
N	-1.19630	-1.59905	-0.06939
N	-3.38802	-1.59893	-0.06946
C	0.18119	-2.07219	-0.08448
H	0.69055	-1.68234	-0.96873
H	0.69292	-1.73295	0.81910
H	0.18043	-3.16163	-0.11547
C	-4.76556	-2.07191	-0.08468
H	-5.27731	-1.73267	0.81889
H	-5.27482	-1.68194	-0.96894
H	-4.76492	-3.16135	-0.11574
C	-2.29220	-2.35517	-0.09286
H	-2.29226	-3.43676	-0.12601

Species 1b (-537.20681911)

C	-2.98783	-0.27095	-0.03449

C	-1.59410	-0.27209	-0.02371
C	-0.86613	0.91254	0.02790
C	-1.57688	2.10647	0.06831
C	-3.00261	2.10764	0.05740
C	-3.71456	0.91486	0.00608
H	0.22137	0.90950	0.03570
H	-4.80206	0.91365	-0.00267
N	-1.19615	-1.60348	-0.07529
N	-3.38720	-1.60162	-0.09223
C	0.18098	-2.07551	-0.08455
H	0.69808	-1.67456	-0.95948
H	0.68569	-1.74656	0.82693
H	0.18208	-3.16459	-0.12881
C	-4.76486	-2.07108	-0.12469
H	-5.28550	-1.73769	0.77614
H	-5.26520	-1.67253	-1.01044
H	-4.76738	-3.16031	-0.16446
C	-2.29207	-2.36028	-0.11508
H	-2.29264	-3.44130	-0.15941
C	-0.83650	3.40738	0.12351
H	-1.09345	3.97749	1.02518
H	0.24514	3.24661	0.12289
H	-1.08484	4.04618	-0.73332
C	-3.74153	3.40979	0.10065
H	-3.48964	3.98458	1.00071
H	-3.48666	4.04354	-0.75811
H	-4.82338	3.25059	0.09339

Species 1c (-497.92511018)

C	-2.98536	-0.32265	-0.02142
C	-1.59073	-0.32244	-0.01167
C	-0.85631	0.85729	0.04741
C	-1.58813	2.03713	0.09584
C	-2.99326	2.03634	0.08660
C	-3.72256	0.85549	0.02823
H	0.22972	0.85987	0.05659
H	-3.52275	2.98406	0.12749
H	-4.80865	0.85385	0.02301
N	-1.19103	-1.65440	-0.07276
N	-3.37951	-1.65345	-0.08833
C	0.20707	-2.06103	-0.08658
H	0.71289	-1.56983	-0.92129
H	0.68046	-1.77119	0.85482

H	0.28699	-3.13879	-0.21266
C	-4.76734	-2.09034	-0.12382
H	-5.26373	-1.81294	0.80966
H	-5.27288	-1.61289	-0.96674
H	-4.81247	-3.17134	-0.24963
C	-2.28543	-2.43147	-0.11408
H	-1.06031	2.98545	0.14348
C	-2.31953	-3.90447	-0.18166
H	-1.32714	-4.33677	-0.05944
H	-2.96123	-4.30598	0.60837
H	-2.71963	-4.23355	-1.14682

Species 2a (-459.36028412)

C	-2.98650	-0.27017	-0.24335
C	-1.57992	-0.28817	-0.18476
C	-0.85705	0.88297	-0.03937
C	-1.56836	2.09382	0.03380
C	-2.95675	2.11125	-0.02365
C	-3.68955	0.91869	-0.15674
H	0.22880	0.87133	0.02342
H	-1.02019	3.02567	0.15173
H	-3.48919	3.05669	0.05001
H	-4.77684	0.93426	-0.18396
N	-1.15229	-1.61349	-0.32161
N	-3.43597	-1.58399	-0.41644
C	0.08995	-2.02573	0.29296
H	0.91993	-1.43151	-0.10024
H	0.06317	-1.91467	1.39164
H	0.28521	-3.07518	0.05164
C	-4.73448	-1.96199	0.09576
H	-4.79703	-1.83954	1.19178
H	-5.51559	-1.35451	-0.37053
H	-4.93268	-3.00944	-0.15155
C	-2.31995	-2.42605	-0.00423
H	-2.31022	-3.38433	-0.53795
H	-2.36822	-2.63126	1.09550

Species 2b (-537.93421799)

C	-2.97715	-0.27358	-0.27326
C	-1.57813	-0.29324	-0.19043
C	-0.86581	0.88077	-0.02322
C	-1.55866	2.10445	0.05286
C	-2.95930	2.12402	-0.03051

C	-3.67175	0.91995	-0.19009
H	0.22076	0.87040	0.05615
H	-4.76002	0.93966	-0.23912
N	-1.14318	-1.61987	-0.33528
N	-3.42959	-1.58772	-0.46998
C	0.07661	-2.03070	0.32427
H	0.91893	-1.43192	-0.03454
H	0.00783	-1.92311	1.42210
H	0.28498	-3.07888	0.08768
C	-4.72846	-1.96228	0.04497
H	-4.78777	-1.84013	1.14180
H	-5.50896	-1.35166	-0.41837
H	-4.93117	-3.00912	-0.20195
C	-2.31960	-2.42715	-0.03421
H	-2.30231	-3.39059	-0.55821
H	-2.38740	-2.62088	1.06765
C	-3.71032	3.42009	0.07001
H	-4.78631	3.26377	-0.05944
H	-3.56187	3.90650	1.04403
H	-3.38493	4.14226	-0.69066
C	-0.78836	3.37899	0.24307
H	-0.98012	4.09854	-0.56421
H	-1.05728	3.88491	1.18046
H	0.28955	3.18829	0.26784

Species 2c (-498.64997096)

C	-2.98989	-0.25883	-0.18534
C	-1.58040	-0.27713	-0.12769
C	-0.85630	0.89558	-0.01368
C	-1.56785	2.11210	0.02393
C	-2.95424	2.12968	-0.03164
C	-3.69098	0.93185	-0.12759
H	0.22976	0.88487	0.04810
H	-1.01726	3.04602	0.11220
H	-4.77846	0.94850	-0.15287
N	-1.16544	-1.60202	-0.22720
N	-3.43027	-1.57216	-0.32045
C	0.14702	-1.99582	0.22605
H	0.91211	-1.46755	-0.35281
H	0.31554	-1.78195	1.29529
H	0.28391	-3.06862	0.05690
C	-4.78584	-1.93068	0.02147
H	-5.03782	-1.70903	1.07266

H	-5.48520	-1.38497	-0.62084
H	-4.93572	-3.00016	-0.15734
C	-2.32501	-2.43954	0.10917
H	-2.31230	-3.35613	-0.50143
H	-3.48613	3.07741	0.01368
C	-2.38980	-2.80520	1.58675
H	-3.28830	-3.39324	1.80212
H	-1.52404	-3.41180	1.87327
H	-2.40547	-1.89973	2.20822

Species 2a + CO_2, TS (-647.83805305, 1174.23*i* imaginary mode at TS)

C	-3.01301	-0.41022	0.17369
C	-1.61049	-0.40419	0.25437
C	-0.87532	0.73486	-0.03493
C	-1.59032	1.88138	-0.39695
C	-2.98489	1.87582	-0.47086
C	-3.72442	0.72245	-0.18930
H	0.21043	0.73986	0.01344
H	-1.04571	2.79215	-0.63198
H	-3.50886	2.78289	-0.76073
H	-4.80908	0.71482	-0.25902
N	-1.21646	-1.67415	0.66658
N	-3.43688	-1.68748	0.51518
C	0.13235	-2.18293	0.55877
H	0.43242	-2.28627	-0.49418
H	0.82579	-1.50563	1.06339
H	0.18753	-3.16021	1.04414
C	-4.79244	-2.17498	0.39087
H	-5.47324	-1.51377	0.93442
H	-5.09501	-2.22458	-0.66269
H	-4.85471	-3.17325	0.82968
C	-2.25486	-3.47550	-1.93478
O	-1.55396	-4.44744	-2.11265
O	-2.96411	-2.65909	-2.48287
C	-2.32592	-2.50929	0.58889
H	-2.36179	-3.38907	1.23704
H	-2.24606	-3.16175	-0.59625

Species 2b + CO_2, TS (-726.41335406, 1171.73*i* imaginary mode at TS)

C	-3.00474	-0.40734	0.21145
C	-1.60615	-0.40478	0.26587
C	-0.88244	0.73654	-0.04044
C	-1.58188	1.89745	-0.39651

C	-2.99282	1.89512	-0.44535
C	-3.71111	0.73092	-0.14175
H	0.20573	0.74090	-0.01226
H	-4.79858	0.72764	-0.19190
N	-1.20392	-1.67589	0.67495
N	-3.42869	-1.68379	0.56312
C	0.13792	-2.18778	0.51486
H	0.39809	-2.29127	-0.54923
H	0.85211	-1.51177	0.99170
H	0.21115	-3.16559	0.99722
C	-4.78528	-2.16869	0.44793
H	-5.46157	-1.50536	0.99479
H	-5.09685	-2.21961	-0.60333
H	-4.84760	-3.16622	0.88890
C	-2.29971	-3.46333	-1.93216
O	-1.60599	-4.43765	-2.11896
O	-3.02070	-2.64648	-2.46179
C	-2.31722	-2.51052	0.60409
H	-2.34384	-3.39276	1.24979
H	-2.25868	-3.14205	-0.58101
C	-3.73245	3.13929	-0.83851
H	-3.47648	3.45746	-1.85783
H	-4.81505	2.98464	-0.79925
H	-3.48889	3.98196	-0.17849
C	-0.82114	3.14443	-0.73731
H	-1.03035	3.47937	-1.76179
H	-1.09125	3.97794	-0.07567
H	0.25812	2.98546	-0.65099

Species 2c + CO_2, TS (-687.13186582, 1091.53*i* imaginary mode at TS)

C	-3.02710	-0.39747	0.24410
C	-1.62423	-0.38758	0.27817
C	-0.90327	0.75823	-0.01966
C	-1.62984	1.90620	-0.35154
C	-3.02498	1.89570	-0.38813
C	-3.74944	0.73655	-0.09242
H	0.18323	0.76901	-0.00544
H	-4.83540	0.72980	-0.13205
N	-1.21294	-1.66322	0.65479
N	-3.44209	-1.67743	0.60667
C	0.13726	-2.16063	0.51703
H	0.29396	-2.60270	-0.47861
H	0.84068	-1.33756	0.65356

H	0.34619	-2.91215	1.28202
C	-4.76875	-2.18810	0.34424
H	-5.50085	-1.39625	0.51342
H	-4.85633	-2.53933	-0.69589
H	-5.00176	-3.01081	1.02366
C	-2.25417	-3.52454	-1.92019
O	-2.43948	-4.72021	-1.89474
O	-2.05184	-2.56844	-2.63609
C	-2.32032	-2.51422	0.60748
H	-2.28832	-3.05537	-0.62580
H	-3.56194	2.80131	-0.65806
H	-1.09348	2.82005	-0.59363
C	-2.32738	-3.77244	1.42263
H	-2.33839	-3.52810	2.49079
H	-3.20454	-4.37936	1.18221
H	-1.44351	-4.37617	1.19835

E. Supporting information – Visible-light organic photocatalysis for latent radical-initiated polymerization via $2e^-/1H^+$ transfers: Initiation with parallels to photosynthesis

E.1 Reaction of alpha-amino radical (derived from DIPEA) and a HEMA monomer

In Figure S1, we calculate the enthalpic barrier (ΔH^0_{act}) for the reaction between an amino-alkyl radical (product of one electron and one proton transfer of DIPEA) and a HEMA monomer. Stationary geometries (transition state and minima) were obtained at uWB97XD/LANL2dz/CPCM-methanol level of theory. ΔH^0_{act} calculated at this level of theory was 0.1 kcal/mol. Single point energy calculations were then performed at uM06/6-311G(d,p) level of theory, where we obtained ΔH^0_{act} = -1.4 kcal/mol (barrierless). The M06 functional was designed to yield accurate thermochemical predictions; and when combined with 6-311G(d,p) basis sets, should yield reasonable predictions to the enthalpic barrier.

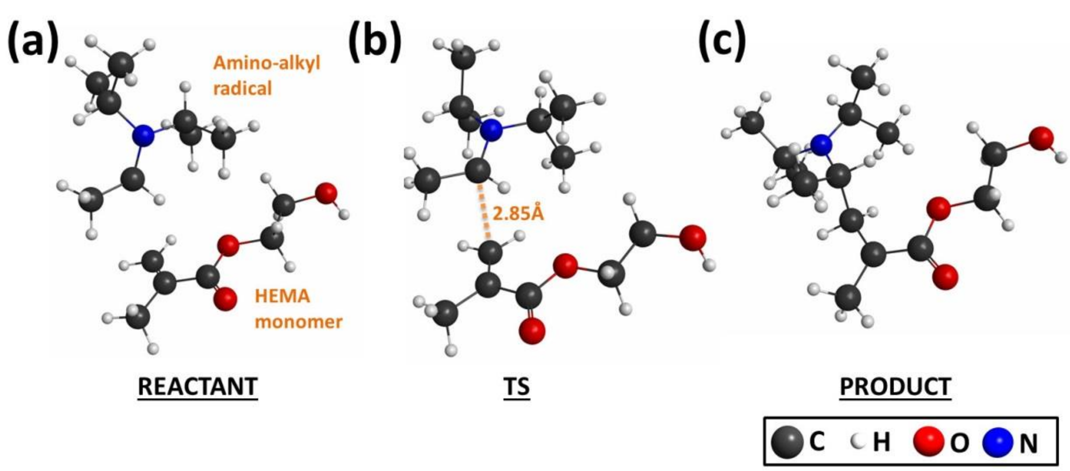

Figure S1 | Reaction between amino-alkyl radical and HEMA monomer, calculated at uM06/6-311G(d,p)//uWB97XD/LANL2dz/CPCM-methanol. (a) Reactant, (b) TS structure and (c) Product

Coordinates of Molecular Structures

All coordinates are reported as XYZ Cartesian coordinates. 0 K energies (not ZPE corrected) reported are calculated using uM06/6-311G(d,p)//uWB97XD/LANL2dz/CPCM-methanol in Hartrees.

E.2 Coordinates of structures

LMB (-1183.1852140093)

S	1.38084	0.00392	1.14593
N	-0.23269	4.95441	0.61194
N	-0.23107	-4.94657	0.60705

C	0.75678	1.39691	0.12754
C	0.75723	-1.38828	0.12617
C	0.66865	1.24177	-1.26554
C	0.66904	-1.23179	-1.26676
C	0.05714	3.74027	-0.00242
C	0.05834	-3.73173	-0.00613
C	0.43851	2.60392	0.75741
C	0.43935	-2.59602	0.75484
C	0.26737	2.35837	-2.01910
C	0.26812	-2.34776	-2.02143
C	-0.01464	3.58585	-1.41223
C	-0.01351	-3.57593	-1.41579
C	-0.64309	6.09831	-0.19834
C	-0.18303	5.06489	2.06709
C	-0.64079	-6.08990	-0.20439
C	-0.18136	-5.05848	2.06208
H	0.50609	2.66117	1.83725
H	0.50698	-2.65433	1.83461
H	0.17776	2.26725	-3.09760
H	0.17847	-2.25560	-3.09984
H	-0.30620	4.41653	-2.04273
H	-0.30484	-4.40607	-2.04710
H	-0.81903	6.95765	0.45013
H	-1.57171	5.89750	-0.75101
H	0.13091	6.37994	-0.92498
H	-0.44767	6.08077	2.36346
H	-0.88883	4.37717	2.55418
H	0.82184	4.85360	2.45790
H	-0.81608	-6.95005	0.44318
H	-1.56961	-5.88915	-0.75677
H	0.13332	-6.37024	-0.93140
H	-0.44573	-6.07473	2.35743
H	-0.88735	-4.37144	2.54985
H	0.82345	-4.84729	2.45309
N	0.97519	0.00535	-1.88365
H	0.98131	0.00585	-2.89448

MB^{+} (-1182.4175828153)

S	0.00000	0.00000	1.42134
N	0.00000	5.07128	0.53149
N	0.00000	-5.07128	0.53149
N	0.00000	0.00000	-1.75698

C	0.00000	1.39897	0.29303
C	0.00000	-1.39897	0.29303
C	0.00000	1.19352	-1.13345
C	0.00000	-1.19352	-1.13345
C	0.00000	3.82498	0.00284
C	0.00000	-3.82498	0.00284
C	0.00000	2.66694	0.84297
C	0.00000	-2.66694	0.84297
C	0.00000	2.36833	-1.96001
C	0.00000	-2.36833	-1.96001
C	0.00000	3.62907	-1.42969
C	0.00000	-3.62907	-1.42969
C	0.00000	6.25956	-0.33974
C	0.00000	5.26487	1.99040
C	0.00000	-6.25956	-0.33974
C	0.00000	-5.26487	1.99040
H	0.00000	2.77932	1.91918
H	0.00000	-2.77932	1.91918
H	0.00000	2.21465	-3.03265
H	0.00000	-2.21465	-3.03265
H	0.00000	4.48139	-2.09438
H	0.00000	-4.48139	-2.09438
H	0.00000	7.15477	0.27927
H	-0.89205	6.28325	-0.97338
H	0.89205	6.28325	-0.97338
H	0.00000	6.33052	2.21088
H	-0.89193	4.82186	2.44522
H	0.89193	4.82186	2.44522
H	0.00000	-7.15477	0.27927
H	-0.89205	-6.28325	-0.97338
H	0.89205	-6.28325	-0.97338
H	0.00000	-6.33052	2.21088
H	-0.89193	-4.82186	2.44522
H	0.89193	-4.82186	2.44522

DPI$^+$ (-7382.0962246181)

I	-0.00001	-1.44433	-0.00001
C	1.60172	-0.02727	-0.00001
C	2.09335	0.41606	1.23306
C	2.09320	0.41620	-1.23310
C	3.13139	1.36151	1.21884
H	1.69597	0.05257	2.17264
C	3.13122	1.36167	-1.21890

H	1.69571	0.05282	-2.17268
C	3.64553	1.83160	-0.00003
H	3.53095	1.72413	2.15806
H	3.53065	1.72442	-2.15812
H	4.44597	2.56206	-0.00004
C	-1.60174	-0.02729	0.00002
C	-2.09322	0.41618	1.23310
C	-2.09335	0.41606	-1.23305
C	-3.13121	1.36167	1.21890
H	-1.69575	0.05276	2.17268
C	-3.13136	1.36154	-1.21883
H	-1.69597	0.05257	-2.17264
C	-3.64549	1.83163	0.00004
H	-3.53064	1.72442	2.15813
H	-3.53090	1.72419	-2.15805
H	-4.44591	2.56213	0.00005

Phenyl radical (-231.4319744629)

C	0.64415	-3.03630	0.00271
C	2.05118	-3.04578	0.00316
C	2.77024	-1.82983	0.00250
C	2.01607	-0.66040	0.00153
C	0.62626	-0.59196	0.00112
C	-0.06749	-1.82261	0.00166
H	0.10222	-3.97572	0.00318
H	2.58997	-3.98766	0.00397
H	3.85466	-1.82159	0.00284
H	0.09138	0.35138	0.00030
H	-1.15260	-1.82648	0.00132

Iodobenzene (-7150.8087915277)

I	-1.52282	2.77274	0.53421
C	-2.37412	0.82403	0.72516
C	-2.27342	-0.07724	-0.34551
C	-3.02515	0.46939	1.91627
C	-2.83774	-1.35751	-0.21546
H	-1.76961	0.20110	-1.26368
C	-3.58499	-0.81434	2.03226
H	-3.10057	1.16936	2.74013
C	-3.49286	-1.72762	0.96993
H	-2.76275	-2.05760	-1.03992

H	-4.08929	-1.09296	2.95070
H	-3.92752	-2.71635	1.06476

DIPEA (-370.8458178021)

N	0.00413	0.26562	0.17904
C	1.03138	-0.80346	0.20464
C	2.13949	-0.45481	1.21684
C	1.65594	-1.15095	-1.17085
H	0.52985	-1.70717	0.56892
H	1.71213	-0.32724	2.21651
H	2.89713	-1.24665	1.25433
H	2.64187	0.47975	0.93751
H	0.88785	-1.36017	-1.92067
H	2.28385	-0.33244	-1.54155
H	2.29156	-2.03879	-1.07359
C	-1.40961	-0.16450	0.06773
C	-1.89053	-0.85967	1.35478
C	-1.72827	-1.03429	-1.17343
H	-1.99158	0.75957	-0.02985
H	-1.70196	-0.22116	2.22361
H	-2.96572	-1.06461	1.29495
H	-1.37945	-1.81687	1.51293
H	-1.38290	-0.55090	-2.09444
H	-1.25075	-2.01829	-1.09729
H	-2.81008	-1.19019	-1.25599
C	-0.18379	2.76356	0.02615
C	0.34174	1.46517	-0.60702
H	0.09683	3.62761	-0.58794
H	-1.27534	2.76035	0.11862
H	0.24273	2.89166	1.02667
H	-0.02499	1.38972	-1.64730
H	1.43192	1.54017	-0.67178

DIPEA-H^+ (-371.3005826892)

N	0.04215	0.30794	0.30429
C	1.06395	-0.85398	0.22025
C	2.17525	-0.59749	1.24688
C	1.62765	-1.06803	-1.19015
H	0.50754	-1.74351	0.51888
H	1.77728	-0.52889	2.26441
H	2.88043	-1.43157	1.21938

H	2.73245	0.31730	1.01933
H	0.85098	-1.17061	-1.94968
H	2.30999	-0.26723	-1.48603
H	2.19954	-1.99977	-1.17461
C	-1.43132	-0.13184	0.16773
C	-1.85277	-0.91829	1.41619
C	-1.70204	-0.89781	-1.12898
H	-1.99178	0.80449	0.15182
H	-1.63913	-0.36463	2.33625
H	-2.93260	-1.07965	1.36973
H	-1.37534	-1.90029	1.47496
H	-1.40232	-0.33802	-2.01878
H	-1.21429	-1.87620	-1.13650
H	-2.77996	-1.06588	-1.19697
C	-0.34065	2.76705	-0.21877
C	0.40657	1.48528	-0.59155
H	0.09808	3.59111	-0.78683
H	-1.40314	2.72696	-0.46781
H	-0.23338	3.00199	0.84499
H	0.20797	1.19481	-1.62249
H	1.48053	1.63913	-0.47693
H	0.11790	0.66083	1.26546

$N(C_3H_7)_2C_2H_4$_radical + HEMA (reactant) (-830.34789677)

N	-0.19714	-2.33973	-0.37374
C	1.22021	-1.98936	-0.13169
C	1.46717	-1.43660	1.28887
C	1.73178	-1.01367	-1.20880
H	1.79514	-2.91559	-0.22509
H	1.08063	-2.12780	2.04460
H	2.54265	-1.30470	1.45574
H	0.97625	-0.46662	1.42537
H	1.62258	-1.45430	-2.20484
H	1.15982	-0.07928	-1.18311
H	2.78904	-0.77585	-1.04410
C	-0.56128	-3.76871	-0.45254
C	-0.33810	-4.50310	0.88780
C	0.15821	-4.47950	-1.61473
H	-1.63123	-3.80167	-0.67418
H	-0.87397	-3.99266	1.69544
H	-0.70390	-5.53389	0.82197
H	0.72717	-4.53790	1.14539

H	-0.00702	-3.94027	-2.55295
H	1.23789	-4.55606	-1.44431
H	-0.23242	-5.49720	-1.72353
C	-2.62216	-1.57448	-0.42283
C	-1.16915	-1.36955	-0.08659
H	-3.16648	-0.65043	-0.20344
H	-2.79252	-1.81699	-1.48625
H	-3.09272	-2.37540	0.16551
H	-0.79492	-0.35339	-0.02011
O	0.36384	2.21959	0.38884
O	4.01266	2.54635	-0.01002
O	-0.89676	3.12593	-1.28694
C	1.59065	2.66748	-0.28115
C	2.74346	2.21078	0.61021
C	-2.02531	2.08990	0.58502
C	-0.83448	2.52803	-0.19694
C	-3.35919	2.33792	-0.07781
C	-1.87884	1.51290	1.79478
H	4.18581	3.50304	0.04437
H	1.56472	3.75623	-0.38871
H	1.65583	2.21297	-1.27337
H	2.65385	2.65911	1.60582
H	2.73492	1.12531	0.70827
H	-3.51320	3.40641	-0.26084
H	-3.41215	1.83202	-1.04792
H	-4.17359	1.97090	0.55145
H	-2.74516	1.18962	2.36328
H	-0.90104	1.35113	2.23421

$N(C_3H_7)_2C_2H_4$_radical + HEMA (TS) (-830.34938384)

N	-4.32431	-2.98054	1.98016
C	-2.88477	-2.77699	2.26135
C	-2.63259	-1.89745	3.50416
C	-2.15564	-2.21385	1.02606
H	-2.46449	-3.76542	2.46822
H	-3.15129	-2.30265	4.37905
H	-1.55886	-1.85915	3.72075
H	-2.98306	-0.87462	3.33500
H	-2.28912	-2.87912	0.16698
H	-2.54258	-1.22382	0.75796
H	-1.08381	-2.11450	1.23058
C	-4.91829	-4.29902	2.28614
C	-4.93544	-4.58569	3.80295

C	-4.23782	-5.43542	1.50003
H	-5.95540	-4.25486	1.94481
H	-5.43916	-3.77255	4.33713
H	-5.46735	-5.52156	4.00693
H	-3.91708	-4.68251	4.19756
H	-4.21883	-5.20305	0.43050
H	-3.20993	-5.61123	1.83567
H	-4.79542	-6.36699	1.64505
C	-6.55526	-1.97157	1.32643
C	-5.13653	-1.85669	1.82099
H	-6.96228	-0.96585	1.18912
H	-6.62948	-2.49982	0.36104
H	-7.21520	-2.49357	2.03247
H	-4.60384	-0.93223	1.62088
O	-3.88636	1.49733	2.99276
O	-0.35418	2.37009	2.38982
O	-5.40142	3.02657	2.21517
C	-2.79245	2.35479	2.52901
C	-1.50233	1.58200	2.80210
C	-6.21672	1.01456	3.27406
C	-5.17518	1.93787	2.78642
C	-7.63939	1.39429	2.93163
C	-5.88183	-0.11664	3.94562
H	-0.19650	3.10604	3.00780
H	-2.81768	3.30155	3.07827
H	-2.91215	2.55888	1.46189
H	-1.44033	1.31035	3.86213
H	-1.46951	0.67159	2.20293
H	-7.90851	2.35908	3.37555
H	-7.77471	1.48932	1.84807
H	-8.33557	0.63666	3.30118
H	-6.64774	-0.80428	4.29044
H	-4.85822	-0.33997	4.21323

$N(C_3H_7)_2C_2H_4$_radical + HEMA (Product) (-830.38246071)

N	-0.12611	-2.09632	-0.40924
C	1.33638	-2.14454	-0.22588
C	1.86262	-1.26325	0.93261
C	2.07663	-1.80493	-1.53624
H	1.58067	-3.18521	0.01744
H	1.40088	-1.54697	1.88386
H	2.94914	-1.37382	1.02937
H	1.64305	-0.20646	0.74484

H	1.74217	-2.46714	-2.34130
H	1.88836	-0.76861	-1.84242
H	3.15900	-1.92354	-1.40812
C	-0.93864	-3.19531	0.14221
C	-0.71503	-3.45651	1.65215
C	-0.74446	-4.49689	-0.66280
H	-1.98674	-2.89896	0.01718
H	-0.87663	-2.54564	2.23738
H	-1.41041	-4.22522	2.00881
H	0.30459	-3.81164	1.84348
H	-0.96879	-4.32338	-1.72012
H	0.28759	-4.86027	-0.58572
H	-1.40624	-5.28595	-0.28633
C	-1.81273	-0.83887	-1.74125
C	-0.75623	-0.79398	-0.62054
H	-2.17109	0.16994	-1.97899
H	-1.36979	-1.27148	-2.64331
H	-2.68185	-1.44529	-1.45857
H	0.03154	-0.10465	-0.93971
O	0.27727	2.02215	0.35059
O	3.64330	3.44416	-0.11434
O	-1.45134	3.51937	0.09411
C	1.23518	3.10393	0.12414
C	2.61804	2.45515	0.16764
C	-1.93555	1.19455	0.49906
C	-1.06997	2.33685	0.29763
C	-3.42006	1.39939	0.49005
C	-1.36794	-0.17669	0.69781
H	3.76200	4.04770	0.64057
H	1.12070	3.86325	0.90459
H	1.05017	3.56463	-0.85023
H	2.78356	1.97761	1.14007
H	2.70465	1.70083	-0.61564
H	-3.83962	1.16098	1.47700
H	-3.69242	2.42490	0.23436
H	-3.89487	0.71305	-0.22261
H	-2.16079	-0.84089	1.06006
H	-0.56799	-0.15364	1.44422

E.3 Supplemental figures

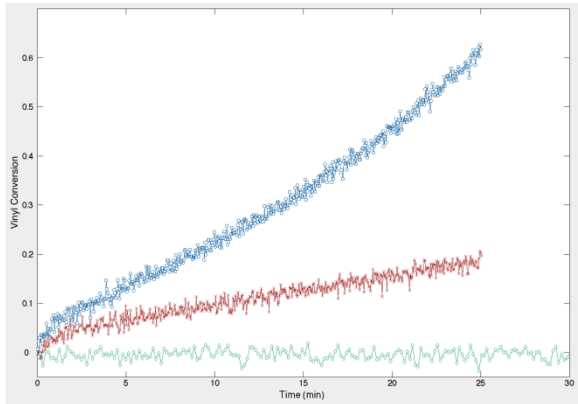

Figure S2 | Vinyl conversion of HEMA with MB$^+$/DIPEA, MB$^+$/MDEA and MB$^+$/TEA. Vinyl conversion of HEMA in solution with MB+/DIPEA (green squares), MB+/MDEA (red crosses), and MB+/TEA (blue dots) at equivalent irradiation conditions and stoichiometric amount of amine.

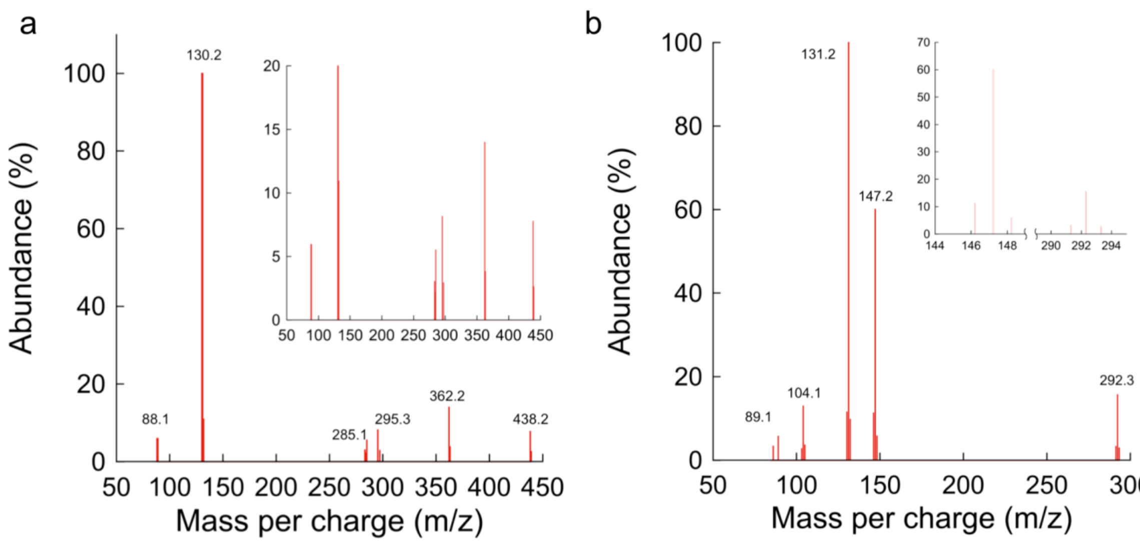

Figure S3 | ESI$^+$- MS monitoring of the photoreaction with MB$^+$/DIPEA and MB$^+$/DIPEA/DPI$^+$. **a,** Photoreduction of MB$^+$ by DIPEA in the presence of DPI$^+$ in methanol. Evidence of iodobenzene is the formation of the molecules with masses 285.1, 295.3, 362.2 and 438.2 m/z as iodobenzene is not very stable. **b,** Photoreduction of MB$^+$ with DIPEA in the absence of DPI$^+$. Peaks at 89.1, 104.1, 147.2 and 292.3 m/z are different decomposition products based on 2-

ethyliminopropane. Evidence of the formation of DIPEA-H due to extensive photoredox cycling is the formation of a higher abundance at 131.2 m/z than in Figure S2 a. [MB] = 0.004 M, [DIPEA] = 0.2 M, [DPI^+] = 0.04 M. Irradiation intensity equal to 37 mW/cm^2. DIPEA-H (131.2 m/z), MB^+ and DPI^+ abundances are less than 1 % abundance, thus not giving reliable signals. This peaks were assigned based on mass balances on the original reagents used and correlated to abundances detected to find iodine-containing molecules.

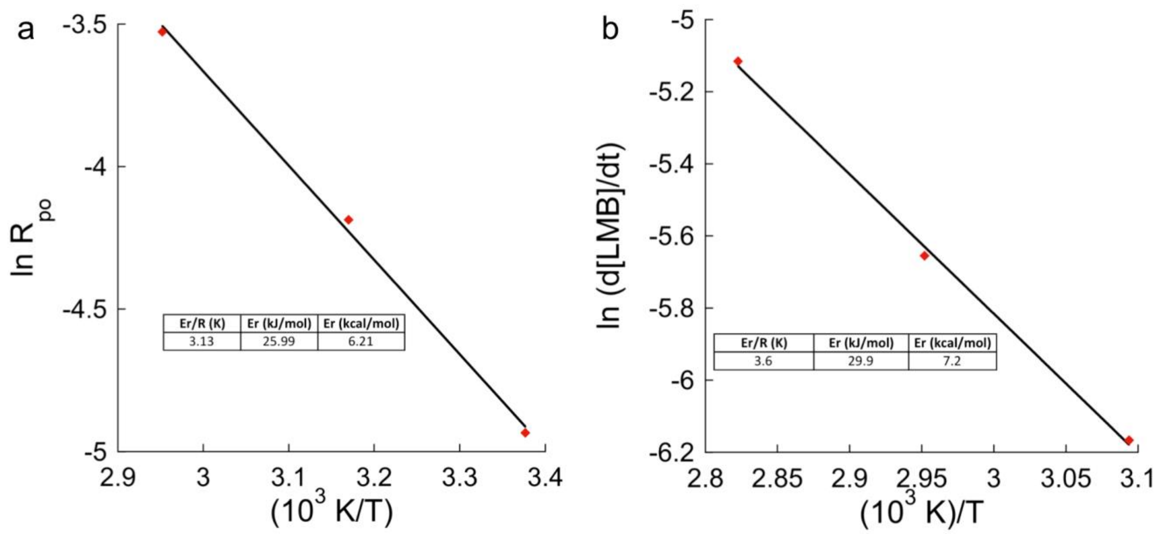

c

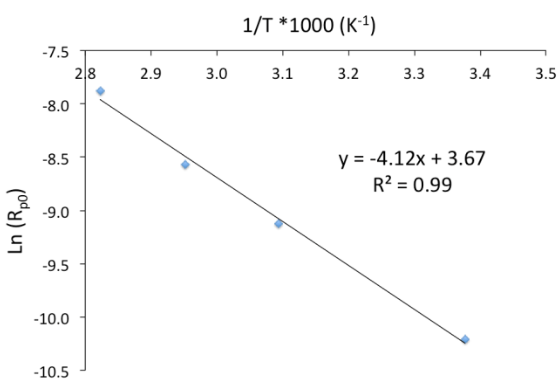

$$R_p = [M]_0 \frac{(A_{6165})_{t_1} - (A_{6165})_{t_2}}{(A_{6165})_{t_0} * (t_2 - t_1)}$$

where A_{6165} is the FT-NIR peak area centered at 6165 cm^{-1} correlated to (meth)acrylates

$$ln\ R_p = ln\left[A_p\left(\frac{A_d}{A_t}\right)^{1/2}\right] + ln\left[(f[I])^{1/2}\right] - \frac{E_R}{RT}$$

first two terms on the right treated as constant for linearization

$$E_R = E_p + \frac{E_d}{2} + \frac{E_t}{2}$$

$$E_p = 5.2342\ kcal/mol$$

$$E_t = 7.4906\ kcal/mol$$

Figure S4 | Activation energy (ΔE_{act}) for reaction between LMB and DPI+, which generates both radicals and MB^+. a, Activation energy for consumption of HEMA. If we subtract the activation energies for propagation and termination, calculated to be 1.5 kcal/mol with DMPA, we obtain an ΔE_{act} for initiation of 6.6 kcal/mol. Intensity equal to 13 mW/cm^2. **b,** Activation energy for the production of MB^+ after 10 s irradiation. Intensity equal to 60 mW/cm^2. [MB] = 0.004 M, [DIPEA] = 0.2 M, [DPI^+] = 0.04 M. Irradiation intensity equal to 12 mW/cm^2. **c**, Activation energy for the radical initiation of HEMA with DIPEA and DPI^+Cl^- without light exposure. The same procedure was used to calculate the activation of initiation after adjusting for propagation and termination. E_p from Goodner et al. (in references), and E_t from the photopolymerization of HEMA with DMPA.

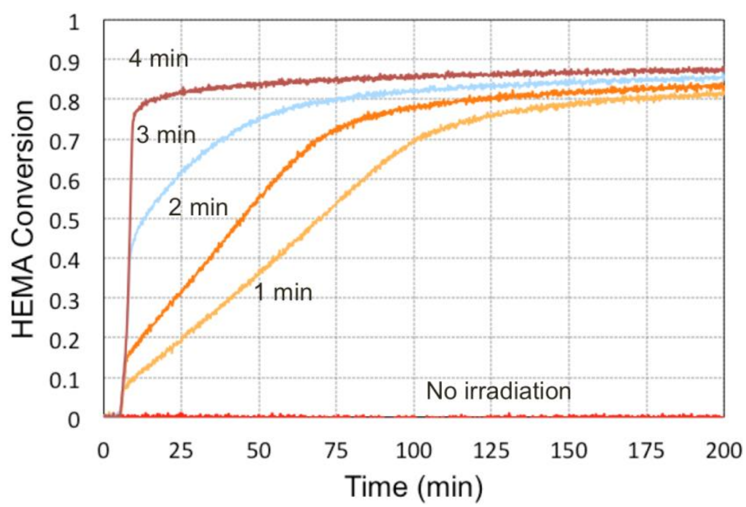

Figure S5 | Polymerization with increasing irradiation times. This shows the final plateau conversion is nearly the same in all cases, and as compared to the result with continuous irradiation. [MB] = 0.004 M, [DIPEA] = 0.2 M, [DPI^+] = 0.04 M. Irradiation intensity equal to 12 mW/cm^2.

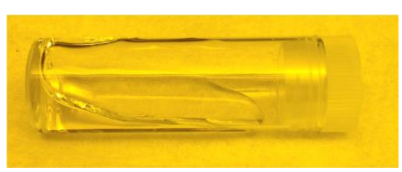

Figure S6 | CQ/EDMAB in HEMA after exposure to 60 s irradiation at equivalent amount of photons absorbed as MB^+/DIPEA/DPI^+ in Fig. 4c. Picture shows low degree of monomer conversion resulting in a liquid-like material after irradiation. Concentrations and exposure were as described in the methods section.

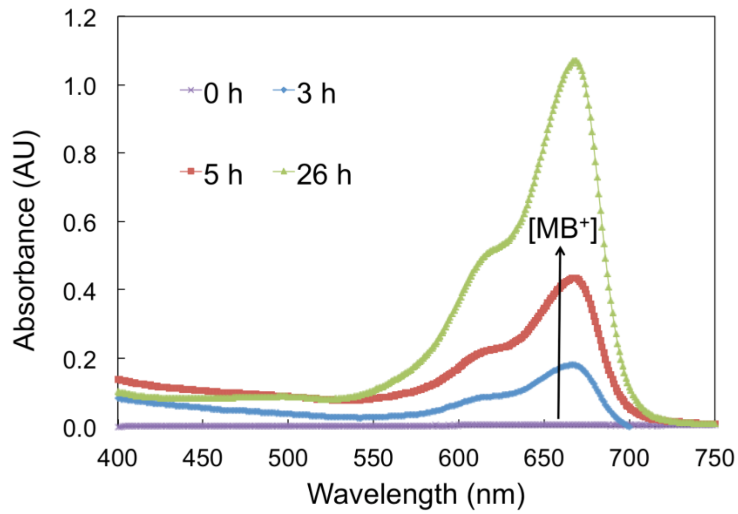

Figure S7 | Methylene blue extraction from poly-HEMA gel into a water solution by swelling of the loosely cross-linked network. [MB^+] was monitored in time by observing the increase in light absorption around 660 nm. As the material swelled at room temperature, MB^+ diffuses into the solvent. Thus, some of the final blue color of the polymer films can be washed out of the polymer network.